Critical dynamics at the yielding transition and creep behavior of amorphous systems : mesoscopic modeling

Chen Liu

To cite this version:

Chen Liu. Critical dynamics at the yielding transition and creep behavior of amorphous systems : mesoscopic modeling. Soft Condensed Matter [cond-mat.soft]. Université Grenoble Alpes, 2016. English. NNT : 2016GREAY066 . tel-01592136

HAL Id: tel-01592136
https://theses.hal.science/tel-01592136v1

Submitted on 22 Sep 2017

Communauté
UNIVERSITÉ Grenoble Alpes

THÈSE

Pour obtenir le grade de

DOCTEUR DE LA COMMUNAUTÉ UNIVERSITÉ GRENOBLE ALPES

Spécialité : **Physique théorique**

Arrêté ministériel : 25 mai 2016

Présentée par

Chen LIU

Thèse dirigée par **Jean-Louis BARRAT** et
codirigée par **Kirsten MARTENS**

préparée au sein du **Laboratoire Interdisciplinaire de Physique**
dans **l'École Doctorale de Physique**

Dynamique critique à la transition d'écoulement et comportements de fluage des systèmes amorphes : modélisation mésoscopique

Thèse soutenue publiquement le **10 novembre 2016**,
devant le jury composé de :

M. Jean-Louis BARRAT
Professeur, Université Grenoble Alpes, Directeur de thèse
Mme. Kirsten MARTENS
Chargé de recherche, CNRS, Co-directrice de thèse
M. David RODNEY
Professeur, Université de Lyon, Rapporteur
M. Alberto ROSSO
Directeur de recherche, CNRS, Rapporteur
Mme. Axelle AMON
Maître de conférence, Université Rennes 1, Examinatrice
M. Jerôme WEISS
Directeur de recherche, CNRS, Président

Critical Dynamics at the Yielding Transition and Creep Behavior of Amorphous Systems : Mesoscopic Modeling

Chen LIU

Supervisors: Dr. Kirsten Martens, Dr. Jean-Louis Barrat

Université Grenoble Alpes

Date of submission: 12-09-2016

Abstract

Amorphous systems deep below the glass transition, as well as colloidal glasses at high packing fractions, concentrated emulsions, foam systems, etc. exhibit divergent microscopic relaxation time scales and flow only upon a large enough external loading. This dynamical phase transition of amorphous systems from the apparent solid state to the apparent liquid state mediated by the external loading, is called the yielding transition. This transition is studied throughout this thesis by a mesoscopic modeling approach, specifically versions of the so-called elasto-plastic model.

After introducing a general background of the glass transition and experimental systems, that are the target of the elasto-plastic model description, a formulation of the elasto-plastic model, slightly different from the conventional ones used in the literature, is introduced for incorporating both the shear rate control and the stress control protocols. It is also shown that the mean-field Hebraud-Lequeux model can be derived from the spatially resolved elasto-plastic model by assuming some approximations.

Using the shear rate control protocol, the yielding transition is firstly probed by studying the shear rate dependence of the avalanche statistics close to criticality. A crossover from a non mean-field behavior to an apparent mean-field behavior with respect to an increasing shear rate is evidenced. Scaling laws in the zero shear rate limit, support the idea that the yielding transition belongs to a non mean-field universality class of a dynamical phase transition. The dependence of the symmetry of the average shape of the stress drops on the stress drop duration, the system size and the shear rate, leads to the interpretation that stress drops at finite shear rates result from the superposition of individual avalanches possessing a cooperative length and time scale.

By studying the macroscopic stress fluctuation, the cooperative length scale ξ_c is identified as the crossover size below which the scaling relation with the system size $\sim \frac{1}{L^d}$ implied by the central limit theorem breaks down. Further a saturation time scale T_c^S can be defined in the analysis of the time series of macroscopic plastic strain rate. Below this time scale one observes the manifestation of Brownian dynamics. The saturation time for systems of sizes smaller than the cooperative length ξ_c scales with the system size as a power law $T_c^S \sim L^{z_s}$, which can be interpreted as the scaling relation between the cooperative time and the cooperative length of individual avalanches.

Further using the stress controlled protocol, the yielding transition is studied by simulating typical creep experiments of the amorphous systems. The mesoscopic models (the elasto-plastic model as well as the mean-field Hébraud-Lequeux model) are shown to be capable to reproduce the response of the macroscopic shear rate to an imposed stress slightly above the yielding point in qualitatively good agreement with several experiments. Within the mesoscopic modeling approach, the results reveal that the creep behavior depends strongly on the initial condition of the amorphous system submitted to creep experiments.

Abstract

Les systèmes amorphes "mous", loin de leur transition vitreuse, comprennent les verres colloïdaux de haute fraction volumique, les émulsions concentrées, les mousses, etc...L'échelle de temps pour leur relaxation microscopique est divergente, et ils ne se mettent en écoulement que lorsque la contraint appliquée est suffisamment grande. Cette transition dynamique d'un état apparemment solide à un état apparemment liquide, suivant la contrainte imposée, est appelé transition d'écoulement. Cette transition est étudiée dans cette thèse par l'intermédiaire d'une modélisation mésoscopique, basé sur un modèle d'éléments élasto-plastiques en interaction.

Après une brève introduction à la transition vitreuse et aux systèmes réels supposés être décrit par le modèle élast-plastique, une formulation du modèle différente de celle qui est habituellement présentée dans la littérature est introduite, pour à la fois incorporer les protocole à taux de cisaillement fixé et le protocole à contraint fixée. A travers des approximations, un modèle mésoscopique de type champ-moyen (à l'origine décrit par Hébraud et Lequeux) est déduit à partir du modèle elasto-plastique qui contient les informations spatiales.

En appliquant le protocole à taux de cisaillement fixé, le transition d'écoulement est dans un premier temps étudiée à travers la dépendance de la statistique des avalanches (chutes de contrainte) en taux de cisaillement. Une transition d'un comportement de champ moyen à un comportement corrélé est observé en variant le taux de cisaillement. Les lois d'échelle observées dans la limite des petits taux de cisaillement supportent l'idée que la transition d'écoulement appartient à une certaine classe d'universalité de transition dynamique. L'étude de la symétrie de la forme moyenne des chutes de contrainte en fonction de leur durée, de la taille de système et du taux de cisaillement appliqué, conduit à l'interprétation que les chutes de contrainte résultent d'une superposition d'avalanches individuelles possédant une longueur coopérative et un temps coopératif.

En étudiant les fluctuations de contrainte macroscopique, la longueur coopérative ξ_c est identifiée par un crossover en taille de système en-dessous de laquelle le loi d'échelle avec la taille de système $\sim \frac{1}{L^d}$ impliquée par la théorème de limite centrale, ne fonctionne plus. En complément, une échelle de temps de saturation T_c^S est trouvé dans le séries temporaire de taux de cisaillement plastique, temps en-dessous duquel la dynamique de la contrainte peut être décrite par un mouvement Brownien. Le temps de saturation, pour les systèmes de taille plus petit que ξ_c obéit à une loi d'échelle avec la taille de système $T_c^S \sim L^{z_s}$. Cette dernière peut être interprétée comme la loi d'échelle entre la longueur coopérative et le temps coopératif des avalanches individuelles.

En appliquant le protocole de contrainte imposée, la transition d'écoulement est étudiée en simulant des expériences de fluage sur les systèmes amorphes. Les modèles mésoscopiques (le modèle elasto-plastique et le modèle champ moyen de Hébraud-Lequeux) sont capables de reproduire la réponse du taux de cisaillement macroscopique pour une contrainte imposée légèrement au-dessus de la contrainte, et ceci qualitativement en accord avec les expériences. A travers cette étude, il apparaît que le condition initiale influence significativement le comportement de fluage des systèmes amorphes.

Acknowledgments

I would like to express my gratitude towards several colleagues in academics.

In the first place, I should thank my supervisors, Kirsten Martens and Jean-Louis Barrat, for their patience and efficient guidance. Kirsten not only gives me lots of detailed suggestions and inspiration for the work of research as a supervisor but also takes care and encourages me often as a friend. Although occupied by the massive work in the position of the director of the lab, Jean-Louis always takes time for important discussions for pointing out key issues of the on going projects and making clear the direction for proceeding projects. Their guidance leads me to transform my vision as a student progressively to the vision of scientific researcher.

I would also like to thank Ezequiel Ferrero, Francesco Puosi and Laura Foini who have significantly helped me and contributed to the projects during this thesis. The discussions with Ezequiel has enlightened me a lot for a better understanding of the physics of the elasto-plastic model. I have learned the usage of the lammps packages for particle based simulation from Francesco. Laura have shared her code for solving the Hebraud-Lequeux model, that was helpful to validate the results for different numerical methods.

A lot of thanks to my group fellows (Elisabeth Agoritsas, Raffaela Cabriolu, Danial A. M. Fernandez, Eric Bertin, Luca Maradi, Alexandre Nicolas, etc) for useful scientific discussions and for their kindness and making a pleasant and healthy atmosphere in the entire group.

I thank also my friends who made the obstacles in life easier to overcome. I thank Xiaohui for her comprehension, support and warm accompany. At the end, I thank my parents who helped me in their way to support me all along my path.

Contents

List of Figures

Chapter 1

Introduction

Background

The time scale of observation is crucial when studying physical phenomena. The general notion of a solid state of a material relies on the following observation: Imagine a cubic block of material, by applying progressively a force dipole onto the two anti-planes of the cube, one can impose a certain deformation of order γ_o during a certain time interval of order τ_o. After removing the force dipole at the end of the time interval, if the deformation is canceled by itself, so that the block of material recovers its original shape, within a time scale $\tau_{recover} \ll \tau_o$, then one gets the idea that this material behaves like a "solid". This property called "elasticity" can be quantified by the ratio of the applied stress to the corresponding deformation, which is the "elastic modulus". Otherwise, if one applies the same deformation γ_o but during a time interval of order $\tau_o^{'}$ much larger than τ_o and if after releasing the applied force the system stays in its deformed shape γ_o , then one should get the idea of plasticity (or flow as a liquid). Moreover one can continue to apply the same force so that the material will deform with a shear rate $\frac{\gamma_o}{\tau_o^{'}}$. The ratio of the applied stress to this shear rate, characterizing how hard it is to deform plastically the material, is the so-called viscosity.

A well-known example of the above phenomenon considering the notion of a complex solid and liquid behaviour is the mixture of water and corn flour at a specific proportion. One can stay on the surface of the mixture of water and corn flour (hold in a big pool) without sinking into the mixture by running fast enough over the surface (i.e. the mixture behaves like a solid). While one sinks into the mixture if one slows down the movement (i.e. the mixture behaves like a liquid). The time scale for the deformation of the mixture, in the former case of running, is much shorter than in the latter case of slowing down the movement. This kind of substance seems to be unusual because most of the materials that we experience in life behaves at the considered time scales either only as a solid or only as a liquid. Whereas the mixture of water and corn flour changes its behavior at this observation time scales from a solid to a liquid, and to define this mixture as a "solid" or "liquid" loses its sharp meaning. Another second famous example is the pitch drop experiment: a pitch at short time scale (deformation by external loading up to a second) shows solid behavior while under gravity it drops 1 droplet for over about 10 years as a very viscous fluid.

The same kind of change from solid to liquid behaviour also resides in many glassy systems such as the window glass at room temperature, but the time scale for the change of behavior is too long to be observed in any experiments. As a consequence, the observation at a fixed time scale on the behavior of glass forming liquid such as silicon-dioxide at from high temperatures to low temperatures (quench to avoid crystallization) gives an impression of a "phase transition" (called "glass transition") from a "liquid state" to a "solid state", while the microscopic structure is identically disordered in both "states". The microscopic relaxation time scale $\tau(T)$ can be roughly considered as the crossover from apparent "solid state" to "liquid state" at a given temperature T. At high temperature the microscopic relaxation time scale is proportional to the apparent viscosity $\eta(T) \sim \tau(T)$, so that the glass transition from high to low temperature in experiments where time scale of observation is fixed, can be monitored by the divergence of viscosity. Empirically the glass transition temperature T_g is defined as the temperature when the viscosity reaches $10^{12} Pa \cdot s$. The glass transition happens also in systems of microscopic components of sizes much larger than molecular size ($\sim \mu m$), in which the dynamics is controlled by the volume fraction. Dynamical arrest i.e. divergence of microscopic relaxation times similar as in the glass transition happens upon a critical volume fraction that depends on the properties of the individual particles (For hard spheres this value is for example $\phi_g \approx 0.58$). The above example of a mixture of water and corn flour can be viewed as one of this category. In summary, the microscopic structural relaxation time scale of systems undergoing a glass transition diverges so that these systems behave like a "solid" for any experimentally accessible deformation rate at early loading stage, that is to say $\dot{\gamma} \gg \tau(T)^{-1}$ as long as the accumulated deformation is below the material dependent yielding threshold.

Above the yielding threshold (reached by the accumulated deformation $\gamma(\Delta t) = \dot{\gamma}\Delta t$ or the corresponding stress $\sigma = \mu\gamma(\Delta t)$ that glassy systems can no longer sustain), glassy systems either fail, e.g. the window glass, or begin to flow. However this flow behavior is *a priori* different in nature compared to the the flow at high temperature or when $\dot{\gamma} < \tau^{-1}$. This apparent transition from solid to liquid behavior when passing through the yielding threshold is referred to as "yielding transition" and the apparent fluid like behavior is characterized by non-linear rheological flow curves with a finite yield stress. In many cases this can be well fitted by the so-called Herschel-Bulkley expression $\sigma = \sigma_y + A\dot{\gamma}^n$, so that these systems are also referred to as "yield stress materials". For glassy systems, the regime $\dot{\gamma} \gg \tau^{-1}$ is mostly encountered in industrial applications, many experiments and particle based simulations have been carried out for studying the mechanical properties of glassy systems under this loading regime, which is also the domain of study of this thesis, but focusing on the mesoscopic approach.

It is important to note that for the temperature range $T < T_g$ or the high volume fraction range $\phi > \phi_g$, ergodicity is broken and the dynamics of glassy systems fall strongly out of equilibrium. Even though there are theoretical approaches to reveal the divergence of microscopic relaxation time, they are supposed to be applied for systems above the glass transition and where the ergodicity is valid. The study of glassy systems well below the glass transition under external driving lacks a substantial general theoretical framework. The theory of statistical physics for equilibrium systems as well as linear response theory for weak out-of-equilibrium systems are no longer valid approaches. Therefore phenomenological models and computer experiments (such as molecular dynamic simulation on quenched systems) play an essential role in this area to reveal physical insights underlying the macroscopic observations.

This thesis focusses on the study of the mechanical behaviors of driven glassy systems by taking phenomenological modeling as the main approach, specifically a mesoscopic elasto-plastic model. Mesoscopic elasto-plastic models have been developed since the early 90s, and have been modified in different ways to study various phenomena in driven glassy systems. Appropriate formulations and versions will also be proposed in the framework of this thesis to tackle different unsolved physical questions. With this approach, one can explore the domain of validity of the concepts and the mechanism proposed at mescoscopic scale to enhance our current understanding of glassy systems.

Organization of this thesis

This thesis is organized into two parts. In part I, first a brief review is given on the physical systems under consideration in the domain of studying driven glassy systems by using MD simulation and by the mesoscopic modeling that is adopted in this thesis. Then different experimental approaches and results on the mechanical behaviors of glassy systems are presented. Further the foundation of the concepts adopted in elasto-plastic model is discussed, and a general frame work of construction of elasto-plastic models is presented. Part II concerns the main work and results that have been achieved during this thesis. Different topics of driven glasses have been tackled by using slightly different versions of elasto-plastic model. The detailed methods and results on various topics are presented, such as avalanche dynamics, creep phenomena and rheology with finite temperature.

Part I

Background & Construction of the Elasto-plastic model

Chapter 2

Glass transition & Systems Under Consideration

In this part a brief review of glass transition is given for fixing the ideas on the properties of the systems studied during this thesis and to identify the main theoretical difficulties for describing glassy systems. Then a few examples are given, which cover most of the systems investigated by experimentalists for studying mechanical properties of glassy systems. The modeling method adopted in this thesis aims at giving some physical insights into the dynamics of these systems when they are mechanically driven.

2.1 Phenomenology of glass transition

A macroscopic measurement of an observable is given as the time average during a time window of duration $\tau_{measure}$ as $\mathcal{O}(t) = \frac{1}{\tau_{measure}} \int_t^{t+\tau_{measure}} \mathcal{O}(\Gamma(t'))dt'$, where $\Gamma(t)$ is the microscopic state (i.e. a point in phase space composed by all momenta and coordinates) of the system at time t and $\tau_{measure}$ is the time scale of the macroscopic measurement which is small compared to the macroscopic time scale so that the measurement can be considered instantaneous. As long as the ergodicity assumption is not violated, $\tau_{measure}$ is considered to be large enough such that the sampling of the phase space according to Hamiltonian equation can be represented by the Gibbs ensemble formalism (e.g. in the canonical ensemble the phase space is sampled with weight $\rho(\Gamma) \sim exp(-\beta\mathcal{H}(\Gamma))$, where $\beta = (k_B T)^{-1}$ and $\mathcal{H}$ is the Hamiltonian describing the equilibrium dynamics). This can only happen when the kinetic energy is large or comparable to the potential energy barriers, which is true in the situation where a system is coupled with a thermostat at high enough temperature.

By decreasing slowly the temperature of the thermostat, at each step of cooling the system, there is enough kinetic energy to overcome potential energy barriers to explore the phase space. Then at some point, the system will find a minimum configurational energy (i.e. the minimum of potential energy) with high energy barriers. Further cooling down will reduce further the kinetic energy so that the system will be trapped for a large timescale in this configurational minimum and will form a solid state. This final state of material is, in general, the crystallization where all particles are arranged in an ordered manner. The corresponding temperature below which crystallisaion takes place is the melting temperature T_m. The crystal structure is a thermodynamically stable state. The phase transition upon T_m by slow enough cooling is an equilibrium phase transition from a liquid to a solid.

If we decrease the temperature of the thermostat abruptly (i.e. quench) from a high temperature where ergodicity holds, the kinetic energy is also reduced suddenly while the particle positions are probably found to correspond to a liquid like configuration which is surrounded by many metastable states in the configuration space. The low kinetic energy prevents the system to overcome rapidly the potential energy barriers of a metastable configuration so that the system cannot sample its phase space efficiently during a macroscopic measurement time window $\tau_{measure}$, meaning that the ergodicity assumption breaks down. The dynamics becomes slow and the system is trapped in one metastable state for a long time before reaching another one at lower configurational energy. The system becomes apparently a solid for all macroscopic mechanical tests on time scales smaller than that of the microscopic relaxation. The system is said to enter a glassy state. The trapping in the metastable states of the system after the quench is affected by the cooling rate, such that the properties of the glassy state depend on it as well. After a rapid quench, the system explores its phase space with a very slow dynamics and eventually falls into deeper metastable states, so that the dynamical properties of the system will also depend on the waiting time after the quench. This is the so-called “aging” phenomenon. The difficulty to form glassy states by quenching depends on the details of the microscopic interaction between particles. It is possible (in computer simulations) to produce a supercooled liquid with pure water as far as there are no crystallization nuclei present. Even though supercooled water is experimentally very unstable and easily transformed to ice with tiny perturbations, this illustrates the physical picture of the rapid cooling down of a system. The first experiment of a rapid quench to avoid crystallization to form a glassy state in metallic systems has been performed on gold-silicon alloys [Klement et al., 1960].

In both the theoretical and the experimental point of view, it is easier to study the nature of the glass transition by quenching step by step to lower temperatures, since at high temperature we have well established theoretical and experimental facilities to extract information about the system. By monitoring this information along the quenching steps to low temperatures, the characteristics of the glass transition can be asymptotically approached.

2.1.1 Viscosity and relaxation time scale upon glass transition

At high temperature where the linear response theory holds, it is possible to derive the Green-Kubo relation between the macroscopic viscosity and the microscopic auto-correlations [Hansen and McDonald, 1990, Binder and Kob, 2011]

$$\eta = \frac{1}{k_B T V} \int_0^\infty dt \langle \sigma_{xy}(0) \sigma_{xy}(t) \rangle$$

of σ_{xy}, the off-diagonal components of the stress tensor. Its microscopic expression reads

$$\sigma_{xy} = \sum_{i=1}^{N} [m v_{i,x} v_{i,y} + \frac{1}{2} \sum_{j \neq i} x_{ij} F_y(r_{ij})]$$

where $x_{ij} = x_j - x_i$ the vector from particle i pointing to particle j, $v_{i,x}$ x-component of the velocity of particle i, $F_y(r_{ij})$ the y-component of force exerted by particle j on i due to the pair interaction. The ensemble average can be taken for instance in the canonical ensemble, since the system is supposed to be weakly out of equilibrium.

It is interesting to notice that the shear viscosity can be viewed as a measure of the relaxation time (relaxation time = time scale beyond which the system dynamics becomes uncorrelated with respect to previous states, equivalent to a loss of memory) up to a normalization prefactor proportional to $\langle \sigma_{xy}^2 \rangle$. Here the relation described in the introduction $\eta(T) \sim \tau(T)$ is roughly justified. By monitoring the viscosity of a glass forming liquid at each temperature along quench steps, one also gets information about the microscopic relaxation time scale at each temperature.

The dependence of the viscosity on temperature has been measured for various glass forming liquids, see figure 2.1 (left). This figure shows that the viscosity increases over about 15 magnitudes if the temperature is decreased only by factor of 3 to 4. This also indicates that the microscopic relaxation time scale increases drastically in a small range of decreasing temperature. To make this relation between viscosity and temperature more comparable for different materials, it is customary to

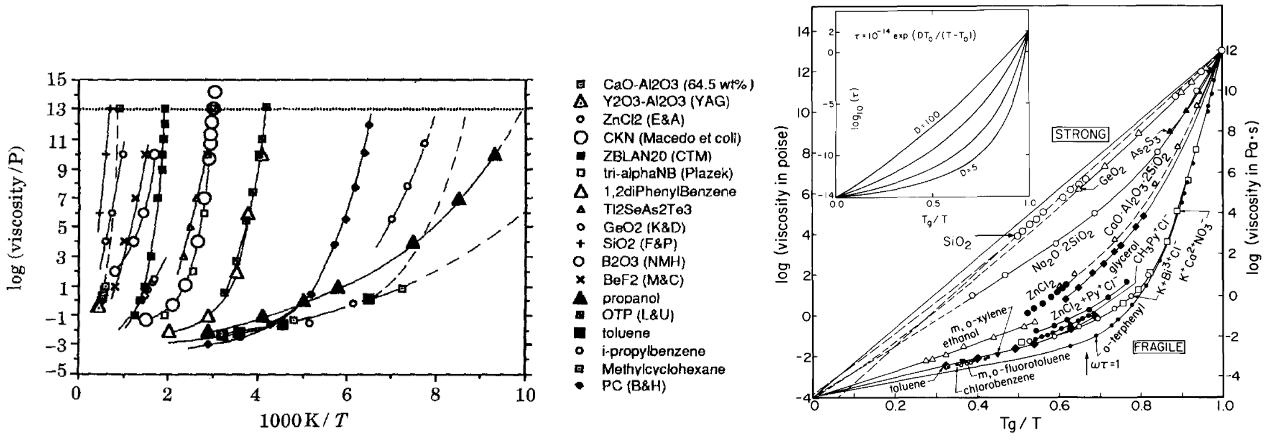

Figure 2.1: Left: "Arrhenius plot" - Viscosity versus inverse of the temperature in log-lin scale. Right: "Angell plot" - Viscosity versus inverse of the temperature rescaled by T_g. [Binder and Kob, 2011]

introduce a reduced temperature scale. This is done by defining a phenomenological "glass transition temperature" T_g such that $\eta(T_g) = 10^{12} Pa \cdot s$ and plotting viscosity versus T_g/T, see figure 2.1(right). For materials such as SiO_2, the viscosity can be well fitted by Arrhenius law $\eta \sim exp(\frac{B}{k_B T})$, while for other systems $\eta(T)$ follows a sub-Arrhenius law. By comparing the slope in the Angell plot at T_g, glassy systems can be divided into two classes: "strong glasses" for those following an Arrhenius law and "fragile glasses" for those following a sub-Arrhenius law.

The tendency of a drastic increase of viscosity indicates that a further quench to lower temperatures will make the system behave apparently as a solid and the underlying microscopic dynamics is long time auto-correlated, longer than any accessible experimental time scale.

2.1.2 Stretched exponential relaxation

A direct measure of microscopic dynamics is the "Van Hove function" $G(\mathbf{r}, t)$ and its spatial Fourier transform the "coherent intermediate scattering function" $F(\mathbf{k}, t)$. The spatial-temporal transform of the "Van Hove function" is the "dynamical structure factor" $S(\mathbf{k}, \omega)$. Precisely

$$G(\mathbf{r}, t) = \frac{1}{N} \sum_i \sum_j \langle \delta(\mathbf{r} - (\mathbf{r}_i(t) - \mathbf{r}_j(0))) \rangle$$

$$F(\mathbf{k}, t) = \int d\mathbf{r}^d \exp(-i\mathbf{k} \cdot \mathbf{r}) G(\mathbf{r}, t) = \frac{1}{N} \langle \rho_{\mathbf{k}}(t) \rho_{-\mathbf{k}}(0) \rangle$$

$$S(\mathbf{k},\omega) = \frac{1}{2\pi}\int dt \exp(i\omega t) F(\mathbf{k},t)$$

The "coherent intermediate scattering function" is actually the auto-correlation function at time interval t of density fluctuations for a given mode $\mathbf{k}$. This quantity is experimentally accessible by light or neutron scattering and has been measured for various glass forming liquids at temperatures approaching glass transition. Experimental results of $F(\mathbf{k},t)$ on glycerol at temperatures above the glass transition is shown in figure 2.2(left). The structural correlation in time becomes longer and longer as the temperature approaches the glass transition. Smaller time intervals for the intermediate scattering function is limited by technical issues. This part of the auto-correlation function corresponds to the second step of relaxation at low temperatures typically shown in the figure 2.2(right). Figure 2.2(right) corresponds to MD model simulation results for silica. At any temperature the small plateau at the beginning represents the ballistic regime where the interaction does not affect the motion of particles. The form of the correlation function after the ballistic regime crosses over from one step relaxation to a two step relaxation function as the temperature decreases. At high temperature the relaxation is simply exponential, while at temperatures approaching the glass transition, a second plateau appears due to the so-called "cage effect" or "β-relaxation" where particles vibrate in a "cage" formed by the surrounding particles. The caging effect takes longer and longer as the temperature decreases. The end of the plateaus corresponds to the typical time of the cage effect. Then a structural reorganization or a "cage break" takes place, which is called "α-relaxation". This "α-relaxation" is reflected in the second decay to zero of the intermediate scattering function. At low temperatures not only the time scale of relaxation becomes larger but also the exponential form becomes stretched. This stretched exponential decay is well fitted by Kohlrausch-Williams-Watts (KWW) function

$$\Phi(t) = A\exp(-(t/\tau_\alpha^\beta))$$

where τ_α refers to the time scale of "α-relaxation". $\tau_\alpha(T)$ is found to be proportional to $\eta(T)/T$ and the stretch exponent $\beta\approx 0.7$ [Wuttke et al., 1996].

From the behavior $F(k,t)$ in the glass forming regime at temperatures approaching the glass transition, it strongly suggests that the "cage effect" will last for ever and τ_α will go to infinity if the temperature is further decreased, which is actually one of the predictions of the mode coupling theory [Binder and Kob, 2011]. A "Cage effect" that lasts forever in systems quenched from high temperature to $T < T_g$ has

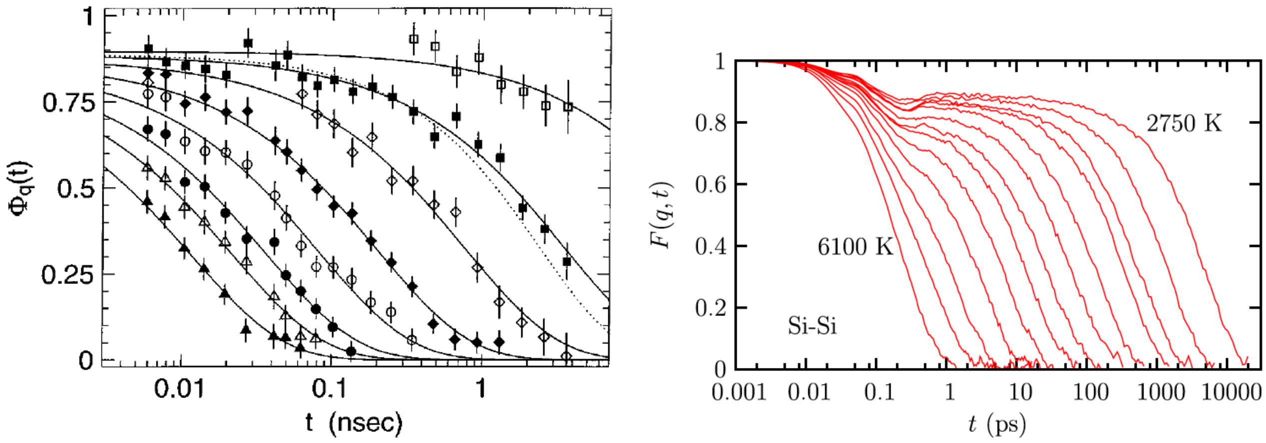

Figure 2.2: Left: Intermediate scattering function of glycerol by neutron scattering $\Phi(q,t) = F(q,t)/F(q,0)$, where q corresponds to the first peak in static structure factor. From the bottom to the top T decreases from $413K$ to $270K$, $T_g \approx 185K$ for glycerol [Wuttke et al., 1996]. Right: $Si - Si$ Intermediate scattering function in model systems of silica [Horbach and Kob, 2001].

as a consequence that the structure of glassy systems look similar to that of its liquid state, see figure 2.3. With its particles being trapped by their neighbors and the similarity concerning the typical configurations compared to a liquid state, glassy states can be viewed as frozen liquids, see figure 2.3.

2.1.3 Dynamical heterogeneities and the break down of the Einstein relation

It is known that the stretched exponential relaxation of the correlation function is related to dynamical heterogeneities. By tracing the mean-square displacement of individual particles in different regions, one observes that (i) one individual particle vibrates around its location for a while followed by periods with rather large jumps and (ii) when particles of some regions are vibrating around their location, particles of other regions may make significant displacements. In other words this means that the dynamics is not homogeneous over space in a glassy state and intermittent in time in a given region. Some regions have an exponential relaxation of shorter time while others take a long time for decorrelating the particle positions. The form of a stretched exponential relaxation over the whole system is the effect of summing up over the heterogeneous relaxation dynamics of all the regions.

Dynamical heterogeneities seem also to be related with the decoupling of diffusion coefficient and viscosity when the temperature approaches the glass transition. At high temperature the diffusion coefficient D and viscosity η are related by the Stokes-

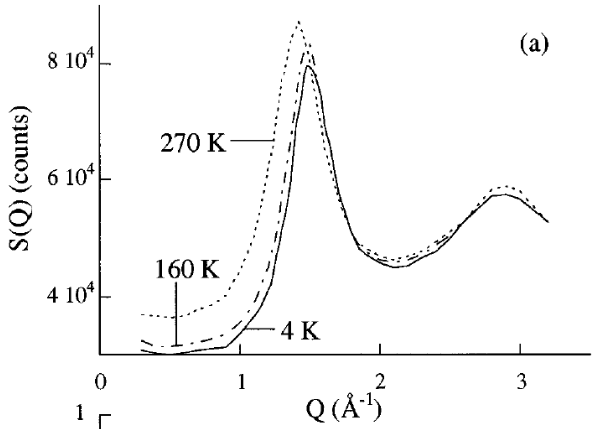

Figure 2.3: Static structure factor of liquid ($T = 270K$) and glassy ($T = 160K$, $4K$) polybutadiene at ambient pressure, obtained from neutron scattering measurements. $T_g = 180K$ [Arbe et al., 1996]

Einstein relation $D\eta/T = Cst$. This means that the time scale of the diffusive process and the one governing the viscous flow are the same up to a constant factor. This relation breaks down as soon as the temperature of the supercooled liquid goes down to T_g. It is commonly found that the diffusion coefficient $D(T \gtrsim T_g)$ becomes 2 to 3 order of magnitudes larger than that computed according to the Stokes-Einstein relation when compared to the measured value of $T/\eta(T \gtrsim T_g)$ [Mapes et al., 2006]. This is proposed to be explained through the existence of the dynamical heterogeneities. The idea is that close to the glass transition, self-diffusion is controlled by fast moving particles whereas viscosity probes the time scale needed for all particles to move [Berthier and Biroli, 2011].

2.1.4 Thermodynamics

Across the phase transition from a liquid state to a crystalline state, some thermodynamic quantities vary not in a continuous fashion. This is typically described by the Clausius-Clapeyron relation $(\frac{dP}{dT}) = \frac{L}{T\Delta v}$. "$L$" is the latent heat of the phase transition, Δv is the change in specific heat at the phase transition. "$\frac{dP}{dT}$" is the slope of the phase coexistence curve in the Pressure-Temperature plan. The discontinuous change in entropy across the phase transition is then computed as $\Delta S_m = LN/T_m$ the sub-index "m" for melting. This is not the case for the entropy of a supercooled liquid across T_m, which appears in fact to be continuous. Thus below T_m there is an excess entropy in the supercooled liquid compared to the crystal $\Delta S(T)$, with $\Delta S(T = T_m) = \Delta S_m$. Extrapolation of this excess entropy in supercooled liquids leads to define the Kauzmann temperature T_K [Kauzmann, 1948] at which the excess entropy vanishes. At T_K, the “ideal glass” state [Gibbs and DiMarzio, 1958] is supposed to appear which is introduced from the idea of separating the kinetic entropy contribution from the configurational entropy contribution.

Since supercooled liquid or glassy systems are trapped in some metastable states by a rapid quench, the kinetic energy per particle depending on the temperature only allows the system to mainly visit metastable states of certain depths among those of the whole potential energy landscape. The dynamics of the supercooled liquid can be divided into two parts: the vibration around the minimum of the potential energy landscape and the temperature dependent sampling of potential energy minima. It is considered that the vibrational dynamics is similar to that of a crystal state, while the crystal has only one potential energy minimum to explore [Binder and Kob, 2011]. So that the excess entropy of the glassy systems is considered due to the multiple metastable configurations allowed to visit. As observed in experiments, the rate of change of the glass entropy with respect to the temperature is faster than that of a crystal state. Extrapolation of this tendency leads to a certain point $T_K > 0$ where the excess entropy becomes zero. If the excess entropy is due to multiple configurational choices, that suggests the hypothesis that the glassy state at T_K has a unique lowest energy configuration, which would correspond to the “ideal glass”.

In practice, the Kauzmann temperature seems to correlate with the fragility of the glass, but this has not been yet clearly confirmed [Debenedetti and Stillinger, 2001].

2.2 Glass forming systems

“Amorphous materials” or “glassy materials” cover a large class of materials with microscopic components of sizes that span from atomistic scale to the macroscopic scale (∼mm). An important common feature of glassy materials is that they are far from equilibrium systems and that the dynamics is so slow that the relaxation time scale is out of the scope of the time scale reached by experiments and computer simulations. With this generic descriptive “definition”, many systems can be included in this category of materials, such as metallic glasses, colloidal assemblies, emulsions, foams, and granular materials etc [Berthier and Biroli, 2011]. There are two subcategories separating these systems: (i) “Hard” glassy systems or atomic glassy systems with components of molecular scale require for a full description quantum mechanics to calculate the electronic structure. The elastic modulus of these systems is of order $100GPa$. These systems easily break beyond yielding and the plastic flow regime is short; (ii) "Soft" glassy systems consist of components that are large enough to be treated in a classical framework. The elastic modulus is of order $100Pa$. These systems typically enter a plastic flow regime beyond yielding. In the first case, as far as the inter-particle distance is large compared with the thermodynamic wave length, it is convenient to treat the system, especially in computer simulations, in a classical manner by adopting adequate semi-empirical interaction potentials, so that in a theoretical point of view, systems in both categories share common features of coarse-grained scales regarding their out-of-equilibrium dynamics despite the differences in the details of their microscopic interactions.

"Hard" glass forming systems

The most prominent example of this category of glass forming systems is the window glass, made primarily of silica SiO_2 (with many network modifying additives). Some other examples are listed in figure 2.1. As mentioned above, in the study of these systems by molecular dynamics simulation, appropriate semi-empirical potentials are adopted. The parameters of these semi-empirical models are adjusted in order to fit some properties such as the melting temperature, microscopic structure, diffusive motion of particles and the elastic moduli [Rodney et al., 2011]. One of the successes of the semi-empirical potential for describing the atomic dynamics of glassy systems can be shown by comparing the static structure factor $S(q)$ of SiO_2 from neutron scattering experiments and that obtained by simulations using a well adopted semi-empirical potential, see figure 2.4. There are several semi-empirical potentials, such as Stillinger-Weber potential, Tersoff potential, EAM and Lennard-Jones type potentials. These potentials have all adjustable parameters and different terms for taking into account for example the directional or electrostatic interactions between atoms, to be able to simulate for example metallic alloys of different components. The binary Lennard-Jones potential developed by Kob and Andersen is the most widely used, which can reproduce the properties of $Ni_{80}P_{20}$ [Rodney et al., 2011]. Once the semi-empirical potential is chosen, either classical molecular dynamics or Monte-carlo simulations can be performed on these systems. The glass transition and the properties of the glassy state of these systems can be studied, even though there are technical issues limited by the computing capacity, such as the cooling rate for preparing a glassy state system which is usually unrealistically fast. But still, despite these shortcomings, MD simulations give important physical insights on the glassy systems under driving.

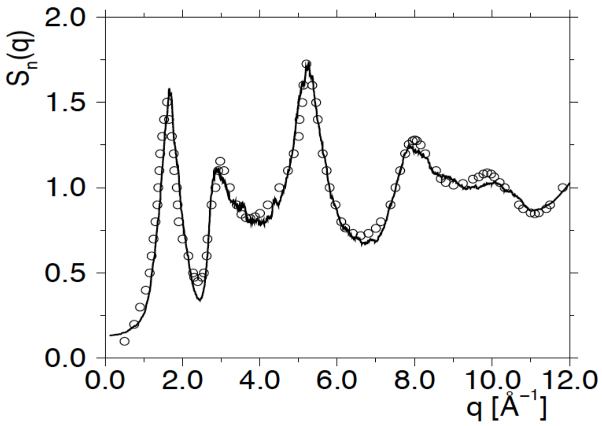

Figure 2.4: Static structure factor of SiO_2 at $T = 300K$. Open circles: Neutron scattering experiments by Price and Carpenter[Price and Carpenter, 1987]. Solid line: Molecular dynamics simulation by Horbach and Kob[Horbach and Kob, 1999]

“Soft” glass forming systems

“Soft” glass forming systems are in general systems of small macroscopic particles, mostly merged in a solvent liquid. In these systems, volume fraction instead of temperature controls the material properties. In the case of low volume fraction, the dynamics of these particles are nothing but brownian motion, and the rheology is dominated by the rheology of the solvent liquid. The glass transition occurs, instead of a quench of temperature in contrast with the atomic glassy systems, upon the increase in volume fraction up to a critical value (e.g. for hard spheres $\phi_c \simeq 0.58$). The effects of the volume fraction on the time correlation function for these “soft” glass systems is similar to that of the temperature on the atomic glassy systems. The “α-relaxation” diverges as the volume fraction approaches ϕ_c [Pusey and van Megen, 1987]. To name some typical “model glass” systems in experimental studies: In the first report of a glass transition of a colloidal system by Pusey & Magen [Pusey and Van Megen, 1986], they used polymethyl-methacrylate (PMMA) particles stabilized by poly-hydroxystearic acid (PHSA), the radius of which is $\simeq$ 300 nm, and for which the interaction potential is effectively a hard sphere potential. N-isoppropylacrylamide (NIPA) gel particles (diameter$\simeq$ 1 μm) used for micro-fluidics experiments [Nordstrom et al., 2010], can be treated as Hertzian spheres. Foams and emulsions (composed by stabilized castor oil droplets of diameter $\simeq 0.3\mu m$) can be well described by a truncated harmonic or Hertzian contacts, at least at high enough packing fractions [Durian, 1995, Bécu et al., 2006, Fall et al., 2010, Bonn et al., 2015]. The interaction potential can be tuned from pure repulsive to attractive for PMMA colloids by adjusting the concentration of added polystyrene, and the attraction which is due to the "depletion" can be approximated by Asakura-Oosawa potential [Lu et al., 2008, Poon et al., 1999]. It is also possible to tune the interactions in emulsions from repulsive to attractive by controlling the surfactant concentration [Durian, 1995, Bécu et al., 2006, Fall et al., 2010, Bonn et al., 2015]. Classical molecular dynamics simulations are also extensively used for studying these systems by adopting the effective interaction potentials, parameterized to mimic the experiments.

By tuning the poly-dispersity of "soft" glass forming systems, one can either obtain a crystalline structure or an amorphous structure. The similarity of the dynamics with the atomic glasses makes it possible to consider "soft" glassy systems as a convenient "model" system to gain physical insight to the dynamics of the atomic glasses.

"Jamming" and "Gelation"

As the effective interaction potential can be tuned in "soft" glasses from pure repulsive to attractive, or from long range to short range interactions and the diameter of particles can be easily varied, the interplay between this interaction and thermal fluctuations can give rise to other complex behaviors in addition to the glass transition.

In the case where pure repulsive interactions are large compared to thermal fluctuations or in the case where the diameter of the particles are large so that the thermal fluctuations become negligible, systems behave like a solid only when the volume fraction increases close to the random close packing fraction $\phi_J = 0.64$, which is the so-called "jamming" point. In the "jammed" state, the degrees of freedom of particles are constrained by a large enough number of contacts. The jamming transition is a pure mechanical phenomenon and corresponds to the transition to a state of mechanically blocked hard spheres, which is of different nature than the glass transition.

In the case where thermal fluctuations are in competition with attractive interactions, bonds between particles are formed and dissociated continuously. At $\phi < \phi_g$ particles may be bonded into a rigid chain network percolating throughout the entire system, so that the system can sustain a finite stress at macroscopic scale and behaves apparently like a solid. This is the so-called "gel transition".

As will be also mentioned in Chapter (4), the elasto-plastic model adopted in this thesis is based on the idea of local shear transformations, which are observed in simulations of systems with different types of interaction potentials and in real

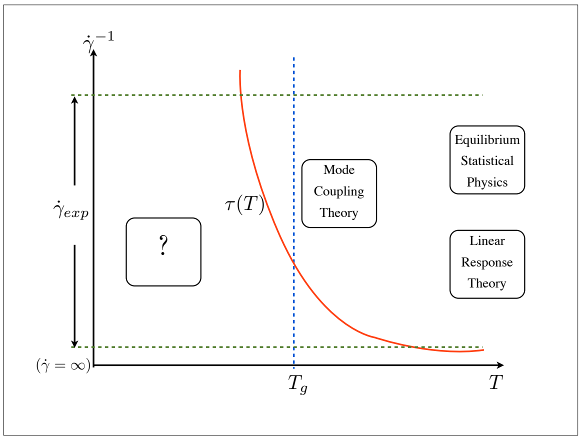

Figure 2.5: Red line: the microscopic structural relaxation time scale as function of temperature. In between the two horizontal dashed lines: the domain of experimentally accessible loading time scale. Box: The applied theoretical frameworks at their corresponding temperature domains

systems as for example in bubble rafts or colloidal glasses. However systems in which local shear transformations are observed, have a typically a high volume fraction, larger than that of network forming gels. Even though the boundary for fixing a domain of validity of the elasto-plastic model is not clearly identified, it seems more appropriate for describing systems that are deep below the glass transition, or strongly above the jamming transition.

2.3 Some theoretical approaches

Figure 2.5 shows roughly the situation for the study of mechanical properties of disordered materials. The microscopic relaxation time scale $\tau(T)$ is a well defined measurable quantity at high enough temperature. This concept resides upon approaching the glass transition from above and $\tau(T)$ tends to diverge at lower temperatures where it is not experimentally accessible. The response of the system to an external loading from a quiescent state depends on the loading time scale, which can be characterized by the loading strain rate. The range of experimentally accessible strain rates is represented by the interval between the two dashed green lines in the figure2.5.

Approach from the liquid side

At high temperature where $\dot{\gamma}^{-1} > \tau$, the sampling of the phase space of a system is dominated by the high temperature fast dynamics, which can be described by equilibrium statistical mechanics. External loading can be regarded as a perturbation of this high rate sampling, so that perturbation theory around equilibrium e.g. linear response theory can be applied to compute macroscopic properties of the system. As the temperature approaches T_g, the dynamics begins to slow down. Nevertheless as far as the ergodicity is maintained, the so-called mode-coupling-theory can be applied.

The mode-coupling-theory is base on the Zwanzig-Mori projection formalism [Zwanzig, 1960, Mori, 1965]. The evolution of a set of observables is expressed, instead of a formal Liouville expression, by a hierarchy of Langevin type equations $\dot{A} = i\Omega A(t) - \int_0^t M(t-t')A(t') + f(t)$. The so-called "fluctuation force" $f(t)$ comes from the orthogonal part of $A(t)$ and $M(t)$ the memory kernel derives from $f(t)$. Further the evolution of $f(t)$ can be expressed by an equation of similar form with higher order terms of memory kernel $M_1(t)$ and fluctuation force $f_1(t)$, where f_1 denotes the orthogonal part in the subspace excluding A. The mode coupling theory consists to truncate the hierarchy at second order and identify a projection subspace with the wave vectors in Fourier space, which correspond to different length scales of observation in real space. Different Fourier modes are then coupled through the memory kernel. Within this formalism, the investigation of density fluctuations makes use of the static structure factor which is computed within the canonical ensemble. That is the reason why applying mode-coupling-theory requires the ergodicity. The success of the mode-coupling-theory for describing supercool liquids is that it can predict a mode-coupling-temperature T_c, slightly higher than T_g, at which the macroscopic viscosity diverges. However since ergodicity is assumed in the procedure of MCT computing, it is not appropriate for glassy systems under mechanical load.

Approach from the solid side: Potential energy landscape (PEL)

At temperatures well below T_g, the dynamics of glasses is very slow and there is still no general valid theoretical frame work for describing this slow dynamics. Under an external loading time scale $\dot{\gamma}^{-1} < \tau$ (here assuming the concept of relaxation time is still meaningful even if it is not measurable at very low temperature) with a small amount of deformation, the system is perturbed by the external loading to explore a little further its phase space around the actual state which is determined by the slow dynamics. The system behaves as a solid. Once the loading amount is large, the sampling of phase space is then dominated by the external loading rather than the low temperature slow dynamics. The glassy system under external loading either yields as a complex fluid or fails. Most of the theoretical and simulation work studying driven glass systems aims at finding proper observables to characterize the stationary states under driving as well as the transient states towards the stationary flow. It is clear from the beginning that in this field of research of strongly out-of-equilibrium dynamics with additional driving no general theory can be applied, so that molecular dynamics simulation and phenomenological modeling play an essential role for acquiring and testing ideas and concepts aiming at understanding physics of glassy systems under external loading. Developing mesoscopic elasto-plastic models, as adopted in this thesis, is one of these approaches. Details of the foundation and the formulation of these models are discussed in chapter 4.

Since the dynamics of glassy systems is slow, an alternative approach, instead of studying the sampling in the complete phase space, is to study how does a glassy system sample its potential energy landscape. The potential energy landscape is defined by $U(\{\mathbf{r}_i\}_i)$, the total potential energy as function of all particle coordinates $\mathbf{r}_i$, which is a hyper-surface in $(Nd+1)$ dimensional space, where N the number of particles and d the system dimension. The link between the dynamics and the way of sampling the potential energy landscape at different temperatures has been studied earlier [Sastry et al., 1998]. The sampling of the potential energy landscape in time can be viewed as the stochastic process of hopping from one metastable state to another, while the hopping rates depend on the temperature. This physical picture is actually adopted by Bouchaud's trap model which provides a mechanism of ergodicity breaking and is in good agreement with spin glassy systems [Bouchaud, 1992]. Following the spirit of the trap model, P. Sollich et al. proposed the so-called "Soft Glass Rheology" model (SGR) [Sollich et al., 1997], aiming at a phenomenological description of a way of sampling the potential energy landscape of driven glassy systems through activated dynamics. As discussed in chapter 4, the mesoscopic elasto-plastic model adopts somehow this picture of hopping energy barriers on a coarse-grained level, that is, instead of considering the potential energy as function of particle coordinates, considering the potential energy of a local block of material as function of deformation.

There are efforts devoted to characterize the structure of the hyper-surface of the potential energy landscape. It is generally known that the total number of metastable states increases exponentially with the number of particles [Stillinger, 1999] and the metastable states are organized in a hierarchical structure. Several metastable states are grouped into a meta-basin. The sampling within a meta-basin corresponds to the β-relaxation, and the sampling over meta-basins corresponds to the α-relaxation [Rodney et al., 2011, Johari and Goldstein, 1970]. The complex structure of an potential energy landscape can be visualized by the “tree graph”. However, the correct way to understand the behavior of glassy systems under driving in terms of energy landscape sampling is still a missing piece of the puzzle and it remains a difficult task.

The sampling of the energy landscape under driving (or even without driving) depends on the underlying processes of large scale observable behaviors in glassy systems. There are several fundamental questions to be answered for bridging the two sides, such as: How to describe the kinetics of sampling? How is the kinetics of sampling dependent on the temperature and on the external driving? And how is the sampling to be described on a macroscopic scale?

Chapter 3

Experimental Mechanical Behaviors

Since this thesis focuses on the study of the mechanical behavior of glassy systems using a mesoscopic modeling approach, a brief review of the corresponding experimental results for amorphous systems (i.e. systems deep in glassy state) is given in this chapter. Within the experimentally accessible time scale, much shorter than the microscopic relaxation time scale, amorphous systems switch from a solid state to a liquid state trough a yielding transition, depending on the loading conditions. Experimental studies are mainly focused on three aspects: (i) Elasticity of the apparent solid like state when loading is weak; (ii) Rheology and flow in the apparently liquid state above yielding; (iii) The transition from solid to liquid when the loading approaches the transition point. Here we focus on the last two aspects.

In this chapter, we review some experimental results as well as some insights from molecular dynamics simulation on the phenomenology that is mainly addressed during this thesis by the "elasto-plastic" model.

3.1 Steady state rheology

The general idea of rheology is to find out a constitutive law relating the local stress with the local strain rate, which makes the continuum mechanics description complete. It is assumed that physical quantities such as velocity vary continuously in space at any instant within the limit of experimentally accessible spatial resolution. In the framework of continuum mechanics, with the knowledge of boundary conditions and the knowledge of the constitutive law, it is then in principle possible to obtain the entire information on the flow.

In the simplest case of Newtonian fluid, the local viscous stress tensor is proportional to the local strain rate $\sigma = 2\eta\dot{\epsilon}$, where the dynamical viscosity η is a material parameter and constant in any situation. This dynamical viscosity can be measured in a simple geometry of a rheological test insuring the homogeneity of a bulk flow so that the bulk viscosity measured as the ratio of the stress applied on the bulk flow to the bulk strain rate can be identified with the constitutive law. By comparing for instance the steady state velocity field coming from the theoretical solution of the Navier-Stokes equation with that coming from experimental measurements in a different geometry, the Newtonian fluid model with constant viscosity η can be validated.

In the study of flow of glassy materials under large deformation, especially for the "soft" glassy systems, most of the works in the literature keep the spirit of continuum mechanics in the sense that the velocity field can be completely computed from the knowledge of the time dependent stress tensor field. However the situation is rather complicated. The steady state flow of yield stress materials may either depend or not on the loading history. This is typically reflected in the bulk rheological testing loop of increasing the strain rate and then decreasing the strain rate. For some of the systems of pure repulsive interaction, normally called "simple yield stress materials", the upward rheological testing (by increasing the bulk strain rate) gives the same bulk rheology flow curve as the downward rheological testing (by decreasing the bulk strain rate), suggesting that the steady state flow at a given bulk strain rate is always the same (see figure (3.1)(a)). For other systems, a hysteresis of bulk flow curve arises from an upward then downward rheological testing loop, suggesting that the steady state flow depends on the loading history (see figure(3.1)(b)). Only in the case of "simple yield stress materials", it is expected to find a simple constitutive law in a similar form to the Newtonian fluid so that the steady state flow depends only on the material properties.

"Simple yield stress materials"

The complexity of "simple yield stress materials" compared to Newtonian fluids is that the viscosity itself depends on the strain rate $\eta(\dot{\epsilon})$ and it diverges in the low strain rate limit because of the existence of finite yield stress. From the point of view of the continuum mechanics, the flow stability is affected by the property of $\eta(\dot{\epsilon})$. This can be illustrated in a simple anti-plane shearing situation. The flow velocity profile for a homogeneous shear rate $\dot{\epsilon}$ in space is unstable if $\frac{d}{d\dot{\epsilon}}\sigma(\dot{\epsilon}) = \frac{d}{d\dot{\epsilon}}(\eta(\dot{\epsilon})\dot{\epsilon}) < 0$, and a shear band arises when shear is started from the solid state, see Appendix A.

From the idea of the existence of a unique local constitutive law relating $\sigma(\mathbf{r}, t)$ and $\dot{\epsilon}(\mathbf{r}, t)$, one can at least deduce two points: (i) Local stress and local stain rate

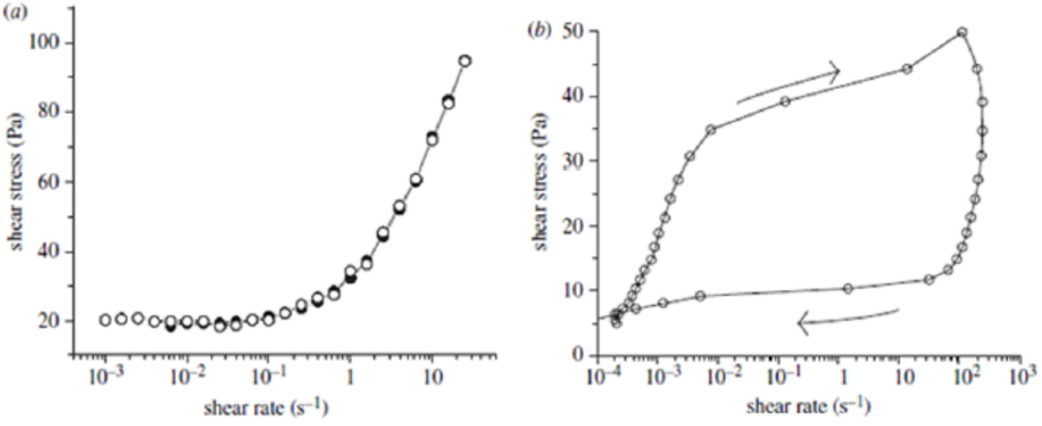

Figure 3.1: (a) 0.1%wt. carbopol microgel under increasing (full circles) and decreasing shear stresses (open circles). (b) 10%wt. bentonite solution under increasing and decreasing stress [Bonn et al., 2015]

measured in any flow condition, if possible, at any location $\mathbf{r}$ and any moment t, should fall on the same curve if one plots $\sigma(\mathbf{r}, t)$ against $\dot{\epsilon}(\mathbf{r}, t)$; (ii) The applied bulk stress versus the bulk strain rate measured in a uniform flow, normally referred as the “engineering flow curve”, should fall on the same curve as the one measured locally, because the flow being uniform, macroscopic flow properties are identical to those of local flow.

Interestingly consistencies and discrepancies with the existence of local constitutive law are both found in experimental studies of simple yield stress fluids.

Experimental method for measuring the engineering flow curve

The engineering flow curve (or macroscopic flow curve) is mostly measured from a rheometer in cone-plate geometry or coaxial-cylinder geometry. After recording the torque versus the corresponding angular velocity, followed by an analysis assuming the existence of the local constitutive law, a macroscopic flow curve can be produced [Ovarlez et al., 2008, Coussot et al., 2009].

Experimental method for measuring local constitutive flow curve

The experimental method for measuring the constitutive law applied in most of the works in the literature relies on the two following points:

1. The local stress is not directly measured by experimental facilities. The stress field is computed by assuming mechanical equilibrium for the steady state flow

in a rather simple geometry (straight channel or co-axial cylinders) and the system is treated as a normal fluid even if the components are of micrometer size much larger than normal fluid molecules. In principle, it is assumed for a non-compressible flow:

$$-\nabla P + \nabla \sigma^s = 0$$

where σ^s is the frictional stress tensor related to the viscosity. By putting this equation into a specific simple geometry and a simple loading condition, it is possible to calculate the stress field $\sigma^s(\mathbf{r})$.

2. The velocity profile is obtained by measuring the particle velocity at a given position within a given time window, during which the particle velocity fluctuates, and by taking the time average of the velocity at that position. A velocity profile $\mathbf{v}(\mathbf{r})$ is obtained, from which a strain rate profile is computed as $\dot{\epsilon}(\mathbf{r}) \equiv \frac{1}{2}(\nabla \otimes \mathbf{v} + \nabla \otimes \mathbf{v}^t)$. By plotting $\sigma(\mathbf{r})$ against $\dot{\epsilon}(\mathbf{r})$ in different experimental situations, e.g. changing bulk loading shear rate, it is possible to validate the existence of a unique constitutive law governing the local stress and the local strain rate.

The constitutive flow curve established in this way is only valid in a statistical meaning involving an averaging time scale, while fluctuations of the stress and the velocity field within this averaging time scale can be important. For fully understanding the flow of amorphous systems, these fluctuation must be taken into account, especially at low shear rate. For this purpose, the elasto-plastic model, which will be discussed in detail in the chapter4, taking the heterogeneous plastic activation as the elementary building blocks could be adequate.

Comparing the engineering flow curve and the local flow curve

It has been found that in carbopol microgels [Divoux et al., 2012, Coussot et al., 2009] dense emulsion [Ovarlez et al., 2008, Bécu et al., 2006] and foams [Ovarlez et al., 2010], the macroscopic flow curve can be well superimposed with the local flow curve in various geometries. The obtained flow curves can be well fitted by the Herschel-Bulkley law with a shear thinning exponent close to one half.

In constrast, for the same dense emulsion system studied in the work of Ovarlez et al. [Ovarlez et al., 2008], it has been reported in the work [Goyon et al., 2008] that local flow curves measured in different loading conditions disagree with each other and they disagree with the macroscopic one. It should be noticed that this discrepancy of experimental results are due to the confined geometry. In the reference [Ovarlez et al., 2008], the rheology is studied in a co-axial cylinder Couette geometry with a gap width about 3000 times the individual particles size, while the gap of the micro-channel in [Goyon et al., 2008] is about 50 times the individual particles size. It is also found in [Bécu et al., 2006] that the flow curve shows some anomalies when the Couette gap becomes too small. This discrepancy may be due to the strongly confined geometry where the gap width is comparable with the length scale of the non-local effects in the flow. It is proposed in the work by Nicolas and Barrat [Nicolas and Barrat, 2013] that this discrepancy can be explained by the fact that the wall roughness may trigger more plastic events along the boundaries.

These experimental results suggest that a local constitutive law for simple yield stress fluids may exist only above a length scale and time scale that are involved in experimental measurements in these specific geometries. What determines these length and time scales can actually be addressed by elastoplastic models, from which the physical interpretation of the obtained local constitutive law may be clarified.

3.2 Avalanches

Avalanche dynamics in amorphous systems

Amorphous systems possess a critical yield stress σ_y above which the global shear rate depends on the applied stress as a power law $\dot{\gamma} \sim (\sigma - \sigma_y)^{\frac{1}{n}}$. Experiments on metallic glasses and foams reveal that the response of amorphous systems under slow external driving ($\dot{\gamma} \to 0$ or $\sigma \to \sigma_y$) is intermittent. Typically the stress strain shows serrations i.e. linear elastic loading regimes alternated by sudden stress drops [Cantat and Pitois, 2006, Shan et al., 2008, Wang et al., 2009, Sun et al., 2010, Sun and Wang, 2011, Sun et al., 2012, Antonaglia et al., 2014, Dennin, 2004, Lauridsen et al., 2002]. This is because the accumulated plastic deformation increases by bursts of plastic activity, see figure 3.2. Statistics of the stress drops observed in the stress strain curve, at vanishing shear rate regime, i.e. close to the critical point, shows a power law distribution [Cantat and Pitois, 2006, Shan et al., 2008, Wang et al., 2009, Sun et al., 2010, Sun and Wang, 2011, Sun et al., 2012, Antonaglia et al., 2014, Salerno et al., 2012] (see figure 3.2). Moreover, a self-affine geometry is observed in driven glassy systems close to critical point. The pattern composed by slip lines during intermittent plastic accumulation has been measured through scanning electronic microscopy [Sun and Wang, 2011], and shows a fractal structure characterized by a fractal dimension close to 1.6. This fractal dimension is close to

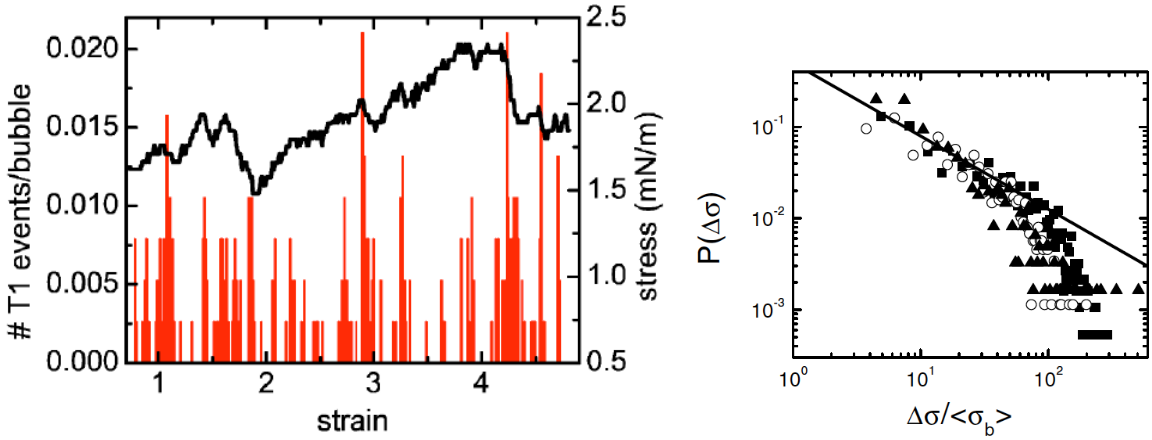

Figure 3.2: Left: Solid line: Stress versus strain; Red line: the number of "T1" events as function of strain[Dennin, 2004]. Right: Stress drop probability distribution function in a foam system [Lauridsen et al., 2002]

the one measured in quasi-statically sheared athermal molecular dynamics systems [Bailey et al., 2007].

In a series of studies on amorphous systems under shear using zero temperature molecular dynamics simulations [Maloney and Lemaitre, 2004, Lemaître and Caroli, 2009], it has been revealed that the dynamics becomes more and more correlated for decreasing shear rate. Typically the spatial stress fluctuations evolve from a law of large numbers statistical behavior $\langle \Delta\sigma^2 \rangle \sim L^{-d}$ at large shear rate to a correlated behavior $\langle \Delta\sigma^2 \rangle \sim L^{-d^*}$ in the low shear rate limit, where d denotes the system dimension and $d^* < d$. The transverse diffusion coefficient follows a master curve $\hat{D} \sim Lf(L\sqrt{\dot{\gamma}})$ for a two dimensional system, where $f(x) \sim x^{-1}$ at $x \gg 1$. This behavior can be accounted for by the assumption that plastic activities take rather randomly place at high shear rate, while at low shear rate, they take place in a correlated fashion into a structured cluster in space, the size of which diverges up to the system size.

Another observable which gives a hint of the collective dynamics close to a critical point is the average avalanche shape, which is the average shape of individual busts. The average avalanche shape has been studied for depinning like systems, in which the average shape of an avalanche can be affected by system properties such as inertia, self-interaction [Laurson et al., 2013, Sethna et al., 2001, Papanikolaou et al., 2011, Zhao et al., 2014, Zapperi et al., 2005, Le Doussal and Wiese, 2013]. The average shape of avalanches in amorphous systems is much less explored [Antonaglia et al., 2014].

These results clearly show that the dynamics of glassy systems in the low shear rate limit is strongly intermittent and self-organized, reminiscent to the phenomenology of critical dynamics due to a phase transition. With these indications, it is natural to think that the plastic dynamics of amorphous systems close to the critical point may be understood in a similar way as the depinning dynamics close to the depinning point.

Avalanche dynamics analogy between the yielding and the depinning

Avalanche dynamics is rather well studied in depinning systems, such as Barkhausen noise in ferromagnets [Durin and Zapperi, 2000, 2006, Barkhausen, 1917], stick-slip motion in earthquakes [Ruina, 1983], serration dynamics in plasticity of solids [Dastur and Lesley, 1981], and avalanche dynamics in crack propagation [Bonamy et al., 2008, Laurson et al., 2010], and domain wall motion [Repain et al., 2004]. A large class of intermittent dynamics under external driving, some of which are stated above, can be described by the universality class of depinning transition.

A depinning model is usually represented as the motion of a interface in d-dimensional space $h(\mathbf{x},t)$ with $\mathbf{x} \in \mathbb{R}^{d-1}$in a quenched disorder potential $V(h,\mathbf{x})$ under an external driving force $f(\mathbf{x})$ and a self interaction of the surface, typically $\nabla^2_{\mathbf{x}} h$. The simplest case is an elastic line moving in a two dimensional quenched disorder potential without thermal fluctuations:

$$\partial_t h(x,t) = \nu \partial_x^2 h - \partial_h V(x, h(x,t)) + f \tag{3.1}$$

The average velocity of the interface $v = \langle \partial_t h \rangle_x$, where the angular brackets denote the average over x, remains zero when the applied force f is smaller than a critical value f_c. When $f \gtrsim f_c$, the line begins to move with a velocity $v \sim (f - f_c)^\beta$ with $\beta < 1$. When $f \gg f_c$, $v \sim f$. The geometry of the interface is characterized by a length scale l_{av} above which the interface is self affine characterized by a roughness exponent ζ_{ff} , and below which the interface is again self affine characterized by another roughness exponent ζ_{dep}. The length scale l_{av} diverges as the applied force approaches the critical value at zero temperature $l_{av} \sim (f - f_c)^{-\nu_{dep}}$. The motion of the line in a quenched disorder under $f \gtrsim f_c$ is typically performed by bursts of segments of typical length $\sim l_{av}$. The motion below l_{av} within a segment bust is strongly specially correlated, which is referred to as an avalanche. This motion is not only heterogeneous in space but also in time. Avalanches happen here and there and separated by a some quiescent states. The statistics on the avalanche size, defined as the area swept by the burst of an avalanche, shows a power law distribution cut by the crossover length scale $\sim l_{av}$ if the system size is infinite [Ferrero et al., 2013].

The first similarity between the yielding and the depinning is the scaling relation $\dot{\gamma} \sim (\sigma - \sigma_y)^{1/n}$ and $v \sim (f - f_c)^{\beta}$. Secondly power law distributions have been found in both situations. Thirdly a divergent length scale spanning the systems size is assumed for explaining the dependence of the diffusion coefficient on the system size in amorphous systems under very low shear rate, which is consistent with the phenomenology in depinning where there exists a length scale $l_{av} \sim (f - f_c)^{-\nu_{dep}}$ below which the dynamics is strongly correlated. Further, as will be discussed in the chapter 5, an analogy resides already at the level of model construction.

Besides the similarity between yielding and depinning, there are intrinsic differences residing in the avalanche dynamics. Answering the question to what extent, yielding dynamics is in analogy with depinning and to what extent they differ from each other, surely will improve our understanding of the two fields.

The avalanche dynamics of amorphous systems in the low shear rate limit is of great interest for understanding the transition from solid state to liquid state. The results in the literature suggests that the yielding transition belongs to a universality class of dynamical phase transition. This topic is addressed in detail during this thesis by a mesoscopic approach in the chapter 5. Detailed definitions of avalanche relevant quantities such as avalanche size, duration, and avalanche shape and method of statistics will be discussed.

3.3 Creep

Creep experiments on soft amorphous systems aim at studying the transient process from the solid state to the liquid state at an imposed stress, larger than the yield stress or smaller when thermally activated. The experiments are performed on soft glassy systems with either attractive or purely repulsive interactions [Divoux et al., 2012, 2011, 2010, Siebenbürger et al., 2012, Grenard et al., 2014, Lindström et al., 2012, Sprakel et al., 2011, Gibaud et al., 2010, Gopalakrishnan and Zukoski, 2007]. As briefly reviewed below, systems with attractive interactions and systems with repulsive interactions share common features, but also display differences in the transient process. To guarantee the reproducibility of experimental results, the creep experiments always follow a well defined preshear protocol to make sure creep experiments are performed with the same initial condition. This suggests that the creep behavior may depend on the initial condition, however there are no creep experiments studying in detail this issue. Most of the experiments in soft materials are performed with a Couette geometry, the gap width of which is about $\sim 10^3$ times individual particles size.

Spatial heterogeneity

Both systems with attractive and repulsive interactions are fluidized in a spatially heterogeneous way when a stress $\sigma > \sigma_y$ is applied. During the early stage of loading, a narrow layer close to the wall begins to flow, allowing the rest of the material to move in a plug like manner. A wall slip is also observed at this stage. Then a rather clear shear band develops, the width of which increases with time until a homogeneous velocity profile established [Gibaud et al., 2010, Divoux et al., 2011]. For systems with repulsive interactions, not only the stress imposed transient state but also in shear rate controlled transient state, a shear band develops, the width of which increases logarithmic in time until it fully occupies the system and a homogeneous flow is established [Divoux et al., 2012].

Given an applied shear rate or an applied stress, by monitoring the spatial heterogeneity of the flow, one can determine a fluidization time scale τ_f^H as the time elapsed between the beginning of loading and the moment where homogeneous flow is established.

Global behavior

The transient state is also investigated by looking at the global strain response after applying a step function of stress of amplitude $\sigma > \sigma_y$. Typically one looks at the curve $\dot{\gamma}(t)$ for different applied stresses. For both attractive systems and repulsive systems, $\dot{\gamma}(t)$ shows a “S” shape in a log-log plot (see figure (3.3)). The typical feature is that a power law decay $\dot{\gamma}(t) \sim t^{-\mu}$ is observed on the early stage of loading, followed by a sudden increase before reaching the final plateau, the value which corresponds to the shear rate on the flow curve at the corresponding stress σ [Gibaud et al., 2010, Sprakel et al., 2011, Lindström et al., 2012]. For attractive systems, e.g. carbon black gel, a two-step increase of $\dot{\gamma}(t)$ after the power law decay has been observed [Grenard et al., 2014]. It is worthy to note that the creep exponent μ is not universal, and depends strongly on the detailed preparation of the systems before the creep experiment is started. μ is reported to be close to 0.8 in carbon black gel [Grenard et al., 2014] and $\sim 2/3$ in microgel [Divoux et al., 2011]. When $\sigma < \sigma_y$, it normally shows a logarithmic creep $\dot{\gamma}(t) \sim t^{-1}$ in the infinite time limit

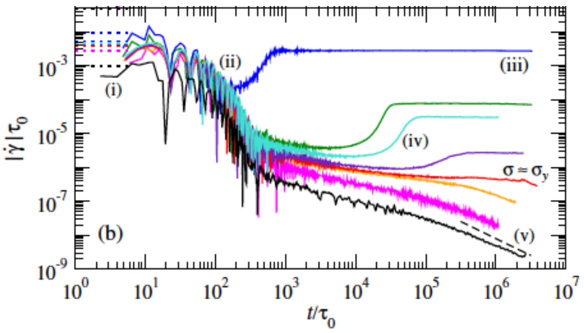

Figure 3.3: Strain rate versus time with different applied stress across the yield stress in colloidal glass [Siebenbürger et al., 2012]

[Siebenbürger et al., 2012].

From the response $\dot{\gamma}(t)$ to an imposed stress $\sigma > \sigma_y$, a fluidization time τ_f^G can be extracted by the time interval from the beginning of loading and the inflection point in $\dot{\gamma}(t)$ where $d\dot{\gamma}/dt$ reaches the maximum. It is found that in repulsive systems, such as carbopol microgel, the fluidization time found in $\dot{\gamma}(t)$ and the one obtained by monitoring the spatial heterogeneity match each other $\tau_f^G = \tau_f^H = \tau_f$. In these systems, the fluidization time depends in a power law fashion on the distance to yield, $\tau_f \sim (\sigma - \sigma_y)^{-\beta}$, where β varies $3 \sim 8$ depending on the system preparation. As stated in the above paragraph, a fluidization time $\tau_f^{(\dot{\gamma})}$can also be defined using a shear rate controlled protocol. For repulsive systems, it is found to scale with the applied shear rate as $\tau_f^{(\dot{\gamma})} \sim \dot{\gamma}^{-\alpha}$ [Grenard et al., 2014, Divoux et al., 2010]. The consistency of the two fluidization times coming from different processes is confirmed [Grenard et al., 2014]. Actually it is verified that the Herschel-Bulkley exponent is close to α/β, which is deduced if one admits $\tau_f \approx \tau_f^{(\dot{\gamma})}$. In attractive systems, such as carbon black gel, it is commonly found that $\tau_f \sim \exp(-\frac{\sigma}{\sigma_o})$ where σ_o is a fitting parameter that depends on the preparation. In [Sprakel et al., 2011], an exponential relations with two regimes between τ_f and σ is reported, and it can be rationalized by the idea of bond dissociation-association balance under thermal fluctuation and applied stress.

Aging is reported to affect the fluidization time in repulsive systems [Siebenbürger et al., 2012]. It is not surprising that more aged systems take longer time to fully fluidize under imposed stress, while it seems not to affect the creep exponent μ.

The mesoscopic elasto-plastic model is found more suitable for soft repulsive jammed systems, such as emulsion of caster oil. In this thesis, the elasto-plastic model will be also used to investigate the transient state when a constant stress is applied. Different behaviors with respect to initial conditions are studied, see 6. A mean-field type mesoscopic model, the “Hebraud-Lequeux” model, is also adopted for studying creep of amorphous systems, since it is well studied at imposed shear rates in the literature. In chapter 6, the “Hebraud-Lequeux” model is reinterpreted such that we can realize a stress control protocol, which at the end captures the “S” shape in creep experiments. Creep power law decay and scaling relations are discussed with respect to different initial conditions.

Chapter 4

Mesoscopic Elasto-Plastic Model

In this chapter, I will introduce and discuss the mesoscopic elasto-plastic model that is used in this thesis to describe the deformation of amorphous materials.

Most of the modern mesoscopic models are based on the idea initiated by Argon in late 70s [Argon, 1979] that the elementary unit of plasticity in glassy systems is the rearrangement of a cluster of particles localized in space. Taking advantage of the strong similarity between a mono-disperse bubble raft and a microscopic crystalline in the structure, the dynamics of dislocations had been studied [Lawrence Bragg, 1947] in this structures. Inspired by these studies, Argon and Kuo [Argon, 1979] studied the shearing of a poly-disperse bubble raft, which forms a disordered structure similar to that of amorphous system as seen from its radial distribution function. They observed that the plasticity of the amorphous bubble raft proceeds by rearrangements of localized clusters of about ~ 5 bubbles. This kind of mechanism of plasticity in amorphous systems has also been supported by other observations [Princen, 1983, Amon et al., 2012, Schall et al., 2007]. Since then this localized local rearrangement, which can be activated either by loading or thermal fluctuations, has been widely accepted as the elementary unit of the plasticity of amorphous systems, at least at the phenomenological level, and various mesoscopic phenomenological models have been built to describe the mechanical behavior under external loading or relaxation at low temperature [Bulatov and Argon, 1994, Baret et al., 2002, Picard et al., 2004].

Various mesoscopic models can be divided into two categories: those ignoring spatial correlations between local rearrangements, considering local rearrangements are triggered by thermal-fluctuation and external loading independently, and those taking into account the internal interactions so that local rearrangements can be triggered by other ones already present in the system. In this section we will focus on the general framework of the second category of mesoscopic models, which is also the kind of model being studied through this thesis.

4.1 Basic concepts of elasto-plastic models

Local plasticity and elasticity matrix

As stated above, the plasticity of a glassy system proceeds in a heterogeneous way, i.e. the global plasticity consists in a series of localized "plastic events". These local "plastic events" correspond to sudden changes of local topology. In an amorphous bubble raft, it is specified by "T1" events, involving typically four bubbles changing their contacts [Argon, 1979]. Similar localized processes are observed in colloidal glasses under low strain rate [Schall et al., 2007] and in slowly sheared granular material [Amon et al., 2012].

More quantitatively, localized plastic events can be identified by defining quantities measuring local non-affine motions. Specifically, for a time interval δt during global deformation, for a particle i, by minimizing $D_i^2 \hat{=} \sum_j (d\mathbf{r}_j(t+\delta t) - \mathbf{\Gamma} d\mathbf{r}_j(t))$ with respect to Γ, where Γ is a strain tensor, $d\mathbf{r}_j = \mathbf{r}_j - \mathbf{r}_i$ with particle j is a first neighbor to particle i, one can obtain a minimized D^2_{min} for particle i with a corresponding Γ_{min}. D^2_{min} is a measure of local non-affine motion and Γ_{min} can be seen as a local strain. There are other quantities that can be defined for measuring local non-affine motion in the same spirit of D^2_{min}. It has been found out that different non-affine measures behave in a similar way [Chikkadi and Schall, 2012]. A region of particles where D^2_{min} exceeds some threshold value is considered to be affected by a plastic event [Falk and Langer, 1998, Schall et al., 2007]. By monitoring these quantities in either molecular simulation or in experimental systems during deformation [Maloney and Lemaitre, 2004, Nicolas et al., 2014b, Falk and Langer, 1998, Chikkadi and Schall, 2012], it has been found out that plastic events take place at very localized regions while the displacement field in other regions is rather regular with respect to the global strain.

An important fact is that local plastic events such as the "T1" events in bubble rafts are not reversible once they have taken place, i.e. the topology remains modified even when the loading is released, while the deformation of the rest of the system shows reversibility, i.e. the original configuration of particles can be recovered when the loading is released and there is no topological changing during the loading. A phenomenological description of this process is that under loading an amorphous system deforms elastically in most regions with localized plastic activity.

This phenomenology has been firstly formulated by Bulatov and Argon [Bulatov and Argon, 1994]. In their formulation, an amorphous system is considered as composed by many blocks, the size of which corresponds to the typical size of particle clusters undergoing plastic events. Once a block undergoes plastic transformation triggered by a thermal fluctuation under local stress, it is treated as Eshelby's inclusion in an elastic matrix, i.e. the stress released by a local plastic event within a block is redistributed through the rest of the system according to the Eshelby propagator computed from mechanical equilibrium [Eshelby, 1957].

The common features of elasto-plastic models [Baret et al., 2002, Picard et al., 2004, Lin et al., 2014a, Budrikis and Zapperi, 2013, Nicolas and Barrat, 2013] are: (i) Bulk systems are considered composed by mesoscopic cells, each of which is considered as a homogeneous medium which can sustain a certain stress. The notion of local stress or stress field is adopted in the elasto-plastic model; (ii) Each mesoscopic cell can undergo elastic strain or plastic strain. In the elastic state, each cell is assumed to obey linear elasticity. (iii) A local criterion should be specified for a cell to initiate plastic events. (iv) Cells are coupled through the elastic matrix. Once a plastic event takes place on one cell, the stress of other cells are perturbed according to a specific form, i.e. the Eshelby propagator. These features are discussed in the following sections.

Local stress tensor

A key concept in various mesoscopic models is the local stress tensor which emerges originally from continuum mechanics. The stress tensor is a unified way to express the fact that a force is uniformly applied onto a flat surface. If the area of the surface is S, the normal unit vector $\mathbf{n} \equiv n_i$, the applied force $\mathbf{F} \equiv F_i$ (where the i indexes the coordinates$x$, y or z), then the force and the surface can be related by the stress tensor σ_{ij} in such way $F_i = \sigma_{ij} S n_j$.

In continuum mechanics, a system is considered to be composed by small elementary parts which are always classical physical systems so that macroscopic physical quantities are associated with each elementary part coordinated by a position $\mathbf{x}$ at a moment t, possessing a volume δv with a mass δm etc. Conservation laws govern the evolution of the system, for which the conserved quantities are defined in a classical manner. The internal interaction between different elementary parts are involved for expressing these conservation laws, e.g. the momentum conservation of a subset of elementary parts enclosed in a volume $\mathcal{D}$ calls the sum of force $F_i \delta t = \delta t \int_{\mathbf{x} \in \partial D} dF_i(\mathbf{x})$, applied on the surface $\partial \mathcal{D}$ during δt. Each $dF_i(\mathbf{x})$ is due to the interaction between elementary parts at the position $\mathbf{x}$, which is a local intrinsic property, independent on the considered volume surface $\partial\mathcal{D}$. On an elementary surface of an elementary part, the force can be considered to be uniformly applied, so that $dF_i(\mathbf{x}) = \Sigma_i(\mathbf{x})[\mathbf{n}(\mathbf{x})ds)]$. Supposing an elementary surface $\mathbf{n}$ can be decomposed as a linear combination of two surfaces $\mathbf{n} = \alpha\mathbf{n}_1 + \beta\mathbf{n}_2$ and supposing that the force felt by $ds\mathbf{n}$ is the same linear combination of the forces felt by the two component surfaces, i.e. $\Sigma_i(\alpha\mathbf{n}_1 ds + \beta\mathbf{n}_2 ds) = \alpha\Sigma_i(\mathbf{n}_1 ds) + \beta\Sigma_i(\mathbf{n}_2 ds)$. These leads to associate with $\Sigma_i(\mathbf{n}ds)$ a matrix form associated to the position $\mathbf{x}$, which is the local stress tensor, i.e. $F_i = \int_{\mathbf{x}\in\partial\mathcal{D}} \sigma_{ij}(\mathbf{x})n_j(\mathbf{x})ds(\mathbf{x})$. With Green's theorem, $F_i = \int_{\mathbf{x}\in\mathcal{D}} \partial_{x_j}\sigma_{ij}(\mathbf{x})dv$, so that $\partial_{x_j}\sigma_{ij}$ can be seen as a body force acting for the local conservation of momentum. Without any external body force and with u_i denoting the velocity field, momentum conservation reads:

$$\frac{D}{Dt}(\rho u_i) = \partial_t(\rho u_i) + \partial_j(\rho u_i u_j) = \partial_l \sigma_{il} \tag{4.1}$$

.This equation gives actually the definition of the local stress tensor from a macroscopic point of view. By substituting the microscopic expression of local momentum in the above equation, it is possible to find out the microscopic expression corresponding to the local stress tensor. This method is adopted in several works [Irving and Kirkwood, 1950, Lutsko, 1988, Goldhirsch and Goldenberg, 2002] for deriving the microscopic expression of the local stress tensor. The microscopic expression for momentum density [Irving and Kirkwood, 1950, Lutsko, 1988] is $\rho(\mathbf{x})u_i(\mathbf{x}) \hat{=} \sum_{k=1}^{N} P_{k,i}(t)\delta(\mathbf{x} - \mathbf{R}_k(t))$ where k denotes the particles. The delta function is replaced by a smooth coarse-grain function [Goldhirsch and Goldenberg, 2002] for expressing the momentum density.

Despite of the different ways for expressing the microscopic local stress tensor, All these studies lead to the conclusion that the local stress tensor comes from one part due to kinetic energy and the other part due to the interaction of particles. Due to the slow dynamics in glassy systems, the kinetic contribution to the local stress tensor is negligible and for any athermal system, the local stress tensor can be computed directly from particle positions.

Mathematically this microscopic expression of the local stress tensor can be associated with a position $\mathbf{x}$ for any wanted precision, while physically the idea of the local stress tensor in continuum mechanics is valid only above a length scale. The local stress tensor $\sigma_{ij}^{m,k}$ has been computed as an average over a coarse-grained block k with a certain linear size w [Yoshimoto et al., 2004, Mizuno et al., 2013]. In the work by Goldhirsch [Goldhirsch and Goldenberg, 2002], this coarse-grain process is systematically done by introducing a smooth coarse-graining function. It is worth to notice that the stress tensor averaged over all blocks gives the bulk stress tensor [Parrinello and Rahman, 1982, Lemaître and Maloney, 2006]

$$\frac{1}{M}\sum_{k=1}^{M}\sigma_{ij}^{m,k}=\frac{1}{M}\sum_{k=1}^{M}\frac{1}{w^d}\int_{\mathcal{D}_k}d\mathbf{x}^d\sigma_{ij}(\mathbf{x})=\sigma_{ij}^B \tag{4.2}$$

In conclusion the local stress tensor is a quantity rather well defined. Its microscopic expression is consistent with its macroscopic physical meaning. A spatial average of the local stress tensor gives the macroscopic stress tensor.

Linear elasticity

In the theory of linear elasticity of solids, the local stress tensor is related with the local deformation, i.e. the strain tensor, through a linear tensor product, Hooke's law:

$$\sigma_{ij}=C_{ij,kl}e_{kl}$$

If the system is isotropic $C_{ij,kl}=\lambda\delta_{ij}\delta_{kl}+\mu(\delta_{ik}\delta_{jl}+\delta_{il}\delta_{jk})$. The strain tensor is given by $e_{ij}=\frac{1}{2}(\partial_i u_j+\partial_j u_i)$ with u_i representing the displacement field. This relation can be interpreted as the fact that in a solid state the internal interaction characterized by the stress tensor is caused by the deformation characterized by the strain tensor from its reference state and this deformation is the apparent macroscopic state of the a microscopic equilibrium state balanced by the external loading and the potential force of the configuration. This linear elasticity can be derived from the assumption that the local free energy density can be approximated, for small deformations, by a quadratic form of strain tensor components. One finds Hooke's linear elasticity if one writes the Taylor expansion of the free energy density up to the second order of the local strain tensor [Landau and Lifshitz, 1986]. In isotropic elasticity:

$$F=F_0+\frac{1}{2}\lambda(e_{ii})^2+\mu e_{kl}e_{kl}$$

where the term after λ is the squared sum of all the diagonal components and after $\mu$is the sum over all the squared components. λ and $\mu$are the Lamme coefficients, from which the bulk modulus $K=\lambda+\frac{2}{3}\mu$ and the shear modulus is identically μ.

Glassy systems below the yielding threshold behave like an isotropic elastic solid. The bulk elasticity of glassy systems is well described by Hooke's law [Maeda and Takeuchi, 1978, Lemaître and Maloney, 2006, Mizuno et al., 2013]. Under a global loading condition below yielding, the particle displacements show a great non-affinity in glassy systems, which is important for the determination of macroscopic elastic properties [Lemaître and Maloney, 2006]. Is it possible to describe a glassy state as composed by elementary blocks with each of them possessing the linear elasticity, which is an important building block of elasto-plastic model.

The attempt to relate the local stress tensor with a local strain requires a well defined displacement field. In contrast with the local stress tensor, there seems no unique way to define a macroscopic displacement field. Two kinds of approaches are adopted in literature: (i) The local elastic constant is computed by assuming a small local strain identical to the global strain, then the local stress computed as the product of the local elastic constant and the bulk strain can be compared with the local stress computed directly by the microscopic expression to validate the local linear elasticity [Lutsko, 1988, Mizuno et al., 2013]; (ii) Introducing a coarse-graining function of width w (the same in the previous section for local stress) to define a smooth displacement field from which the local strain tensor is computed [Goldhirsch and Goldenberg, 2002, Tsamados et al., 2009], the elastic constant involving six independent tensor components can be determined with two loading modes. By applying a third loading mode, the local stress computed by the microscopic expression and the local stress computed from elastic constant can be compared to validate the local linear elasticity. It is found that the deviation from the linear elasticity approach decreases as a power law with the coarse-grain width w and converges to zero if w goes to the system size. This indicates that even if there is no typical length scale above which the local linear elasticity approach can be considered exact, beyond a reasonable value of coarse-grain length scale, the error remains below an acceptable value $\sim 5\%$.

These studies made a reasonable analysis of the condition under which the local linear elasticity approach holds for glassy materials. Beside, the local elastic constant is not homogeneous in space and during the loading, the elastic constant of a region close to a plastic rearrangement decreases drastically [Tsamados et al., 2009].

Criteria for local plastic events

Efforts for correlating local properties of amorphous systems with local plastic events have been made through molecular dynamics simulations. Several local properties are studied, such as the local density [Spaepen, 1977], local potential energy [Shi et al., 2007], the short range order [Shi and Falk, 2005], shear modulus [Tsamados et al., 2009]. A recent paper [Patinet et al., 2016], compared the capability of predicting plastic events of all the above local properties along with the local yield stress. It is found out that the local yield stress is the most relevant quantity to quantify the susceptibility of plastic events to loading. From the state where the local yield stress is measured, about the first 35 plastic events during shear can be identified with the lowest yield stress regions at the beginning. The maximum strain for which the local yield stress is strongly correlated with plastic events is about 0.07 [Patinet et al., 2016].

The local criteria for a plastic event taking place differs one from each other in various mesoscopic elasto-plastic model in the literature. In a recent study [Patinet et al., 2016], a relatively important correlation is found between local plastic events and the local plastic property in an quenched molecular dynamic system. An usual macroscopic athermal quasi-static shear was applied onto the prepared glassy system from a reference state, allowing non-affine motions of particles only inside a chosen mesoscopic scale block and the difference between the local stress at which a plastic event takes place and the local stress before quasi-static shear was computed as the local yield stress for the mesoscopic scale block. The local yield stress was computed for each of the blocks inside the system and they performed again from the same reference state, allowing non-affine motions of all particles, to observe where to happen plastic events. They showed that there is an important correlation between the smallest values of local yield stress and plastic events, i.e. blocks with small value of local yield stress have more chance to occur plastic events. The predictive capacity of local yield stress probed in this way remains reasonable at least for about the first 75 plastic events. Although in the study [Patinet et al., 2016], the local stresses at which local plastic events take place are not compared directly with the local yield stresses determined before the macroscopic loading, to take a random local stress threshold for plastic event criteria seems to be the most adequate.

Interaction via the elastic matrix

Interaction among plastic events in glassy systems has been studied in both experiments [Schall et al., 2007, Chikkadi and Schall, 2012, Chikkadi et al., 2012, 2011, Le Bouil et al., 2014, Jensen et al., 2014] and in molecular simulations [Maloney and Lemaitre, 2004, Lemaître and Caroli, 2007, 2009, Puosi et al., 2014, Tanguy et al., 2006].

In experimental studies, the non local effect is revealed by looking at the spatial correlation of non-affine motion, e.g. D^2_{min} and local strain Γ_{min}. The results are quite robust. The correlation function of D^2_{min} shows isotropic power law decay in

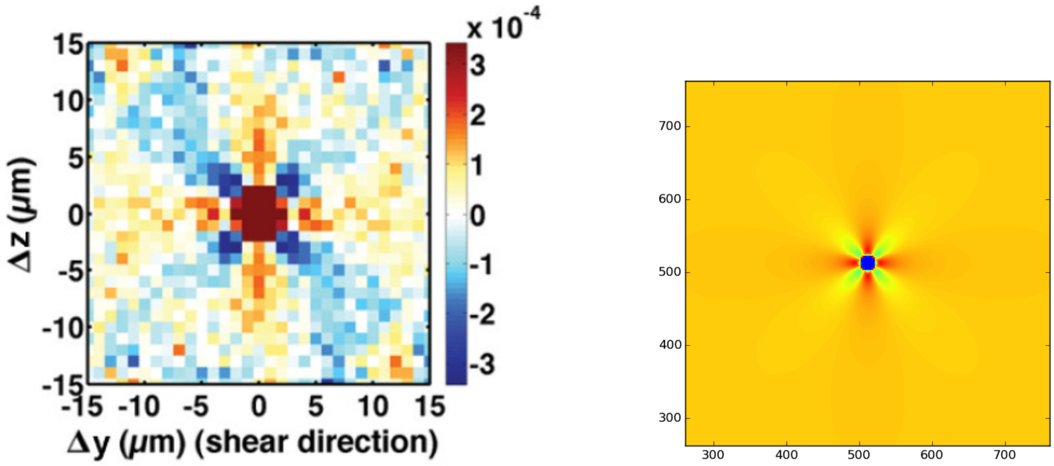

Figure 4.1: Left: Spatial correlation of local plastic strain within a global strain. Bulk shear along y direction [Jensen et al., 2014]. Right: The exact solution of the response of the elastic matrix to a spherical inclusion, i.e. Eshelby's propagator, computed numerically

space, see the references above. The correlation function of the local strain Γ_{min} has a quadrupolar symmetry and show both correlation and anti-correlation, decaying as a power law. This is very reminiscent to the strain field of an Eshelby inclusion, see figure 4.1.

The agreement between the correlation map and the response of the elastic matrix to an inclusion strongly supports the idea that a plastic event redistributes positive and negative stress according to the quadrupolar form so that regions with positive perturbation have more chance to produce a positive plastic strain and regions with negative perturbation have more chance to produce negative plastic strain. In this way, one plastic event triggers other plastic events in a specific geometry.

In molecular simulation, non-local effects can be directly revealed by looking at the non-affine displacement field in athermal systems sheared quasi statically. Typically during global plastic deformation, several spots with outstanding non-affine motion amplitude can be identified. These spots are identified as local plastic events. In addition, the non-affine displacement field shows a long range quadrupolar form. The pattern of highly non-affine spots surrounded by long range quadrupoles of correlated motion persists even when the applied deformation rate is finite [Lemaître and Caroli, 2009]. Not only the non-affine motion but also the stress field display a long range quadrupolar response around plastic events. This non-local effect of a local plastic event has been well investigated by introducing an artificial plastic event in the middle of a system and averaging over several realization of the surrounding displacement field. The averaged result is very well in agreement with the Eshelby theory at long range and deviates a bit at short range [Puosi et al., 2014].

In the elastoplastic model, once a mesoscopic cell undergoes plastic strain, it is treated as an Eshelby inclusion. The non-local effect is modeled by the response of an homogeneous linear elastic matrix to this inclusion [Argon, 1979], which has been widely adopted in various elastoplastic model. This response can be computed analytically if the shape of the inclusion is considered as elliptical [Eshelby, 1957]. The basic assumption is that at each local position linear elasticity holds and the elastic constants are uniform in space. Even if this assumption is not true according to a work by Tsamados [Tsamados et al., 2009], the interaction propagator derived from this assumption represents well the averaged feature of the response to local plastic events [Puosi et al., 2014].

Discussion of the assumptions in mesoscopic elasto-plastic modeling

Global plasticity is well defined in the athermal quasi-static limit. A non reversible process at the scale of the system is evidenced by the drastic global stress (or energy) drop within a very small, ideally zero, global strain increment. The global plasticity finds its clear interpretation in the picture of potential energy landscape (PEL). That is the hopping from one basin to the neighboring one, which is directly reflected in a drastic energy drop within a tiny strain increment in the energy strain curve. According to the study [Maloney and Lemaitre, 2004], a global stress drop in athermal quasi-static sheared glassy system involves several clusters of particles with large values of relative displacement, i.e. plastic events. The ensemble of several local rearrangements correspond to a well defined global non reversible process.

The notion of plastic events is introduced by direct observation of localized non-reversible particle rearrangement as discussed above. As far as the stress redistribution due to one plastic event is modeled by the Eshelby propagator, the cluster of particles having undergone a plastic rearrangement is seen as an inclusion. It means that this cluster of particles after the plastic event admits a stress free eigenstrain compared to the stress free state before the plastic event. Particle clusters of a typical plastic event size are treated as an elementary cell of homogeneous material. An Eshelby inclusion can be understood as follows: one part of an elastic matrix is taken away outside of the matrix, undergoes a plastic strain, i.e. the eigenstrain, is forced back to its original shape and put back to the matrix. From this point of view, by performing a plastic event, a cluster (or an elementary cell in the elasto-plastic model) undergoes a non-reversible process independently of the rest of the system. One can pursue the reasoning further along this line: since the independent plastic deformation of the cluster involves several particles interacting with each other (the number of particles of order $10 \sim 100$), it is natural to introduce a "local potential energy landscape" constructed by the coordinates of these particles. It is then possible to interpret the local plastic event as the hopping from one basin to the next, allowing a collective particle motion looking like the apparent eigenstrain. Here comes the idea of a local yield stress or a local energy barrier [Nicolas et al., 2014a, Bulatov and Argon, 1994] which is a specific concept of mesoscopic modeling. Note that the idea of this local yield stress is similar but different from the local yield stress studied in [Patinet et al., 2016] related with plastic events, which takes into account of the interaction with all particles in the system but neglects their non-affine motion, while the local yield stress introduced here is based on the local potential energy landscape.

This interpretation of the local plastic event as the hopping in a local-PEL has an obvious weakness, that particles inside the cluster of plastic event interact with particles elsewhere. The potential energy landscape of a cluster of particles changes its form due to the motion of particles outside of the cluster during the bulk deformation. This makes the hopping from one basin to another loosely defined at the level of a restricted subsystem.

Apart from the direct visualization of local plastic events, a way to reveal the local non-reversible process suggested by mesoscopic modeling, would be to look for sudden drops in local stress strain curve in the same way that it is used to identify global non-reversible process. This turns out to be difficult. In most cases, the local stress at a mesocopic scale is defined in two ways: the first one consists in dividing space on a regular grid and averaging over particles in the block the microscopic stress discussed above. Upon increasing strain, an artifact can be introduced because the number of particles inside the small box fluctuates, so that the drastic change in local stress defined in this way can hardly be interpreted physically. The second way is to define a mesoscopic local stress using a coarse-graining function $\phi(x)$ as in [Goldhirsch and Goldenberg, 2002], which also has the same pathology as the first one. Meanwhile it is a little improved because if the $\phi(r)$ is taken smooth enough such that the number fluctuations contribute smoothly to the local stress, the drastic change of local stress may give some physical insight at the mesoscopic scale. But there has been, to my knowledge, no effort in the literature to investigate this question.

Another question is the following: with the discussion above about the local plastic event in the elasto-plastic modeling, one global stress drop (one global non-reversible process) is seen as composed by several coupled local non-reversible processes. How can this picture be justified and connected with the full Nd degree of freedom description? No effort has been done in the literature about this question.

The observed local reversible deformation and local non reversible deformation of an amorphous system are actually two facets of the same physical process as the system undergoes a global plasticity, the microscopic interpretation of which is the hopping between inherent structures. The distinction of local elasticity and local plasticity in the elasto-plastic model remain phenomenological.

Even though there are no answers to the questions asked above, it has been shown that by carefully fitting the Eshelby's inclusion parameter with plastic events in molecular dynamics simulation, a mesoscopic model can very well reproduce the bulk stress strain curve obtained from molecular dynamics [Albaret et al., 2016]. This can be taken as a practical justification of using this decomposition into elementary local plastic events in elastoplastic models, in spite of the questions raised above concerning the link to the global PEL picture.

4.2 Formulation

A general formalism incorporating the qualitative elements discussed in the previous sections is introduced in this section. The general assumptions will be the following: the system is composed of elementary cells which are assumed to be homogeneous. Each cell can individually undergo, in a heterogeneous fashion, plastic deformation and elastic deformation obeying linear elasticity. The elastic moduli of all cells are assumed to be identical. Cells interact with each other as a response to the heterogeneity of plasticity, following mechanical equilibrium in continuum mechanics (Eshelby's problem).

The formalism will be presented in this chapter in a little different way than it was done in the literature, for incorporating both the shear rate control and the stress control protocol. An absolute plastic interface is introduced, which moves constantly forward under the external loading.

4.2.1 Static state: Mechanical equilibrium & Heterogeneity of the stress field and the plastic strain field

Reference state

A reference frame has to be always fixed for defining a displacement field and further for defining the strain of a system. By taking the state of an amorphous system at $t = t_o$ as the reference state, it is possible to define the apparent displacement field at moment $t_o + \Delta t$ noted as $\mathbf{u}(\mathbf{x}, t_o + \Delta t) \equiv u_i(x_j, t_o + \Delta t)$. As long as the deformation is weak, it is usual to define the strain tensor as:

$$\epsilon_{ij}^{\Delta} = \frac{1}{2}(\partial_i u_j + \partial_j u_i) \tag{4.3}$$

where $\partial_i = \frac{\partial}{\partial x_i}$. The upper index Δ is for making correspondence with the Δt and refers to the the deformation from the reference state. The apparent displacement field u_i is assumed to be a sum of a displacement field of plastic nature and a displacement field of elastic nature, i.e. $u_i = u_i^{pl} + u_i^{el}$. One elementary volume $\mathcal{D}$ at $\mathbf{x} \equiv x_i$, undergoing $u_i = u_i^{pl} + u_i^{el}$ during Δt, undergoes plastic strain:

$$\epsilon_{ij}^{pl,\Delta} = \frac{1}{2}(\partial_i u_j^{pl} + \partial_j u_i^{pl})\bigg|_{\mathbf{x}} \tag{4.4}$$

and elastic strain:

$$\epsilon_{ij}^{el,\Delta} = \frac{1}{2}(\partial_j u_i^{el} + \partial_i u_j^{el})\bigg|_{\mathbf{x}} \tag{4.5}$$

. The total strain is also composed by the two parts

$$\epsilon_{ij}^{\Delta} = \epsilon_{ij}^{pl,\Delta} + \epsilon_{ij}^{el,\Delta} \tag{4.6}$$

The reference state can be chosen arbitrarily as far as it is in a mechanical equilibrium. The stress field of the reference state can be of any form σ_{ij}^{R} without any specification, except for

$$\partial_j \sigma_{ij}^{R} = 0 \tag{4.7}$$

. The general assumption of linear elasticity implies then that a residual elastic field satisfying $\sigma_{ij}^{R} = \lambda \delta_{ij} \epsilon_{kk}^{el,R} + 2\mu \epsilon_{ij}^{el,R}$ is embedded in the reference state.

Local plasticity

The plastic strain field $\epsilon_{ij}^{pl,\Delta}$ characterizes the non-reversible plastic events of all elementary cells over all the system during Δt. The phenomenology of local rearrangement during bulk deformation is formulated by writing $\epsilon_{ij}^{pl,\Delta}(\mathbf{x}, t_o + \Delta t) = \sum_{\mathbf{x}_a} A(\mathbf{x} - \mathbf{x}_a)\epsilon_{ij}^{a\Delta}$, where $\mathbf{x}_a$ is the position of one plastic event during Δt, ϵ_{ij}^{a} the amplitude of local plastic strain and $A(\mathbf{x})$ equals to 1 (0) inside (outside) the region of a local rearrangement. In the extreme case where there is only one plastic event, we have $\epsilon_{ij}^{pl,\Delta}(\mathbf{x}) = A(\mathbf{x} - \mathbf{x}_o)\epsilon_o^{pl,\Delta}$.

Mechanical equilibrium

The elastic deformation $\epsilon_{ij}^{el,\Delta}$ during Δt can be viewed as the response of an homogeneous elastic medium to the non-homogeneous plastic deformation $\epsilon_{ij}^{pl,\Delta}$. As a result, after Δt, any elementary volume $\mathcal{D}$ sustains a local stress perturbation:

$$\sigma_{ij}^{\Delta} = \lambda\delta_{ij}\epsilon_{kk}^{el,\Delta} + 2\mu\epsilon_{ij}^{el,\Delta} \tag{4.8}$$

The stress field at $t_o + \Delta t$ is then $\sigma_{ij}^{R} + \sigma_{ij}$. The apparent displacement field u_i can be computed by assuming mechanical equilibrium which requires

$$\partial_j(\sigma_{ij}^{\Delta} + \sigma_{ij}^{R}) = 0 \tag{4.9}$$

Taking into account expressions (4.7), (4.8), (4.3) and (4.6), one arrives at

$$(\lambda + \mu)\partial_i(\partial_l u_l) + \mu(\partial_l\partial_l)u_i = -f_i \tag{4.10}$$

with

$$f_i = -(\lambda\partial_i\epsilon_{kk}^{pl,\Delta} + 2\mu\partial_j\epsilon_{ij}^{pl,\Delta}) \tag{4.11}$$

for any plastic strain field.

Because of the linearity of this equation, it is convenient to solve it in Fourier space,

$$\hat{u}_i = \Xi_{ij}^{-1}\hat{f}_j$$

with

$$\hat{f}_i = \mathbf{i}(\lambda q_i\hat{\epsilon}_{kk}^{pl,\Delta} + 2\mu q_j\hat{\epsilon}_{ij}^{pl,\Delta}) \tag{4.12}$$

Ξ_{ij} is detailed in Appendix B.

One can further assume, for simplification, that the medium is incompressible :

$$\partial_l u_l = \partial_l u_l^{pl} = 0 \tag{4.13}$$

With this assumption the mechanical equilibrium changes its general form to:

$$-\partial_i P^T + \partial_j \sigma_{ij}^T = 0$$

The upper index indicates the final pressure $P^T = P^R + P^\Delta$ and the final stress $\sigma_{ij}^T = \sigma_{ij}^R + \sigma_{ij}^\Delta$. Mechanical equilibrium in the reference state requires $-\partial_i P^R + \partial_j \sigma_{ij}^R = 0$. The above equations and the constraint of incompressibility (4.13) result in the equation required by the mechanical equilibrium for the perturbed stress and pressure field due to plastic events

$$-\partial_i P^\Delta + \mu(\partial_l \partial_l) u_i = -f_i^I \tag{4.14}$$

with

$$f_i^I = -2\mu \partial_j \epsilon_{ij}^{pl,\Delta} \tag{4.15}$$

The solution in Fourier space is straightforward, from which one deduces the expression for the stress perturbation field due to plastic events in Fourier space

$$\hat{\sigma}_{ij}^\Delta = 2\mu \hat{G}_{ij,kl} \hat{\epsilon}_{kl}^{pl,\Delta} \tag{4.16}$$

with

$$\hat{G}_{ij,kl} = \frac{\delta_{jl} q_i q_k + \delta_{ik} q_j q_l}{q2} - 2\frac{q_i q_j q_k q_l}{q^4} - \delta_{ik}\delta_{jl} \tag{4.17}$$

The detail of calculation is in Appendix B.

It is important to note that (i) the symmetry $\hat{G}(-\mathbf{q}) = \hat{G}(\mathbf{q})$ implies that in real space G is a even function $G(\mathbf{x}) = G(-\mathbf{x})$. (ii)the propagator $\hat{G}_{ij,kl}$ is not defined at $q_i = 0$ This zero wavevector value is the integral of the response over space: $\hat{G}_{ij,kl}(\mathbf{q} = \mathbf{0}) = \int G_{ij,kl}(\mathbf{x}) d\mathbf{x}^d$. To determine the zero wavevector Fourier component, we use the property that the total stress response to an internal plastic event taking place in the material is zero, we rewrite the expression (4.16) in real space:

$$\sigma_{ij}^\Delta(\mathbf{x}) = 2\mu \int G_{ij,kl}^N(\mathbf{x} - \mathbf{y}) \epsilon_{kl}^{pl,\Delta}(\mathbf{y}) d\mathbf{y}^d \tag{4.18}$$

where we have introduced the total response function $G_{ij,kl}^N$instead of $G_{ij,kl}$. The condition of zero total stress then imposes

$$\frac{1}{V} \int \sigma_{ij}^\Delta(\mathbf{x}) d\mathbf{x}^d = 2\mu \hat{G}_{ij,kl}^N(\mathbf{0}) \int \epsilon_{kl}^{pl,\Delta}(\mathbf{y}) d\mathbf{y}^d = 0$$

from which

$$\hat{G}^N_{ij,kl}(\mathbf{0}) = 0 \tag{4.19}$$

and

$$\hat{G}^N_{ij,kl}(\mathbf{q} \neq \mathbf{0}) = \hat{G}_{ij,kl} \tag{4.20}$$

So any internal stress fluctuation only due to the heterogeneous plastic strain field can be expressed by (4.18) with the above definition of $\hat{G}^N_{ij,kl}$ which guarantees a macroscopically stress free state.

Superposition of stress fields

σ^R_{ij} in the above section is the stress field in the reference state. It can be in general of any form as long as it satisfies the mechanical equilibrium. Let us assume it to be the internal heterogeneous stress field due to the heterogeneous feature of amorphous systems in a (macroscopic) stress free state, so that the integral of σ^R_{ij} over space vanishes.

Using the notation σ^{INT}_{ij} for $\sigma^{\Delta}_{ij} + \sigma^R_{ij}$ described above for the internal stress only due to the heterogeneous plastic strain field changing, i.e. local plastic events. Similarly P^{INT} for $P^{\Delta} + P^R$ described above. The mechanical equilibrium is guaranteed by (4.14). Thanks to the linearity of this mechanical equilibrium equation, any external perturbation σ^{EXT}_{ij} and P^{EXT} satisfying the mechanical equilibrium can be added to the internal stress and pressure without violating mechanical equilibrium.

We can write the total stress field

$$\sigma_{ij} = \sigma^{EXT}_{ij} + \sigma^{INT}_{ij}$$

with

$$\frac{1}{V}\int \sigma^{INT}_{ij}(\mathbf{x})d\mathbf{x}^d = 0$$

and the bulk stress

$$\langle\sigma_{ij}\rangle = \frac{1}{V}\int \sigma_{ij}(\mathbf{x})d\mathbf{x}^d = \frac{1}{V}\int \sigma^{EXT}_{ij}(\mathbf{x})d\mathbf{x}^d$$

Also we can decompose the local elastic strain into two parts $\epsilon^{el}_{ij} = \epsilon^{el,INT}_{ij} + \epsilon^{el,EXT}_{ij}$, in the case of an incompressible medium:

$$\sigma^{INT}_{ij} = 2\mu\epsilon^{el,INT}_{ij} = 2\mu(\epsilon^{el,\Delta}_{ij} + \epsilon^{el,R}_{ij})$$

and

$$\sigma_{ij}^{EXT} = 2\mu\epsilon_{ij}^{el,EXT}$$

Since mechanical equilibrium is assumed for the stress field in the reference state (4.7), a fictitious plastic strain field can be always reconstructed by replacing σ_{ij} and ϵ_{ij}^{pl} by σ_{ij}^{R} and $\epsilon_{ij}^{pl,R}$ respectively in (4.18). In Fourier space for $\mathbf{q}$ without zero components:

$$\hat{\epsilon}_{ij}^{pl,R} = \frac{1}{2\mu}\left(\hat{G}^{N}\right)^{-1}_{ij,kl}\hat{\sigma}_{kl}^{R}$$

For $\mathbf{q}$ with zero components, it is simple to impose $\hat{\epsilon}_{ij}^{pl,R} = 0$. This fictitious plastic strain field has no specific physical meaning and is simply introduced to make the formulation more elegant.

Let us cite two specific examples of an external applied stress field (i) a uniform shear with imposed shear stress $\sigma_{ij}^{EXT} = constant$ over all the system; (ii) a uniform gradient of pressure applied on a two dimensional channel along x: $\partial_x P^{EXT} = C_p^{st}$, mechanical equilibrium and geometric symmetry implies that the external stress is given by $\sigma_{xy}^{EXT} = \sigma_{yx}^{EXT} = C_p^{st} y + constant$ and $\sigma_{xx}^{EXT} = -\sigma_{yy}^{EXT} = constant$.

Summary

To summarize, at every instant an amorphous system is supposed to be in a mechanical equilibrium state, which can be characterized by a plastic strain field, which is heterogeneous in general:

$$\epsilon_{ij}^{pl}(\mathbf{x}, t) = \epsilon_{ij}^{pl,R} + \epsilon_{ij}^{pl,\Delta} \tag{4.21}$$

The internal stress field due to plastic heterogeneity can be uniquely defined by the plastic strain field through

$$\sigma_{ij}^{INT}(\mathbf{x}, t) = 2\mu \int d\mathbf{y}^{d} G_{ij,kl}^{N}(\mathbf{x} - \mathbf{y})\epsilon_{kl}^{pl}(\mathbf{y}, t) \tag{4.22}$$

An external stress field, which can be applied in any form for simulating the external loading condition, adds up with the internal stress to give the total stress field

$$\sigma_{ij}(\mathbf{x}, t) = \sigma_{ij}^{INT}(\mathbf{x}, t) + \sigma_{ij}^{EXT}(\mathbf{x}, t) \tag{4.23}$$

Outside the plastic regions, the elastic strain field is related to the stress field using linear elasticity $\sigma_{ij}^{*} = 2\mu\epsilon_{ij}^{el,*}$ for an incompressible material, where the upper index $*$ represents any of “total”, “internal” and “external”.

For simplicity a scalar version of this description is adopted in the thesis. Only the pure shear along x direction is considered, i.e. only the xy component is taken into account. In this case, by writing σ for σ_{xy} and similarly for other quantities, the equations above become

$$\sigma^{INT}(\mathbf{x},t) = 2\mu \int d\mathbf{y}^d G^N(\mathbf{x}-\mathbf{y})\epsilon^{pl}(\mathbf{y},t) \tag{4.24}$$

$$\sigma(\mathbf{x},t) = \sigma^{INT}(\mathbf{x},t) + \sigma^{EXT}(\mathbf{x},t) \tag{4.25}$$

with $\hat{G}^N(\mathbf{0}) = 0$ and in a 2d system

$$\hat{G}^N(\mathbf{q}) = -4\frac{q_x^2 q_y^2}{q^4} \tag{4.26}$$

and in a 3d system

$$\hat{G}^N(\mathbf{q}) = -\frac{4q_x^2 q_y^2 + q_z^2 q^2}{q^4} \tag{4.27}$$

4.2.2 Dynamics

At every instant, an amorphous system is assumed to be in a mechanical equilibrium state which comes from the assumption that the system is in the strongly overdamped regime because of internal dissipation. This is taken into account by the relation instantaneously satisfied at all time by the internal stress field and the heterogeneous plastic strain field, i.e. equation (4.22).

From equations (4.22) and (4.23), at moment t, the state of a system is independently determined by the plastic strain field ϵ_{ij}^{pl} and the external loading σ_{ij}^{EXT}. The time evolution of these two quantities determines then the complete dynamics of the system. The dynamics of σ_{ij}^{EXT} is an input signal corresponding to the external loading, which should be independent on any state variable of the system. The dynamics of ϵ_{ij}^{pl} should be a functional of state variables, reflecting the internal properties of the system.

The dynamics of ϵ_{ij}^{pl} consists of two parts: (I) Where and when takes place a plastic event, and when a plastic event stops. As shown in many molecular dynamic simulations and in experiments, plastic events occur in a random and localized fashion over all the system (II) When a plastic event is taking place at a position $\mathbf{x}$, how does the plastic strain $\epsilon_{ij}^{pl}(\mathbf{x})$ vary with respect to the state variables, i.e. a functional should be specified $\partial_t\epsilon_{ij}^{pl}(\mathbf{x},t)[\sigma_{ij}(\mathbf{y},t);\epsilon_{ij}^{pl}(\mathbf{y},t)]$. These two parts of dynamics of local plastic strain have been chosen in various ways in the literature.

In the following sections, the rules for the scalar version of the model adopted in this thesis will be introduced.

Criteria for the activation and the relaxation of local plastic events

An elementary cell at $\mathbf{x}$ undergoing a plastic event is said to be in its plastic state, in which the local plastic strain rate is non zero $\dot{\epsilon}^{pl}(\mathbf{x}) \neq 0$, otherwise it is said to be in its elastic state $\dot{\epsilon}^{pl}(\mathbf{x}) = 0$. A state variable $n(\mathbf{x}, t)$ is introduced: $n(\mathbf{x}, t) = 0$ if the cell at $\mathbf{x}$ is in the elastic state and $n(\mathbf{x}, t) = 1$ if the cell is in the plastic state.

A local stress barrier of stress $\sigma^Y(\mathbf{x})$ is introduced to determine whether a cell in the elastic state becomes plastic. For a cell $n(\mathbf{x}, t) = 0$, it will becomes plastic $n(\mathbf{x}, t + \delta t) = 1$, if $\sigma(\mathbf{x}) = \sigma^Y_{ij}(\mathbf{x})$ and it will remain elastic if $\sigma(\mathbf{x}) < \sigma^Y(\mathbf{x})$. The local stress barrier σ^Y is drawn from a probability distribution independently for each site. The stress barrier σ^Y corresponds to a energy barrier $E^Y = \frac{\left(\sigma^Y\right)^2}{4\mu}$. It is assumed there is a minimum energy barrier below which the probability is zero and above which the energy barrier is exponentially distributed

$$P(E^Y)dE^Y = dE^Y \Theta(E^Y - E_{min})\nu \exp\big(-\nu(E^Y - E_{min})\big) \tag{4.28}$$

where $\Theta(x)$ is the Heaviside function, ν a normalization factor. Each time a cell becomes plastic, the plastic event happening in this cell as well as the plastic events happening before the next plastic event in this cell make changes of the particles configuration, which in turn modify the local stress barrier for the cell to encounter the next plastic event, so that the local stress barrier is renewed, once a plastic event occurs, by randomly choosing its value from the above distribution, that is also to say that there is no strain hardening or strain softening effect built into the model.

Once a cell becomes plastic, local plastic strain begins to accumulate within this plastic event. Another parameter γ_c is introduced for deciding when the cell will become elastic again. It becomes elastic when the totally accumulated strain reaches γ_c

$$2\int dt(\dot{\epsilon}^{pl}(t) + \dot{\epsilon}^{el}(t)) \geq \gamma_c \tag{4.29}$$

For consistency, it is considered that the minimum energy barrier is related to the plastic threshold γ_c through

$$E_{min} = \frac{\mu\gamma_c^2}{4} \tag{4.30}$$

The elastic strain rate in formula (4.29), comes from both the external loading and the plastic events of other cells which perturbs the stress of the cell in consideration.

Local dynamics

Elementary cells are modeled as “dashpot” modules, i.e. a resistance in series with a spring. The plastic strain plays the role of the resistance and the elastic strain plays the role of the spring. The stress proportional to the elastic strain is exerted on the resistance. The local plastic strain rate, when the cell is in plastic state $n(\mathbf{x}) = 1$, is proportional to the local stress and it is zero if it is in elastic state $n(\mathbf{x}) = 0$.

$$\partial_t \epsilon^{pl}(\mathbf{x}, t) = n(\mathbf{x}, t)\frac{\sigma(\mathbf{x}, t)}{2\mu\tau} \tag{4.31}$$

where τ is a time scale parameter.

Summary

These rules of alternation of local state and the local dynamics equation (4.31) complete the model with equations (4.24)(4.25).

Within this formulation, it is natural to make a stress control protocol by defining the function $\sigma^{EXT}(\mathbf{x}, t)$, injecting it into the model and solving the model by numerical integration.

It is also useful to define the global strain for making a shear rate control protocol, which is mostly encountered in experiments and molecular dynamics simulation. The local total strain writes $\epsilon(\mathbf{x}) = \epsilon^{pl}(\mathbf{x}) + \epsilon^{el}(\mathbf{x}) = \epsilon^{pl}(\mathbf{x}) + \epsilon^{el,INT}(\mathbf{x}) + \epsilon^{el,EXT}(\mathbf{x})$. The global strain is the average over space

$$\langle\epsilon\rangle = \frac{1}{V}\int d\mathbf{x}^d \epsilon(\mathbf{x}) = \langle\epsilon\rangle^{pl} + \langle\epsilon\rangle^{el} = \langle\epsilon\rangle^{pl} + \langle\epsilon\rangle^{el,EXT} \tag{4.32}$$

For imposing a constant shear rate $\langle\dot{\epsilon}\rangle$, one should adjust the applied stress with respect to the global plastic strain rate. If an uniform stress field is applied for pure shear, it should be updated according to global plastic strain, from equation (4.32):

$$\dot{\sigma}^{EXT} = 2\mu\langle\dot{\epsilon}\rangle - 2\mu\langle\dot{\epsilon}\rangle^{pl} \tag{4.33}$$

The stress field evolves as $\partial_t\sigma(\mathbf{x}, t) = \dot{\sigma}^{EXT} + \partial_t\sigma^{INT}(\mathbf{x}, t)$ which is equivalent to

$$\partial_t\sigma(\mathbf{x}, t) = 2\mu\langle\dot{\epsilon}\rangle + 2\mu\int d\mathbf{y}^d\left(G^N(\mathbf{x} - \mathbf{y}) - \frac{1}{V}\right)\partial_t\epsilon^{pl}(\mathbf{y}, t) \tag{4.34}$$

One can define a propagator $G(\mathbf{x}) = G^N(\mathbf{x}) - \frac{1}{V}$. This form of the elasto-plastic model is what has been used in references [Picard et al., 2004, Nicolas and Barrat, 2013].

4.2.3 Algorithm scheme

The numerical implementation of the elasto-plastic model described above is summarized by the following algorithm schemes providing a complete vision of the elasto-plastic model. In the following for simplicity all strain ϵ is replaced by $\gamma/2$.

Shear rate control protocol

Algorithm 4.1 Shear rate control protocol

```
Fixing the applied shear rate $\dot{\gamma} = 2\dot{\epsilon}$
Initialization of $\sigma(\mathbf{x})$,$\sigma^Y(\mathbf{x})$,$n(\mathbf{x})$
Initialization $t = 0$
while $t < T_{max}$ do
    Compute local plastic strain rate: $\partial_t \gamma^{pl}(\mathbf{x}, t) = n(\mathbf{x}, t)\frac{\sigma(\mathbf{x},t)}{\mu\tau}$
    Compute local stress changing rate: $\partial_t \sigma(\mathbf{x}, t) = \mu\dot{\gamma} + \mu\int d\mathbf{y}^d G(\mathbf{x}-\mathbf{y})\partial_t \gamma^{pl}(\mathbf{y}, t)$
    Update local stress: $\sigma(\mathbf{x}, t + \delta t) = \sigma(\mathbf{x}, t) + \delta t \partial_t \sigma(\mathbf{x}, t)$
    Update local state:
    if $n(\mathbf{x}, t) == 0$ then
        if $\sigma(\mathbf{x}, t) > \sigma^Y(\mathbf{x})$ then
            $n(\mathbf{x}, t + \delta t) = 1$
            $\sigma^Y(\mathbf{x})$ is renewed from $P(\sigma^Y)$
        end if
    else
        if $\gamma^{ac}(\mathbf{x}, t) >= \gamma_c$ then
            $n(\mathbf{x}, t + \delta t) = 0$
            $\gamma^{ac}(\mathbf{x}, t + \delta t) = 0$
        else
            Compute local strain accumulation during the ongoing plastic event:
            $\gamma^{ac}(\mathbf{x}, t + \delta t) = \gamma^{ac}(\mathbf{x}, t) + \delta t\big[\partial_t \gamma^{pl}(\mathbf{x}, t) + \frac{1}{\mu}\partial_t \sigma(\mathbf{x}, t)\big]$
        end if
    end if
    $t+ = \delta t$
end while
```

Stress control protocol

Algorithm 4.2 Stress control protocol

```
Fixing the applied shear stress $\sigma^{EXT}(\mathbf{x})$
Initialization of the plastic interface $\gamma^{pl}(\mathbf{x})$
Initialization of $\sigma^Y(\mathbf{x})$,$n(\mathbf{x})$
Initialization $t = 0$
while $t < T_{max}$ do
    Compute Internal stress: $\sigma^{INT}(\mathbf{x}, t) = \mu \int d\mathbf{y}^d G^N(\mathbf{x} - \mathbf{y})\gamma^{pl}(\mathbf{y}, t)$
    Compute local stress: $\sigma(\mathbf{x}, t) = \sigma^{INT}(\mathbf{x}, t) + \sigma^{EXT}(\mathbf{x})$
    Compute local plastic strain rate: $\partial_t\gamma^{pl}(\mathbf{x}, t) = n(\mathbf{x}, t)\frac{\sigma(\mathbf{x},t)}{\mu\tau}$
    Update the plastic interface: $\gamma^{pl}(\mathbf{x}, t + \delta t) = \gamma^{pl}(\mathbf{x}, t) + \delta t\partial_t\gamma^{pl}(\mathbf{x}, t)$
    Update local state:
    if $n(\mathbf{x}, t) == 0$ then
        if $\sigma(\mathbf{x}, t) > \sigma^Y(\mathbf{x})$ then
            $n(\mathbf{x}, t + \delta t) = 1$
            $\sigma^Y(\mathbf{x})$ is renewed from $P(\sigma^Y)$
        end if
    else
        if $\gamma^{ac}(\mathbf{x}, t) >= \gamma_c$ then
            $n(\mathbf{x}, t + \delta t) = 0$
            $\gamma^{ac}(\mathbf{x}, t + \delta t) = 0$
        else
            Compute local strain accumulation during the ongoing plastic event:
            $\gamma^{ac}(\mathbf{x}, t + \delta t) = \gamma^{ac}(\mathbf{x}, t) + \delta t\big[\partial_t\gamma^{pl}(\mathbf{x}, t) + \frac{1}{\mu}\partial_t\sigma(\mathbf{x}, t)\big]$
        end if
    end if
    $t+ = \delta t$
end while
```

4.2.4 Mean-field approach at the mesoscopic scale

At each moment t, it is possible to construct a stress probability distribution $\mathcal{P}(\sigma, t)d\sigma$ from the stress field $\sigma(\mathbf{x}, t)$. The probability distribution $\mathcal{P}(\sigma, t)$ represents at a given moment t how the local stress is distributed over the system. Schematically

$$\mathcal{P}(\sigma, t)d\sigma \hat{=} \frac{1}{V}\int d\mathbf{x}^d \Theta\big(\sigma(\mathbf{x}, t) - \sigma\big)\Theta(\sigma + d\sigma - \sigma(\mathbf{x}, t)) \tag{4.35}$$

An effective evolution equation on $\mathcal{P}(\sigma, t)$ can be constructed for describing the evolution of the system. In the literature the Hebraud-Lequeux model [Hébraud and Lequeux, 1998] and the KEP model [Bocquet et al., 2009] are of this kind. These models were built for amorphous systems under fixed shear rate. By making approximations, the Hebraud-Lequeux model can be deduced from the KEP model. The Hebraud-Lequeux model reads

$$\partial_t\mathcal{P}(\sigma, t) = -\mu\dot{\gamma}\partial_\sigma\mathcal{P}(\sigma, t) + \alpha\Gamma(t)\partial_\sigma^2\mathcal{P}(\sigma, t) + \Gamma(t)\delta(\sigma) - \frac{1}{\tilde{\tau}}\Theta(|\sigma| - \sigma_c)\mathcal{P}(\sigma, t) \tag{4.36}$$

The Hebraud-Lequeux model assumes that local plastic events take only place with a probability per unit time $\frac{1}{\tilde{\tau}}$, when local stress exceeds in absolute value a uniform threshold, i.e. $\big|\sigma\big| > \sigma_c$. Once a plastic event takes place, the local stress drops back to the origin. This mechanism gives the last two terms on the right hand side of the equation (4.36), where $\Gamma(t) = \frac{1}{\tilde{\tau}}\int d\sigma\Theta(|\sigma| - \sigma_c)\mathcal{P}(\sigma, t)$ represents the total rate of plastic events. The first term comes from a global driving shear rate $\dot{\gamma}$ which would instantaneously shift the whole distribution function up to $\mu\dot{\gamma}$ per unit of time. The second term comes from the mechanical coupling between different sites in the system induced by the propagator $G^N(\Delta\mathbf{x})$. This mechanical coupling is modeled by a diffusion of the local stress, with the diffusion coefficient proportional to the rate of plastic events and α the coupling strength. This model is shown to reproduce well the Herschel-Bulkley law in the small shear rate limit.

It will be shown in the following that, by changing a little the local yielding criteria and making approximating assumptions, the Hebraud-Lequeux type model can be derived from the spatial resolved elasto-plastic model, and similarly the mean-field model can also be used to describe an amorphous system under either fixed shear rate or fixed shear stress.

From the elasto-plastic model to the Hebraud-Lequeux type model

Let us make two modifications in the elasto-plastic model presented above.

1. Local criteria of plastic events: If the local stress is larger than a unique threshold $|\sigma(\mathbf{x},t)| > \sigma_c$, the small region at $\mathbf{x}$ has probability $\frac{1}{\tilde{\tau}}$ per unit of time to undergo a local plastic event.

2. Plastic events are instantaneous, i.e. local rearrangements are considered much faster than the any time scale of external loading. If t_a is one of the moments where a plastic event happens at $\mathbf{x}$, the plastic shear rate at $\mathbf{x}$ is schematically represented:
$$\partial_t \gamma^{pl}(\mathbf{x},t) = -\frac{\sigma(\mathbf{x},t)}{G_o^N \mu} \sum_{t_a} \delta(t - t_a) \tag{4.37}$$
where a time scale is omitted due to the delta function. This formula means that the plastic strain $\delta\gamma^{pl}(\mathbf{x})$ at a small time interval after and before the moment of plastic event t_a is finite and equals to $-\frac{\sigma(\mathbf{x},t_a)}{G_o^N \mu}$, with $G_o^N = G^N(\mathbf{0}) < 0$. This design makes the stress drop at $\mathbf{x}$ only due to local plastic event at $\mathbf{x}$ equal to the local stress itself $\sigma(\mathbf{x}, t_a - 0^+)$. Precisely if only one plastic event takes place at $\mathbf{x}$
$$\delta\sigma^{INT}(\mathbf{x}) = \mu \int d\mathbf{y}^d G^N(\mathbf{x}-\mathbf{y})\delta\gamma^{pl}(\mathbf{y}) = \mu G^N(\mathbf{0})\big(-\frac{\sigma(\mathbf{x})}{G_o^N \mu}\big) = -\sigma(\mathbf{x}) \tag{4.38}$$
This design is consistent with the assumption of Hebraud-Lequeux model [Hébraud and Lequeux, 1998] and another version of the elasto-plastic model [Lin et al., 2014a].

With the above modifications, let us check how the local stress varies during a small time interval δt
$$\delta\sigma(\mathbf{x}) = \delta\sigma^{EXT} - \frac{1}{G_o^N} \sum_{\mathbf{y}\in A} G^N(\mathbf{x}-\mathbf{y})\sigma(\mathbf{y}) \tag{4.39}$$
where $\mathbf{y} \in A$ denotes the regions where a plastic event takes place during the small δt and the integral is replaced by a summation for simplification. Since δt is small and the local stress will drop close to zero if one plastic event happens at the same place, there can only happen one plastic event for a given position during δt. The second part of the right hand side of equation (4.39) can be seen as a random variable over all $\mathbf{x}$ with zero mean value because of $\frac{1}{V}\sum_{\mathbf{x}} G^N(\mathbf{x}-\mathbf{y}) = 0$. We can regard this random variable as a mechanical noise ξ^C as function of $\mathbf{x}$:
$$\xi^C(\mathbf{x}) = -\frac{1}{G_o^N} \sum_{\mathbf{y}\in A} G^N(\mathbf{x}-\mathbf{y})\sigma(\mathbf{y}) \tag{4.40}$$
with $\langle \xi^C \rangle_{\mathbf{x}} = 0$.

For regions where there happen a plastic event during δt , i.e. $\mathbf{x} \in A$, equation (4.39) can be written in another form:

$$\delta\sigma(\mathbf{x}) = \delta\sigma^{EXT} - \sigma(\mathbf{x}) - \frac{1}{G_o^N} \sum_{\mathbf{y}\neq\mathbf{x},\mathbf{y}\in A} G^N(\mathbf{x}-\mathbf{y})\sigma(\mathbf{y}) \tag{4.41}$$

For regions where no plastic events happen, i.e. $\mathbf{x} \in A^C$, the equation (4.39) keeps its form. Let us denote $\xi^{'}$

$$\xi^{'}(\mathbf{x}) = \left\{ \begin{array}{ll} -\frac{1}{G_o^N}\sum_{\mathbf{y}\neq\mathbf{x},\mathbf{y}\in A} G^N(\mathbf{x}-\mathbf{y})\sigma(\mathbf{y}) & \mathbf{x} \in A \\ -\frac{1}{G_o^N}\sum_{\mathbf{y}\in A} G^N(\mathbf{x}-\mathbf{y})\sigma(\mathbf{y}) & \mathbf{x} \in A^C \end{array} \right. \tag{4.42}$$

the average of which

$$\langle\xi^{'}\rangle_{\mathbf{x}} = \langle\xi^C\rangle_{\mathbf{x}} + \langle\sigma\rangle_{\mathbf{x}\in A} = \langle\sigma\rangle_{\mathbf{x}\in A} \tag{4.43}$$

A zero mean mechanical noise can be defined as

$$\xi(\mathbf{x}) \hat{=} \xi^{'}(\mathbf{x}) - \langle\sigma\rangle_{\mathbf{x}\in A} \tag{4.44}$$

For regions $\mathbf{x} \in A$ during δt

$$\delta\sigma(\mathbf{x}) = \big(\delta\sigma^{EXT} + \langle\sigma\rangle_{\mathbf{x}\in A}\big) - \sigma(\mathbf{x}) + \xi(\mathbf{x}) \tag{4.45}$$

For regions $\mathbf{x} \in A^C$during δt

$$\delta\sigma(\mathbf{x}) = \big(\delta\sigma^{EXT} + \langle\sigma\rangle_{\mathbf{x}\in A}\big) + \xi(\mathbf{x}) \tag{4.46}$$

The $\mathcal{P}(\sigma, t)$ defined in (4.35) evolves under three effects according to (4.45) and (4.46): (i) An uniform driving $\delta\sigma^{EXT} + \langle\sigma\rangle_{\mathbf{x}\in A}$; (ii) For those undergoing plastic events, local stress drops back to origin; (iii) Zero mean noise $\xi(\mathbf{x})$.

The first two effects give rise to a partial derivative equation of $\mathcal{P}(\sigma, t)$:

$$\partial_t\mathcal{P}(\sigma,t) = -\big(\frac{\delta\sigma^{EXT} + \langle\sigma\rangle_{\mathbf{x}\in A}}{\delta t}\big)\partial_\sigma\mathcal{P}(\sigma,t) + \Gamma(t)\delta(\sigma) - \frac{1}{\tilde{\tau}}\Theta(|\sigma|-\sigma_c)\mathcal{P}(\sigma,t) \tag{4.47}$$

with

$$\Gamma(t) = \frac{1}{\tilde{\tau}}\int d\sigma\Theta(|\sigma|-\sigma_c)\mathcal{P}(\sigma,t) \tag{4.48}$$

representing the quantity of plastic events per unit time. We can also write:

$$\langle\sigma\rangle_{\mathbf{x}\in A} = \frac{\delta t}{\tilde{\tau}}\int d\sigma\Theta(|\sigma|-\sigma_c)\mathcal{P}(\sigma,t)\sigma \tag{4.49}$$

If we assume that the noise $\xi(\mathbf{x})$ is Gaussian distributed noise with an amplitude proportional to the number of plastic events during δt, the effect of the mechanical noise $\xi(\mathbf{x})$ gives rise to a diffusion term $D(t)\partial_\sigma^2\mathcal{P}(\sigma,t)$ adding up to the evolution equation of $\mathcal{P}(\sigma,t)$. The diffusion coefficient is proportional to the rate of plastic events, i.e. $D(t)=\alpha\Gamma(t)$ with α representing the coupling strength.

A straightforward calculation from definition (4.37) leads to $\mu\delta t\langle\dot\gamma^{pl}\rangle = -\frac{1}{G_o^N}\langle\sigma\rangle_{\mathbf{x}\in A}$. We can define a bulk plastic shear rate up to a constant prefactor $-\frac{1}{G_o^N}$, always keeping the same physical meaning

$$\dot\gamma^{pl} \hat{=} -G_o^N\langle\dot\gamma^{pl}\rangle = \langle\sigma\rangle_{\mathbf{x}\in A} = \frac{1}{\mu\tilde\tau}\int d\sigma\Theta(|\sigma|-\sigma_c)\mathcal{P}(\sigma,t)\sigma \tag{4.50}$$

The external loading σ^{EXT} is of pure elastic nature and it is interpreted in the context of the elasto-plastic model as the bulk stress. By changing the notation $\mu\dot\gamma^{el} = \frac{\delta\sigma^{EXT}}{\delta t}$ and $\dot\gamma = \dot\gamma^{el} + \dot\gamma^{pl}$, the full evolution of $\mathcal{P}(\sigma,t)$ reads:

$$\partial_t\mathcal{P}(\sigma,t) = -\mu\dot\gamma\partial\mathcal{P}(\sigma,t) + \alpha\Gamma(t)\partial_\sigma^2\mathcal{P}(\sigma,t) + \Gamma(t)\delta(\sigma) - \frac{1}{\tilde\tau}\Theta(|\sigma|-\sigma_c)\mathcal{P}(\sigma,t) \tag{4.51}$$

which is the Hebraud-Lequeux (HL) model [Hébraud and Lequeux, 1998]. The new thing that we can add here is that the $\dot\gamma$ in HL model is interpreted as composed by a pure elastic part and a pure plastic part. The elastic part is the external loading playing the role of input signal and the plastic part is expressed by equation (4.50). It can be verified by integrating on both sides of (4.51) with $\int d\sigma\sigma$:

$$\frac{d}{dt}\langle\sigma\rangle = \mu\dot\gamma - \mu\dot\gamma^{pl} = \mu\dot\gamma^{el} = \dot\sigma^{EXT} \tag{4.52}$$

Shear stress and shear rate control protocol

If one wants to apply shear rate control protocol, it is nothing but the original HL model by letting $\dot\gamma(t)$ vary and implementing a feedback algorithm.

If one wants to apply a constant shear stress, it consists to initiate the $\mathcal{P}(\sigma,t=0)$ such that $\langle\sigma\rangle(t=0)$ equals the stress one wants to apply and to replace $\dot\gamma$ by $\dot\gamma^{pl}$ according to equations (4.50) and (4.52).

If one wants to apply a variable shear stress, for example the oscillatory shear stress, it consists to replace $\dot\gamma$ by the sum of the desired $\dot\gamma^{el}(t)$ and $\dot\gamma^{pl}$ according to equation (4.50) after initialization giving the wanted bulk stress at the $t=0$ and to let the equation evolve. The implementation of this protocol resembles to a linear feedback loop on $\dot\gamma(t)$ often encountered in experiments, but we have here a zero delay time.

4.3 The analogy with depinning model

Let us briefly recall the formalism of the elasto-plastic model and the formalism of the depinning model.

1. Depinning model

$$\eta \partial_t h(x,t) = \nu \partial_x^2 h + f - \partial_h V(x, h(x,t))$$

2. Elasto-plastic model, with $\eta^{'} = \mu\tau$

$$\eta^{'} \partial_t \gamma^{pl}(\mathbf{x},t) = n(\mathbf{x},t)\big(\mu \int d\mathbf{y} G^N(\mathbf{x}-\mathbf{y})\gamma^{pl}(\mathbf{y},t) + \sigma^{EXT}\big)$$

One can identify some similarities between these two equations. The depinning model describes the motion of the interface motion $h(x,t)$ under self-interaction, the external driving and the quenched disorder potential energy landscape. The elasto-plastic model describes the motion of the plastic interface $\gamma^{pl}(\mathbf{x}) = 2\epsilon^{pl}(\mathbf{x})$ under self-interaction, external driving and plastic events activation.

The kinetic object

$$h(x,t) \leftrightarrow \gamma^{pl}(\mathbf{x},t)$$

The self-interaction

$$\nu \partial_x^2 h \leftrightarrow \mu G^N(\mathbf{x}) * \gamma^{pl}(\mathbf{x},t)$$

The external driving

$$f \leftrightarrow \sigma^{EXT}$$

The alternation dynamics of plastic events $n(\mathbf{x}) : 0 \rightleftharpoons 1$ can be viewed as pinning disorder analogue to the quenched disorder in the depinning model $-\partial_h V(x,h)$. This kind of analogy between the two models are also discussed in [Lin et al., 2014a, Tyukodi et al., 2016, Weiss et al., 2014].

The important difference between these two models is that the self-interaction in the depinning model is convex while the self-interaction of the elasto-plastic model is not.

The dynamical phase transition of the depinning model can be summarized by $v = \langle \partial_t h \rangle \sim (f - f_c)^\beta$ while the amorphous systems admit the Herschel-Bulkley law, for stress control protocol or for large enough system size shear rate control protocol, $\dot{\gamma} = \langle \partial_t \gamma^{pl} \rangle \sim (\sigma - \sigma_c)^{1/n}$. If there is any critical dynamics associated with a dynamical phase transition at the yielding point of an amorphous system, it is natural to draw the physical picture of this critical phenomenon by inspiration from the depinning model.

Part II

Topics

Chapter 5

Critical dynamics close to the yielding transition

Broadly speaking, the yielding transition for an amorphous system deep below the glass transition refers to the transition between a liquid like behavior and a solid like behavior when the globally applied stress varies across a critical value, i.e. the macroscopic yield stress. In this chapter, the yielding transition of an athermal amorphous system is probed using the mesoscopic elasto-plastic model described in the previous chapter.

From a microscopic point of view, below the yielding point, an athermal glassy system is trapped into a metastable basin of the potential energy landscape. Beyond the yielding point, the global strain rate response can be interpreted microscopically as the traveling through the potential energy landscape with an averaged velocity in the configuration space compatible with the global strain rate. The manner by which the system of Nd degrees of freedom travels across the potential energy landscape, corresponding to the steady state shear, is *a priori* different depending on the loading conditions, e.g. higher or lower applied external stress (or shear rate). Using molecular dynamics simulations, it has been shown that:

1. Not only in the quasi-static regime but also at relatively high shear rate, the localized plastic events are still the relevant process for the global deformation, which supports the idea of using mesoscopic modeling for probing the change of dynamical regimes as the value of the applied external shear rate approaches zero.

2. The steady state dynamics becomes more and more collective when the applied shear rate tends to zero, in contrast with a rather random uncorrelated

dynamics at high shear rate. Dynamical properties converge to the quasi-static limit for decreasing shear rate.

From a mesoscopic point of view of athermal systems, a plastic event is activated only due to a local stress increase. Higher shear rates or higher applied stresses will clearly activate more plastic events per unit time randomly in space, while the elastic interactions described by the Eshelby stress propagator becomes more and more dominant for the activation of plastic events if the applied shear rate or external stress is relatively low. In the limit of zero shear rate, each of the successive plastic events must be activated by the previous ones. As a consequence a more collective steady state dynamics is expected to emerge when the applied shear rate approaches zero from a finite value.

Using the elasto-plastic model for probing the steady state dynamics for different shear rates approaching the low driving limit, will give some insights for understanding the yielding transition of amorphous systems at larger scales than the molecular dynamics. Comparing the results from mesoscopic model with those coming from molecular dynamics will also help to improve the understanding of the physics in a mesoscopic picture.

Throughout this chapter, a shear rate controlled elasto-plastic model is used to study the steady state dynamics of athermal glassy systems under different applied shear rates approaching the quasi-static shear limit. In the first section, the shear rate dependent avalanche statistics is investigated, showing critical behavior in the low shear rate limit. It is proposed in the literature that the critical behavior at the yielding transition involves a cooperative length scale. In the second, third and the fourth sections, different approaches are tested for probing this cooperative length scale. It is found, as discussed in the fourth section, that this length scale is evidenced by studying the macroscopic stress fluctuations.

The shear rate control protocol of the elasto-plastic model is used throughout this chapter for studying the steady state critical dynamics close to the yielding transition. The mathematical representation given in equations (4.34) and (4.31) is recalled here (Note that the notations have slightly changed $\dot{\gamma} = 2\langle\dot{\epsilon}\rangle$ and $\gamma^{pl} = 2\epsilon^{pl}$):

$$\partial_t \sigma(\mathbf{x}, t) = \mu\dot{\gamma} + \mu \int d\mathbf{y}^d G(\mathbf{x} - \mathbf{y}) \partial_t \gamma^{pl}(\mathbf{y}, t) \tag{5.1}$$

$$\partial_t \gamma^{pl}(\mathbf{x}, t) = n(\mathbf{x}, t) \frac{\sigma(\mathbf{x}, t)}{\mu\tau} \tag{5.2}$$

The criteria of activation and relaxation of plastic events are those presented in the previous chapter 4. Details of the numerical implementation can be found in the Appendix C.

5.1 Avalanche statistics

The collective motion of athermally driven amorphous systems is well defined in the zero shear rate limit in both molecular dynamics and in the elasto-plastic modeling approach. As the shear rate increases, the evidence of collective motion may be obscured gradually by the external loading. For probing the shear rate dependent properties of the different dynamical regimes, we should construct an object that can be clearly defined from the observables at any given shear rate and that can represent as much as possible the collective motion in zero shear rate limit.

Inspired by experimental studies and molecular dynamics simulations in the low shear rate limit, we consider sudden macroscopic stress drops as signatures of global plasticity, these are commonly referred to as avalanches. One such avalanche is a collective motion of many particles, inducing the transition from one metastable basin of the system to another. This process involves several local plastic rearrangements. The interpretation of global stress drops as avalanches may be less adequate for high shear rates, however macroscopic stress drops can always be clearly defined from the stress time series as long as the dynamics is intermittent. In this framework global stress drops correspond to a negative time derivative of the stress.

It is straightforward, by averaging over space on both sides of equation (5.1), that

$$\frac{1}{\mu}\frac{d}{dt}\langle\sigma\rangle_{\mathbf{x}} = \dot{\gamma} - \langle\dot{\gamma}^{pl}\rangle_{\mathbf{x}} \tag{5.3}$$

where $\langle\bullet\rangle_{\mathbf{x}} \hat{=} \frac{1}{V}\int d\mathbf{x}^d \bullet$. The time derivative of the stress represents how the global velocity of the plastic interface fluctuates around the macroscopic strain rate. The equation can be schematically represented by the figure 5.1. In the case where there are few plastic events, the plastic interface grows much more slowly than the global shear rate, so that the global elastic strain would accumulate and so does the macroscopic stress. In the case where there happens a burst of plastic events, releasing the energy stored in the elastic deformation, the average level of the plastic interface would catch up with the global total strain and the averaged macroscopic stress would drop. The situation where the global stress increases can be interpreted as a passive state of the system with respect to the applied shear rate and the situation where the global stress decreases can be interpreted as an active state of the system, i.e. the plastic interface is “ready to catch up” with the global

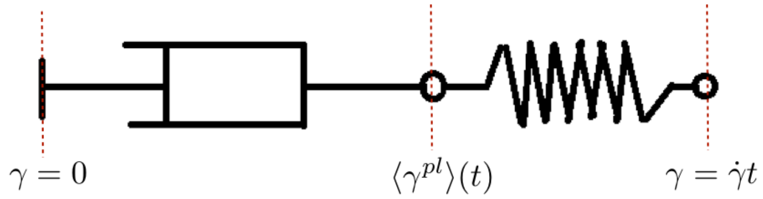

Figure 5.1: An amorphous system described by the elasto-plastic model can be globally represented by a visco-elastic modulus. The left extremity is assumed to be the zero deformation. The right extremity represents the global deformation composed by a global plastic deformation that is represented by the node linking the viscous modulus and the spring representing the global elastic strain, which is proportional to the macroscopic stress.

shear rate.

Another hint on how to define avalanches within our dynamics could come from the analogy between the formulation of the elasto-plastic model and that of the depinning model. In the depinning scenario one collective event, i.e. an avalanche, can be clearly identified from the motion of the elastic line in a two dimensional disordered environment. When the driving force is approaching the critical force from above $f \to f_c + 0^+$, because of the convexity of the self-interaction in the depinning model, the intermittent forward motion of the elastic line is always manifested by a forward motion of compact segments. The size of one avalanche can be identified as the area swept by one of these segments of the elastic line (see figure 5.2).

From the analogy discussed in Chapter 4, the plastic interface plays somehow the same role as the elastic line. However, the difficulty for the elasto-plastic model to define an avalanche in a similar way as in the depinning model, is that the forward motion of the plastic interface has a sparse geometry because of the non-convex self-interaction given by the quadrupolar geometry of the Eshelby propagator (see figure 5.2). The only situation in which the forward motion of the plastic interface can be regarded as an event of pure internal collective motion, i.e. an avalanche, is the quasi-static shear. In this case, the shear strain is increased for activating only one plastic event and then kept constant. Thus, the following forward motion of the plastic interface is only due to the plastic events that are activated by previous ones through the internal self-interactions. In analogy with the avalanche definition in the depinning model and also for probing the non-trivial dimensionality of the plastic interface increment within one collective event (one avalanche), it is convenient to define, in the quasi-static shear limit, the avalanche size as $S_{av} = \int d\mathbf{x} \Delta\gamma^{pl}(\mathbf{x}) = L^d \langle \Delta\gamma^{pl} \rangle_{\mathbf{x}}$. This is consistent with the meaning of the macroscopic stress drop at

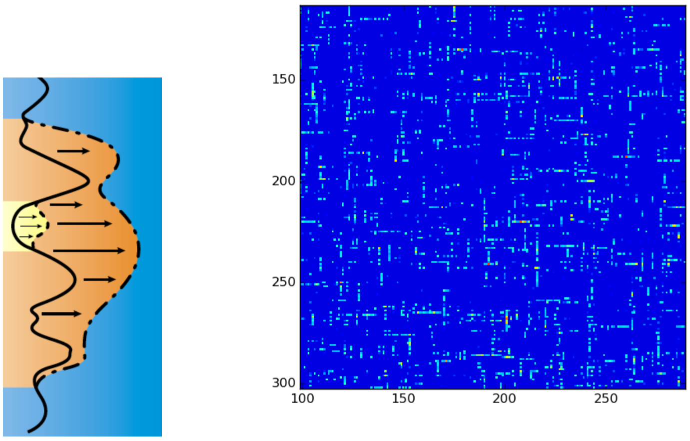

Figure 5.2: Left: The collective motion of one avalanche of a one dimensional elastic interface in a two dimensional disordered environment; Right: A schematic presentation of the increment of the two dimensional plastic interface for one event of collective motion in the quasi-static shear limit. Colors correspond to the amplitudes of the strain increment.

$\dot{\gamma} = 0$ in equation (5.3) up to a factor of L^d.

From the above analysis, the steady state time series of the stress velocity can be a good observable to study the intermittent dynamics of a flowing amorphous system crossing over from a regime dominated by external activations at high shear rates to a fully self-correlated regime close to the zero shear rate limit, i.e. the critical point of the yielding transition. In the following the precise definitions of the different studied quantities and results will be presented.

5.1.1 Definitions

By numerical integration of the elasto-plastic model, defined in equations (5.1) and (5.2), for a given linear system size L and a given applied shear rate $\dot{\gamma}$, one can easily obtain the time series of the rate of change of the macroscopic stress $\frac{d}{dt}\langle\sigma\rangle_{\mathbf{x}}$. The simulation is performed for both three dimensional ($d = 3$) and two dimensional ($d = 2$) systems. Since the quantity of interest is the stress drop, for simplicity the time series of the negative time derivative of the macroscopic stress $v_n(t) \hat{=} -\frac{d}{dt}\langle\sigma\rangle$ is taken for further analysis. A typical shape of $v_n(t)$ is shown in figure 5.3.

Stress drop

From the time series $v_n(t)$, if $v_n(t)$ is a ideal continuous function of time t, one *stress drop*, noted $V(t)$, refers to one segment of the time series of the negative stress time

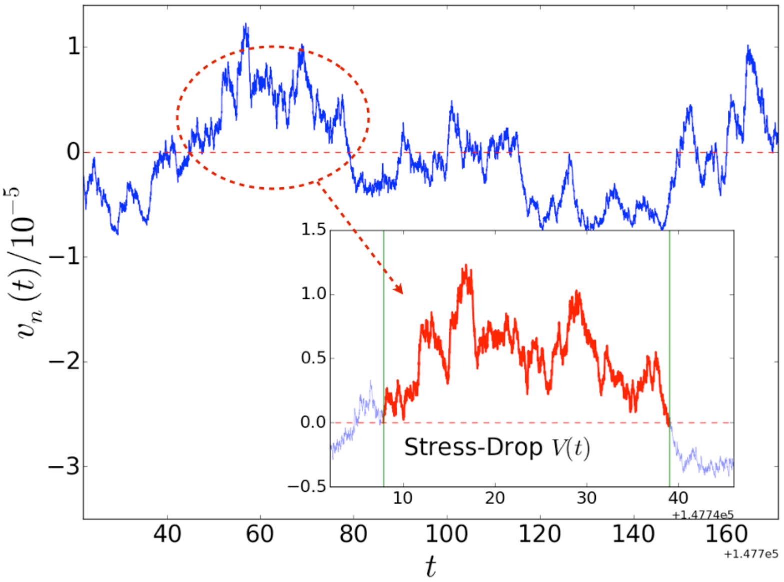

Figure 5.3: The negative time derivative of the macroscopic stress of a two dimensional system, $\dot{\gamma} = 10^{-4}$, $L = 512$. Inset: A typical segment of stress drop $V(t)$ marked by red color.

derivative $v_n(t)$ that is defined on the time interval $[t_S, t_E]$, such that $\forall t \in (t_S, t_E)$, $V(t)\hat{=}v_n(t) > 0$ and $V(t_S)\hat{=}v_n(t_S) = V(t_E)\hat{=}v_n(t_E) = 0$.

Because of the numerical discretization, it is mostly encountered that a time interval $[t_S + \Delta t, t_E - \Delta t]\hat{=}\{t_S + \Delta t, t_S + 2\Delta t, ..., t_E - \Delta t\}$ such that $\forall t \in \{t_S + \Delta t, t_S + 2\Delta t, ..., t_E - \Delta t\}$, $v_n(t) > 0$ is however in the middle of the two extremities t_S and t_E such that $v_n(t_S) < 0$ and $v_n(t_E) < 0$. The numerical correction of the stress drop definition is simply $V(t)$ with $t \in [t_S, t_E]\hat{=}\{t_S, t_S + \Delta t, t_S + 2\Delta t..., t_E\}$, such that $\forall t$ satisfying $t_E + \Delta t \leqslant t \leqslant t_E - \Delta t$, $V(t)\hat{=}v_n(t) > 0$ and $V(t_S) = V(t_E) = 0$ with $v_n(t_E) \leq 0$ and $v_n(t_S) \leq 0$.

Several stress drops can be identified from one time series $v_n(t)$, as shown in the figure 5.3. In the inset a zoom on one individual stress drop is shown. We can distinguish each stress drop from others by adding an index $V_i(t)$. Given a stress drop $V_i(t)$ defined on $[t_S^i, t_E^i]$, we characterize it by defining the following quantities.

The size of one stress drop

The size of one stress drop $V_i(t)$ is meant to capture the signature of a collective motion when the shear rate approaches quasi-static limit $\dot{\gamma} \to 0$. The size of one stress drop, noted S_i is defined as

$$S_i \hat{=} L^d \int_{t_S^i}^{t_E^i} dt V_i(t) \tag{5.4}$$

where L denotes the linear system size and d the dimension of the system. It is straightforward to see that S_i is equivalent to the avalanche size $S_{av} = L^d \langle \Delta\gamma^{pl} \rangle_{\mathbf{x}}$ in the quasi-static limit.

The duration of one stress drop

The duration T_i of one stress drop $V_i(t)$ is defined as

$$T_i \hat{=} t_E^i - t_S^i \tag{5.5}$$

The average shape of stress drops of a given duration T

Given a long enough time series $v_n(t)$, we can extract M_{total} stress drops $\{V_i(t)\}_{i=1,..,M_{total}}$ with corresponding durations $\{T_i\}_{i=1,...M_{total}}$. Defining $M(T)$ the number of stress drops with a duration $T_i \leq T$, i.e. $M(T) \hat{=} \sum_{i=1}^{M_{total}} \Theta(T - T_i)$, $\Delta M_T(\Delta T) = M(T + \Delta T/2) - M(T - \Delta T/2)$ is the number of stress drops with duration $T_i \in I(T, \Delta T) \hat{=} [T - \frac{\Delta T}{2}, T + \frac{\Delta T}{2}]$.

For a given stress drop $V_i(t)$ of duration T_i, one can define the rescaled form $\tilde{V}_i(\tilde{t}) \hat{=} V_i(\tilde{t} T_i)$ which is defined on $\tilde{t} \in [0, 1]$. The average shape of stress drops of duration T within a time window ΔT, noted as $V_T(\tilde{t}; \Delta T)$, is defined as

$$V_T(\tilde{t}; \Delta T) \hat{=} \frac{1}{\Delta M_T(\Delta T)} \sum_{i, T_i \in I(T, \Delta T)} \tilde{V}_i(\tilde{t}) \tag{5.6}$$

If we have an infinitely long time series $v_n(t)$ which gives rise to $M_{total} \to \infty$, the limit of $V_T(\Delta T \to 0)$ can be assumed to exist, i.e.

$$V_T(\tilde{t}) \hat{=} \lim_{\Delta T \to 0} V_T(\tilde{t}; \Delta T) \tag{5.7}$$

The function $V_T(\tilde{t})$ defined on $[0, 1]$ is the *average stress drop shape of duration* T. The numerical integration cannot be infinitely long, practically a time window ΔT is always chosen of finite duration for obtaining a compromise regarding significant statistics without biasing too strongly the real form of $V_T(\tilde{t})$.

Distance to the instability

Taking a snapshot of the stress field $\sigma(\mathbf{x}, t)$ and the yield stress field $\sigma^Y(\mathbf{x}, t)$, one can define the field of the distance to the instability $x(\mathbf{x}, t) \hat{=} \sigma^Y(\mathbf{x}, t) - \sigma(\mathbf{x}, t)$. Discarding the negative values of x which are mainly undergoing plastic events, one can produce the probability distribution of x over all the system $\mathcal{P}(x)$. This quantity is supposed to be crucial for the mechanical stability of the system. In the quasi-static shear limit, if $\mathcal{P}(x) \sim x^{\theta}$ is assumed for small x [Lin et al., 2014b], θ is required to be larger than zero for an unique firstly activated plastic event triggering in the following a finite number of plastic events, i.e. any avalanche should stop at some point in the quasi-static shear limit, as far as the self-interaction intensity decreases with the distance in a power law with an exponent equal to the system dimension [Lin et al., 2014b]. Numerically several snapshots of $x(\mathbf{x}, t)$ at well separated moments are taken for producing $\mathcal{P}(x)$ regarding of the finite size effect.

5.1.2 Results

A brief summary of the results is given in this section, followed by the published paper in the next section, which includes all the details of these results.

Scaling law when $\dot{\gamma} \to 0$

For a given $\dot{\gamma}$, a linear system size L and a dimensionality d(2 or 3), by a long time simulation, a long enough time series of negative stress velocity segments $v_n(t)$ is obtained, from which an ensemble of stress drop sizes $\{S_i\}$ and an ensemble of stress drop durations $\{T_i\}$ are extracted. A statistical analysis is performed on these quantities. For shear rates $\dot{\gamma} \leq 10^{-3}$, the results begin to converge, so that these results are supposed to reveal the critical dynamics of the yielding transition. The results presented in this section are mainly for $\dot{\gamma} \leq 10^{-3}$.

1. **The probability distribution of stress drop sizes $\mathcal{P}_S(S; L)$.** $\mathcal{P}_S(S; L)$ does not show any shear rate dependence for $\dot{\gamma} \leq 10^{-3}$, but manifests finite size effects. For large enough S, such that the numerical precision does not affect the results, $\mathcal{P}_S(S; L)$ shows a power law distribution with a cut-off S_c at large values, determined by finite size effects. $\mathcal{P}_S(S; L)$ can be represented in a universal form $\mathcal{P}_S(S; L) \sim S^{-\tau} f_S(S/L^{d_f})$. This is supported by the collapsing the data of all distributions $\mathcal{P}_S(S; L)$ onto a master curve, when rescaling $\mathcal{P}_S \to \mathcal{P}_S L^{\tau d_f}$ and $S \to S/L^{d_f}$.

    (a) We find that the size distribution exhibits power law behavior with an exponent $\tau \approx 1.28$ for two dimensional system and $\tau \approx 1.25$ for a three dimensional system, consistent with the results from molecular dynamics simulation [Salerno et al., 2012, Salerno and Robbins, 2013] and previous results from elasto-plastic models [Budrikis and Zapperi, 2013, Talamali et al., 2011, Lin et al., 2014a]. The values of τ for the two space dimensions are clearly different from the mean-field value commonly used in the avalanche literature $\tau^{MF} = 1.5$. This suggests that the mean-field approach, by assuming equal interaction strength among all sites of an amorphous system, may not be adequate.

(b) As discussed in the previous section, in the low shear rate limit the size of a stress drop approximates the size of one avalanche in the quasi-static shear limit, the largest linear extension is limited by the finite size of the system, so that the exponent d_f characterizes how one avalanche size scales with its linear extension. We find that d_f reveals a fractal dimension of the avalanches of order ≈ 0.9 for a 2-D system and ≈ 1.3 for a 3-D system. This suggests that the avalanches in the quasi-static shear limit as well as the largest event at a finite but small shear rate, exhibits a non-trivial structure of fractal geometry ($d_f \neq d$).

2. **The probability distribution of the stress drop durations** $\mathcal{P}_T(T;\dot{\gamma})$. In contrast with $\mathcal{P}_S(S;L)$, $\mathcal{P}_T(T;\dot{\gamma})$ displays a shear rate dependence without finite size effects. For a large enough duration T where numerical precisions do not affect the results, $\mathcal{P}_T(T;\dot{\gamma})$ shows a power law distribution with a cut-off T_c at large values, determined by the external shear rate $\dot{\gamma}$. All curves collapse onto a master curve if one plots the rescaled quantities $\mathcal{P}_T \to \mathcal{P}_T\dot{\gamma}^{\alpha\tau'}$ and $T \to T\dot{\gamma}^{\alpha}$, suggesting the scaling $\mathcal{P}_T(T;\dot{\gamma}) \sim T^{-\tau'} f_T(T\dot{\gamma}^{\alpha})$. In both 2-D and 3-D systems, τ' is found close to 1.4. α is an exponent characterizing how the duration of the largest stress drop scales with the finite shear rate. α is found to be approximately 0.38 in a 2-D system and approximately 0.3 in a 3-D system.

3. **The scaling between stress drop size** S **and duration** T. Similar to the definition of the average shape of stress drops of duration T, one can define the average stress drop size, noted $\bar{S}(T;L,\dot{\gamma})$:

$$\bar{S}(T;L,\dot{\gamma}) \hat{=} \lim_{\Delta T \to 0} \frac{1}{\Delta M_T(\Delta T)} \sum_{i, T_i \in I(T,\Delta T)} S_i \tag{5.8}$$

An averaging time window is taken to generate $\bar{S}(T)$ from numerical results.

(a) For any given $\dot{\gamma}$ and L, a perfect scaling relation is found $\bar{S} \sim T^{\delta}$, with $\delta \approx 1.58$ for both 2-D and 3-D systems.

(b) The prefactor of this relation $C(\dot{\gamma}, L)$ depends on shear rate and on the linear system size. Precisely $\bar{S} \approx C(\dot{\gamma}, L)T^{\delta}$, with the scaling relation $C \sim \dot{\gamma}^{\alpha\delta} L^{d_f}$. The last scaling relation is derived by the observation that the straight segments in log-log scale of $\bar{S}(T; \dot{\gamma}, L)$ for different $\dot{\gamma}$ and L, collapse onto one segment when performing the rescaling $\bar{S}/L^{d_f}$ and $T\dot{\gamma}^{\alpha}$.

(c) It is worthy to notice that the large value extremity of one segment $\bar{S}(T)$ is determined by the larger value cut-off S_c and T_c. S_c scales only with the systems size L with the exponent d_f and T_c scales only with the shear rate $\dot{\gamma}$ with the exponent $-\alpha$.

4. **Probability distribution of the distance to the instability** $\mathcal{P}(x; \dot{\gamma})$. For $\dot{\gamma} \to 0$, $\mathcal{P}(x)$ converges to the same curve for any system size at small value of x: $P(x) \sim x^{\theta}$ with $\theta \approx 0.52$ for 2-D and ≈ 0.37 for 3-D, which compares fairly well with the former results in the literature [Lin et al., 2014b].

Crossover to mean-field description as $\dot{\gamma}$ increases

1. **Rheology**. The rheological flow curve is probed by computing time average of macroscopic stress over a large strain window of order 10 within the stationary state for a given shear rate $\dot{\gamma}$. $\sigma(\dot{\gamma}) = \frac{1}{\Delta\gamma}\int_{\gamma_o}^{\gamma_o+\Delta\gamma} d\gamma \langle\sigma\rangle_{\mathbf{x}}$. For small shear rates ($\dot{\gamma} < 10^{-3}$) one can find a dynamical yield stress σ_c, well fitting $\dot{\gamma} \sim (\sigma(\dot{\gamma}) - \sigma_c)^{\beta}$ with $\beta \approx 1.55$. For larger shear rates above $\dot{\gamma} > 10^{-3}$, β is found to be close to 2, as predicted by Hebraud and Lequeux [Hébraud and Lequeux, 1998, Agoritsas, Elisabeth et al., 2015]. This crossover towards the mean-field picture for the estimation of the flow curve can be justified by the fact that the mechanical noise changes to be consistent with the mean-field assumption as $\dot{\gamma}$ increases above a value of 10^{-3}.

2. **Mechanical noise**. The mechanical noise can be derived from equation (5.1)

$$\frac{d}{dt}\sigma(\mathbf{x}) = \mu\dot{\gamma} + n(\mathbf{x}, t)G(\mathbf{0})\frac{\sigma(\mathbf{x})}{\tau} + \xi(\mathbf{x}) \tag{5.9}$$

with

$$\xi(\mathbf{x}) = \frac{1}{\tau}\sum_{\mathbf{y}\neq\mathbf{x}} G(\mathbf{x} - \mathbf{y})n(\mathbf{y})\sigma(\mathbf{y}) \tag{5.10}$$

By taking enough independent statistics of the local stress velocity field, local state field and local stress field, it is possible to obtain a representative ensemble of the mechanical noise, from which a probability distribution can be

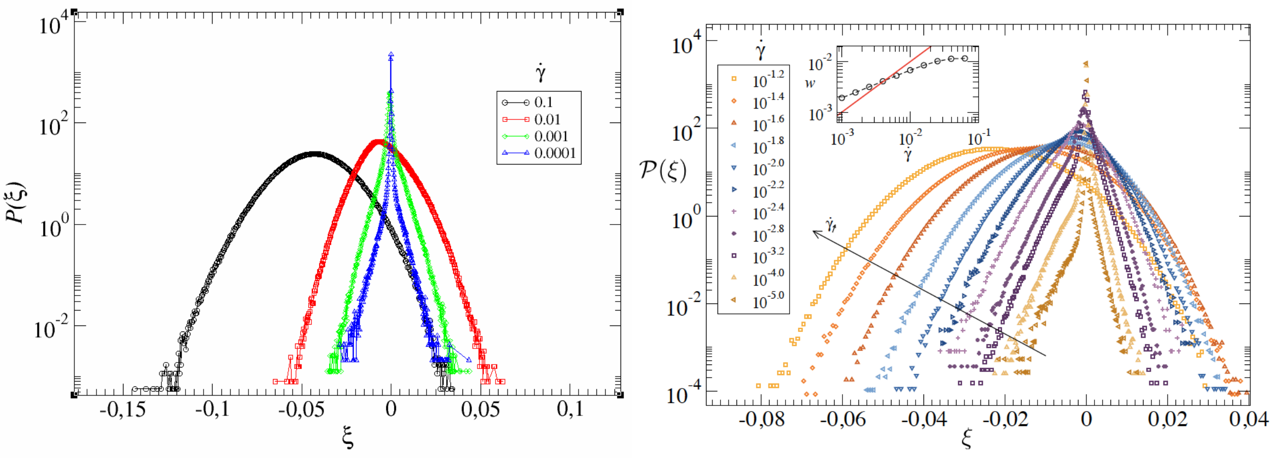

Figure 5.4: Left: pdf of the mechanical noise in 2 dimensions, for different shear rates; Right: same as left panel, in 3 dimensions. Inset: Open circles represent the standard deviation of the probability distribution versus shear rate. The red straight line is a guide for the eye.

derived. The results for different shear rates and different dimensionalities are shown in figure 5.4. It is clear from these results that the probability distribution of the mechanical noise depends on the shear rate regime, justifying the adequate description of the diffusion in the stresses at large enough shear rates [Hébraud and Lequeux, 1998]. For small shear rates, the diffusive description for the local stresses is no longer valid. This crossover of the mechanical noise from a mean-field behavior to a non mean-field behavior will be discussed in details in [Ferrero et al., 2016].

3. **Probability distribution of stress drop size $\mathcal{P}_S(S)$.** The exponent τ of the power law distribution $\mathcal{P}_S(S)$ increases monotonically with the shear rate $\dot\gamma > 10^{-3}$. At a relatively high shear rate $\dot\gamma \gtrsim 10^{-2}$, an exponent comparable with the mean-field exponent $\tau^{MF} = 1.5$ is recovered [Dahmen et al., 2009, 2011, Antonaglia et al., 2014], which may explain why this exponent is measured in many occasions, although one would expect the true critical exponent to be smaller.

4. **Probability distribution of the distance to the instability $\mathcal{P}(x)$.** For small value of x the distribution exhibits a power law behavior with $\mathcal{P}(x) \sim x^\theta$. The exponent θ decreases monotonically as the shear rate increases form 10^{-3} to 10^{-1}. For higher shear rates ($\dot\gamma \approx 10^{-1.4}$) , the exponent θ reaches a value very close to zero. This crossover of the exponent θ indicates that the local dynamics of x crosses over from mechanical noise dominated regime at low

shear rate to a shear rate dominated regime, which resembles that of depinning problem. The random kicks from plastic events on x are much smaller than the decrease caused by the high shear rate. In the depinning problem, x goes monotonously to zero as the kicks have always the same sign, because of the convex self-interaction.

Avalanches & stress drops

The average shape of stress drops of duration T, $V_T(\tilde{t})$ is found to be well fitted by the formula proposed for depinning problem [Laurson et al., 2013]

$$V_T(\tilde{t}) \propto B\big(\tilde{t}(1-\tilde{t})\big)^c\big(1-a_s(\tilde{t}-\frac{1}{2})\big) \tag{5.11}$$

c is found to be independent of other parameters and the relation proposed in [Laurson et al., 2013] $c = \delta - 1$ is confirmed. a_s is a parameter characterizing the degree of asymmetry of $V_T(\tilde{t})$. The amplitude B depends on the duration T. As c is fixed for all durations and a_s conserves the integral of V_T on $[0, 1]$, B determines the average size of stress drops of the same duration. From the definition (5.8), $\bar{S} \propto TB(T) \sim T^{\delta}$. By consequence $B \sim T^{\delta-1}$. It is actually found $B \sim T^{0.6}$, recalling that $\delta \approx 1.58$ independent on the dimension, so that the relation $B \sim T^{\delta-1}$ is confirmed, justifying the good fitting of the formula (5.11).

For characterizing the asymmetry of the average shape, another purely geometrical asymmetry parameter a_g can be defined as

$$a_g \hat{=} \int_0^1 d\tilde{t} \frac{\big|V_T(\tilde{t}) - V_T(1-\tilde{t})\big|}{V_T(\tilde{t}) + V_T(1-\tilde{t})} \tag{5.12}$$

The larger a_g, the more asymmetric is the shape, as is the case for the formerly introduced a_s. Qualitatively a_s and a_g show the same dependence on system size L, shear rate $\dot{\gamma}$ and the duration of an stress drop T. For the system sizes and shear rates that are tested, a_g is found, for a 3-D system, to scale with these three quantities as

$$a_g \sim T^{-0.43}\dot{\gamma}^{-0.37}L^{-1.25} \tag{5.13}$$

Assuming that plastic events take place in a purely random fashion without any correlation in space and in time, the spatial-temporal plastic activity map should be isotropic and no privileged time direction can be identified, in which case the average shape of stress drops should be symmetric in time, i.e. $a_s = a_g = 0$. As far as a_g (or a_s) is significantly different from zero, it implies that correlations in space and in time in the arrangement of plastic events begin to manifest themselves.

The duration T and the linear system L can be regarded as a spatial-temporal window of observation. Increasing either T or L makes the observation window larger. a_g can be seen as the intensity of correlation over the entire observation window. The larger a_g is, the more pronounced is the manifestation of the correlations in the occurrence of plastic events. We can infer from (5.13), that increasing the observation domain by either increasing T or L will decrease the intensity of correlations over the entire observation window. For a fixed observation window, the intensity of correlation is inversely proportional to the shear rate.

A unified interpretation of this observation is that the intensity of correlations over the entire observation window is determined by the ratio of the spatio-temporal correlation domain to the observation window. Let us denote D_c the domain of correlation and D_o for the window of observation. The intensity of correlation over the observation window is weak and tends to vanish if $\frac{D_c}{D_o} \to 0$ and the intensity of correlation is large if $\frac{D_c}{D_o} \gtrsim 1$. The size of the domain of correlation D_c is inversely related with the shear rate as shown in equation (5.13).

Equation (5.13) indicates that a_g diverges with $\dot{\gamma} \to 0$, which can be interpreted for a finite system as system spanning spatio-temporal correlations.. This is what happens in the quasi-static shear limit, where each stress drop corresponds to one avalanche, i.e. one event composed by fully correlated local plastic activities, the upper bound of which is only limited by the system size. This conceptual domain of spatial-temporal correlations D_c can be clearly identified with one avalanche in the limit of quasi-static shear.

As soon as the shear rate increases to finite values, the avalanches as well as the correlation domain D_c become loosely defined. With the above analysis of the dependence of the asymmetric parameter on the shear rate, the duration and the system size, we propose the following scenario: One avalanche is an event composed by fully self-correlated plastic activities. Avalanches are interrupted for any reasonable finite shear rate. One avalanche can be characterized by a domain of spatio-temporal correlations D_c, the measure of which, even it is not clear how to access it, is inversely proportional to the shear rate $\dot{\gamma}$. In the zero shear rate limit each domain of plasticity corresponds to one avalanche, the largest of which spans the whole system. Macroscopic stress drops as well as the plasticity in an amorphous system at a finite shear rate proceeds with the spatial-temporal superposition of avalanches. The intensity of correlation measured as the symmetry of the average shape of stress drops is weaker or stronger dependent on the ratio of the typical size of the correlation domain of an avalanche to the size of the observation window.

5.1.3 Publication associated with this chapter - Liu et al., Physical Review Letters 116, 065501 (2016).

Driving Rate Dependence of Avalanche Statistics and Shapes at the Yielding Transition

Chen Liu,[1,2] Ezequiel E. Ferrero,[1,2] Francesco Puosi,[3,1,2] Jean-Louis Barrat,[1,2] and Kirsten Martens[1,2]
[1]*Université Grenoble Alpes, LIPHY, F-38000 Grenoble, France*
[2]*CNRS, LIPHY, F-38000 Grenoble, France*
[3]*Ecole Normale Supérieure de Lyon, Laboratoire de Physique CNRS, 46 allée d'Italie, 69364 Lyon Cedex 7, France*

(Received 30 June 2015; published 11 February 2016)

We study stress time series caused by plastic avalanches in athermally sheared disordered materials. Using particle-based simulations and a mesoscopic elastoplastic model, we analyze system size and shear-rate dependence of the stress-drop duration and size distributions together with their average temporal shape. We find critical exponents different from mean-field predictions, and a clear asymmetry for individual avalanches. We probe scaling relations for the rate dependency of the dynamics and we report a crossover towards mean-field results for strong driving.

DOI: 10.1103/PhysRevLett.116.065501

Many materials respond to slow driving with strongly intermittent dynamics. Examples include Barkhausen noise in ferromagnets [1–3], stick-slip motion in earthquakes [4], serration dynamics in plasticity of solids [5], and avalanche dynamics in crack propagation [6,7], driven foams [8], and domain wall motion [9].

As in equilibrium critical phenomena, global quantities linked to such bursting collective events are usually power-law distributed and allow for the introduction of scaling functions. In the slow driving limit, the onset of motion can be interpreted as an out-of-equilibrium phase transition, suggesting the existence of families of systems that display similar avalanche statistics. To better identify this universality classes, both experimental [10–17] and theoretical [13,18–21] works have discussed the avalanche "shapes," going beyond the study of scaling exponents.

In deformation experiments of amorphous systems, such as grains, foams, or metallic glasses, avalanche dynamics are typically evidenced in the time series of the deviatoric component of the stress tensor. In the limit of vanishing deformation rate, we approach the so-called "yielding transition." The question of whether or not yielding can be characterized as a continuous dynamical phase transition, belonging to a specific universality class, is still under debate. The analysis of avalanche statistics close to yielding has, therefore, a particular relevance.

In this Letter, we study the emerging yielding dynamics in a simple shear geometry with imposed driving rate. Our focus lies on the shear-rate dependence of the avalanche statistics and thus complements recent quasistatic (QS) studies [22–25]. To address the low shear-rate regime, we use a coarse-graining approach, proven to yield qualitative and quantitative relevant predictions [26–31], and compare the low shear-rate results of our mesoscale model with quasistatic particle-based simulations.

Molecular dynamics (MD).—We consider a mixture of A and B particles interacting via a Lennard-Jones potential: $V_{AB}(r) = 4\epsilon_{AB}[(\sigma_{AB}/r)^{12} - (\sigma_{AB}/r)^{6}]$, with r being the distance between two particles. Units of energy, length, and mass are defined by ϵ_{AA}, σ_{AA} and m_A, the unit of time is given by $\tau_0 = \sigma_{AA}\sqrt{(m_A/\epsilon_{AA})}$. The potential is truncated at $R_c = 2.5$ and a force smoothing is applied between an inner cutoff $R_{\text{in}} = 2.2$ and R_c. The two species of particles have equal mass m, but different interaction parameters to prevent crystallization. We set $\epsilon_{AA} = 1.0$, $\epsilon_{AB} = 1.5$, $\epsilon_{BB} = 0.5$, $\sigma_{AA} = 1.0$, $\sigma_{AB} = 0.8$, $\sigma_{BB} = 0.88$, and $m = 1$. The ratio of particles of species A and B is chosen $N_A/N_B = 13/7$ and $8/2$ for $2d$ and $3d$ systems, respectively. Glassy states are obtained (with LAMMPS [32]) by quenching to zero temperature at constant volume systems equilibrated at $T = 1$. An athermal system is achieved by applying to each particle a viscous drag force $\mathbf{F}_{\text{drag}} = -\Gamma\mathbf{v}$, where $\mathbf{v}$ is the particle peculiar velocity. We condition the dynamics to be strongly overdamped [22,33] ($\Gamma = 1$). Avalanche statistics are obtained following a quasistatic protocol [22,23]. We impose simple shear at rate $\dot{\gamma} = 10^{-6}$ by deforming the box dimensions and remapping the particle positions. Following Ref. [22], the shear rate $\dot{\gamma}$ is set to zero when a steep increase in kinetic energy occurs (onset of plastic deformation) and only restored when the kinetic energy drops below a threshold.

Elastoplastic (EP) model.—We coarse grain an amorphous medium onto a mesoscopic lattice: each node represents a block of material holding exactly one shear transformation [33–36], for which we assume the same geometry as the globally applied simple shear. To each site i we associate a local scalar shear stress σ_i and a state variable n_i, indicating whether the site plastically deforms ($n = 1$) or not ($n = 0$). Local stresses evolve with the overdamped dynamics:

$$\partial_t \sigma_i = \mu\dot{\gamma} + \mu \sum_j G_{ij} \partial_t \gamma_j^{\text{pl}}, \tag{1}$$

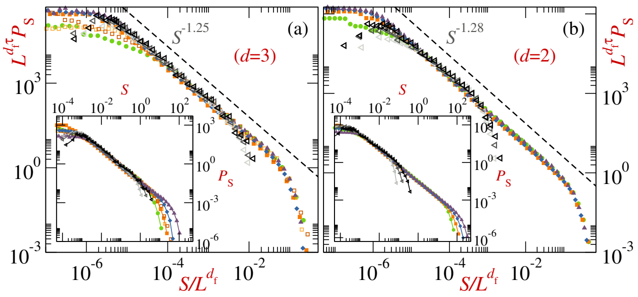

FIG. 1. Stress-drop size distributions. Main panels show rescaled distributions $L^{d_f\tau}P_S$ versus S/L^{d_f} of the EP model compared to MD quasistatic simulations (arbitrary shift applied for the comparison). Insets show not-scaled curves. (a) 3D EP model data for linear system sizes $L = 16$ (green circles), 32 (orange squares), 64 (blue diamonds), 128 (plum triangles), and shear rate 10^{-4} (full symbols). For $L = 32$, $\dot{\gamma} = 10^{-3}$, 10^{-5} are also shown (light and dark orange open squares). Gray scale triangles correspond to quasistatic 3D MD with $L = 40, 60, 80$ (from light to dark). (b) 2D EP data for linear system sizes $L = 256$ (green circles), 512 (orange squares), 1024 (blue diamonds), and 2048 (plum triangles) at $\dot{\gamma} = 10^{-5}$. Gray scale triangles correspond to quasistatic 2D MD with $L = 80$, 160, 320 (from light to dark).

with $\mu = 1$ the elastic modulus, $\dot{\gamma}$ the externally applied shear rate, $\tau = 1$ a mechanical relaxation time, and $\partial_t\gamma_j^{\rm pl} = n_j\sigma_j/\mu\tau$ the strain rate produced by a plastic rearrangement at site j. G_{ij} denotes the discretized Eshelby propagator [37], which obeys a quadrupolar symmetry in the shear plane with a dipolar long-range character, $G(\boldsymbol{r},\boldsymbol{r}') = \cos(4\theta_{\boldsymbol{rr}'})/|\boldsymbol{r}-\boldsymbol{r}'|^d$. A site yields ($n_i = 0 \to 1$) when its stress reaches a local threshold, $\sigma_i \geq \sigma_i^y$, and recovers its elastic state ($n_i = 1 \to 0$) when a prescribed local deformation increment is attained after yielding, $\int|\partial_t\sigma_i/\mu + \partial_t\gamma_i^{\rm pl}|dt \geq \gamma_c$. Each time a site yields a new yield stress, σ_i^y is drawn from a distribution of mean σ_0. Model details and parameter choices can be found in Ref. [38] and in the Supplemental Material [39].

Stress-drop statistics and shear-rate dependence.—From the stress-time series we individualize stress drops and define an extensive quantity S proportional to the absolute stress difference multiplied by the system volume. We compare in Fig. 1 the stress-drop distributions P_S in the limit of low $\dot{\gamma}$ for the elastoplastic (EP) model with the quasistatic molecular dynamics (MD) results. In both two (2D) and three dimensions (3D), apart from a plateau regime for small stress drops that depends on shear rate, numerical integration step, and system size, we fit the data using a power law $P_S \sim S^{-\tau}f(S/S_c)$, with f an exponentially decaying cutoff function (exponent definitions in Table I). Noticing that the distributions P_S become independent of $\dot{\gamma}$ in the zero shear-rate limit and in agreement with previous works [23,25], we postulate a system-size-dependent cutoff $S_c \sim L^{d_f}$, with d_f the fractal dimension of the avalanches [23,25,49]. The comparison of these stress-drop statistics with MD results reveals a fair agreement, up to an arbitrary scaling factor related to the difference in simulated length scales.

TABLE I. Measured exponents for the avalanche statistics.

	Expression	EP 2D	EP 3D	$(1/r^2)$ depinning 1D	MF
β	$\dot{\gamma} \sim (\Delta\sigma)^\beta$	1.54(2)	1.55(2)	0.625(5) [50]	2 [51]
τ	$P_S \sim S^{-\tau}$	1.28(5)	1.25(5)	1.25(5) [6,7]	1.5 [52]
d_f	$S_c \sim L^{d_f}$	0.90(7)	1.3(1)	~1.38 [50]	⋯
τ'	$P_T \sim T^{-\tau'}$	1.41(4)	1.44(4)	~1.43 [6]	2 [52]
α	$T_c \sim \dot{\gamma}^{-\alpha}$	0.38(4)	0.30(4)	⋯	⋯
z	$T \sim \ell^z$	~0.57	~0.82	0.77(1) [50]	⋯
δ	$S \sim T^\delta$	1.58(7)	1.58(5)	~1.7 [6]	2 [52]
θ	$P_x \sim x^\theta$	0.52(3)	0.37(5)	0	1 [53]

The fitted values of τ for the EP model, both in two and three dimensions ($\tau_{\rm 2D} \simeq 1.28$, $\tau_{\rm 3D} \simeq 1.25$), compare very well with our and earlier obtained MD results [22,23], are compatible with previous lattice models [54], and lie within error bars of those provided by FEM models [55]. Still, they disagree with what was obtained with quasistatic protocols in cellular automaton models [25] (especially in 3D, where $\tau_{\rm 3D}^{\rm QS} \simeq 1.43$), and they contrast even more with the usual mean-field (MF) prediction [52] $\tau^{\rm MF} = 3/2$ (see Ref. [56] for an alternative analysis). The values obtained for d_f ($d_f^{\rm 2D} \simeq 0.9$, $d_f^{\rm 3D} \simeq 1.3$) are compatible with quasistatic MD simulations, but slightly smaller than those reported in automaton models [25]. They suggest a line geometry of the correlated slip events [24,57], with a modest but clear trend towards a more compact structure in 3D.

Some main results concerning the finite driving rate are summarized in Fig. 2 for the 3D EP model; similar results are found for the 2D case (not shown). The consequences of applying a finite shear rate are twofold [58].

(I) The first important observation is that with increasing driving rate the critical exponents tend towards the mean-field predictions. The yielding exponent β, for example, defined through $\dot{\gamma} \propto (\sigma - \sigma_c)^\beta$, can be derived from the fits in Fig. 2(a) rendering a nontrivial value $\beta \simeq 1.55$ in the low shear-rate regime. For larger shear rates, this value crosses over to $\beta \sim 2$ predicted by the Hebraud-Lequeux model [51]. By sliding a fixed size logarithmic window in $\dot{\gamma}$ (comprising ~12 points of the main plot data set) and fitting within, we show the resulting $1/\beta$ as a function of the starting position of the window in the inset of Fig. 2(a). Similarly we observe a crossover of the exponents in the steady-state distribution P_x of the local stress excess [53,59], $x_i \equiv \sigma_i^y - \sigma_i$; see Fig. 2(b). Again, in the limit of vanishing shear rates, we observe the curves approaching a shape that initially grows as $P_x \sim x^\theta$, with a nontrivial exponent, as found in the quasistatic case [25,53], attributed to an anomalous random walk process of the local stress with an absorbing boundary condition at $x = 0$ [60]. However, as we increase the shear rate, P_x changes, eventually yielding $\theta \simeq 0$. The driving progressively

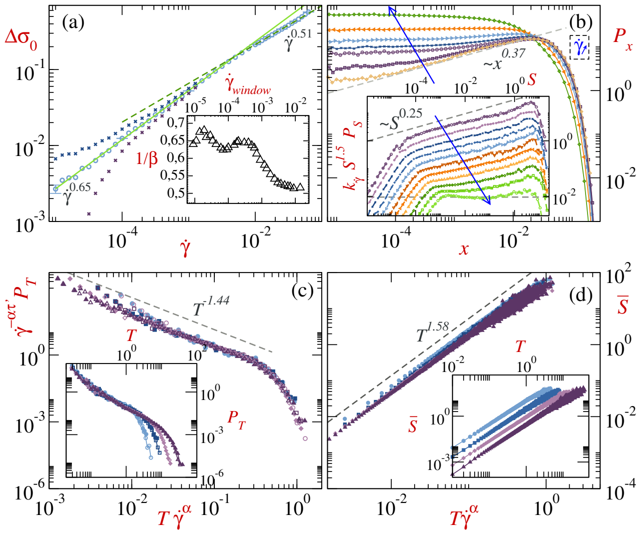

FIG. 2. Shear-rate dependency of the dynamics for the 3D EP model. (a) Log-log plot of $\Delta\sigma_0 \equiv (\sigma - \sigma_c)/\sigma_0$ versus $\dot\gamma$. Circles correspond to the best estimation of $\sigma_c/\sigma_0 = 0.687$, and crosses, to choices of 0.683 and 0.691 instead. Full and dashed lines are power-law fits in selected ranges (extrapolated for comparison). Inset: Crossover of $1/\beta$ as explained in the text. (b) Steady-state distributions P_x of the local distances to threshold $x \equiv \sigma_y - \sigma$ for different shear rates $\dot\gamma \in \{10^{-1.4}, \ldots, 10^{-5}\}$. Inset: Stress-drop distributions for $\dot\gamma \in \{10^{-1}, \ldots, 10^{-3}\}$, rescaled and shifted as explained in the text. Arrows indicate the sense of increasing shear rate. (c) Rescaled distributions of stress-drop duration $\dot\gamma^{-\alpha\tau'} P_T$ versus $T\dot\gamma^{\alpha}$ for $\dot\gamma = 10^{-2}$, 10^{-3}, 10^{-4}, 10^{-5} (from light blue to dark plum, left to right in inset), and system sizes $L = 64$ (closed symbols) and 128 (open symbols). The dashed line shows a law $P_T \sim T^{-1.44}$. Inset: Unscaled data. (d) Average size $\bar S$ for stress drops of the same duration as a function of $T\dot\gamma^{\alpha}$ for $L = 64$ and $\dot\gamma = 10^{-2}, 10^{-3}, 10^{-4}, 10^{-5}$. The dashed line shows $\bar S \sim T^{1.58}$. Inset: Unscaled data, shear rate decreases from left to right.

dominates over the signed kicks from elastic interactions, yielding a biased diffusion of the x's values. This ultimately produces a strictly positive local stress evolution, resembling the x dynamics of the depinning problem [25]. The inset of Fig. 2(b) shows a feature compatible with the shear-rate dependence of P_x and with the β crossover. For different shear rates, we plot $k_{\dot\gamma} S^{1.5} P_S$ versus S, where $k_{\dot\gamma}$ is an arbitrary scaling coefficient to separate the curves and improve visualization. We observe a range of low shear rates where the slope of the transformed distributions is almost unchanged and fully consistent with Fig. 1(a). Above a rate of deformation of about ~0.015, curves progressively flatten, eventually becoming horizontal. Plotting $S^{1.5}P_S$, we show the departure of P_S from the MF expectation $P_S^{\mathrm{MF}} \propto S^{-1.5}$ as the critical point is approached. When investigating the distribution of stress fluctuations $\eta_i = \sum_{j\neq i} G_{ij}(n_j\sigma_j/\tau)$ on each site, we find consistently a change from a peaked distribution with fat tails towards Gaussian-like distributions as we increase the shear rate. We infer from this that the strong correlations at vanishing shear rates (reason for the nontrivial criticality) become negligible for stronger driving, so that the exponents end up being well described by mean-field assumptions.

(II) The second consequence of a finite driving rate is that the critical scaling regime shows not only finite size but also finite shear-rate effects [57,61]. When imposing a finite deformation rate, each stress drop is characterized not only by its magnitude or size S, but also by its duration T. For each stress drop we define a given duration T as the time elapsed between the beginning and the end of the drop. In Fig. 2(c) we present the distributions of durations P_T for a fixed system size and different shear rates. In the probed shear-rate regime we find the dependence on L to be negligible; thus, $P_T(T, L, \dot\gamma) \equiv P_T(T, \dot\gamma)$. The main panel of Fig. 2(c) shows rescaled curves assuming the functional dependence $P_T \sim T^{-\tau'} g(T\dot\gamma^{\alpha})$, with g an exponentially decaying function. We obtain for the 3D case, $\tau'_{3\mathrm{D}} = 1.44$ and $\alpha_{3\mathrm{D}} = 0.3$. Naturally, we expect the scaling of P_T to be dominated by a growing length scale ξ in the critical limit, where the relations $T \sim \xi^z$ and $S \sim \xi^{d_f}$ hold. Therefore, we expect a scaling relation $S \sim T^{\delta}$ with $\delta = d_f/z$, that we observe over a range of shear rates, yielding the exponent $\delta_{3\mathrm{D}} \sim 1.58$ [see Fig. 2(d)], in contrast to the mean field $\delta_{\mathrm{MF}} = 2$. More generally, we observe empirically a power-law scaling of S with T, $\dot\gamma$, and L. Actually, extending the dependencies of the cutoff values in size $S_c = L^{d_f}$ and duration $T_c = \dot\gamma^{-\alpha}$, the mean S at each T should follow $\bar S(T, L, \dot\gamma) = C(L, \dot\gamma)T^{\delta}$, with $C(L, \dot\gamma) \sim L^{d_f}\dot\gamma^{\alpha\delta}$. This relation is fairly verified for the dependence on $\dot\gamma$, illustrated in Fig. 2(d). A rescaling of the size dependence leads to an exponent larger by 15% than d_f estimated from P_S.

Stress-drop shapes.—We address now the analysis of the functional form of the stress drops, i.e., the time evolution of the stress-drop velocity [15–17,52]. In Fig. 3(a) we show rescaled stress-drop velocities V_T (stress-drop shapes) for a 3D system, averaged over drops of the same duration T within the power-law scaling regime of Fig. 2(d). We observe that drops of short duration show a noticeable asymmetric shape, with faster velocities at earlier times. As duration increases, the shape becomes gradually more symmetric. To analyze this asymmetry of stress-drop shapes for different durations, system sizes, and applied shear rates, we fit them with a formula proposed in Ref. [16], $V_T(\tilde t) \propto B[\tilde t(1-\tilde t)]^c[1 - a_s(\tilde t - 0.5)]$ (see also Refs. [15,62]), with B the amplitude of the shape and a_s a parameter quantifying the deviation from a symmetric inverted parabola. We confirm the expected relation $c = \delta - 1$ [recall $S \propto T^{\delta}$ and compare Figs. 3(b) and 2(d)]. In our range of parameters c is almost independent of L and $\dot\gamma$. More relevant for our analysis is the behavior of the fitting parameter a_s [see Fig. 3(b), inset], which shows clearly the crossover from nearly symmetric to asymmetric shapes as we focus on

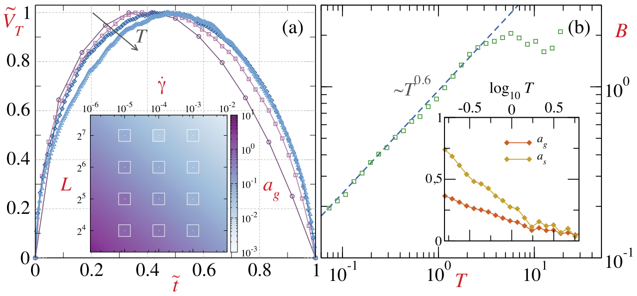

FIG. 3. Stress-drop shape properties for a 3D EP model. (a) Rescaled stress-drop shape $\tilde{V}_T(t) = V_T(t)/\max_t[V_T(t)]$ averaged over stress drops of duration $T \pm \epsilon$, as a function of rescaled time $\tilde{t} = t/T$. From left to right, we show curves at increasing T. Inset: Bordered squares represent fitted values of the asymmetry parameter a_g for different choices of $(\dot{\gamma}, L)$. Color code depicts the fit $a_g = 10^{-0.42} T^{-0.43} \dot{\gamma}^{-0.37} L^{-1.25}$ for $T = 0.5$. (b) Amplitude B of the stress drops versus T, for $L = 32$ and $\dot{\gamma} = 10^{-4}$, as obtained from the fits. The inset shows corresponding $a_s(T)$ and $a_g(T)$ (see text).

shorter durations T. To avoid a fit with various parameters, we use an alternative, purely geometrical measurement of the asymmetry that is relevant even beyond the scaling regime, $a_g = \int_0^1 \{[|V_T(\tilde{t}) - V_T(1-\tilde{t})|]/[V_T(\tilde{t}) + V_T(1-\tilde{t})]\} d\tilde{t}$. When computing $a_g(T)$ for different shear rates at fixed T and L, a_g increases as $\dot{\gamma}$ decreases, whereas for fixed T and $\dot{\gamma}$, a_g decreases as L increases [see inset of Fig. 3(a)]. In the quasistatic limit, where just one independent avalanche occurs at a time, we expect asymmetric stress-drop shapes characterizing individual avalanches. When we increase the driving rate at fixed system size or, equivalently, increase the system size at a fixed rate, we expect stress drops to result from many independent avalanches, since the density of plastic regions is determined and increased by the driving strength [57]. Here, the resulting stress-drop shape draws closer to the mean-field symmetric shape.

Conclusions.—We studied, with a mesoscopic model, the avalanche statistics close to the yielding transition, verifying the relevance of our approach by comparing with particle-based quasistatic simulations. In Table I we summarize the critical exponents obtained for 2D and 3D. Our results clearly reinforce the idea of a nontrivial universality class for the yielding transition, in agreement with earlier findings [23,25,54]. Our estimated exponents confirm within error bars the scaling relations proposed by Lin *et al.* [25]. We also note that our values of τ and τ' are indistinguishable from the exponents expected for the 1D long-range $(1/r^2)$ depinning universality class [6,7]. Although the loading path dependence of the critical exponents remains an open issue, this is an interesting accordance and points towards the role played by the avalanche slip-line geometry.

In the regime of larger shear rates we find that several exponents of the stress-drop statistics draw closer to mean-field predictions. The rise of an increasing number of independent regions with yielding activity (parallel occurring avalanches) justifies the crossover to trivially random statistics. In particular, our data reveal a yielding exponent approaching the prediction of the Hébraud-Lequeux model [51,63,64]. Further, the finite shear-rate protocol allows for the introduction of an additional exponent α that should enter the scaling relations, given $T_c \sim \dot{\gamma}^{-\alpha}$. If we assume a usual scaling scenario, we expect a diverging length scale depending on the distance to the yielding point $\xi \sim (\sigma - \sigma_c)^{-\nu}$, such that $\xi \sim \dot{\gamma}^{-\nu/\beta}$, since $\dot{\gamma} \sim (\sigma - \sigma_c)^{\beta}$. Then, $T_c \sim \xi^z$ yields directly the scaling relation $\alpha = z\nu/\beta$. We have not measured ν, but assuming $\nu = 1/(d - d_f)$ [25] to be valid, we get $\alpha_{2\mathrm{D}} = 0.34$ and $\alpha_{3\mathrm{D}} = 0.31$, close to our estimated values.

Within the scaling regime for T we observe both asymmetric and symmetric stress-drop shapes depending on system size, shear rate, and duration. This is why we propose to distinguish between individual avalanches (resulting from correlated plastic events) and stress-drop shapes (resulting from many independently occurring avalanches).

The combined study of avalanche size and duration distributions and avalanche shapes has played an essential role in our understanding of the universal aspects of crackling noise and depinning dynamics. With this work, we provide a first numerical prediction of similar quantities in the case of the yielding transition, with a clear indication of a complex non-mean-field behavior. We hope this work will stimulate and provide a benchmark for future experimental studies on systems undergoing a continuous yielding transition, for which detailed data on noise statistics are presently very scarce.

J.-L. B., E. E. F., and C. L. acknowledge financial support from ERC Grant No. ADG20110209. J.-L. B. is supported by IUF. K. M. acknowledges financial support from the ANR Grant No. ANR-14-CE32-0005 (project FAPRES). E. E. F. and J.-L. B. acknowledge the hospitality of the KITP, supported in part by the National Science Foundation under Grant No. NSF PHY11-25915. Most of the computations were performed using the Froggy platform of the CIMENT infrastructure supported by the Rhône-Alpes region (Grant No. CPER07-13 CIRA) and the Equip@Meso project (Reference No. ANR-10-EQPX-29-01). Further, we would like to thank Alexandre Nicolas, Elisabeth Agoritsas, Eric Bertin, Jordi Ortín, and Stéphane Santucci for fruitful discussions, and Mark Robbins and Matthieu Wyart for a useful correspondence.

[1] H. Barkhausen, Phys. Z. **20**, 401 (1919).
[2] G. Durin and S. Zapperi, Phys. Rev. Lett. **84**, 4705 (2000).
[3] G. Durin and S. Zapperi, in *The Science of Hysteresis*, edited by G. Bertotti and I. Mayergoyz (Elsevier, Amsterdam, 2006), pp. 181–267.

[4] A. Ruina, J. Geophys. Res. **88**, 10359 (1983).
[5] Y. N. Dastur and W. C. Leslie, Metall. Trans. A **12**, 749 (1981).
[6] D. Bonamy, S. Santucci, and L. Ponson, Phys. Rev. Lett. **101**, 045501 (2008).
[7] L. Laurson, S. Santucci, and S. Zapperi, Phys. Rev. E **81**, 046116 (2010).
[8] I. Cantat and O. Pitois, Phys. Fluids **18**, 083302 (2006).
[9] V. Repain, M. Bauer, J.-P. Jamet, J. Ferr, A. Mougin, C. Chappert, and H. Bernas, Europhys. Lett. **68**, 460 (2004).
[10] D. C. Chrzan and M. J. Mills, Phys. Rev. B **50**, 30 (1994).
[11] D. Spasojevic, S. Bukvic, S. Milosevic, and H. E. Stanley, Phys. Rev. E **54**, 2531 (1996).
[12] M. C. Kuntz and J. P. Sethna, Phys. Rev. B **62**, 11699 (2000).
[13] S. Zapperi, C. Castellano, F. Colaiori, and G. Durin, Nat. Phys. **1**, 46 (2005).
[14] L. Laurson and M. J. Alava, Phys. Rev. E **74**, 066106 (2006).
[15] S. Papanikolaou, F. Bohn, R. L. Sommer, G. Durin, S. Zapperi, and J. P. Sethna, Nat. Phys. **7**, 316 (2011).
[16] L. Laurson, X. Illa, S. Santucci, K. T. Tallakstad, K. J. Maloy, and K. J. Måløy, Nat. Commun. **4**, 2927 (2013).
[17] J. Antonaglia, W. J. Wright, X. Gu, R. R. Byer, T. C. Hufnagel, M. LeBlanc, J. T. Uhl, and K. A. Dahmen, Phys. Rev. Lett. **112**, 155501 (2014).
[18] J. P. Sethna, K. A. Dahmen, and C. R. Myers, Nature (London) **410**, 242 (2001).
[19] A. P. Mehta, A. C. Mills, K. A. Dahmen, and J. P. Sethna, Phys. Rev. E **65**, 046139 (2002).
[20] P. Le Doussal and K. J. Wiese, Phys. Rev. E **88**, 022106 (2013).
[21] Z. Zhao, X. Ding, J. Sun, and E. K. H. Salje, J. Phys. Condens. Matter **26**, 142201 (2014).
[22] K. M. Salerno, C. E. Maloney, and M. O. Robbins, Phys. Rev. Lett. **109**, 105703 (2012).
[23] K. M. Salerno and M. O. Robbins, Phys. Rev. E **88**, 062206 (2013).
[24] Z. Budrikis and S. Zapperi, Phys. Rev. E **88**, 062403 (2013).
[25] J. Lin, E. Lerner, A. Rosso, and M. Wyart, Proc. Natl. Acad. Sci. U.S.A. **111**, 14382 (2014).
[26] G. Picard, A. Ajdari, F. Lequeux, and L. Bocquet, Phys. Rev. E **71**, 010501 (2005).
[27] D. Rodney, A. Tanguy, and D. Vandembroucq, Model. Simul. Mater. Sci. Eng. **19**, 083001 (2011).
[28] K. Martens, L. Bocquet, and J.-L. Barrat, Phys. Rev. Lett. **106**, 156001 (2011).
[29] M. Talamali, V. Petäjä, D. Vandembroucq, and S. Roux, C.R. Mec. **340**, 275 (2012).
[30] A. Nicolas and J.-L. Barrat, Phys. Rev. Lett. **110**, 138304 (2013).
[31] E. E. Ferrero, K. Martens, and J.-L. Barrat, Phys. Rev. Lett. **113**, 248301 (2014).
[32] S. Plimpton, J. Comput. Phys. **117**, 1 (1995).
[33] F. Puosi, J. Rottler, and J.-L. Barrat, Phys. Rev. E **89**, 042302 (2014).
[34] A. Argon, Acta Metall. **27**, 47 (1979).
[35] A. Tanguy, F. Leonforte, and J.-L. Barrat, Eur. Phys. J. E **20**, 355 (2006).
[36] C. E. Maloney and A. Lemaître, Phys. Rev. E **74**, 016118 (2006).
[37] J. D. Eshelby, Proc. R. Soc. A **241**, 376 (1957).
[38] A. Nicolas, K. Martens, and J. L. Barrat, Europhys. Lett. **107**, 44003 (2014).
[39] See Supplemental Material at http://link.aps.org/supplemental/10.1103/PhysRevLett.116.065501, which includes Refs. [40–48], for a detailed description of the EP model used in the manuscript and explanations of our parallel numerical implementation and post-processing techniques.
[40] G. Picard, A. Ajdari, F. Lequeux, and L. Bocquet, Eur. Phys. J. E **15**, 371 (2004).
[41] E. E. Ferrero, S. Bustingorry, and A. B. Kolton, Phys. Rev. E **87**, 032122 (2013).
[42] NVIDIA Corporation, CUDA C Programming Guide Version 7.0, 2015.
[43] NVIDIA Corporation, CUDA library for the Fast Fourier Transform, DU-06707-001_v7.0, 2015.
[44] J. Hoberock and N. Bell, 2010, http://thrust.github.io/.
[45] J. K. Salmon, M. A. Moraes, R. O. Dror, and D. E. Shaw, in *Proceedings of the 2011 International Conference for High Performance Computing, Networking, Storage and Analysis, 2011 (SC'11)* (Association for Computing Machinery, New York, USA, 2011), pp. 16:1–16:12.
[46] https://bitbucket.org/ezeferrero/epm.
[47] Python Software Foundation. Python Language Reference, version 2.7.6, http://www.python.org.
[48] R. Planet, S. Santucci, and J. Ortín, Phys. Rev. Lett. **105**, 029402 (2010).
[49] N. P. Bailey, J. Schiøtz, A. Lemaître, and K. W. Jacobsen, Phys. Rev. Lett. **98**, 095501 (2007).
[50] O. Duemmer and W. Krauth, J. Stat. Mech. (2007) P01019.
[51] P. Hébraud and F. Lequeux, Phys. Rev. Lett. **81**, 2934 (1998).
[52] K. A. Dahmen, Y. Ben-Zion, and J. T. Uhl, Nat. Phys. **7**, 554 (2011).
[53] J. Lin, A. Saade, E. Lerner, A. Rosso, and M. Wyart, Europhys. Lett. **105**, 26003 (2014).
[54] M. Talamali, V. Petäjä, D. Vandembroucq, and S. Roux, Phys. Rev. E **84**, 016115 (2011).
[55] S. Sandfeld, Z. Budrikis, S. Zapperi, and D. F. Castellanos, J. Stat. Mech. (2015) P02011.
[56] E. A. Jagla, Phys. Rev. E **92**, 042135 (2015).
[57] A. Lemaître and C. Caroli, Phys. Rev. Lett. **103**, 065501 (2009).
[58] To extrapolate our results we assume that the yielding transition is continuous.
[59] M. Müller and M. Wyart, Annu. Rev. Condens. Matter Phys. **6**, 177 (2015).
[60] J. Lin and M. Wyart, Phys. Rev. X **6**, 011005 (2016).
[61] S. Karmakar, E. Lerner, I. Procaccia, and J. Zylberg, Phys. Rev. E **82**, 031301 (2010).
[62] P. L. Doussal and K. J. Wiese, Europhys. Lett. **97**, 46004 (2012).
[63] E. Agoritsas, E. Bertin, K. Martens, and J.-L. Barrat, Eur. Phys. J. E **38**, 71 (2015).
[64] F. Puosi, J. Olivier, and K. Martens, Soft Matter **11**, 7639 (2015).

5.2 Geometry of the plastic interface

As mentioned in chapter 4, the dynamics of the elasto-plastic model can be viewed as the motion of the plastic interface under the self-interaction via the propagator $G^N(\mathbf{x})$, an external driving and the system disorder. This point of view establishes an analogy between the elasto-plastic model and the depinning model. The essential difference is that the self-interaction in the depinning model is convex while it is non-convex in the elasto-plastic model.

In the depinning model the geometry of the interface is relevant for interpreting the avalanche dynamics, as mentioned in chapter 3. Typically in two dimensional depinning models, a crossover length scale l_{av} can be identified from the structure factor of the elastic line, above and below which the elastic line manifests self-affine geometry characterized by different roughness exponents reflected in the different power law below and above l_{av}^{-1} in the structure factor. The length scale l_{av} is interpreted as the typical cooperative length scale of the collective motion, i.e. avalanches.

It is then natural to ask how the motion of the plastic interface and its geometry are related to the avalanche dynamics in the elasto-plastic model. Is it possible to determine the cooperative length scale by studying the geometry of the plastic interface? A preliminary study of this question in two dimensional systems is presented in this section. Specifically the geometry of the plastic interface is characterized by its power spectral density considering only the "hard" Fourier modes, as explained below.

Hard and soft modes

In the depinning model, the self-interaction term $\nabla^2 h$ gives on a Fourier mode of wave vector $\mathbf{q}$ a restoring force $-\left|\mathbf{q}\right|^2 \hat{h}$, which is always <u>opposite</u> to the mode amplitude. It means that there is no soft mode in the depinning model, i.e. if left to move freely only under self-interaction, the elastic line becomes always flat at the end. With additional external driving and quenched disorder, the force exerted on any Fourier mode, (except for the $\mathbf{q} = \mathbf{0}$, which is the global forward motion), is balanced between the self-interaction and the quenched disorder. As a result, the width of the elastic line is always finite as long as the system size is finite. This leads to an alternative way of measuring the roughness exponent, which is to measure how does the width of a segment scale with the segment size.

In contrast with the self-interaction in the depinning model, the self-interaction of the elasto-plastic model in Fourier space written as $\hat{G}^N \propto -\frac{q_x^2 q_y^2}{q^4}$, admits soft modes, i.e. Fourier modes $\mathbf{q}$ such that $q_x q_y = 0$. We define the "hard" modes $\mathbf{q}$ are such that $q_x q_y \neq 0$. The internal stress $\hat{\sigma}^{INT}$ exerted on the soft modes vanishes, while it is always opposite to the amplitude of the plastic interface for the hard modes. This means that the width of the plastic interface in the elasto-plastic model is not bounded by its self-interaction. The self-interaction ignores any superposition of one directional variation of the plastic interface. Under the external driving and the system disorder, the force exerted on hard modes are balanced between the self-interaction and the system disorder, while the amplitude of the soft modes is amplified constantly by the disorder. As a consequence, during the growth of plastic interface, soft modes grow linearly with time, with an average velocity that fluctuates around a stationary value, while hard modes reach and then fluctuate around a stationary value instead of growing infinitely with time. This effect is well studied in [Tyukodi et al., 2016] and here visualized in the figure 5.5, where the contribution of all hard modes to the interface width $W_H(t)$ and the corresponding contribution of all soft modes $W_S(t)$ are plotted versus the global strain γ. $W_S(t)$ and $W_H(t)$ are defined as

$$W_H(t) = \sum_{\mathbf{q}, q_x q_y \neq 0} \left|\hat{\gamma}^{pl}\right|^2(\mathbf{q}, t) \tag{5.14}$$

$$W_S(t) = \sum_{\mathbf{q}, q_x q_y = 0} \left|\hat{\gamma}^{pl}\right|^2(\mathbf{q}, t) - \left|\hat{\gamma}^{pl}\right|^2(\mathbf{0}, t) \tag{5.15}$$

Because of these non bounded soft modes, the roughness exponent, if there is any for the elasto-plastic model, can not be accessed by the the scaling of the width with the system size and it would be more adequate to characterize the geometry of the plastic interface only for the hard modes in Fourier space, since the plastic interface in the stationary state admits a stationary geometry only on these hard modes.

Structure factor on the hard Fourier modes of the plastic interface

The structure factor $S(\mathbf{q})$ of the plastic interface in the stationary state is obtained by the time average of the instantaneous structure factor, i.e.

$$S(\mathbf{q}) = \overline{\left|\hat{\gamma}^{pl}\right|^2(\mathbf{q})} \tag{5.16}$$

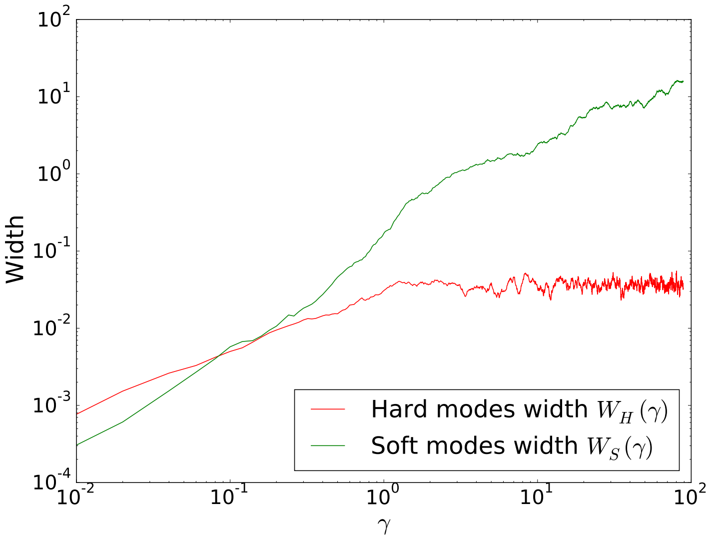

Figure 5.5: The contribution of the soft modes to the width of the plastic interface $W_S(\gamma)$ (green) and the contribution of the hard modes to the width of the plastic interface $W_H(\gamma)$ (red) as a function of strain γ.

where the “$\overline{\bullet}\hat{=}\lim_{T\to\infty}\frac{1}{T}\int dt\bullet$” stands for the time average. The stationary structure factor of the plastic interface (without the soft modes) for different shear rates and for a system size $L^d = 512^2$ are shown in the figure 5.6 on a logarithmic scale.

The stationary structure factor seems not to depend on the applied shear rate $\dot{\gamma}$. The form of the logarithm of the structure factor is very reminiscent of the self-interaction kernel, i.e. $\hat{G}^N(\mathbf{q})$ in Fourier space (see right panel of figure 5.7), which is not isotropic. Since the local yield stress is picked randomly independently from one site to another, the system disorder, i.e. the local yield stress field $\sigma^Y(\mathbf{x})$, can be viewed as a spatial white noise applied on the plastic interface, i.e. the average intensity of the noise applied on each mode of the plastic interface is the same, denoted as n_s. In the stationary state, the amplitude of the plastic interface on a mode $\hat{\gamma}^{pl}(\mathbf{q})$ is due to the compromise between the self-interaction and the system disorder, i.e. $n_s \approx \left|\hat{G}(\mathbf{q})\right|\left|\hat{\gamma}^{pl}(\mathbf{q})\right|$ in a schematic way, which implies $\left|\hat{\gamma}^{pl}(\mathbf{q})\right| \sim 1/\left|\hat{G}(\mathbf{q})\right|$. As a consequence, softer modes, i.e. the modes with smaller $\left|\hat{G}^N(\mathbf{q})\right|$, have to be stretched more than the harder modes, i.e. the modes with larger $\left|\hat{G}^N(\mathbf{q})\right|$, to balance the effect of system disorder, and hence contribute larger amplitudes to the stationary structure factor.

To characterize the profile of the structure factor $S(\mathbf{q})$, $S(q_x)$ for the system size $L = 512$ at fixed q_y equal to the largest wave vector is shown in the figure 5.8(left). A scaling regime over about one decade can be seen. Even if there is an important scatter in the data, a power law can be roughly measured as $S(q_x) \sim q_x^{-2.5}$. For

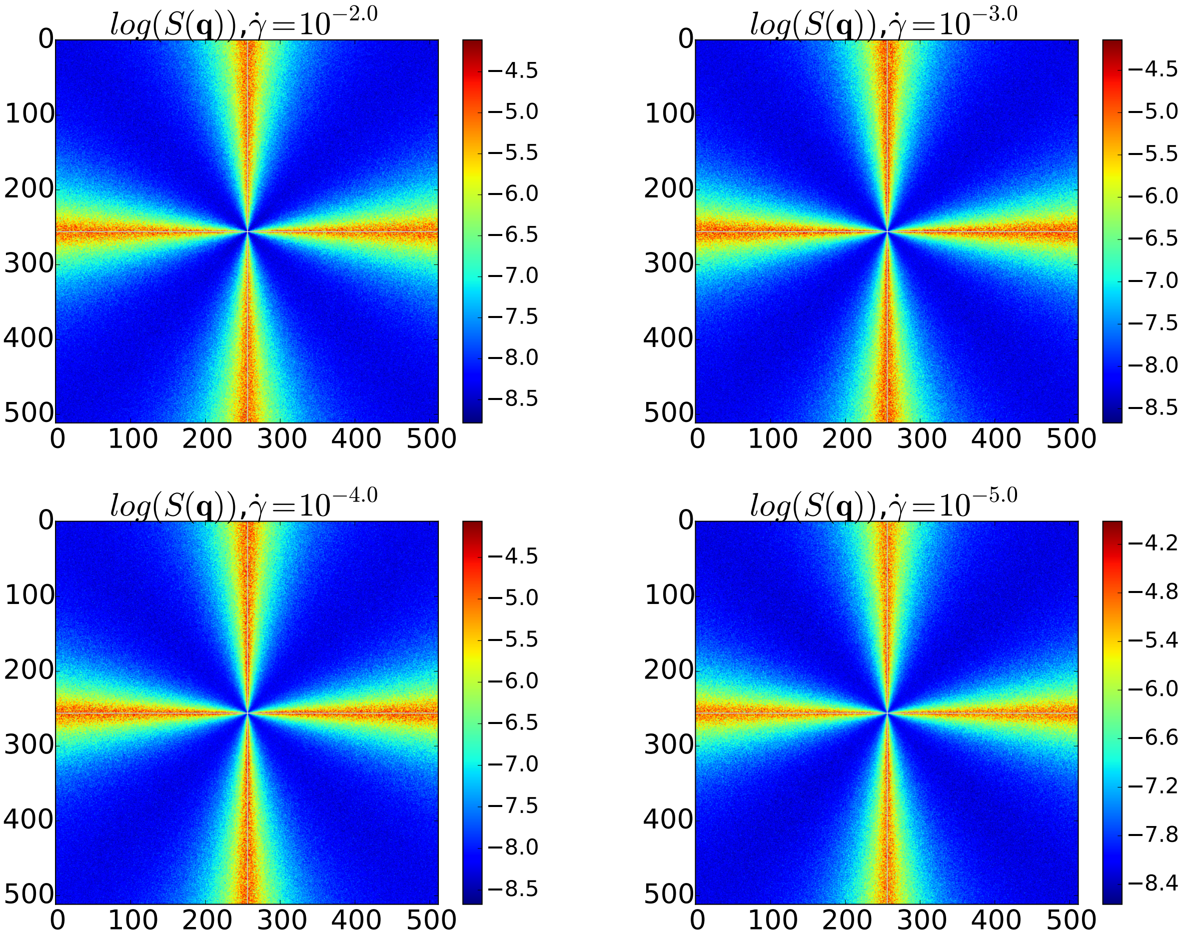

Figure 5.6: Logarithm of the stationary structure factor of system size $L^d = 512^2$ for the shear rates $\dot{\gamma} = 10^{-2}$, 10^{-3}, 10^{-4}, 10^{-5}.

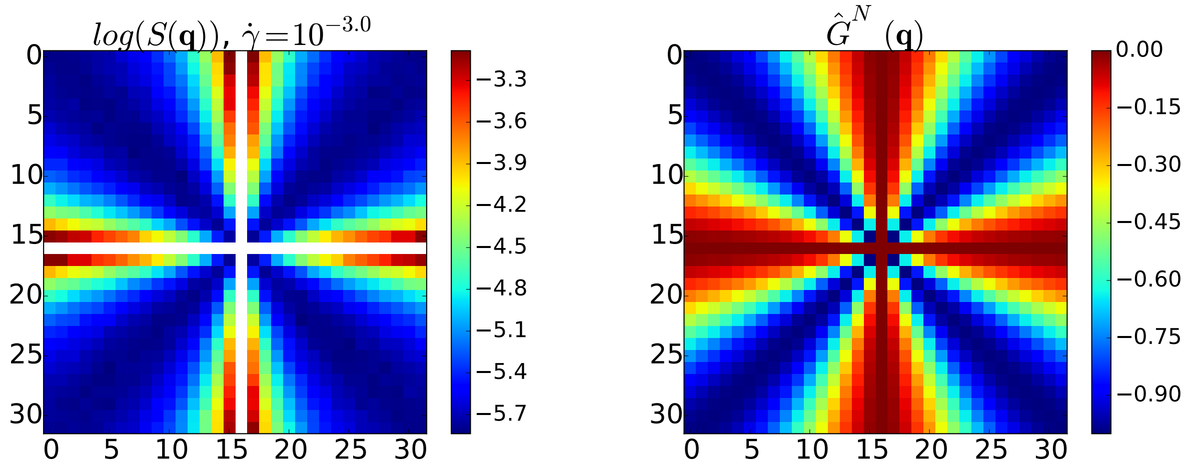

Figure 5.7: Left: Stationary structure factor of a system of $L = 32$ with $\dot{\gamma} = 10^{-3}$. Right: The self-interaction kernel $\hat{G}^N(\mathbf{q})$.

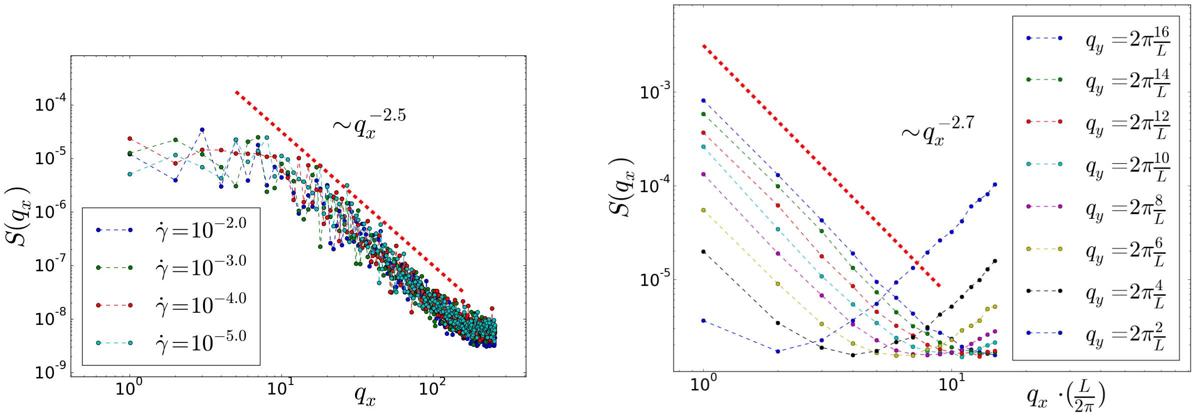

Figure 5.8: Left: Stationary structure factor of a system of $L = 512$ along q_x at the largest q_y. Right: Stationary structure factor of a system of $L = 32$ along q_x at various q_y. for a shear rate of $\dot{\gamma} = 10^{-3}$.

having a good statistics the same structure factor is computed for a system of size $L = 32$ at a shear rate $\dot{\gamma} = 10^{-3}$. This structure factor is shown in the left panel of figure 5.7. The profile $S(q_x)$ at different q_y is shown in the right panel of figure 5.8. Because of the quadrupolar symmetry of the structure factor, the series of $S(q_x)$ at different q_y can represent quantitatively the whole structure factor. The scaling regime on q_x is limited from 0 up to $q_x = q_y$ and the scaling exponent is measured close to 2.7, which is consistent with the result for the larger system size $L = 512$.

The fact that the scaling regime for the directional component q_x (or q_y) is limited from zero to $q_x = q_y$ (or $q_y = q_x$), can be interpreted as a complex self-affine geometry of the plastic interface. The self affine geometry can be observed along the direction x only if the wave length scale that is chosen to coarse grain along the other direction y is large enough.

Conclusion

By analyzing the stationary structure factor of the plastic interface, we find that the geometry of the plastic interface seems insensitive to the shear rate, i.e. the dynamical information is not encoded in the geometry of the plastic interface. The structure factor keeps information about the self-interaction kernel, and a scaling law is found in a specific situation, suggesting a complex self-affine geometry not directly observable on the plastic interface due to the existence of soft modes.

5.3 Two point correlations

The cooperative dynamics is encoded in the spatio-temporal map of plastic events. The spatio-temporal pattern of plastic events, if there is any, characterizes the dynamical regime of the system. The dynamical cooperative length scale may be found by investigating the spatio-temporal map of plastic events. A quantity which is equivalent to the plastic events and contains even more information, is the velocity field of the plastic interface $\partial_t \gamma^{pl}(\mathbf{x}, t)$. The two point correlation function of the plastic strain field of a two dimensional system is investigated in this section in an attempt to directly visualize the spatial-temporal extension of the cooperative dynamics.

A temporally coarse-grained local increment of the plastic strain field can be constructed from the velocity field of the plastic interface

$$\delta\gamma^{pl}(\mathbf{x}, t; \delta T) = \int_{t-\frac{\delta T}{2}}^{t+\frac{\delta T}{2}} \partial_t \gamma^{pl}(\mathbf{x}, s) ds \tag{5.17}$$

where δT is the coarse-grained time scale which is fixed such that $\delta T \dot{\gamma} = \delta\gamma = 0.002$. This strain field increment is therefore indicative of the plastic activity taking place during a fixed amount of strain. Hereafter $\delta\gamma^{pl}(\mathbf{x}, t; \delta T)$ is replaced by $\delta\gamma^{pl}(\mathbf{x}, t)$ for δT fixed in this way. For investigating how the plastic strain taking place at position $\mathbf{x}$ at moment t correlates with the plastic strain at $\mathbf{x}' = \mathbf{x} + \Delta\mathbf{x}$ at moment $t' = t + \Delta t$, a two point correlator $C_{\delta\gamma^{pl}}(\Delta\mathbf{x}, \Delta t)$ is estimated from the entire spatial-temporal map of the velocity of the plastic interface $\partial_t \gamma^{pl}(\mathbf{x}, t)$. $C_{\delta\gamma^{pl}}(\Delta\mathbf{x}, \Delta t)$ is numerically defined as

$$C_{\delta\gamma^{pl}}(\Delta\mathbf{x}, \Delta t) \hat{=} \frac{\overline{\langle \delta\gamma^{pl}(\mathbf{x}, t)\delta\gamma^{pl}(\mathbf{x} + \Delta\mathbf{x}, t + \Delta t)\rangle_{\mathbf{x}}} - \overline{\langle \delta\gamma^{pl}\rangle_{\mathbf{x}}}^2}{\overline{\langle \left(\delta\gamma^{pl}\right)^2\rangle_{\mathbf{x}}} - \overline{\langle \delta\gamma^{pl}\rangle_{\mathbf{x}}}^2} \tag{5.18}$$

where the spatio-temporal average $\overline{\langle\rangle_{\mathbf{x}}}$ (replacing the ensemble average because of the stationary state of stochastic dynamics) is the average over space and time of the spatio-temporal map of $\delta\gamma^{pl}(\mathbf{x}, t)$.

For comparing the correlation among plastic events for different shear rates, it is more convenient to compute the quantity at a fixed macroscopic strain, i.e. $C_{\delta\gamma^{pl}}(\Delta\mathbf{x}, \frac{\Delta\gamma}{\dot{\gamma}})$, since both local yielding criteria and local healing criteria involve a strain scale ($\langle\sigma_y\rangle/\mu$ and γ_c) rather than a time scale. It is worth noticing that $C_{\delta\gamma^{pl}}(\Delta\mathbf{x}, \Delta t) \approx C_{\delta\gamma^{pl}}(\Delta\mathbf{x}, \Delta t = 0)$ for $\Delta t \ll \delta T$, because of the integral over δT in expression (5.17) implying that $\delta\gamma^{pl}(\mathbf{x}, t; \delta T) \approx \delta\gamma^{pl}(\mathbf{x}, t + \Delta t; \delta T)$ if $\Delta t \ll \delta T$.

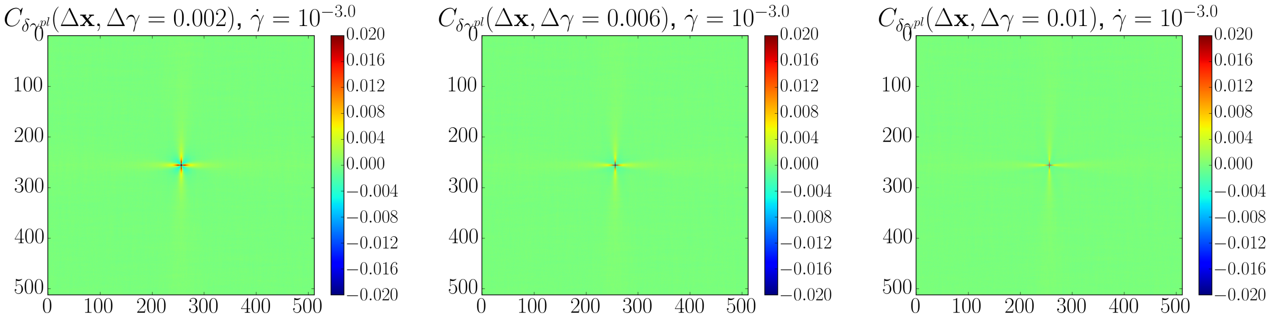

Figure 5.9: Two point correlation map for $\dot{\gamma} = 10^{-3}$ at $\Delta\gamma = 0.002,\ 0.006,\ 0.010$ form the left to the right.

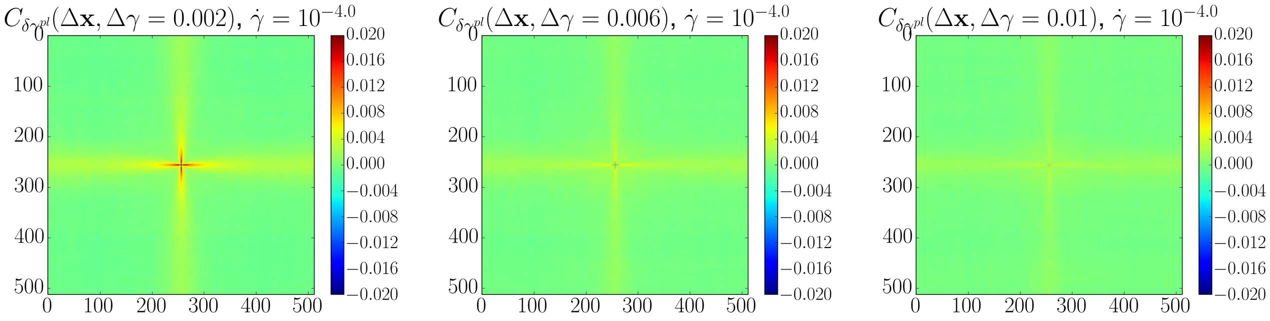

Figure 5.10: Two point correlation map for $\dot{\gamma} = 10^{-4}$ at $\Delta\gamma = 0.002,\ 0.006,\ 0.010$ form the left to the right.

The spatio-temporal maps of the correlation $C_{\delta\gamma^{pl}}(\Delta\mathbf{x}, \Delta t = \Delta\gamma/\dot{\gamma})$ are shown in figure 5.9 for $\dot{\gamma} = 10^{-3}$, in figure 5.10 for $\dot{\gamma} = 10^{-4}$ and in figure 5.11 for $\dot{\gamma} = 10^{-5}$. From these results, we have the following observations:

1. The two point correlations for a given $\Delta t = \Delta\gamma/\dot{\gamma}$ follow the shape of the propagator $G^N(\mathbf{x})$. Plastic strain is more correlated along the positive branches of the propagator $G^N(\mathbf{x})$, showing the quadrupolar symmetry. For a delay time corresponding to a given strain difference, with $\Delta t = \Delta\gamma/\dot{\gamma}$, systems

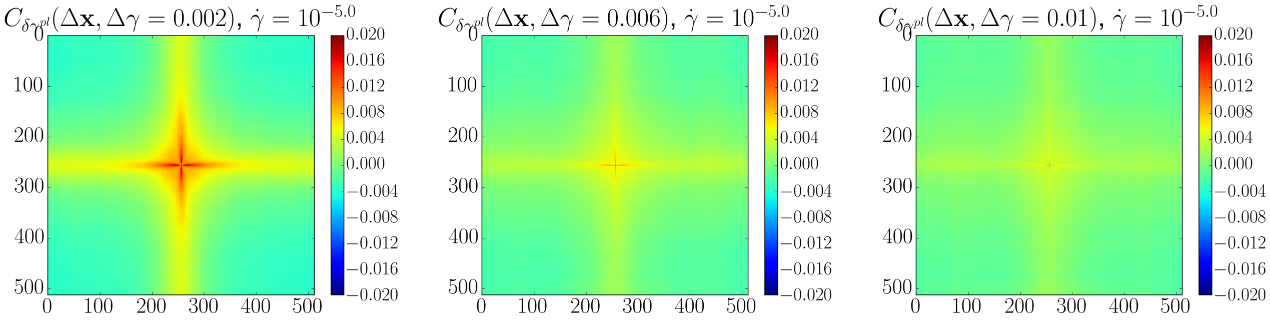

Figure 5.11: Two point correlation map for $\dot{\gamma} = 10^{-5}$ at $\Delta\gamma = 0.002,\ 0.006,\ 0.010$ form the left to the right.

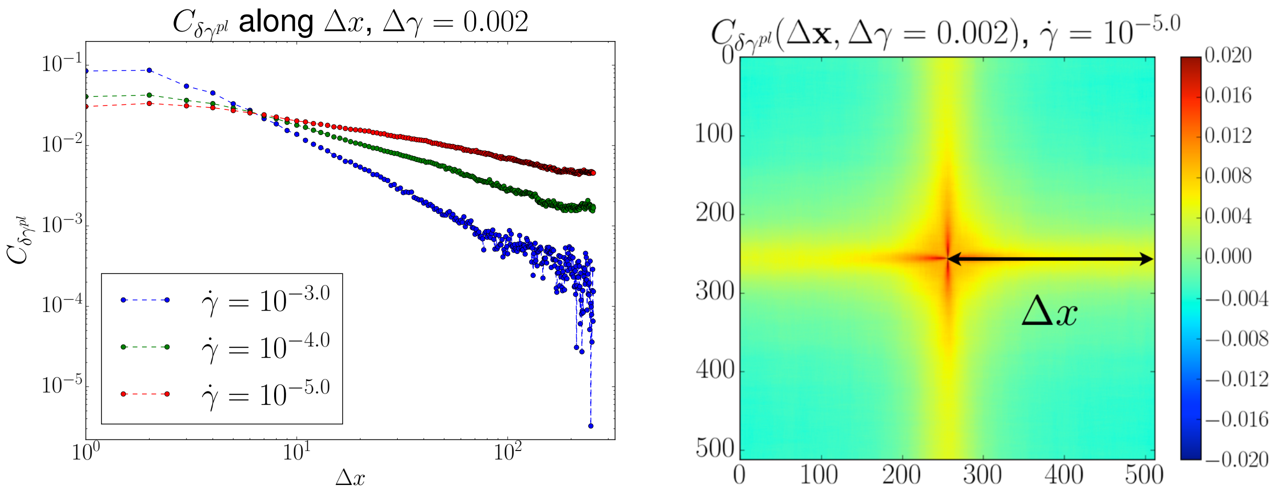

Figure 5.12: Left: The two point correlation function at $\Delta\gamma = 0.002$ for different shear rates along the strongly correlated direction as marked by the black line with double arrows in the right figure.

with a lower applied shear rate show stronger spatial correlations. This can be seen by plotting the correlation $C_{\delta\gamma^{pl}}$ along one of the strongly correlated directions for different shear rates, as shown in figure 5.12. The correlation along the strongly correlated direction decays as a power law with the distance to the center. It is clear from the data that the correlations decay slower for lower shear rate, suggesting the dynamics is more cooperative for lower shear rates. However since the decay of the correlation in space follows a power law, there is no characteristic length to be identified by looking at the two point correlation.

2. The intensity of the two point correlations decays with the delay time in a monotonic way. This time dependence of the correlations can be characterized by the intensity of correlation at $\Delta\gamma = \dot\gamma\Delta t$ defined as

$$I_c(\Delta\gamma) = \frac{1}{V}\int d\Delta\mathbf{x}^d \big|C_{\delta\gamma^{pl}}(\Delta\mathbf{x}, \Delta t = \frac{\Delta\gamma}{\dot\gamma})\big| \tag{5.19}$$

where the absolute value is used to avoid compensations between positive and negative parts in the correlations. $I_c(\Delta\gamma)$ for different shear rates are shown in the figure 5.13. A power law decay can be seen in the figure. Large fluctuations in the tail are due to the lack of statistics which makes it difficult to identify a characteristic time scale of correlation.

In conclusion, by looking at the two point correlations, it is found that the dynamics is more cooperative and a larger spatial domain is involved in the correlation for

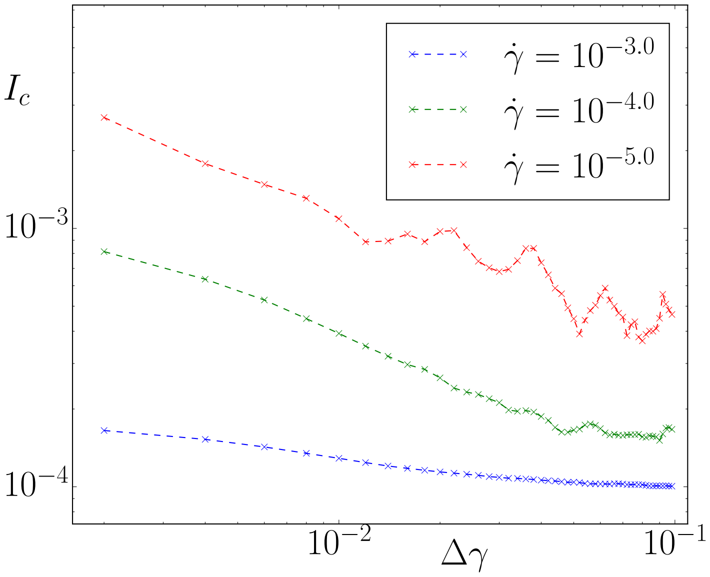

Figure 5.13: Intensity of the two-point correlations as function of $\Delta\gamma$ for different shear rates.

lower shear rates. However the spatial decay as well as the temporal decay follows a power law, which makes it impossible to extract a characteristic length and time scale for the cooperative dynamics.

5.4 Macroscopic stress fluctuations

Our study of avalanche statistics of the elasto-plastic model in the low shear rate limit reveals the critical behavior of the yielding transition, which is consistent with the results under quasi-static shear reported by Lin et al [Lin et al., 2014a]. A dynamical cooperative length ξ_c is assumed to be an important quantity for the yielding transition [Lin et al., 2014a], and is supposed to diverge as the system approaches to the yielding point. However this length scale has not yet been clearly evidenced.

On another hand, most studies of avalanches rely on the stress drops as prominent observable. A phenomenological characterization of the time series of the time derivative of the stress may be useful to understand the behavior of the stress time series and further to understand the stress drop statistics.

According to equation (5.3), the time derivative of the macroscopic stress $\frac{d}{dt}\langle\sigma\rangle_{\mathbf{x}}$

is equivalent to the macroscopic plastic strain rate $\langle\dot{\gamma}^{pl}\rangle_{\mathbf{x}}$, which is

$$\langle\dot{\gamma}^{pl}\rangle_{\mathbf{x}} = \frac{1}{\mu\tau}\left(\frac{1}{L^d}\sum_{\mathbf{x}} n(\mathbf{x})\sigma(\mathbf{x})\right) \tag{5.20}$$

If $n(\mathbf{x})\sigma(\mathbf{x})$ can be considered as identically distributed and independent random variables from a distribution of finite mean and variance, then $\langle\dot{\gamma}^{pl}\rangle_{\mathbf{x}}$, as the average of L^d identical independent random variables, should follow the central limit theorem. This typically corresponds to the situation where the dynamical cooperative length scale ξ_c, if there exists any, is much smaller than the system size, so that plastic events are activated independently in a random manner by the external loading. If the central limit theorem behavior breaks down in some situations, it is then expected to indicate that the system size gets close to, or is smaller than, the dynamical cooperative length scale ξ_c.

In this section, the dynamical cooperative length scale ξ_c is first probed by looking at the dependence of the variance of $\langle\dot{\gamma}^{pl}\rangle_{\mathbf{x}}$ on the system size L^d at different applied shear rates. Then, by studying the power spectral density, the mean-square displacement and the covariance function of the time series $\langle\dot{\gamma}^{pl}\rangle_{\mathbf{x}}$ for system sizes both larger or smaller than ξ_c, it is shown that a saturation time scale T_c^S resides in the time series $\langle\dot{\gamma}^{pl}\rangle_{\mathbf{x}}$, below which the macroscopic plastic strain rate exhibit dynamics well approximated by a Brownian motion. Above T_c^S the stationary state begins to show up in the time series $\langle\dot{\gamma}^{pl}\rangle_{\mathbf{x}}$. For systems of size above the cooperative length scale ξ_c, T_c^S only depends on the applied shear rate $\dot{\gamma}$ and diverges with decreasing $\dot{\gamma}$ as a power law. For systems of size below ξ_c, T_c^S is shown to be system size dependent in a power law fashion $T_c^S \sim L^{z_s}$, which can be interpreted as the scaling relation between the full temporal extension and the cooperative length of the cooperative dynamics. At the end of this section, the assumption of Brownian motion in short time ($T < T_c^S$) dynamics of $\langle\dot{\gamma}^{pl}\rangle_{\mathbf{x}}$ are then used to rationalize some behaviors of the macroscopic plastic strain. Since according to equation (5.3), $\langle\dot{\gamma}^{pl}\rangle_{\mathbf{x}}$ is equivalent to the time derivative of the stress, we will mainly talk about the plastic shear rate which can fully stand for the macroscopic stress velocity. These studies are done for two dimensional systems, using time series of the macroscopic plastic strain in the stationary state.

5.4.1 Observed quantities

Variance of the macroscopic plastic strain rate $Var(\langle\dot\gamma^{pl}\rangle_{\mathbf{x}})$

Thanks to the stationary state of the time series of $\langle\dot\gamma^{pl}\rangle_{\mathbf{x}}(t)$, the numerical estimate of its variance can be realized by taking the time average

$$Var(\langle\dot\gamma^{pl}\rangle_{\mathbf{x}}) = \overline{\langle\dot\gamma^{pl}\rangle^2_{\mathbf{x}}} - \overline{\langle\dot\gamma^{pl}\rangle_{\mathbf{x}}}^2 \tag{5.21}$$

This quantity is a characterization of the global stationary state of the time series of $\langle\dot\gamma^{pl}\rangle_{\mathbf{x}}(t)$ for a given system size L^d under a given applied shear rate $\dot\gamma$.

Power spectral density of the time series of $\langle\dot\gamma^{pl}\rangle_{\mathbf{x}}$

By rescaling the time series of $\langle\dot\gamma^{pl}\rangle_{\mathbf{x}}(t)$ in time and in the amplitude with a proper ratio, i.e. $t \to \lambda t$ and $\langle\dot\gamma^{pl}\rangle_{\mathbf{x}} \to \lambda^{\alpha_s}\langle\dot\gamma^{pl}\rangle_{\mathbf{x}}$ where α_s is introduced to characterize the rescaling procedure, it is observed that the new time series $\langle\dot\gamma^{pl}\rangle^*_{\mathbf{x}}(t)\hat{=}\lambda^{\alpha_s}\langle\dot\gamma^{pl}\rangle_{\mathbf{x}}(\lambda t)$ looks quite similar, in a statistical sense, to the original time series in the same time scale and the amplitude scale. This scale invariance and the exponent α_s are accessible by looking at the power spectral density of $\langle\dot\gamma^{pl}\rangle_{\mathbf{x}}(t)$. Specifically such a scale invariant time series shows power law power spectral density $\left|\langle\hat{\dot\gamma}^{pl}\rangle_{\mathbf{x}}\right|^2 \sim \omega^{-\alpha_p}$, and $\alpha_p = 2(1-\alpha_s)$, where the power spectral density $\left|\langle\hat{\dot\gamma}^{pl}\rangle_{\mathbf{x}}\right|^2(\omega)$ is the squared modulus of the Fourier transform of $\langle\dot\gamma^{pl}\rangle_{\mathbf{x}}$. The derivation of the relation between α_p and α_s is found in the Appendix D.

The time frequency ω has the unit $[T]^{-1}$. For comparing results from different shear rate with respect to the macroscopic strain γ, a dimensionless "strain frequency" $\bar\omega\hat{=}\omega/\dot\gamma$ is defined. In the following, the power spectral density of the time series of $\langle\dot\gamma^{pl}\rangle_{\mathbf{x}}$ for different system sizes L^d under different applied shear rates $\dot\gamma$ are considered as a function of the "strain frequency" $\bar\omega$.

The mean-square displacement of $\langle\dot\gamma^{pl}\rangle_{\mathbf{x}}$

Given the time series of $\langle\dot\gamma^{pl}\rangle_{\mathbf{x}}(t)$ for a given shear rate $\dot\gamma$ and a given system size L^d, under the assumption that the time series is stationary, the mean square displacement of $\langle\dot\gamma^{pl}\rangle_{\mathbf{x}}$, noted $\overline{\left(\Delta\langle\dot\gamma^{pl}\rangle_{\mathbf{x}}\right)^2}$ is measured as

$$\overline{\left(\Delta\langle\dot\gamma^{pl}\rangle_{\mathbf{x}}\right)^2}\hat{=}\lim_{T\to\infty}\frac{1}{T}\int_0^T dt\left(\langle\dot\gamma^{pl}\rangle_{\mathbf{x}}(t+\frac{\Delta\gamma}{\dot\gamma}) - \langle\dot\gamma^{pl}\rangle_{\mathbf{x}}(t)\right)^2 \tag{5.22}$$

The mean-square displacement $\overline{\left(\Delta\langle\dot{\gamma}^{pl}\rangle_{\mathbf{x}}\right)^2}$ is actually equivalent to the variance $Var(\Delta\langle\dot{\gamma}^{pl}\rangle_{\mathbf{x}})$, since $\overline{\Delta\langle\dot{\gamma}^{pl}\rangle_{\mathbf{x}}}^2 = \left(\overline{\langle\dot{\gamma}^{pl}\rangle_{\mathbf{x}}(t+\Delta t)} - \overline{\langle\dot{\gamma}^{pl}\rangle_{\mathbf{x}}(t)}\right)^2 = 0$.

It is also worth mentioning that $\overline{\left(\Delta\langle\dot{\gamma}^{pl}\rangle_{\mathbf{x}}\right)^2}$ at relatively large $\Delta\gamma = \dot{\gamma}\Delta T$ where the correlation between $\langle\dot{\gamma}^{pl}\rangle_{\mathbf{x}}(t+\Delta T)$ and $\langle\dot{\gamma}^{pl}\rangle_{\mathbf{x}}(t)$ becomes weak, is proportional to the variance $Var(\langle\dot{\gamma}^{pl}\rangle_{\mathbf{x}})$. This implies that at such large $\Delta\gamma$, $\overline{\left(\Delta\langle\dot{\gamma}^{pl}\rangle_{\mathbf{x}}\right)^2}$ scales with the system size in the same way as $Var(\langle\dot{\gamma}^{pl}\rangle_{\mathbf{x}})$. Actually

$$\overline{\left(\Delta\langle\dot{\gamma}^{pl}\rangle_{\mathbf{x}}\right)^2} = \overline{\left(\langle\dot{\gamma}^{pl}\rangle_{\mathbf{x}}(t+\Delta T) - \langle\dot{\gamma}^{pl}\rangle_{\mathbf{x}}(t)\right)^2} = 2\overline{\langle\dot{\gamma}^{pl}\rangle_{\mathbf{x}}^2} - 2\overline{\langle\dot{\gamma}^{pl}\rangle_{\mathbf{x}}}^2 = 2Var(\langle\dot{\gamma}^{pl}\rangle_{\mathbf{x}}) \tag{5.23}$$

where $\overline{\langle\dot{\gamma}^{pl}\rangle_{\mathbf{x}}(t+\Delta T)\langle\dot{\gamma}^{pl}\rangle_{\mathbf{x}}(t)} \approx 0$ implied by the weak correlation.

For comparing results from different applied shear rates $\dot{\gamma}$, the mean-square displacement as function of the macroscopic strain $\Delta\gamma$ is considered in the following.

Covariance of a plastic strain rate series starting from the origin$\dot{\gamma}^{pl}_w$

A plastic strain rate time series starting from the origin can be constructed using $\dot{\gamma}^{pl}_w(\Delta t; t_o)$. This quantity, labeled by time t_o, is defined as

$$\dot{\gamma}^{pl}_w(\Delta t; t_o) \hat{=} \langle\dot{\gamma}^{pl}\rangle_{\mathbf{x}}(t_o+\Delta t) - \langle\dot{\gamma}^{pl}\rangle_{\mathbf{x}}(t_o) \tag{5.24}$$

where $\Delta t > 0$ and $\dot{\gamma}^{pl}_w(\Delta t = 0; t_o) = 0$ as can be verified from the definition. t_o labels the starting point for the construction of $\dot{\gamma}^{pl}_w(\Delta t)$.

It will be argued in the following that, this time series $\dot{\gamma}^{pl}_w(\Delta t)$ behaves as a Brownian motion departing from the origin within a saturation time scale T^S_c. For the numerical estimate of the two-time covariance of $\dot{\gamma}^{pl}_w(\Delta t)$ for a series measured over the total time range Δt^T, the amount of $\dot{\gamma}^{pl}_w(\Delta t; t^i_o)$ can be constructed from the time series of $\langle\dot{\gamma}^{pl}\rangle_{\mathbf{x}}$ with $0 < \Delta t < \Delta t^T$ and $t^{i+1}_o - t^i_o = \Delta t^T$. The ensemble of all time series $\dot{\gamma}^{pl}_w(\Delta t; t^i_o)$ can be regarded as an ensemble of realizations, with $i = 1, 2, ..., N_r$. Thanks to the stationary state of the whole time series, the ensemble average $\langle\bullet\rangle_E$ can be estimated by the realization average $\frac{1}{N_r}\sum_i \bullet$, if the realization is large enough. This leads to the estimation of the two time covariance of $\dot{\gamma}^{pl}_w(\Delta t)$, denoted $C_w(s,t)$, as

$$C_w(s,t) = \langle\dot{\gamma}^{pl}_w(s)\dot{\gamma}^{pl}_w(t)\rangle_E = \frac{1}{N_r}\sum_{i=1}^{N_r}\dot{\gamma}^{pl}_w(t; t^i_o)\dot{\gamma}^{pl}_w(s; t^i_o) \tag{5.25}$$

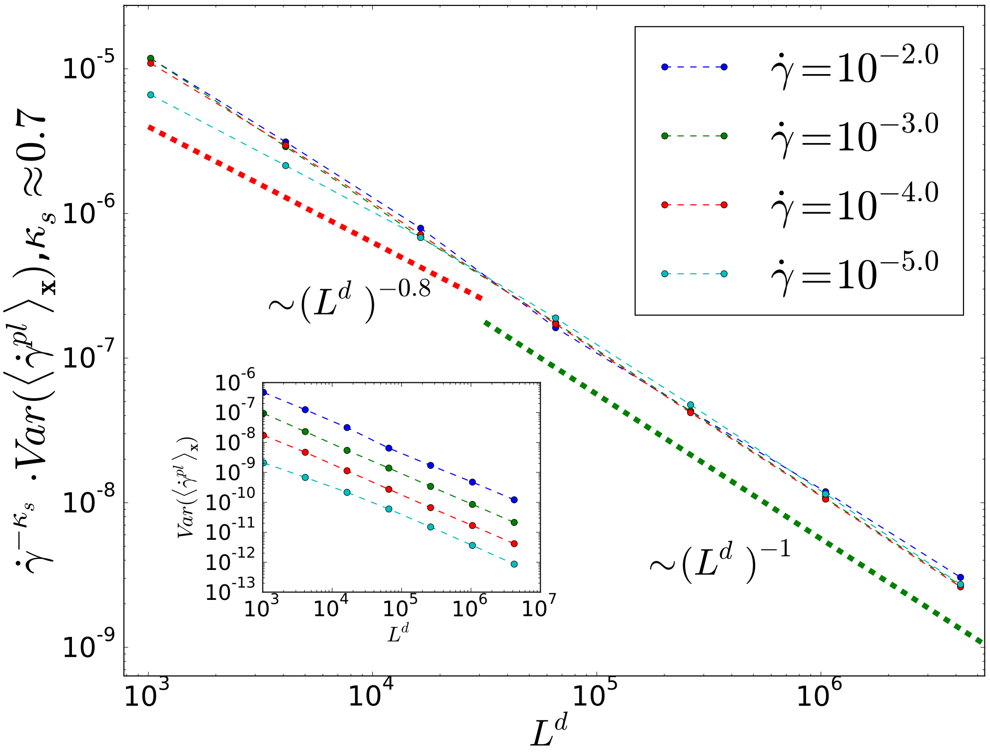

Figure 5.14: Rescaled variance of macroscopic plastic strain rate $\dot\gamma^{-\kappa_s} \cdot \overline{\left(\Delta\langle\dot\gamma^{pl}\rangle_{\mathbf{x}}\right)^2}$ as a function of system size L^d. $\kappa_s \approx 0.7$ for the best collapse. System sizes $L = 32$, 64, 128, 256, 512, 1024, 2048. Red and green dashed lines of different scaling regimes as a guide for the eyes. Inset: non rescaled variance of global plastic strain rate as a function of system size.

5.4.2 Existence of the cooperative length scale ξ_c

The cooperative length ξ_c can be accessed by looking at the variance of the macroscopic plastic strain rate and the long time mean-square displacement of the macroscopic strain rate, which are shown in figure 5.14 and figure 5.15.

Firstly, at high shear rates $\dot\gamma \geq 10^{-4}$, the variance of the macroscopic plastic strain rate follows well the behavior implied by the central limit theorem, i.e. $Var(\langle\dot\gamma^{pl}\rangle_{\mathbf{x}}) \sim L^{-d}$, see the figure 5.14. This central limit theorem behavior for $\dot\gamma \geq 10^{-4}$ can also be confirmed in the power spectral density of the time series $\langle\dot\gamma^{pl}\rangle_{\mathbf{x}}(t)$. As shown in figure 5.16, for collapsing all power spectral density functions for applied shear rates $\dot\gamma \geq 10^{-4}$, it is sufficient to rescale the function vertically by $\left|\langle\hat{\dot\gamma}^{pl}\rangle_{\mathbf{x}}\right|^2 \to L^d \left|\langle\hat{\dot\gamma}^{pl}\rangle_{\mathbf{x}}\right|^2$ (the large strain frequency discrepancy is a technical issue

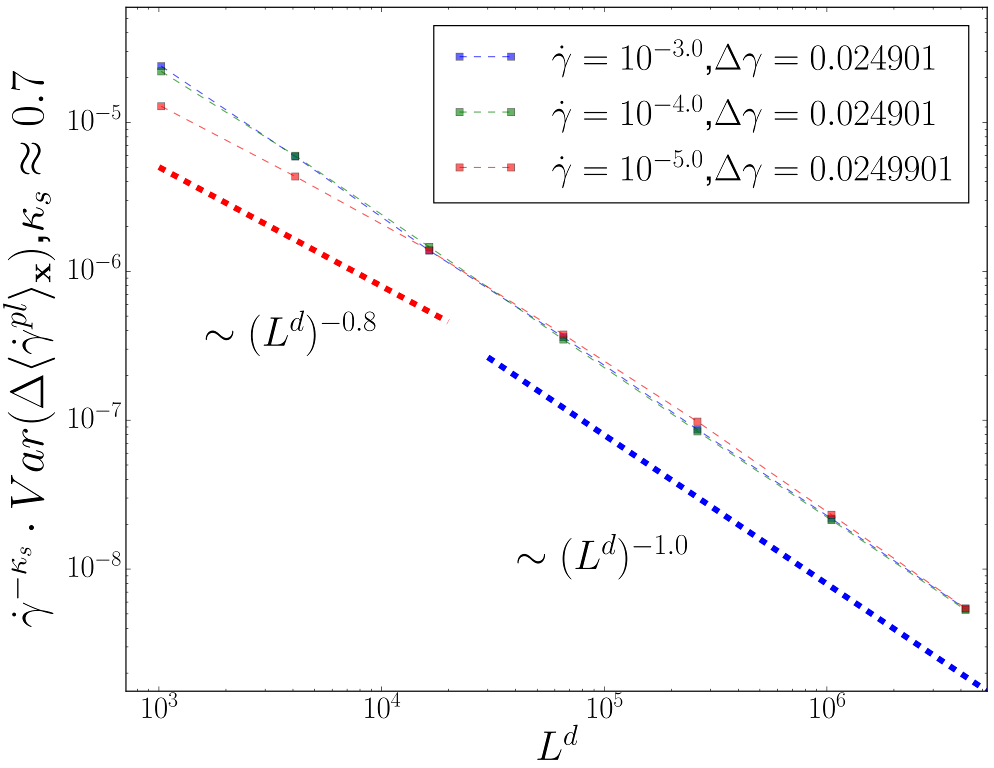

Figure 5.15: Rescaled mean-square displacement of the macroscopic plastic strain rate $\dot{\gamma}^{-\kappa_s} \cdot \overline{\left(\Delta\langle\dot{\gamma}^{pl}\rangle_{\mathbf{x}}\right)}^2$ at a large $\Delta\gamma$ as function of system size L^d. $\kappa_s \approx 0.7$ gives the best collapse. Red and blue dashed lines characterizing different scaling regimes are shown as guide for the eye. The curve for $\dot{\gamma} = 10^{-2}$ is omitted because of its relatively large fluctuation making the different scaling regimes less distinguishable.

that will be discussed in the following). It is worth noticing that

$$Var(\langle\dot{\gamma}^{pl}\rangle_{\mathbf{x}}) \propto \int d\bar{\omega}\left|\langle\hat{\dot{\gamma}}^{pl}\rangle_{\mathbf{x}}\right|^2(\bar{\omega}) - \left|\langle\hat{\dot{\gamma}}^{pl}\rangle_{\mathbf{x}}\right|^2(0)$$

Hence the collapse obtained by rescaling with the system size confirms that the variance of the instantaneous macroscopic plastic strain rate scales with the system size as $Var(\langle\dot{\gamma}^{pl}\rangle_{\mathbf{x}}) \sim 1/L^d$ for $\dot{\gamma} \geq 10^{-4}$. This strongly indicates that, at these relatively high shear rate, the probed system sizes are large enough to not let the cooperative dynamics manifest and to let $\langle\dot{\gamma}^{pl}\rangle_{\mathbf{x}}$ behave as the average of L^d identically distributed independent random variables.

However at shear rate $\dot{\gamma} = 10^{-5}$, two scaling regimes of different scaling exponents can be clearly identified across a crossover length scale ξ_c, residing between $L = 128$ and $L = 256$ in the variance of the macroscopic plastic strain rate, see figure 5.14. Below ξ_c the central limit theorem behavior breaks down and the variance of the global plastic shear rate scales with the system size as $Var(\langle\dot{\gamma}^{pl}\rangle_{\mathbf{x}}) \sim (L^d)^{-0.8}$, from which one can define a dimensionality $d_v \approx 0.8d$. In the power spectral density (figure 5.16) for $\dot{\gamma} = 10^{-5}$, because of lack of statistics, the scatter in the data does not allow one to determine the scaling with the system size.

The fact that below ξ_c the central limit theorem type behavior breaks down and the variance $Var(\langle\dot{\gamma}^{pl}\rangle_{\mathbf{x}})$ decreases with system size more slowly than $\frac{1}{L^d}$, suggests that the spatial extension of the cooperative dynamics differing from a totally random dynamics under the applied shear rate $\dot{\gamma} = 10^{-5}$ saturates to the system size. Hence the crossover length scale ξ_c can be used as a measure for the spatial extension of the cooperative dynamics (i.e. the cooperative length scale) at a given shear rate. According to the assumption that ξ_c diverges as the system approaches the yielding transition, i.e. $\dot{\gamma} \to 0$ [Lin et al., 2014a, Lemaître and Caroli, 2009], the fact that we see only the crossover length scale for the lowest shear rate, can be interpreted through the fact that the dynamical cooperative length ξ_c becomes so small for higher shear rates that it falls out of the domain of system sizes investigated here. For probing how ξ_c depends on the shear rate $\dot{\gamma}$, leading to a direct measurement of the scaling relation hypothesized for the yielding transition, one would need to simulate slower shear rates, which is limited here by the computational capacity. Nevertheless there is a direct evidence of the existence of a dynamic cooperative length scale across which the dynamics changes qualitatively.

Secondly by rescaling vertically $Var(\langle\dot{\gamma}^{pl}\rangle_{\mathbf{x}}) \to \dot{\gamma}^{-\kappa_s} \cdot Var(\langle\dot{\gamma}^{pl}\rangle_{\mathbf{x}})$, it is possible to collapse all curves at length scales larger than ξ_c (figure 5.14). That is to say above the cooperative length $L > \xi_c$, the variance scales with shear rate as $Var(\langle\dot{\gamma}^{pl}\rangle_{\mathbf{x}}) \sim$

$\dot{\gamma}^{\kappa_s}$, with $\kappa_s \approx 0.7$.

Finally as implied by equation (5.23), the long time mean-square displacement of the macroscopic plastic strain rate should scale with system size L and the applied shear rate $\dot{\gamma}$ in the same way as the variance of the macroscopic plastic strain rate $Var(\langle\dot{\gamma}^{pl}\rangle_{\mathbf{x}})$, as is confirmed in the figure 5.15. The same crossover length scale ξ_c can be identified.

In conclusion, the cooperative length of the cooperative dynamics is evidenced by both the variance and the long time mean-square displacement of the macroscopic plastic strain rate. Below this length scale a new dimensionality $d_v \approx 0.8d$ can be extracted, and above both quantities obey the central limit theorem and an exponent $\kappa_s \approx 0.7$ is measured for the scaling relation $Var(\langle\dot{\gamma}^{pl}\rangle_{\mathbf{x}}) \sim \dot{\gamma}^{\kappa_s}$.

5.4.3 The saturation time scale T_c^S in the time series of $\langle\dot{\gamma}^{pl}\rangle_{\mathbf{x}}$

A saturation timescale T_c^S can be identified in the time series of $\langle\dot{\gamma}^{pl}\rangle_{\mathbf{x}}$ by looking at the power spectral density and the mean-square displacement of macroscopic plastic strain rate $\langle\dot{\gamma}^{pl}\rangle_{\mathbf{x}}(t)$.

Power spectral density of $\langle\dot{\gamma}^{pl}\rangle_{\mathbf{x}}(t)$ The power spectral density of $\langle\dot{\gamma}^{pl}\rangle_{\mathbf{x}}$ as function of the “strain frequency” $\bar{\omega}$ is shown in the figure 5.16.

First, let us mention some technical issues about the large strain frequency discrepancy in the collapse by the system size rescaling and the small frequency boundary.

- (i) For all shear rates and system sizes, a large characteristic frequency (i.e. small time scale) and a small characteristic strain frequency $\bar{\omega}_c^v$ (i.e. a large time scale) can be identified, separated by a clear scaling regime regime. The power spectral density beyond the large characteristic frequency seems to differ from each other, depending on the system size. This large frequency behavior is related to the numerical precision of recording the time series of stress. The numerical precision being fixed, information is gradually lost at small time scales from larger system sizes, because macroscopic stress fluctuations at small time scales decrease below the numerical precision for increasing system sizes. The large frequency behavior is therefore better reflected by that of small system size results. The large frequency boundary of the power spectral density is limited by the precision of the elementary numerical integration step. By increasing the precision of the elementary numerical integration time step, it is expected that the scaling regime will continue until very large frequency.

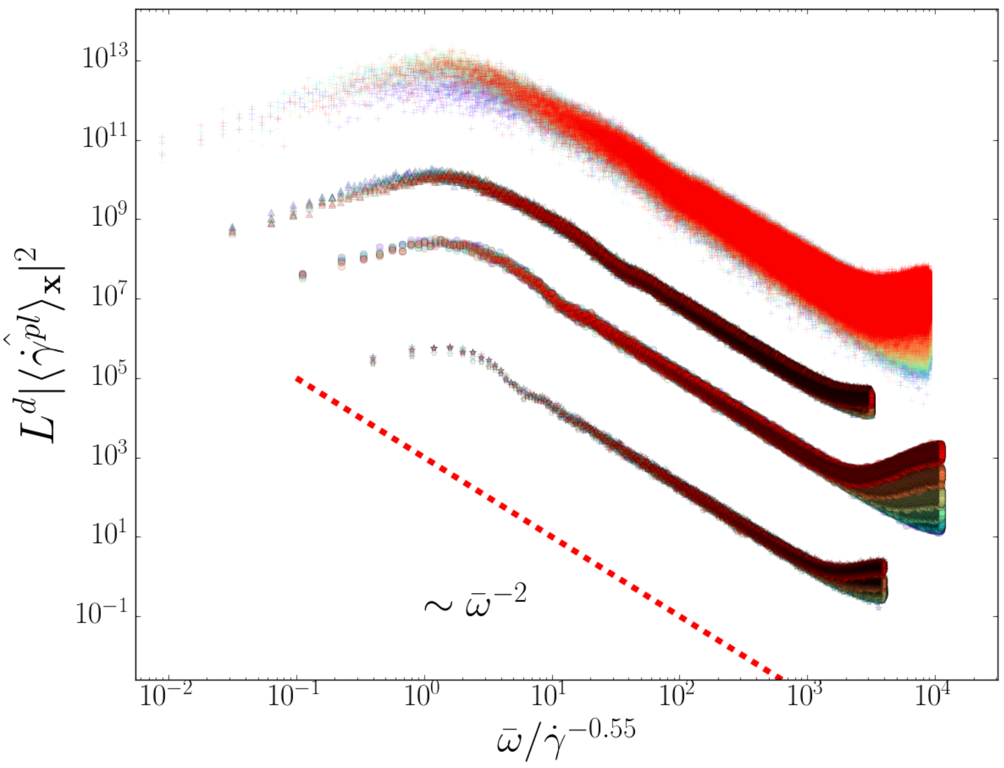

Figure 5.16: Rescaled power spectral density $\left|\langle\hat{\dot{\gamma}}^{pl}\rangle_{\mathbf{x}}\right|^2$ as function of the rescaled "strain frequency" $\bar{\omega} = \omega/\dot{\gamma}$. Curves of different shear rate are shifted vertically for better visualization by dividing a power three of their shear rates. Shear rate decreases form 10^{-2} to 10^{-5} from bottom to top. Red dashed line with slope of -2 for guiding eyes. For each shear rate, there are curves for the linear system sizes $L = 32$, 64, 128, 256, 512, 1024, 2048. For a given shear rate $\dot{\gamma} \geq 10^{-4}$, the vertical rescaling $\left|\langle\hat{\dot{\gamma}}^{pl}\rangle_{\mathbf{x}}\right|^2 \to L^d\left|\langle\hat{\dot{\gamma}}^{pl}\rangle_{\mathbf{x}}\right|^2$ is enough to collapse all curves of different system sizes.

- (ii) The small frequency boundary of power spectral density $\bar{\omega}_{min}$ is limited by the longest segment of time series that can be taken for having a satisfactory statistics over all the time series, i.e. $\bar{\omega}_{min} = 1/\Delta\gamma_{max}$ with $\Delta\gamma_{max} = 0.2$, since the length of the time series is limited by the simulation time and the capacity of data treatment of the used software. Actually the cloud of points for the shear rate $\dot{\gamma} = 10^{-5}$ is due to the lack of statistics, nevertheless the scaling regime and the smaller characteristic frequency are still statistically well captured.

A small characteristic frequency $\bar{\omega}_c^v$ can be identified beyond which the power spectral density behaves as a power law with the strain frequency $\bar{\omega}$. Below $\bar{\omega}_c^v$ the amplitude of the power spectrum becomes smaller and smaller. This is consistent with the fact that the fluctuation of $\langle\dot{\gamma}^{pl}\rangle_{\mathbf{x}}(t)$ at large time scale is bounded for all shear rate and system size by the local yield stress, since $\langle\dot{\gamma}^{pl}\rangle_{\mathbf{x}}(t) = \frac{1}{L^d}\sum_{\mathbf{x}} n(\mathbf{x},t)\sigma(\mathbf{x},t)$, with $\langle n\rangle_{\mathbf{x}}(\dot{\gamma}) < L^d$ and $\langle\sigma\rangle_{\mathbf{x}}(\dot{\gamma}) < \langle\sigma_y\rangle_{dym}(\dot{\gamma})$, where $\langle\sigma_y\rangle_{dym}(\dot{\gamma})$ is the average yield stress averaged for the shear rate $\dot{\gamma}$.

The smaller characteristic frequency $\bar{\omega}_c^v$ delimiting one extremity of the scaling regime depends on the applied shear rate $\dot{\gamma}$. For $\dot{\gamma} \geq 10^{-4}$ for which all system sizes are larger than the cooperative length $L > \xi_c$, it is possible to rescale the frequency $\bar{\omega} \to \bar{\omega}/\dot{\gamma}^{-\eta}$, with η a new exponent, to place the crossover region for all shear rates at the same horizontal position, see figure 5.16, with η measured to be approximately 0.55. A strain scale can be defined as $\gamma_c^v = 1/\bar{\omega}_c^v \sim \dot{\gamma}^{\eta}$ and a time scale $T_c^v = \gamma_c^v/\dot{\gamma} \sim \dot{\gamma}^{\eta-1}$. One can conclude that the plastic shear rate time series (as well as the stress time derivative) of a system under shear rate $\dot{\gamma}$, exhibits scale invariance within a strain scale $\gamma_c^v \sim \dot{\gamma}^{\eta}$ (or a time scale $T_c^v \sim \dot{\gamma}^{\eta-1}$). This scaling relation is only valid for systems approaching the yielding transition, i.e. $\dot{\gamma}$ small.

For $\dot{\gamma} = 10^{-5}$ because of the lack of statistics, the characteristic frequency $\bar{\omega}_c^v$ is not precisely accessible.

It will be argued, in the following, that the strain scale γ_c^v (or the time scale T_c^v) found in the power spectral density for $\dot{\gamma} \geq 10^{-4}$ also characterizes the mean-square displacement of $\langle\dot{\gamma}^{pl}\rangle_{\mathbf{x}}$ as function of the macroscopic strain $\Delta\gamma$.

Mean-square displacement of $\langle\dot{\gamma}^{pl}\rangle_{\mathbf{x}}(t)$ The mean-square displacement as a function of global strain $\Delta\gamma$ for different system sizes and applied shear rates are shown in figure 5.17.

For systems of all sizes under the applied shear rate $\dot{\gamma} \geq 10^{-4}$ and for systems of size $L \geq 256 > \xi_c > 128$ under the applied shear rate $\dot{\gamma} = 10^{-5}$, it is possible to

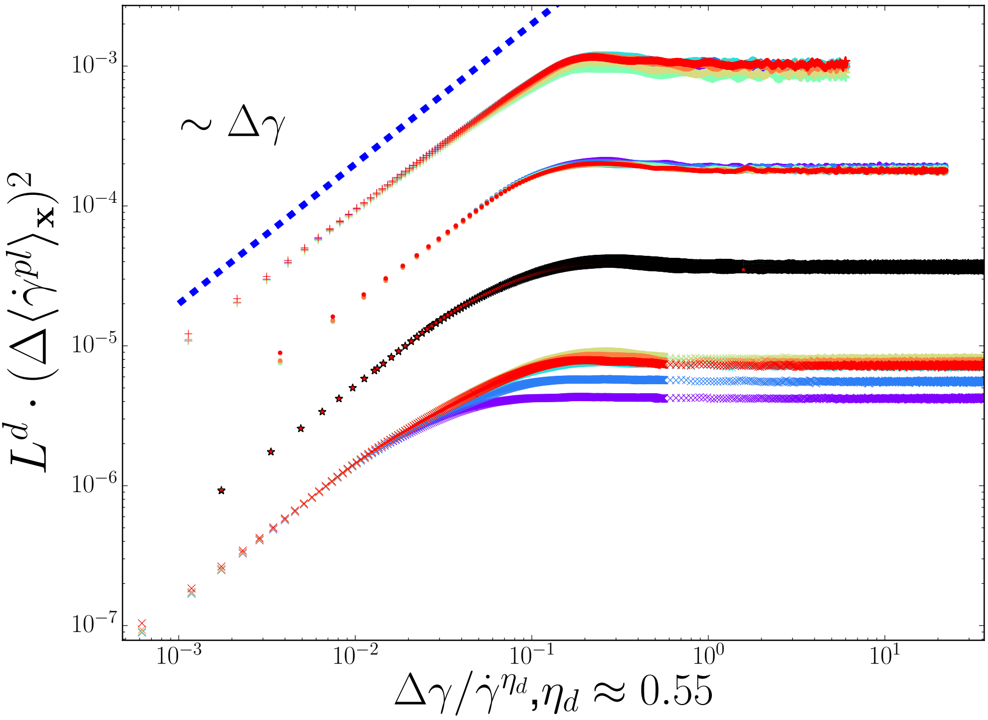

Figure 5.17: Rescaled mean-square displacement $\overline{(\Delta\langle\dot\gamma^{pl}\rangle_{\mathbf{x}})^2}$ as function of the rescaled global strain $\Delta\gamma/\dot\gamma^{\eta_d}$. Shear rate decreases from 10^{-2} to 10^{-5} from top to bottom. $+$: $\dot\gamma = 10^{-2}$; $\bullet$: $\dot\gamma = 10^{-3}$; $*$:$\dot\gamma = 10^{-4}$; $\times$: $\dot\gamma = 10^{-5}$; For each shear rate, the curves plotted are for the linear system sizes $L = 32$, 64, 128, 256, 512, 1024, 2048. For shear rate $\dot\gamma \geq 10^{-4}$, the vertical rescaling is enough for collapsing all curves for different system sizes onto one master curve. Dashed blue line of linear growth for guiding eyes.

collapse the entire mean-square displacement curves for a given shear rate just by a vertical rescaling $\overline{(\Delta\langle\dot{\gamma}^{pl}\rangle_{\mathbf{x}})^2} \rightarrow L^d\overline{(\Delta\langle\dot{\gamma}^{pl}\rangle_{\mathbf{x}})^2}$, see figure 5.17. This confirms the central limit theorem behavior for systems of size $L > \xi_c$ as discussed previously. It is worth noticing that not only the long time mean-square displacement but also the short time mean-square displacement behave as implied by the central limit theorem, since the entire curves collapse to a unique one after rescaling by the system size.

A unique crossover macroscopic strain γ_c^d can be identified for all mean-square displacement curves obtained for different system sizes L for a given shear rate $\dot{\gamma}$. Below γ_c^d the mean-square displacement of $\langle\dot{\gamma}^{pl}\rangle_{\mathbf{x}}$ grows linearly with global strain $\Delta\gamma$ (also linearly with $\Delta T = \Delta\gamma/\dot{\gamma}$) and beyond γ_c^d the mean-square displacement saturates to a constant. For a given shear rate $\dot{\gamma}$, the unique collapse curve for systems of size $L > \xi_c$ suggests that a unique γ_c^d is associated with a given shear rate $\dot{\gamma}$ when $L > \xi_c$. As shown in figure 5.17, it is possible to put the crossover region in the same horizontal position for systems of size $L > \xi_c$ by rescaling $\Delta\gamma \rightarrow \Delta\gamma/\dot{\gamma}^{\eta_d}$ and $\eta_d \approx 0.55$.

Since only one macroscopic strain scale (or one time scale $= strain/\dot{\gamma}$) is found in both the mean-square displacement and the power spectral density of the same time series for a given shear rate, the strain scales found in either of the two observations have to be the same, which is indeed observed by finding the same dependence on the shear rate $\gamma_c^v \sim \dot{\gamma}^\eta$ and $\gamma_c^d \sim \dot{\gamma}^{\eta_d}$ with $\eta \approx 0.55 \approx \eta_d$. It is then adequate to define a unique scale for the saturation of the macroscopic strain $\gamma_c^S = \gamma_c^d = \gamma_c^v$ (or an unique time scale $T_c^S = T_c^d = T_c^v = \gamma_c^S/\dot{\gamma}$). For the case $L > \xi_c$, γ_c^S (T_c^S) depends only on the shear rate as $\gamma_c^S \sim \dot{\gamma}^\eta$ ($T_c^S \sim \dot{\gamma}^{\eta-1}$), with $\eta \approx 0.55$. One should mention as a side remark, that as the quality of the data for the shear rate $\dot{\gamma} = 10^{-5}$ in the figure 5.16 is not very good, it is difficult to distinguish the crossover frequency $\omega_c^v = 1/\gamma_c^v$ for different system sizes $L \leq 128$ for $\dot{\gamma} = 10^{-5}$, which is not contradictory with the observations here.

Conclusion A saturation time scale T_c^S (or equivalently a saturation strain scale $\gamma_c^S = \dot{\gamma}T_c^S$) resides in the time series of the $\langle\dot{\gamma}^{pl}\rangle_{\mathbf{x}}(t)$ below which the time series exhibits statistically meaningful self-similarity and the mean-square displacement grows linearly with time (or the macroscopic strain). When $L > \xi_c$, T_c^S (or γ_c^S) depends only on the shear rate as $T_c^S \sim \dot{\gamma}^{\eta-1}$ (or equivalently $\gamma_c^S \sim \dot{\gamma}^\eta$). The saturation time scale T_c^S for $L < \xi_c$ is discussed in the next section.

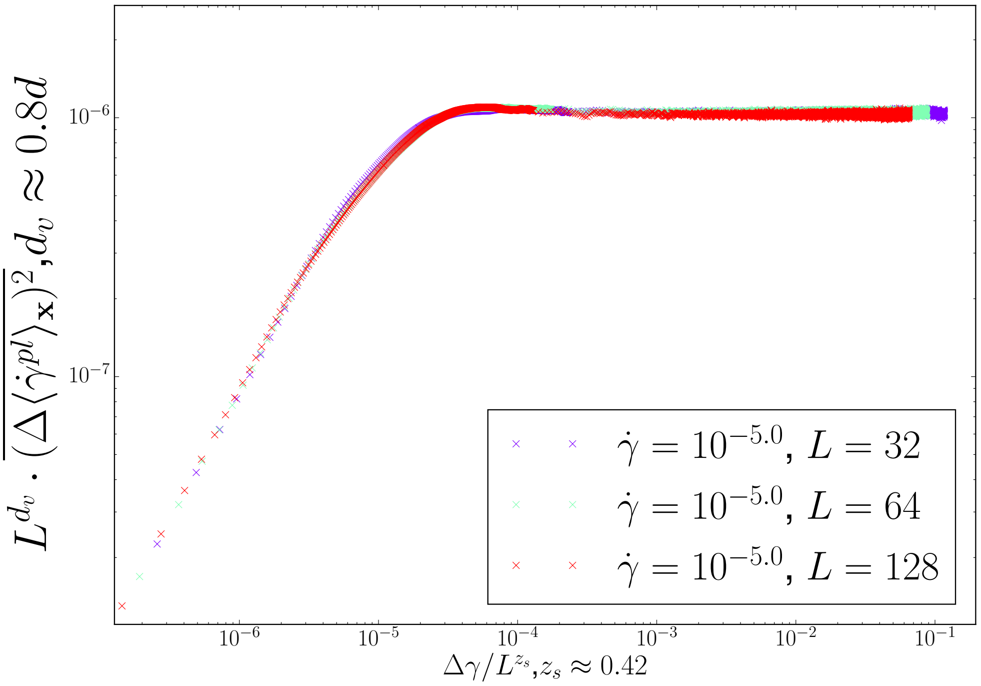

Figure 5.18: Rescaled mean-square displacement $L^{d_v} \cdot \overline{(\Delta\langle\dot{\gamma}^{pl}\rangle_{\mathbf{x}})^2}$ as function of rescaled global strain $\Delta\gamma/L^{z_s}$ for shear rate $\dot{\gamma} = 10^{-5}$ and system size $L < \xi_c$. z_s is measured to be ≈ 0.42

5.4.4 A scaling relation between the cooperative time and the cooperative length

For an applied shear rate $\dot{\gamma} = 10^{-5}$, by doing the vertical rescaling $\overline{(\Delta\langle\dot{\gamma}^{pl}\rangle_{\mathbf{x}})^2} \to L^d\overline{(\Delta\langle\dot{\gamma}^{pl}\rangle_{\mathbf{x}})^2}$, it is only possible to collapse the whole mean-square displacement curves of system sizes $L > \xi_c$, while for $L < \xi_c$ only the linear growth regime, i.e. $\Delta\gamma < \gamma_c^S$, can be collapsed together, see figure 5.17. For $L < \xi_c$ the mean-square displacement of the macroscopic plastic strain rate at large $\Delta\gamma > \gamma_c^S$ scales as studied above with the system size in a power law as $\overline{(\Delta\langle\dot{\gamma}^{pl}\rangle_{\mathbf{x}})^2} \sim L^{-d_v}$. This indicates that the saturation strain γ_c^S begins to depend on the system size when $L < \xi_c$, as seen in figure 5.17.

If we interpret the saturation global strain scale γ_c^S as an indicator of the moment of full development of cooperative dynamics limited by the spatial extension under a certain applied shear rate $\dot{\gamma}$, the dependence of γ_c^S on the system size $L < \xi_c$ can be seen as the temporal extension of the cooperative dynamics induced by the spatial constraint. It is then possible to obtain the relation between the spatial extension and the temporal extension of the cooperative dynamics under a given shear rate, by using the fact that the spatial extension of the dynamics ξ_c reaches the system size at this specific value of the strain.

Practically this relation can be accessed by trying to collapse the mean-square displacement curves for $\dot{\gamma} = 10^{-5}$ and $L < \xi_c$ in the figure 5.17 by firstly shifting vertically according to the scaling relation between the long time mean-square displacement and system size, i.e. $\overline{\left(\Delta\langle\dot{\gamma}^{pl}\rangle_{\mathbf{x}}\right)^2} \rightarrow L^{d_v} \cdot \overline{\left(\Delta\langle\dot{\gamma}^{pl}\rangle_{\mathbf{x}}\right)^2}$, and then shifting horizontally with $\Delta\gamma \rightarrow \Delta\gamma/L^{z_s}$, where the exponent z_s is to be measured. If all curves collapse to a master curve, the horizontal shifting leads to a scaling relation $T_c \sim \xi_c^{z_s}$, since $\Delta T = \Delta\gamma/\dot{\gamma}$. The figure 5.18 shows the result, and the exponent z_s is measured to be close to 0.42. A similar scaling relation between a length scale and a time scale $T \sim \xi^z$ is also suggested in a former work [Lin et al., 2014a], and the exponent is measured to be $z \approx 0.57$ [Lin et al., 2014a] similar to the value of our study of avalanche dynamics earlier in this chapter. Since it is still not clear if z and z_s should be interpreted in the same way, they are not supposed to be comparable quantitatively.

5.4.5 Brownian motion signatures blow the saturation time scale T_c^S

Several signatures of the Brownian motion (i.e. Wiener process) are observed below the saturation time scale T_c^S in the time series of $\langle\dot{\gamma}^{pl}\rangle_{\mathbf{x}}$ by looking at the power spectral density, the mean-square displacement and the covariance function $C_w(s,t)$. The object which behaves as a Wiener process starting from zero is the reconstructed plastic strain rate time series $\dot{\gamma}_w^{pl}(\Delta t; t_o)$, see the equation (5.24), with $\Delta t < T_c^S$.

Power spectral density The first signature of Brownian motion resides in the power spectral density $\left|\hat{\dot{\gamma}}^{pl}\right|^2(\bar{\omega})$. The power spectral density of a Brownian motion is a power law in frequency of exponent two, i.e. $\sim \omega^{-2}$. This is actually observed in the power spectral density of the macroscopic plastic strain rate. A clear scaling regime covers about three decades for shear rates $\dot{\gamma} \geq 10^{-4}$ above the saturation strain frequency $\bar{\omega}_c^S = 1/\gamma_c^S$. The power law in the spectral density for $\dot{\gamma} \geq 10^{-4}$ is measured to be $\left|\hat{\dot{\gamma}}^{pl}\right|^2 \sim \bar{\omega}^{-\alpha_p}$ with $\alpha_p \approx 2$, (see the figure 5.16). This power law with exponent -2 in the power spectral density above $\bar{\omega}_c^S$ suggests that Brownian motion signatures reside in the time series of $\langle\dot{\gamma}^{pl}\rangle_{\mathbf{x}}$ for a time scale smaller than T_c^S. For $\dot{\gamma} = 10^{-5}$ the lack of statistics induces a large scatter in the power spectral density, which makes it difficult to measure a power law, see figure 5.16. From the power spectral density, the Brownian motion signature is more pronounced for $\dot{\gamma} \geq 10^{-4}$.

Mean-square displacement The second signature of Brownian motion is found in the linear growth of the mean-square displacement with the macroscopic strain below γ_c^S, see the figure 5.17. Comparing the expression of the mean-square displacement 5.22 and the definition 5.24 of $\dot{\gamma}_w^{pl}(\Delta t; t_o)$, one finds that $\overline{(\Delta\langle\dot{\gamma}^{pl}\rangle_{\mathbf{x}})^2} = \overline{\left(\dot{\gamma}_w^{pl}\right)^2}$. The fact that for all shear rates $\overline{\left(\dot{\gamma}_w^{pl}\right)^2} \sim \Delta\gamma \sim \Delta t$ for $\Delta\gamma < \gamma_c^S$ suggests that $\dot{\gamma}_w^{pl}(\Delta t)$ behaves like a Brownian motion for $\Delta t < T_c^S$ (or equivalently $\Delta\gamma < \gamma_c^S$).

It is worth to notice that the diffusion coefficient within the linear growth regime, i.e. $\Delta\gamma < \gamma_c^S$, is inversely proportional to the system size L^d, which is confirmed by the fact that by rescaling the mean-square displacement with the system size according to the central limit theorem, all curves of different system sizes collapse to an unique curve for a given shear rate, even for $L < \xi_c$, as far as $\Delta\gamma < \gamma_c^S$, see the figure 5.17.

Covariance The last signature of Brownian motion is the covariance function of $\dot{\gamma}_w^{pl}(\Delta t)$. If W_t is a standard Brownian motion process which is not a stationary process, the covariance $C_v(s,t) = \langle W_t W_s\rangle$ depends on the two times t and s, and $C_v(s,t) = min(t,s)$. For testing this property, the covariance function $C_w(s,t)$ of the reconstructed plastic strain rate (starting from zero), estimated as the expression 5.25, is investigated for all shear rates within a total time interval smaller than T_c^S. The covariance C_w is shown as function of $\Delta\gamma \hat{=} t\dot{\gamma}$ for a fixed $\Delta\gamma_s \hat{=} s\dot{\gamma}$. We have $0 < \Delta\gamma < \gamma^{tot} < \gamma_c^S(\dot{\gamma}, L)$, and $\Delta\gamma_s$ is set to be one fifth of the γ^{tot}. Shown in the figure 5.19, the behavior of the covariance function, as required by the property of Brownian motion, grows linearly with $\Delta\gamma$ when $\Delta\gamma < \Delta\gamma_s$ and becomes a constant once $\Delta\gamma > \Delta\gamma_s$. It is worth to notice that the short time (smaller than T_c^S) covariance behaves in the same way for all system sizes, as far as the time scale is within the saturation time T_c^S. This behavior of the covariance is another strong signature of the Brownian motion of $\dot{\gamma}_w^{pl}$ within the saturation time scale T_c^S.

Conclusion With the signatures of the Brownian motion in the power spectral density, the mean-square displacement and the covariance function within the saturation time scale T_c^S, the time series of $\langle\dot{\gamma}^{pl}\rangle_{\mathbf{x}}$ can be described in a phenomenological way as a Brownian motion. Specifically given the macroscopic plastic strain rate at moment t_o of a system of size L under shear rate $\dot{\gamma}$, the macroscopic plastic strain rate at a time $t = t_o + \Delta t$ with $\Delta t < T_c^S$ can be expressed as

$$\langle\dot{\gamma}^{pl}\rangle_{\mathbf{x}}(t) = \langle\dot{\gamma}^{pl}\rangle_{\mathbf{x}}(t_o) + \dot{\gamma}_w^{pl}(\Delta t) \tag{5.26}$$

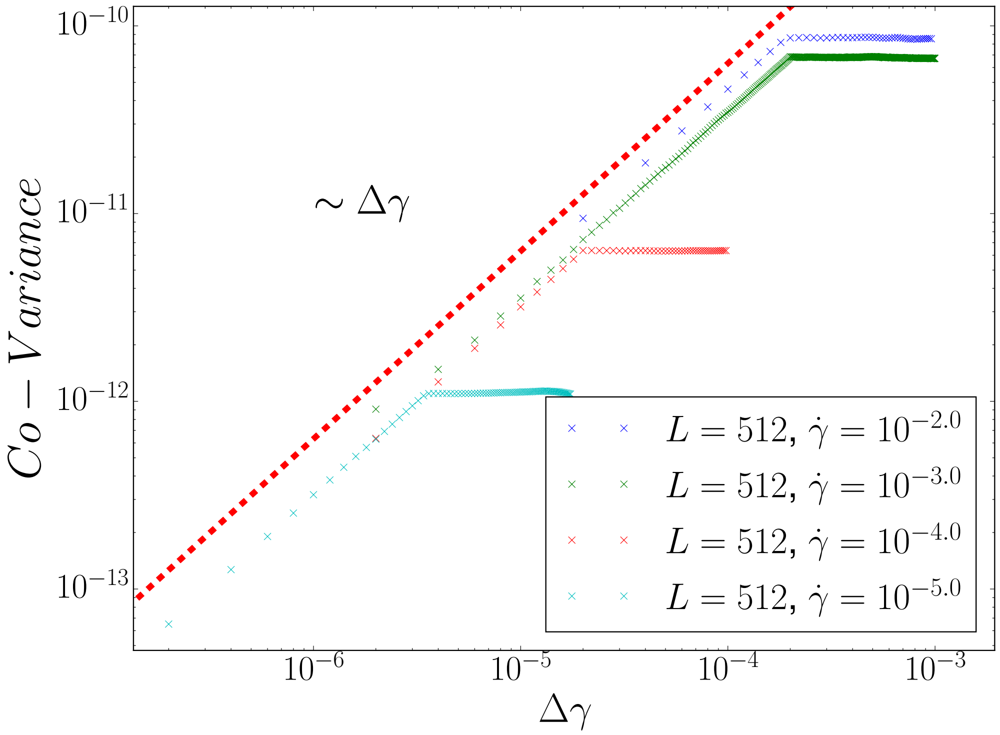

Figure 5.19: covariance $C_v(s,t) = \langle \dot{\gamma}_w^{pl}(s)\dot{\gamma}_w^{pl}(t)\rangle_E$ as function of global strain $\Delta\gamma$. The total length is chosen differently for different shear rates, for that $\gamma_c^S \sim \dot{\gamma}^\eta$ and for reasons of numerical precision. The fixed moment $s = \Delta\gamma_s/\dot{\gamma}$ is chosen to be one fifth of the total length. Red dashed line of linear growth for guiding eyes.

where $\dot{\gamma}^{pl}_{w}(\Delta t)$ is zero departing Brownian motion, the diffusion constant of which is inversely proportional to the system size L^d. If the system size is larger than the cooperative length $L > \xi_c$, $T_c^S \sim \dot{\gamma}^{\eta-1}$ with $\eta \approx 0.55$, otherwise if $L < \xi_c$, $T_c^S \sim L^{z_s}$ with z_s. Rationalizing the above scaling relations and the Brownian motion behavior would significantly improve our understanding of the elasto-plastic model.

5.4.6 Conclusion

The full spatial extension ξ_c of the cooperative dynamics in the elasto-plastic model is evidenced by numerical tests, even though the dependency of ξ_c on the shear rate $\dot{\gamma}$ is not accessible because of numeric computing capacity. The temporal extension and the spatial extension of the cooperative dynamics are related by $T_c \sim \xi_c^{z_s}$ with $z_s \approx 0.42$.

Above the cooperative dynamic length scale $L > \xi_c$, the fluctuations of the macroscopic plastic strain rate behave as implied by the central limit theorem, i.e. $Var(\langle\dot{\gamma}^{pl}\rangle_{\mathbf{x}}) \sim L^{-d}\dot{\gamma}^{\kappa_s}$ with $\kappa_s \approx 0.7$. Below the dynamical cooperative length scale $L < \xi_c$, the fluctuations of the macroscopic plastic strain rate decrease slower than the central limit theorem would predict, i.e. $Var(\langle\dot{\gamma}^{pl}\rangle_{\mathbf{x}}) \sim L^{-d_v}$ with $d_v \approx 0.8d$.

The time series of the macroscopic plastic strain rate $\Delta\langle\dot{\gamma}^{pl}\rangle_{\mathbf{x}}(\Delta t) = \langle\dot{\gamma}^{pl}\rangle_{\mathbf{x}}(t+\Delta t) - \langle\dot{\gamma}^{pl}\rangle_{\mathbf{x}}(t)$ behaves apparently as a Brownian motion at small global strain scale $\Delta\gamma < \gamma_c^S$ (or equivalently a short time scale $\Delta T < T_c^S = \gamma_c^S/\dot{\gamma}$). Above the cooperative dynamical length scale $L > \xi_c$, $\gamma_c^S \sim \dot{\gamma}^{\eta}$ with $\eta \approx 0.55$ (equivalently $T_c^S \sim \dot{\gamma}^{\eta-1}$). Below this value the dynamical length scale $L < \xi_c$, we obtain $\gamma_c^S \sim L^{z_s}$ (equivalently $T_c^S \sim L^{z_s}$). Below the crossover global strain scale γ_c^S, the diffusion coefficient of the Brownian motion scales like the inverse of the system size, i.e. $\overline{(\Delta\langle\dot{\gamma}^{pl}\rangle_{\mathbf{x}})^2} \sim L^{-d}\Delta\gamma$, for $\Delta\gamma < \gamma_c^S$.

5.4.7 Rationalizing the variance of $\langle\Delta\gamma^{pl}\rangle_{\mathbf{x}}$ using the conclusions for $\langle\dot{\gamma}^{pl}\rangle_{\mathbf{x}}(t)$

The macroscopic plastic strain during $\Delta\gamma$ is the integral of global plastic strain rate. The macroscopic plastic strain between t and $t + \Delta T = t + \Delta\gamma/\dot{\gamma}$ is

$$\langle\Delta\gamma^{pl}\rangle_{\mathbf{x}}(\Delta\gamma; t) = \int_t^{t+\Delta T} \langle\dot{\gamma}^{pl}\rangle_{\mathbf{x}}(s)ds \tag{5.27}$$

Thanks to the stationary state, a numerical estimate of the variance $\langle \Delta\gamma^{pl}\rangle_{\mathbf{x}}(\Delta\gamma)$ is obtained from

$$Var(\langle \Delta\gamma^{pl}\rangle_{\mathbf{x}}) = \overline{\langle \Delta\gamma^{pl}\rangle_{\mathbf{x}}^2} - \overline{\langle \Delta\gamma^{pl}\rangle_{\mathbf{x}}}^2 \tag{5.28}$$

we have the average macroscopic plastic strain

$$\overline{\langle \Delta\gamma^{pl}\rangle_{\mathbf{x}}} = \int_0^{\Delta T} \overline{\langle \dot\gamma^{pl}\rangle_{\mathbf{x}}}(t)dt = \dot\gamma \Delta T = \Delta\gamma \tag{5.29}$$

and the average square macroscopic plastic strain

$$\overline{\langle \Delta\gamma^{pl}\rangle_{\mathbf{x}}^2} = \lim_{T\to\infty} \frac{1}{T} \int_{-\frac{T}{2}}^{+\frac{T}{2}} dt_0 \left\{ \int_{t_0}^{t_0+\Delta T} dt \int_{t_0}^{t_0+\Delta T} ds \langle \dot\gamma^{pl}\rangle_{\mathbf{x}}(t) \langle \dot\gamma^{pl}\rangle_{\mathbf{x}}(s) \right\} \tag{5.30}$$

At short times$\Delta T < T_c^S$, we assume a Brownian motion for the dynamics of $\langle \dot\gamma^{pl}\rangle_{\mathbf{x}}(t)$, i.e.

$$\langle \dot\gamma^{pl}\rangle_{\mathbf{x}}(t) = \langle \dot\gamma^{pl}\rangle_{\mathbf{x}}(t_0) + \dot\gamma_w^{pl}(t-t_0)$$

where $\dot\gamma_w^{pl}(t-t_0)$ is a Wiener process starting from zero. By changing variables $t \to \Delta t = t - t_0$ and $s \to \Delta s = s - t_0$, the equation (5.30) becomes

$$\overline{\langle \Delta\gamma^{pl}\rangle_{\mathbf{x}}^2} = \int_0^{\Delta T} d\Delta t \int_0^{\Delta T} d\Delta s \left\{ \overline{\langle \dot\gamma^{pl}\rangle_{\mathbf{x}}^2} + \overline{\dot\gamma_w^{pl}(\Delta t) \dot\gamma_w^{pl}(\Delta s)} \right\} \tag{5.31}$$

The cross terms vanish due to the independence between $\dot\gamma_w^{pl}(t-t_0)$ and $\langle \dot\gamma^{pl}\rangle_{\mathbf{x}}(t_0)$, which is a property of a Wiener process. Taking into account of the covariance of a Wiener process$\overline{\dot\gamma_w^{pl}(\Delta t)\dot\gamma_w^{pl}(\Delta s)} = C_v(\Delta t, \Delta s) \sim \min(\Delta t, \Delta s)$, equation (5.31) leads to

$$\overline{\langle \Delta\gamma^{pl}\rangle_{\mathbf{x}}^2} \sim \left(\overline{\langle \dot\gamma^{pl}\rangle_{\mathbf{x}}^2} \right) \Delta T^2 + \mathcal{O}(\Delta T^3) \tag{5.32}$$

Inserting equations (5.32), (5.29) into (5.28), It is straightforward to show, by replacing $\dot\gamma^2 = \overline{\langle \dot\gamma^{pl}\rangle_{\mathbf{x}}}^2$,

$$Var(\langle \Delta\gamma^{pl}\rangle_{\mathbf{x}}) \sim Var(\langle \dot\gamma^{pl}\rangle_{\mathbf{x}}) \cdot \Delta T^2 + \mathcal{O}(\Delta T^3) \tag{5.33}$$

By changing variable $\Delta\gamma = \dot\gamma \Delta T$, one gets

$$Var(\langle \Delta\gamma^{pl}\rangle_{\mathbf{x}}) \sim \frac{Var(\langle \dot\gamma^{pl}\rangle_{\mathbf{x}})}{\dot\gamma^2} \cdot \Delta\gamma^2 + \mathcal{O}(\Delta\gamma^3) \tag{5.34}$$

These predictions can be tested by the following observations on the data from simulations that are shown in the figure 5.20 and 5.21:

1. For small time scales $\Delta T < T_c^S$ (or equivalently $\Delta\gamma < \gamma_c^S$) the variance of the macroscopic plastic strain should increase quadratically with the strain $\Delta\gamma$ (see figure 5.20).

2. The variance of the plastic strain $Var(\langle\Delta\gamma^{pl}\rangle_{\mathbf{x}})$ should scale in the same way as the variance of the plastic strain rate $Var(\langle\dot{\gamma}^{pl}\rangle_{\mathbf{x}})$ with the system size, as long as $\Delta\gamma$ is small and relatively far from γ_c^S so that the Brownian motion description works well. Curves collapse well by rescaling with the system size $L^d \cdot Var(\langle\Delta\gamma^{pl}\rangle_{\mathbf{x}})$ implying that $Var(\langle\Delta\gamma^{pl}\rangle_{\mathbf{x}}) \sim L^{-d}$ as $Var(\langle\dot{\gamma}^{pl}\rangle_{\mathbf{x}})$ does for $L > \xi_c$, see figure 5.20 and left panel of figure 5.21. For $L < \xi_c$, see left panel of figure 5.21 at $\dot{\gamma} = 10^{-5}$ and $L^d \leq 128^2$, the variance of the plastic strain scales with the system size as $Var(\langle\Delta\gamma^{pl}\rangle_{\mathbf{x}}) \sim L^{-0.8d}$, and so does the variance of the macroscopic plastic strain $Var(\langle\dot{\gamma}^{pl}\rangle_{\mathbf{x}}) \sim L^{-0.8d}$ in the left panel of figure 5.14.

3. Since the variance of the plastic strain rate scales with the shear rate $Var(\langle\dot{\gamma}^{pl}\rangle_{\mathbf{x}}) \sim \dot{\gamma}^{\kappa_s}$ with $\kappa_s \approx 0.7$, as seen in figure 5.14(left), the variance of the plastic strain should scale with the shear rate $Var(\langle\Delta\gamma^{pl}\rangle_{\mathbf{x}}) \sim \dot{\gamma}^{(\kappa_s-2)}$. Figure 5.21(left) shows the scaling of the variance of the plastic strain with shear rate at a small $\Delta\gamma$ by the collapsing all curves obtained for $L > \xi_c$ after rescaling $Var(\langle\Delta\gamma^{pl}\rangle_{\mathbf{x}}) \rightarrow \dot{\gamma}^{\kappa_p} \cdot Var(\langle\Delta\gamma^{pl}\rangle_{\mathbf{x}})$. That is to say $Var(\langle\Delta\gamma^{pl}\rangle_{\mathbf{x}}) \sim \dot{\gamma}^{-\kappa_p}$ with $\kappa_p \approx 1.3$ for the best collapse, which is consistent with $2 - \kappa_s \approx 1.3$.

4. The predictions work less well when $\Delta\gamma$ approaches from below to the saturation strain $\Delta\gamma \lesssim \gamma_c^S$, as shown in figure 5.21(left). The variance of the macroscopic plastic strain for large systems $L > \xi_c$ still follows the central limit theorem predictions, i.e. $Var(\langle\Delta\gamma^{pl}\rangle_{\mathbf{x}}) \sim L^{-d}$, and the scaling with the shear rate is still close to that when $\Delta\gamma$ is small, i.e. $\kappa_p \approx 1.2$ for the best collapse. For small system sizes $L < \xi_c$, one finds $Var(\langle\Delta\gamma^{pl}\rangle_{\mathbf{x}}) \sim L^{-0.65d}$ which is not consistent with the above predictions, indicating that some complexity appears when approaching $\Delta\gamma \approx \gamma_c^S$ which gives a different scaling exponent $d_s \approx 0.65d < d_v \approx 0.8d$. The variance of the macroscopic plastic strain $Var(\langle\Delta\gamma^{pl}\rangle_{\mathbf{x}})$ after entering the saturation regime can be estimated roughly by assuming that $Var(\langle\Delta\gamma^{pl}\rangle_{\mathbf{x}})$ grows monotonically until γ_c^S then turns to be a constant, noted $V^S \hat{=} Var(\langle\Delta\gamma^{pl}\rangle_{\mathbf{x}})\Big|_{\Delta\gamma > \gamma_c^S}$, within the saturation. With these assumptions, according to the equation (5.34), $V^S \sim \frac{Var(\langle\dot{\gamma}^{pl}\rangle_{\mathbf{x}})}{\dot{\gamma}^2} \cdot \left(\gamma_c^S\right)^2 \sim \dot{\gamma}^{\kappa_s+2\eta-2} \sim \dot{\gamma}^{-0.2}$, implying that the saturated variance of the macroscopic plastic strain diverges with decreasing shear rate for

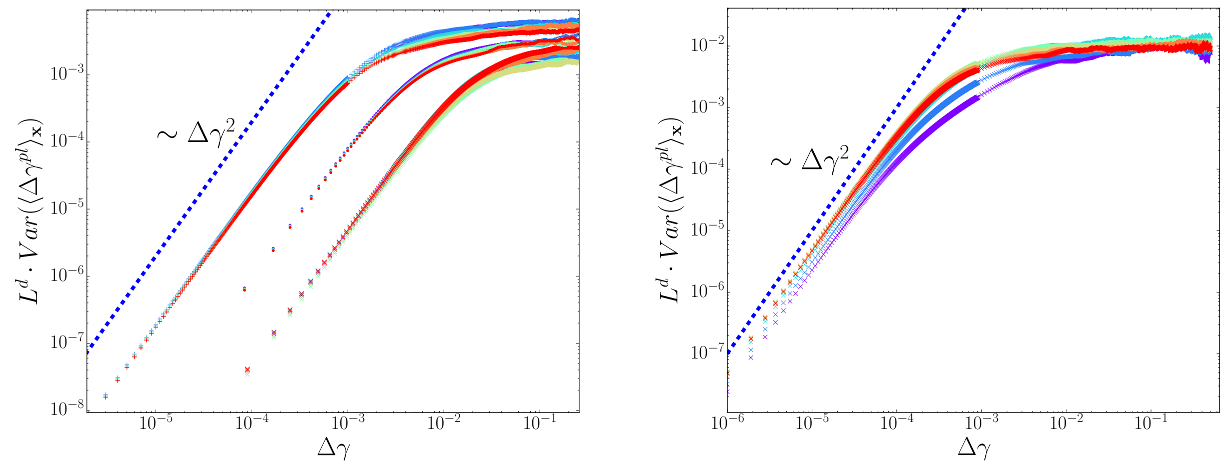

Figure 5.20: Rescaled variance of global plastic strain $L^d \cdot Var(\langle\Delta\gamma^{pl}\rangle_{\mathbf{x}})$ as function of global strain $\Delta\gamma$. Left: Shear rate decreases from 10^{-2} to 10^{-4} from bottom to top. $\times$: $\dot{\gamma} = 10^{-2}$; $\bullet$: $\dot{\gamma} = 10^{-3}$; $+$: $\dot{\gamma} = 10^{-4}$. Different colors correspond to system sizes $L = 32, 64, 128, 256, 512, 1024, 2048$. The collapse is rather good when rescaling with the system size. Large fluctuations at high strain $\Delta\gamma$ are due to lack of statistics. Right: Shear rate $\dot{\gamma} = 10^{-5}$. The correspondence between the color and the system size is the same as it is in the left panel. Only curves for large system sizes $L > 128$ collapse well after rescaling with L to the power d. Blue dashed lines show a quadratic growth as a guide to the eye.

$L > \xi_c$. This is confirmed by the curves in the figure 5.20, where despite the relatively large fluctuations, the tendency of the saturated variance of the macroscopic plastic strain to increase with decreasing shear rate is evidenced. Because of the fluctuations, the scaling $V^S \sim \dot{\gamma}^{-0.2}$ can not be measured precisely. It is worth to notice that for a given system size L the scaling $V^S \sim \dot{\gamma}^{\kappa_s+2\eta-2}$ can only be valid above a shear rate $\dot{\gamma}_L$, with $\xi_c(\dot{\gamma}_L) = L$. For smaller shear rate, the cooperative length exceeds the systems, and the scaling between the variance $Var(\langle\dot{\gamma}^{pl}\rangle_{\mathbf{x}})$ and the shear rate $\dot{\gamma}$ is not known.

5.5 Conclusion

The critical dynamics close to the yielding transition has been probed by various approaches in this chapter. First, the driving rate dependence of the avalanche statistics is systematically studied. Various power laws and scaling relations in the zero shear rate limit are found to be consistent with the results in the literature, which reinforces the idea that the yielding transition belongs to the universality class of a dynamical phase transition. The crossover from non-mean-field to a mean-

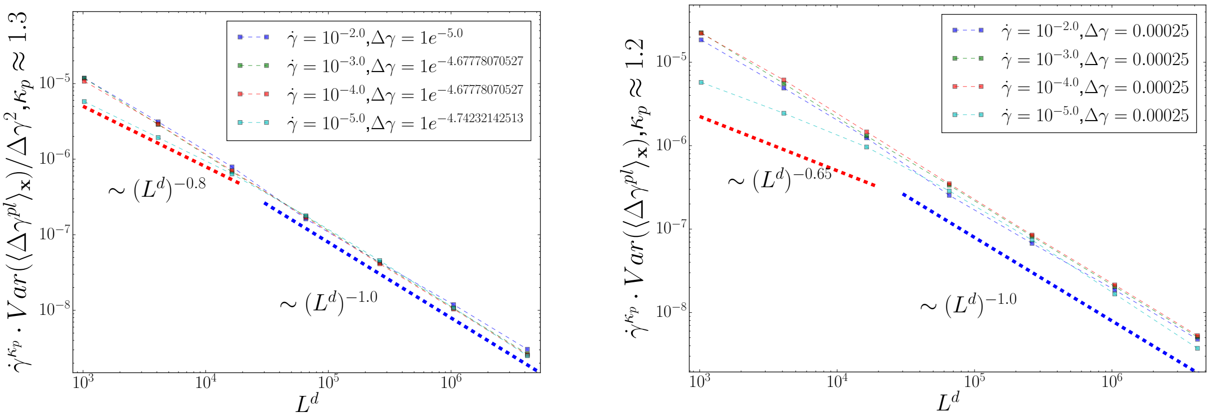

Figure 5.21: Left: Rescaled variance of global plastic strain $\dot{\gamma}^{\kappa_p} \cdot Var(\langle \Delta\gamma^{pl} \rangle_{\mathbf{x}})$ as function of system size at $\Delta\gamma \ll \gamma_c^S$. $\kappa_p \approx 1.3$ for the best collapse. Red and blue dashed lines guiding eyes for different scaling regimes. Right: Rescaled variance of global plastic strain $\dot{\gamma}^{\kappa_p} \cdot Var(\langle \Delta\gamma^{pl} \rangle_{\mathbf{x}})$ as function of system size at $\Delta\gamma$ close to γ_c^S. $\kappa_p \approx 1.2$ for the best collapse. Red and blue dashed lines guiding eyes for different scaling regimes. Inset non-rescaled variance.

field like behavior of the mechanical noise, the distribution of the distance to the instability $\mathcal{P}(x)$ as well as the distribution of the stress drop sizes with respect to the applied shear rate are evidenced. The idea that macroscopic stress drops result from the spatial-temporal superposition of individual collective motions, i.e. avalanches coming from the cooperative dynamics, is justified by the observation that the symmetry of the average avalanche shape depends on the duration, the system size and the applied shear rate. However the hypothesis of the existence of a dynamical cooperative length scale diverging as approaching the yielding transition can not be probed directly by the statistics of the stress drops.

Inspired by the analogy between the elasto-plastic model and the depinning model, the geometry of the plastic interface is characterized by its "hard" Fourier modes. Unlike in depinning models, the geometry of the plastic interface is not isotropic and seems to be insensitive to the shear rate. The non isotropic form in Fourier space of the plastic interface is related with the strength of the self-interaction kernel, i.e. the propagator $\hat{G}^N$. Because of the complexity of the geometry of the plastic interface, there is no characteristic length scale that can be identified, such as the l_{av} in the depinning elastic line, for characterizing the cooperative dynamics of the elasto-plastic model.

For probing the cooperative length scale, the two point correlations of the plastic shear rate field is investigated for different shear rates. It is evidenced that spatio-temporal correlations become increasingly important as the shear rate decreases. A power law decay of the correlations along the strong correlation axis from the center at a given time delay is found. The overall system correlation intensity decays as a power law with the delay time. Because of the power law behavior, there is no characteristic length scale to be identified for the dynamical cooperative length.

Finally, by comparison with the central limit theorem predictions, the study on the macroscopic stress fluctuation (equivalent to the macroscopic plastic strain rate fluctuation) reveals the existence of a cooperative length scale ξ_c below which the central limit theorem breaks down indicating dynamical correlations. A saturation time scale T_c^S is revealed to depend only on the shear rate when $L > \xi_c$ and to depend on the system size L for $L < \xi_c$. From the dependence of T_c^S on the system size, a scaling relation between the cooperative time and the cooperative length is obtained $T_c \sim \xi_c^{z_s}$. This scaling relation is reminiscent of the one proposed in the literature, however this similarity should be interpreted prudently. It is not clear if the relation found here can be interpreted in the same way as the one found in the literature. Furthermore we found that the short time ($\Delta t < T_c^S$) dynamics of the macroscopic plastic strain rate closely resembles the one of a Brownian motion. The assumption of the short time Brownian dynamics of the macroscopic plastic strain rate is then used to rationalize the behavior of the variance of the macroscopic plastic strain.

From these studies, it is clear that a finite size effect manifests when the applied shear rate decreases, indicating that a cooperative length scale is involved in the dynamics close to the yielding transition. Power laws found close to the yielding transition, strongly suggests that the yielding transition exhibits critical dynamics at a dynamical phase transition involving a divergent dynamical length scale. This length scale is evidenced in the system size dependent fluctuation of the macroscopic stress. More detailed simulations and lower shear rates should be used for revealing the divergence of the cooperative length scale as the system approaches at the yielding point to deepen our understanding of the critical dynamics.

Chapter 6

Creep

As argued already in chapter 3, the creep experiment is an important part of the study of the mechanical behavior of the soft glassy systems. In this chapter, the creep behavior of amorphous systems is investigated by mesoscopic modeling approaches. The mean-field Hebraud-Lequeux model and the elasto-plastic model are discussed, respectively, in the first and second part of this chapter.

This study is focused on the macroscopic behavior during creep experiments on amorphous systems, i.e. the macroscopic shear rate evolution when a constant macroscopic shear stress is imposed to the system. In experiments, it is mainly observed that (i) the macroscopic shear rate undergoes a power law decay with time $\dot{\gamma}(t) \sim t^{-\mu}$, where the exponent μ depends on the material and the preparation protocol, followed by a rapid increase up to the steady state value that should correspond to the flow curve value at the imposed macroscopic stress, if σ is larger than the macroscopic yield stress σ_y. $\dot{\gamma}(t)$ shows an "S" shape, see the figure 6.1. (ii) The fluidization time scale τ_f scales with the distance to the yield stress, i.e. $\tau_f \sim (\sigma - \sigma_y)^{-\beta}$, the exponent β again dependent on the material and the preparation protocol. (iii) If the imposed stress is smaller than the yield stress, a logarithmic creep is found in the large time limit, i.e. $\dot{\gamma} \sim t^{-1}$ as $t \to \infty$.

Besides, for creep experiments in soft matter systems, the systems are usually pre-sheared according to a well defined protocol, in order to achieve reproducible results. This suggests strongly that the creep behavior depends on the initial condition of the system.

In the following sections, these macroscopic observables are probed by the mesoscopic models using a stress controlled creep protocol. The main discussion will focus on the dependence of the creep behavior on the initial conditions.

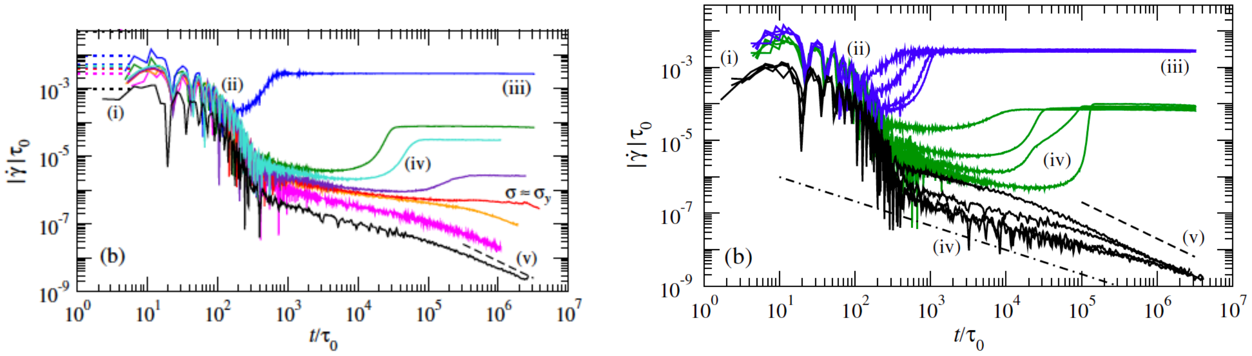

Figure 6.1: Strain rate versus time for different applied stresses across the yield stress in a colloidal glass. Left: Creep for different imposed stresses. Right: the three colors correspond to three different imposed stresses. From the left to the right of the four curves for each imposed the stress, the waiting times are $t_w = 60, 600, 3600, 6000s$, i.e. the age of the sample is increasing [Siebenbürger et al., 2012].

6.1 Creep via the mean-field model

The main framework for the mean-field description of the creep has already exposed in the chapter 4. We recall the model equation here:

$$\partial_t \mathcal{P}(\sigma,t) = -\mu\dot\gamma(t)\partial\mathcal{P}(\sigma,t) + \alpha\Gamma(t)\partial_\sigma^2\mathcal{P}(\sigma,t) + \Gamma(t)\delta(\sigma) - \frac{1}{\tilde\tau}\Theta(|\sigma|-\sigma_c)\mathcal{P}(\sigma,t) \tag{6.1}$$

The stress controlled protocol consists of setting $\dot\gamma(t) = \frac{1}{\mu\tilde\tau}\int d\sigma\Theta(|\sigma|-\sigma_c)\mathcal{P}(\sigma,t)\sigma$, which makes sure that the macroscopic stress $\langle\sigma\rangle = \int d\sigma\sigma\mathcal{P}(\sigma,t)$ stays constant.

The consistency of the stress controlled protocol with the shear rate controlled protocol is checked by comparing the flow curves coming from the two protocols for different values of the model parameter α, as shown in figure 6.2.

Defining the initial condition In the stress controlled version of the model, the evolution of $\mathcal{P}(\sigma,t)$ is automatically determined by the dynamics and the initial condition $\mathcal{P}_o(\sigma) = \mathcal{P}(\sigma, t=0)$. The imposed stress is given by $\langle\sigma\rangle = \sigma^{IMP} = \int d\sigma\sigma\mathcal{P}_o(\sigma)$. Thus the imposed stress is adjusted by varying the shape of $\mathcal{P}_o(\sigma)$ while keeping the mean equal to σ^{IMP}.

A Gaussian distribution of $\mathcal{P}_o(\sigma)$ is chosen for simplicity. The mean of the Gaussian distribution is set to be the imposed stress. The second parameter that defines the Gaussian distribution is the standard deviation. The standard deviation can be interpreted as the aging effect on the system. A more relaxed system, i.e. a system with larger age, is expected to be more homogeneous in its local stress field, which leads to more peaked stress distributions, i.e. a smaller standard deviation.

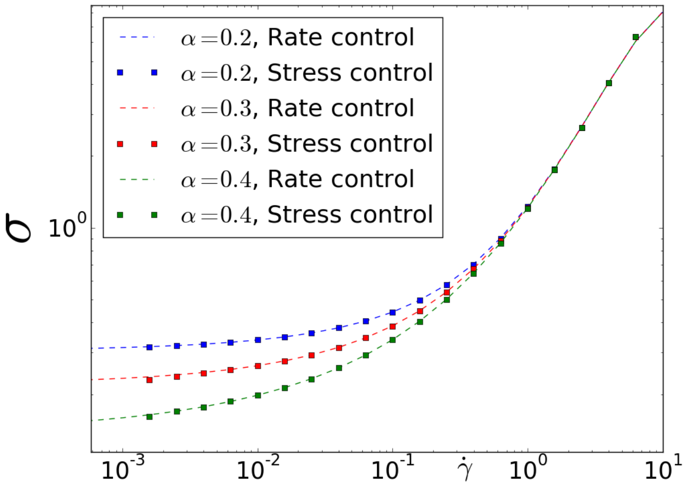

Figure 6.2: The flow curves of the Hebraud-Lequeux model with two protocols are compared. Three values of α are tested.

A less relaxed system, i.e. younger age, for the same reason, should admit a larger stress distribution, i.e. larger standard deviation. By noting *std* for the standard deviation of $\mathcal{P}_o(\sigma)$, the degree of relaxation can be characterized by the inverse of this quantity given by $(std)^{-1}$.

Another model parameter is the α parameter representing the strength of the mechanical coupling between the mechanical noise and the surrounding activity, which also determines the dynamical yield stress, i.e. $\sigma_y(\alpha)$. Given a parameter α, we choose to set a series of $\Delta\sigma = \sigma^{IMP} - \sigma_y(\alpha)$ between 0.1 and 0.3 ($\sigma_c = 1$). The domain of $\Delta\sigma$ is chosen to have a as small as possible lower limit such that the numerical resolution is still reliable and σ^{IMP} still remains in the scaling regime of the flow curve. Technically the numerical cost for a reliable result increases as $\Delta\sigma$ approaches zero.

Three values of α, 0.2, 0.3, 0.4 are chosen. For each value of α the creep behavior is investigated for several standard deviations of the initial condition $\mathcal{P}_o(\sigma)$ and of the distance to the yield stress $\Delta\sigma$.

Method For resolving numerically the partial derivative equation (6.1), a usual finite difference method is adopted. The domain of σ is chosen from -10 to 10, while at $|\sigma| \geq 5$ the $\mathcal{P}(\sigma, t)$ is of order of magnitude $\leq 10^{-9}$. Periodic boundary conditions are used. It is worth noting that for having a stable time integration and a reasonable accumulated error, the time step of the numerical integration δt should be smaller that $(\delta\sigma^2/2)$, where $\delta\sigma$ the finite difference in σ.

To regularize the equations for the numerical integration, the delta function and the step function in the equation (6.1) are replaced by a Gaussian distribution of a very narrow width and hyperbolic functions with very sharp derivatives at $\left|\sigma\right| = \sigma_c = 1$ respectively.

Results

The macroscopic shear rate $\dot{\gamma}(t)$ Interestingly, the macroscopic shear rate $\dot{\gamma}(t)$ as function of time under creep at a fixed shear stress shows a qualitative agreement with experimental results. Typically the non-linear response of the early stage decay and the late sudden increase are reproduced by the imposed stress version of the model. Within the domain of $\Delta\sigma$ that is investigated here, the power law decay does not converge to a unique creep exponent as $\Delta\sigma$ approaches zero. The power law decay regime covers a larger area and the creep exponent μ becomes larger as $\Delta\sigma$ becomes smaller. Among all the value of tested parameters and $\Delta\sigma$, we can identify a creep exponent $\mu \approx 1$ for a specific setting of parameters, as shown in figure 6.3(left), which is not far from the experimental result on the colloidal glass, as shown in figure 6.1.

The dependence of the macroscopic shear rate $\dot{\gamma}(t)$ under creep on the age of the system is also qualitatively captured by 6.3(right) to compare with figure 6.1(right). The fluidization time increases with the age of the system, i.e. more relaxed systems take a longer time to fully fluidize under the imposed stress.

The scaling relations. The fluidization time τ_f is defined here as the inflection point of the creep curve $\dot{\gamma}(t)$, i.e.

$$\frac{d}{dt}\dot{\gamma}\bigg|_{t=\tau_f} = Max(\frac{d}{dt}\dot{\gamma}\bigg|_{t>0}) \tag{6.2}$$

The way τ_f depends on the imposed stress $\Delta\sigma$ for different values of the model parameter α and for different degrees of relaxation of the system, i.e. the standard deviation of $\mathcal{P}_o(\sigma)$, is shown in the figure 6.4.

As shown in figure 6.4, the power law between the fluidization time τ_f and the $\Delta\sigma$ is more pronounced in less relaxed systems, i.e. larger standard deviations, and for weaker coupling strengths. Besides, the scaling exponent β (recalling $\tau_f \sim \Delta\sigma^{-\beta}$) depends on the coupling strength and on the relaxation of the system. The measured exponent β as function of α and *std*, is shown in figure 6.5. However we should keep in mind that β measured for small *std* (well relaxed systems) does not make sense

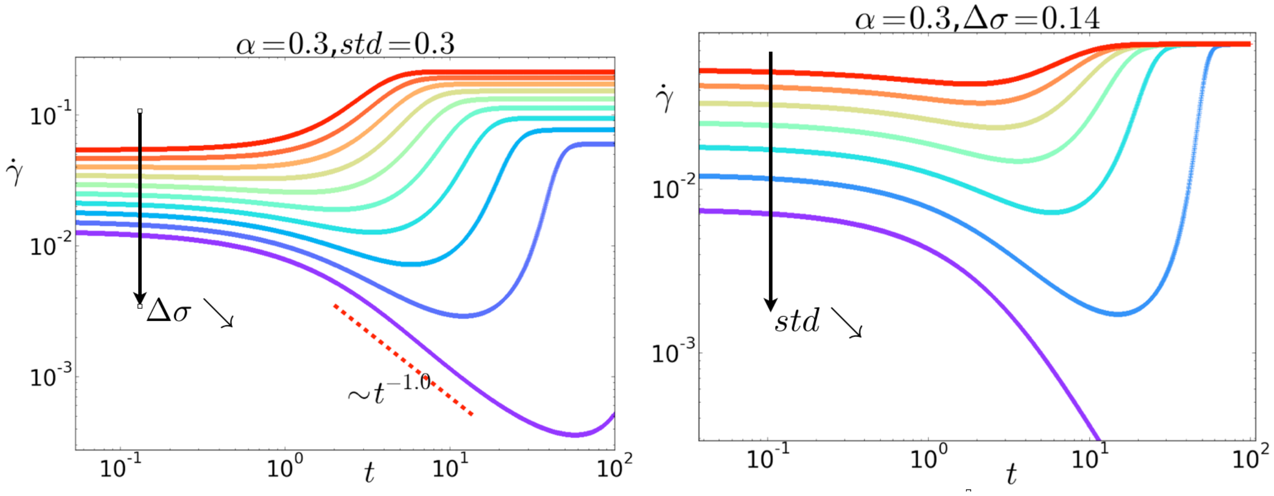

Figure 6.3: Macroscopic shear rate $\langle \dot{\gamma}^{pl} \rangle_{\mathbf{x}}(t)$ as a function of time. Left: Creep for different $\Delta\sigma$ (from top to bottom, $\Delta\sigma = 0.28$, 0.26, 0.24, 0.22, 0.2, 0.18, 0.16, 0.14, 0.12, 0.1) for $\alpha = 0.3$ and the standard deviation of $\mathcal{P}_o(\sigma)$ equal to 0.3; Right: Creep for different standard deviations (from top to bottom, $std = 0.38$, 0.36, 0.34, 0.32, 0.3, 0.28, 0.26) for $\alpha = 0.3$ and $\Delta\sigma = 0.14$.

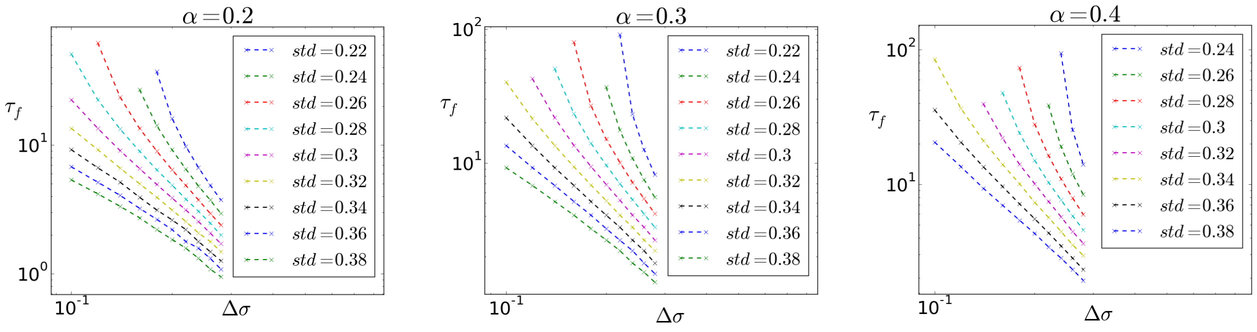

Figure 6.4: The scaling between τ_f and $\Delta\sigma$ for different degrees of relaxation of the system. Right $\alpha = 0.2$; Middle$\alpha = 0.3$; Left $\alpha = 0.4$

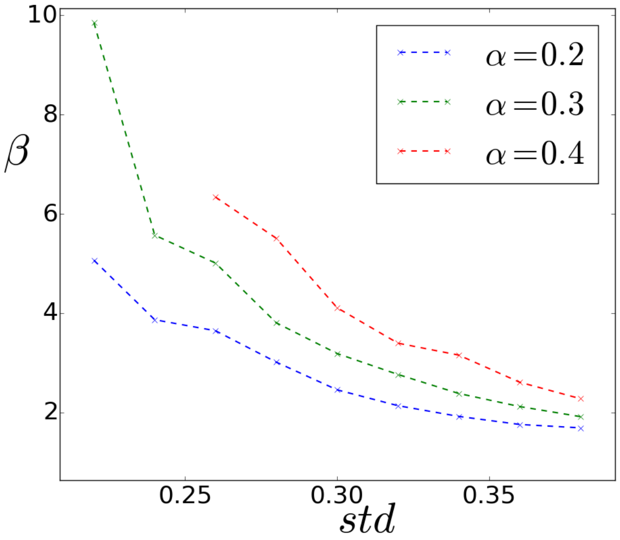

Figure 6.5: β as function of the degree of relaxation of the system characterized by the standard deviation *std* of the initial distribution of the stresses for different coupling strengths.

for the power law but for characterizing how fast the τ_f decreases with $\Delta\sigma$. The larger β is, the faster τ_f decreases with $\Delta\sigma$, i.e. the fluidization time τ_f is more sensitive to $\Delta\sigma$. From the figure 6.5, it can be observed that the fluidization time τ_f is less sensitive to the distance to the yielding point $\Delta\sigma$ for systems of weaker coupling and for systems that are less relaxed.

Conclusion According to the above results, the mechanism of mechanical coupling between noise fluctuations of the local stresses and the plastic activity, is able to reproduce a typical creep behavior and the dependence of the creep on the degree of relaxation of the system. These findings are in good qualitative agreement with experimental observations. As one typical feature for example the “S” shape in the macroscopic shear rate response is reproduced. Further by adjusting the coupling strength and the degree of relaxation, the model reveals that the fluidization time scale becomes less sensitive to the imposed stress as the system is less relaxed or if the different regions inside the system are only weakly coupled mechanically.

Attempt to rationalize the non-linear response in $\dot{\gamma}(t)$ An analysis of effective dynamical equations is performed to gain some qualitative understanding of the non-linear response in $\dot{\gamma}(t)$ under fixed stress, as shown in figure 6.3.

Effective dynamics One can use equation (6.1), with

$$\dot{\gamma} = \frac{1}{\mu\tilde{\tau}} \int \Theta(|\sigma| - \sigma_c)\mathcal{P}(\sigma)\sigma d\sigma$$

$$\Gamma = \frac{1}{\tilde{\tau}} \int \Theta(|\sigma| - \sigma_c)\mathcal{P}(\sigma) d\sigma$$

assuming that at σ_c, $\mathcal{P}(\sigma)$ admits second derivative i.e. $\mathcal{P}''(\sigma = \sigma_c)$ exists. By performing the integral on both sides of the Hebraud-Lequeux equation over $\sigma > \sigma_c$, we can obtain the dynamics of Γ and by multiplying σ on both sides then performing the integral over $\sigma > \sigma_c$, we can obtain the dynamics of $\dot{\gamma}$. As a result, an effective dynamics of $\Gamma(t)$ and $\dot{\gamma}(t)$ is derived in the following expressions:

$$\frac{d}{dt}\dot{\gamma} = A(t)\dot{\gamma} + B(t)\Gamma + \dot{\gamma}\Gamma \tag{6.3}$$

$$\frac{d}{dt}\Gamma = C(t)\dot{\gamma} + D(t)\Gamma \tag{6.4}$$

with $C = \frac{G_0}{\tau}(P_c - P_{-c})$, $D = \frac{\alpha(P'_{-c} - P'_c) - 1}{\tau}$, $A = \frac{(P_{-c} + P_c)\sigma_c - 1}{\tau}$, $B = \frac{\alpha}{\tau G_0}(P_c - P_{-c} - \sigma_c(P'_{-c} + P'_c))$ and where $P_c(t) \hat{=} \mathcal{P}(\sigma_c, t)$, $P_{-c}(t) \hat{=} \mathcal{P}(-\sigma_c, t)$, $P'_c(t) \hat{=} \partial_\sigma \mathcal{P}(\sigma_c, t)$, $P'_{-c}(t) \hat{=} \partial_\sigma \mathcal{P}(-\sigma_c, t)$.

The equation (6.3) and (6.4) constitute an effective dynamical system of the state variable $(\dot{\gamma}, \Gamma)$, while the coefficients A, B, C, D vary in time.

Instantaneous dynamical flow The instantaneous velocity of $\dot{\gamma}$ and Γ is then determined by the instantaneous dynamical flow of the effective dynamics defined by the coefficients $A(t)$, $B(t)$, $C(t)$, $D(t)$, while the evolution of the coefficients are determined by the full dynamics equation (6.1). Therefore the effective dynamical equations above are not closed equations describing the full dynamics.

The evolution of $\dot{\gamma}$ and Γ can then be regarded as the time integration of their instantaneous velocity according to the effective dynamics determined by the coefficients A, B, C, D varying in time. For testing this idea, the coefficients A, B, C, D as well as the $\dot{\gamma}(t)$ and $\Gamma(t)$ are recorded during a simulation of the full Hebraud-Lequeux model. Then the recorded time series of A, B, C, D and the initial values $\dot{\gamma}_o = \dot{\gamma}(t = 0)$ and $\Gamma_o = \Gamma(t = 0)$ are injected into the effective dynamical equations (6.3) (6.4) for computing the "effective dynamic" time series of $\dot{\gamma}_{ed}(t)$ and $\Gamma_{ed}(t)$, which are then, together with $\dot{\gamma}(t)$ and $\Gamma(t)$, plotted in the same figure 6.6(right). It can be seen that they agree very well.

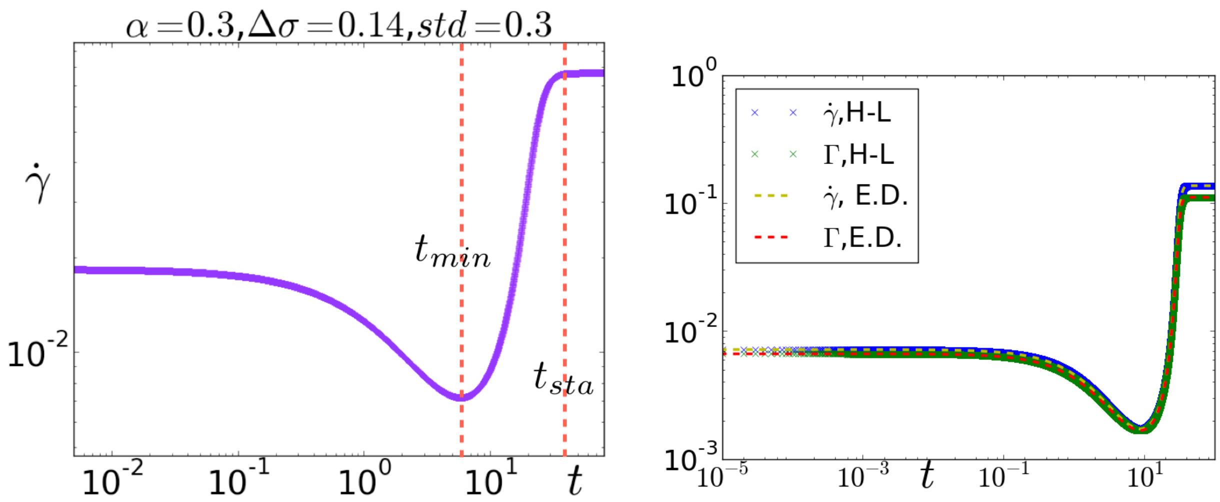

Figure 6.6: Left: A typical macroscopic shear rate response to an imposed stress. Three regimes are separated by two time scales t_{min} and t_{sta}. Right: Validation of the idea of the effective dynamics.

From the macroscopic shear rate response $\dot{\gamma}(t)$, we can identify three regimes, separated by two time scales t_{min} and t_{sta}, see the figure6.6(left). The time t_{min} is defined as the moment where $\dot{\gamma}(t)$ reaches the minimum and t_{sta} is the moment where the system enters the stationary state. The three regimes are (i) the decaying regime, $t < t_{min}$; (ii) the increasing regime, $t_{min} < t < t_{sta}$; (iii) and the stationary regime, $t > t_{sta}$.

At any given time, it is interesting to study the stability of the effective dynamical system as if the coefficients were fixed in time with respect to regimes for a qualitative understanding of the non linear behavior of the shear rate $\dot{\gamma}(t)$, especially for the first two regimes where the assumption is that the coefficients evolve more slowly than the variables themselves . The fictitious dynamical system obtained for fixed coefficients A, B, C and D has two fixed points, with a stability that depends on the values of the coefficients.

At any instant t, the effective dynamical system admits two fixed points:

$$\Gamma_{s,1} = 0, \dot{\gamma}_{s,1} = 0 \tag{6.5}$$

and

$$\Gamma_{s,2}(t) = \frac{C(t)B(t)}{D(t)} - A(t), \dot{\gamma}_{s,2}(t) = \frac{A(t)D(t)}{C(t)} - B(t) \tag{6.6}$$

The stability analysis of the two instantaneous solutions is given in the Appendix E using the method of linearization around the fixed points. The dynamical flow of the effective dynamical system within the three regimes are shown respectively in figure 6.7.

(i) In the decaying regime $t < t_{min}$, the zero fixed point is stable, all states around zero are attracted toward the origin, which leads to the decay of $\dot{\gamma}(t)$ and $\Gamma(t)$, see the figure 6.7(left); (ii) In the increasing regime $t_{min} < t < t_{sta}$, the zero fixed point becomes unstable and the far away non zero fixed point $\dot{\gamma}_{s,2} > 0$, $\Gamma_{s,2} > 0$ becomes stable. The actual state $\big(\dot{\gamma}(t), \Gamma(t)\big)$ lies in between the two fixed point following a velocity towards the non zero fixed point, which gives rise of the increase of $\dot{\gamma}$ and Γ, see the figure 6.7(right).

When running the complete model, one observes that the transition from the decay to the increase of the variation of the shear rate corresponds to an exchange of stability of the fixed points due to the actual time evolution of the coefficients A, B, C and D, thus the system first appears to converge to the zero fixed point, then departs from it rapidly.

(iii) In the stationary regime $t > t_{sta}$, the zero fix point is stable and the non-zero one is unstable. The only true fix point derived from the effective dynamics is the zero fix point, whereas the stability of the steady state solution must be tested using the whole formalism, i.e. the equation (6.1), the effective dynamics is not sufficient. However when analyzing the effective dynamics one can observe that at the beginning of the stationary regime, the dynamical flow changes rapidly from pointing outward from the origin to pointing inward towards the origin, while the non-zero fixed point of the effective dynamics moves (remember the time dependence of the coefficients) much faster than the actual state $\big(\dot{\gamma}(t), \Gamma(t)\big)$. Very quickly, the non-zero fixed point catches up with the actual state, and finally the system state point $\big(\dot{\gamma}(t), \Gamma(t)\big)$ remains on the non-zero fixed point and stays there forever, as shown in the figure 6.7(bottom).

That the stationary state cannot be analyzed in the same way as in the first two regimes may be related to the fact that now everything A, B, C, D, $\dot{\gamma}$, Γ evolves on comparable time scales so that describing things with the effective equations becomes meaningless. This has to be investigated further in the future.

Conclusion The effective dynamics can be used to rationalize the different trends the non-linear response of the macroscopic shear rate to an imposed stress. However this method is limited to a qualitative analysis and does not allow for quantitative predictions.

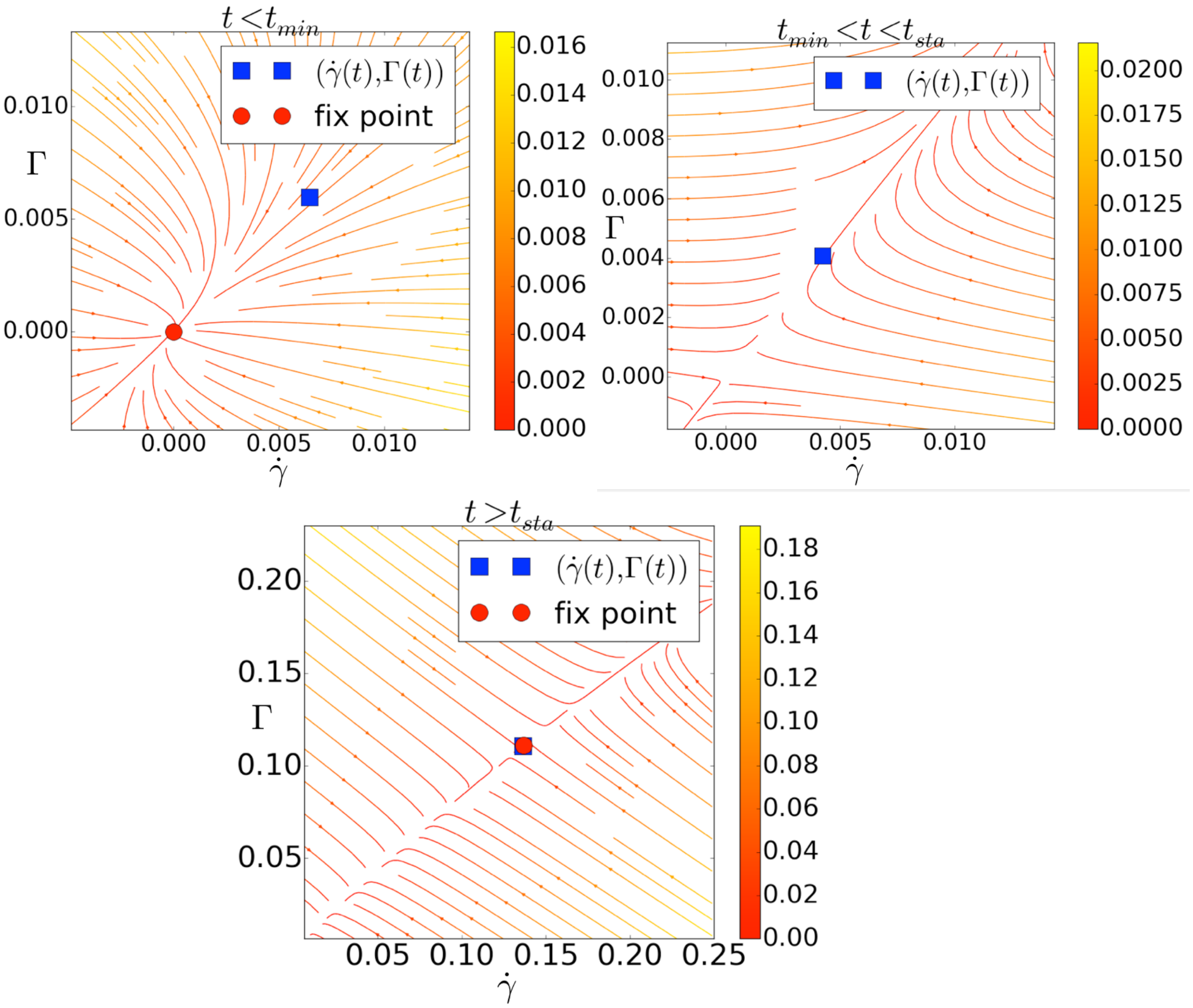

Figure 6.7: The stream lines of the effective dynamical system at time t; Blue square: the actual state $\big(\dot{\gamma}(t), \Gamma(t)\big)$; Red circle: the relevant fixed point of the effective dynamic system; Left: $t < t_{min}$; Right: $t_{min} < t < t_{sta}$; Bottom: $t > t_{sta}$.

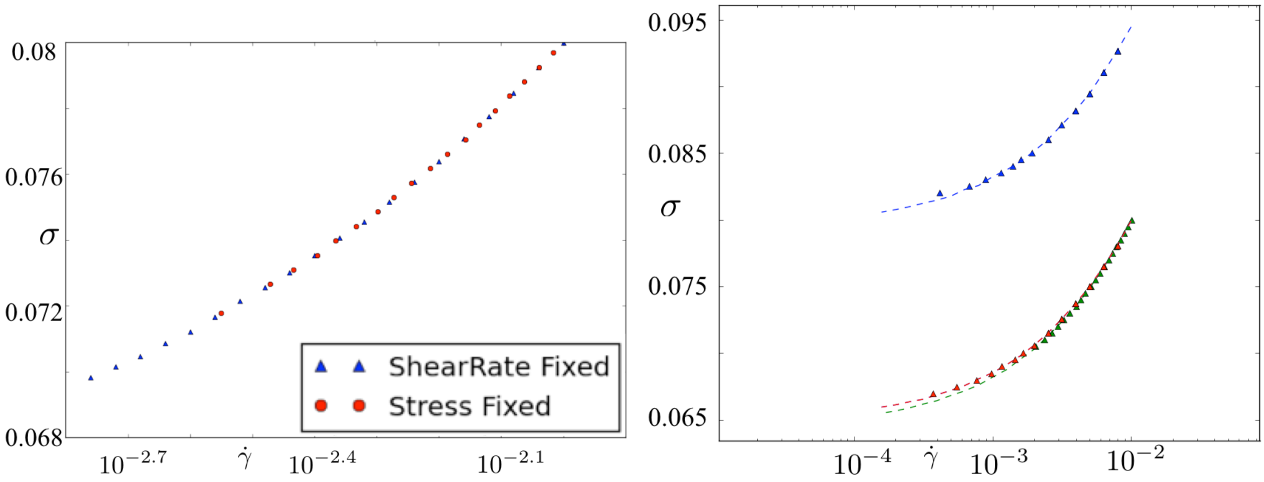

Figure 6.8: Left: The flow curves obtained from the stress controlled protocol and from the shear rate controlled protocol with $\mathcal{P}_Y(\sigma^Y)$ being a Rayleigh distribution. Right: Dashed lines: shear rate control protocol; Triangles: stress control protocol; Blue: $\mathcal{P}_Y(\sigma^Y)$ uniform distribution; Red: Gaussian; Green: Rayleigh. The Herschel-Bulkley fitting exponent $n \approx 0.58$ for the uniform distribution and $n \approx 0.57$ for both the Gaussian and Rayleigh distribution

6.2 Creep via the elasto-plastic model

Modeling the mechanical coupling of different mesoscopic regions as a diffusion of the local stress, according to the analysis of the mechanical noise in the chapter 5, is only valid at a relatively high shear rate, corresponding to a relatively high imposed stress. For a more realistic spatially resolved description of the creep behavior of amorphous systems, the elasto-plastic model using the fixed stress protocol is studied. The study of the creep of amorphous systems by the elasto-plastic model in this section is done only for two-dimensional systems. A couple of preliminary results of the creep dynamics of the elasto-plastic model are presented in the following.

The stress controlled protocol of the elasto-plastic model was introduced in chapter 4. It is worth recalling that, in the stress controlled protocol, the macroscopic shear rate is equivalent to the macroscopic plastic shear rate, i.e. $\dot{\gamma}(t) = \langle \dot{\gamma}^{pl} \rangle_{\mathbf{x}}(t)$.

Before discussing the creep behavior of the elasto-plastic model, the consistency between the stress control protocol and shear rate control protocol is verified by comparing the flow curves produced by the two protocols. The steady state flow curves of the two protocols are in agreement, see figure 6.8.

Defining the initial condition of the elasto-plastic model Given the dynamical rules, the initial condition of the elasto-plastic model is defined by the initial plastic interface $\gamma^{pl}(\mathbf{x}, t = 0)$, which gives the initial internal stress field through

$\sigma^{INT}(\mathbf{x}) = \mu G^N(\mathbf{x}) * \gamma^{pl}(\mathbf{x})$ and the initial local yield stress field $\sigma^Y(\mathbf{x}, t = 0)$ which is chosen for each site independently from a probability distribution $\mathcal{P}_Y(\sigma^Y)d\sigma^Y$. Together with the imposed stress $\langle\sigma\rangle_{\mathbf{x}} = \sigma^{EXT} = \sigma^{IMP}$, $\sigma^{INT}(\mathbf{x})$ and $\sigma^Y(\mathbf{x})$ determine how many plastic events will occur and where these plastic events will be activated. Once this first step of activation at time $t = 0$ is determined, the following behavior at $t > 0$ is automatically determined by the dynamics of the model.

Since in studies using molecular dynamics of quenched glassy systems, no spatial correlations of either the local stress or the local yield stress (the measurement of the later one is still under investigation, the last result is found in reference [Patinet et al., 2016]) has been found, the spatial correlations are also discarded in this study, which implies that the spatial distribution of the first step of activation of plastic events has no specific structure and is almost homogeneous over the system. In this case, the initial condition is effectively only determined by the probability distribution $\mathcal{P}(x)$, where $x \hat{=} \sigma^Y(\mathbf{x}) - \sigma(\mathbf{x})$. The sites of negative x are almost uniformly distributed over the system, and will be the activated at time zero $t = 0$.

To simplify the numerical implementation of the initial condition, we choose to make the initial plastic interface flat which makes the internal stress uniformly zero and we choose to change the initial condition by changing the probability distribution of local yield stresses $\mathcal{P}_Y(\sigma^Y)$. By applying the external stress as the imposed stress $\sigma^{EXT} = \sigma^{IMP}$ leading to $\mathcal{P}(x) \equiv \mathcal{P}_Y(x + \sigma^{IMP})$, a spatially uniformly distributed portion $P = \int_{-\infty}^{0} \mathcal{P}(x)dx$ of all sites of the system are activated at $t = 0$.

The functional forms of the probability distribution of local yield stresses that are tested for simulating the creep of amorphous systems are the followings: (1) uniform distribution; (2) Gaussian distribution and (3) Rayleigh distribution, introduced in chapter 4. All these three forms of probability distributions are set to the same mean and the same variance for the results to be comparable.

To confirm that the specific form of the local yield stress distribution does not lead to a drastic change in the dynamics, the flow curves of the dynamics for all three types of $\mathcal{P}_Y(\sigma^Y)$ using both stress control and shear rate control protocols are compared, see the figure 6.8(right). The Herschel-Bulkley exponent is not sensitive to $\mathcal{P}_Y(\sigma^Y)$, which confirms that the dynamics is neither.

Results

The macroscopic shear rate $\dot{\gamma}(t)$ The macroscopic shear rate $\dot{\gamma} = \langle\dot{\gamma}^{pl}\rangle_{\mathbf{x}}(t)$ as function of time for a number of imposed stresses close to the dynamical yield stress for the three type of $\mathcal{P}_Y(\sigma^Y)$ are shown in the figure 6.9.

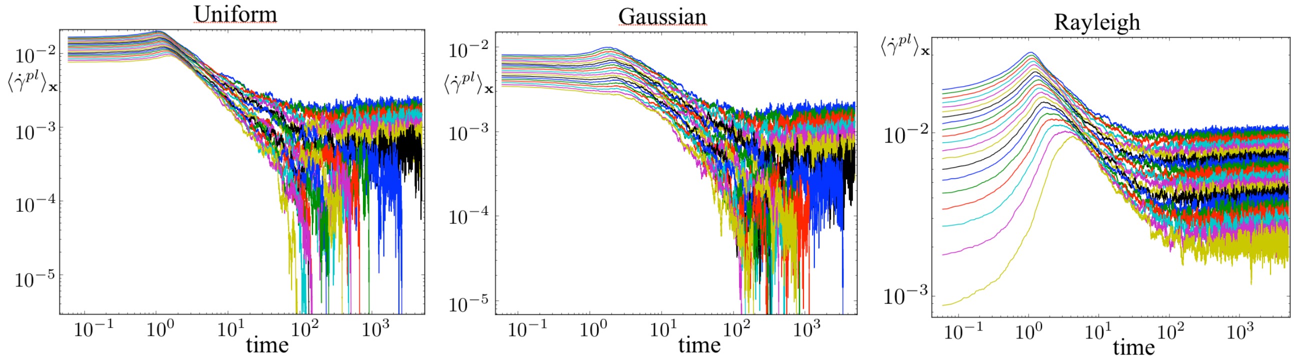

Figure 6.9: Macroscopic shear rate$\langle\dot{\gamma}^{pl}\rangle_{\mathbf{x}}(t)$ as function of time for three types of $\mathcal{P}_Y(\sigma^Y)$. The imposed stress decreases from the top to the bottom in each figure. Left: $\mathcal{P}_Y(\sigma^Y)$ uniform; Middle: $\mathcal{P}_Y(\sigma^Y)$ Gaussian; Right: $\mathcal{P}_Y(\sigma^Y)$ Rayleigh

The behavior for uniform and Gaussian distributions of $\mathcal{P}_Y(\sigma^Y)$ appear quite similar. The macroscopic shear rate starts with plateau, then decays as a power law, and finally reaches the shear rate of the stationary state corresponding to the imposed shear stress. For the small stresses, some of the shear rates suddenly go to zero due to finite size effects. The behavior of the Rayleigh distribution differs slightly from the others, but only in the early stages, where the shear rate starts with a remarkable increase. However in all of these cases, the "S" shape, that was found in the mean-field description, does not appear here.

The scaling relations For all the three types of probability distributions of $\mathcal{P}_Y(\sigma^Y)$, it is possible to collapse the decaying and the stationary parts of all the curves $\dot{\gamma}(t)$ by rescaling the shear rate with $\dot{\gamma} \to \dot{\gamma}/\dot{\gamma}_s$ where $\dot{\gamma}_s$ indicates the shear rate of the stationary state for the corresponding shear stress, and by rescaling the time with $t \to t/\dot{\gamma}_s^{-\alpha_c}$ with $\alpha_c \approx 1.25$. See the figure 6.10. This suggests that the fluidization time $\tau_f \sim \dot{\gamma_s}^{-\alpha_c}$, which, together with the Herschel-Bulkley law $\dot{\gamma}_s \sim (\sigma - \sigma_y)^{\frac{1}{n}}$, implies that $\tau_f \sim (\sigma - \sigma_y)^{-\beta_c}$ with $\beta_c = \alpha_c/n \approx 1.25/0.57 \approx 2.2$. Let us just mention that in experiments on carbopol gel systems the exponent β_c is found to reside between $3 \sim 8$ depending on the preparation protocol.

A power law decay can be identified from the rescaled macroscopic shear rate creep curves in the figure 6.10. The decaying exponent μ is measured to be close to 0.5, i.e.$\dot{\gamma} \sim t^{-\mu}$ with $\mu \approx 0.5$, for the Gaussian distribution and the uniform distribution of $\mathcal{P}_Y$ and slightly smaller than 0.5 for the Rayleigh distribution. The measured exponent $\mu \approx 0.5$ is not too far from the decaying exponent measured for the carbopol gel, which is given to be approximately 2/3.

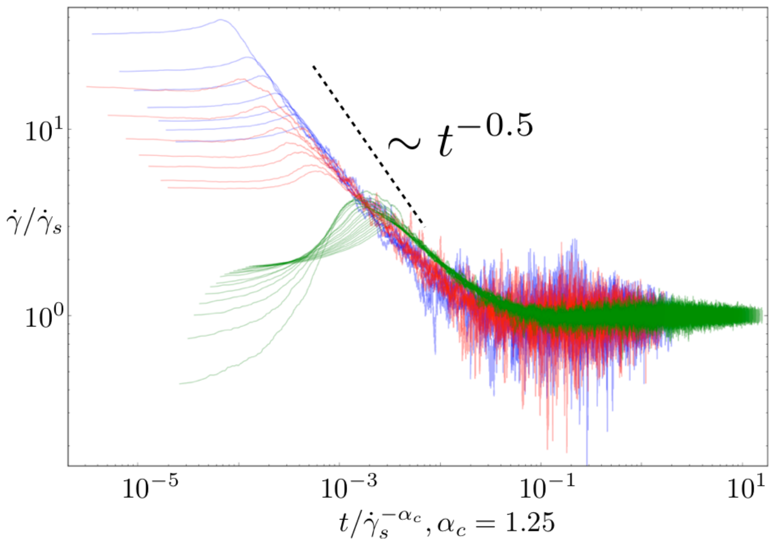

Figure 6.10: The rescaled macroscopic shear rate $\dot{\gamma}/\dot{\gamma}_s$ as function of the rescaled time $t/\dot{\gamma}^{-\alpha_c}$, $\alpha_c \approx 1.25$.

Conclusion By a simple mechanical coupling mechanism, i.e. plastic events interact with each other through the elastic medium through the Eshelby propagator, the elasto-plastic model can qualitatively reproduce the scaling relations in the creep experiments of amorphous systems.

However to reproduce the “S” shape in the macroscopic shear rate and to obtain more quantitatively comparable results, a more sophisticated way for defining the initial condition is required. One way is to compare carefully the elasto-plastic model with the molecular dynamics [Sentjabrskaja et al., 2015, Chaudhuri and Horbach, 2013] to obtain a more realistic representation of the initial condition, e.g. the initial stress distribution and the initial threshold distribution.

Chapter 7

Outlook

During this thesis, the elasto-plastic model has been used to study the yielding transition of athermal amorphous systems. Signatures of critical dynamics close to a dynamical phase transition are revealed by the investigation of the statistics of avalanches in the zero shear rate limit. The idea that the jerky motion of the macroscopic stress under external shearing results from the composition of individual avalanches, where the term "individual avalanche" refers to a spatio-temporal domain related by cooperative dynamics, is supported by the study of the stress drop shapes and the study of the macroscopic stress fluctuations. Finally it is shown that the elasto-plastic model version for externally applied stress reproduces a creep behavior that agrees qualitatively well with typical experimental data.

Despite the success of the elasto-plastic model for describing the mechanical behavior of amorphous systems, the dynamics of the model under different loading conditions, i.e. stress control or rate control and the distance to the yielding point, is not completely understood. Understanding the activation dynamics of the elasto-plastic model should be an important step forward for revealing the nature of plasticity in amorphous systems. Comparing results from molecular dynamics simulations and experiments with the activation dynamics of the elasto-plastic model will lead to either a validation or means to enhance the ingredients adopted in the mesoscopic elasto-plastic approach. A specific question would be, in which sense, the activation dynamics of the elasto-plastic model under quasi-static shear is consistent with the process of hopping from one meta-stable basin to another in the molecular dynamic systems under athermal quasi-static shear.

The study of the macroscopic stress fluctuation in this thesis provides a clue for a deeper understanding of the cooperative dynamics. More system sizes and lower shear rates in both two dimensional and three dimensional systems should be tested for revealing how the cooperative length scales with the applied shear rate. Some remaining questions are the question of what is the origin of the apparent Brownian dynamics for the velocity of the macroscopic plastic strain rate below the saturation time scale and why does the saturation time depend on the system size when smaller than the cooperative length in such a way. Answering these questions may provide explications for the shear rate dependent cutoff in the stress drop duration distribution function in our study of the statistics of avalanches.

As mentioned earlier, for now the elasto-plastic model can not produce the typical "S" shape in the creep curve. It is argued in the chapter 6 that the initial condition strongly affects the creep behavior. Usually these initial conditions are created by a pre-shearing protocol in the experiments for guaranteeing reproducible results. A direct characterization at the level of the structure, stress field, etc, and the link of this characterization with the creep behavior are very scarce. This can be tackled on one hand by the elasto-plastic model, concretely by systematically tuning the initial stress field and studying how the creep behavior is affected by this tuning, and on the other hand by taking the initial condition from actual molecular dynamics simulations for a quenched amorphous system. Like this one can try to understand how this initial conditions affect the creep behavior through its build-in dynamics.

Up to now, we are always talking about the athermal elasto-plastic model and its properties. A way for introducing the thermal activation of plastic events is by introducing an additional probability for activating plastic regions $\propto \exp(-D/T)$, where T representing the temperature, and D for the free energy barrier of local plastic rearrangement [Bulatov and Argon, 1994]. The issue of what is the most adequate way for introducing temperature in the elasto-plastic model is still under debate. By introducing the thermal activation, various phenomena under the thermal effect can be addressed. For example the rheology of amorphous system under finite temperature using the modified elasto-plastic model has been tested during this thesis, it is not presented in a separate chapter because the results remain still very preliminary. One short presentation of the rheology under finite temperature is shown in the figure 7.1. At zero temperature, the Herschel-Bulkley law with exponent ≈ 0.5 is recovered. As the temperature increases, the system changes from a shear thinning material to a shear thickening material.

Even though the mesoscopic elasto-plastic model is more likely a very phenomenological model involving a set of parameters which are difficult to access experimentally, it contains the main ingredients of the mechanism of the plasticity of amorphous system coming from realistic systems. Understanding how the

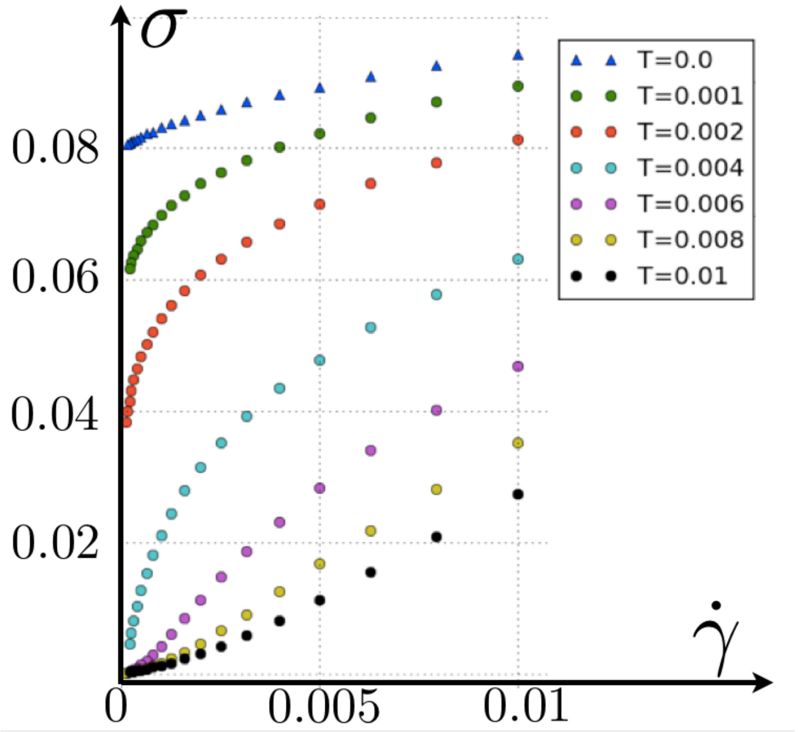

Figure 7.1: Flow curves at different temperatures, stress versus shear rate. The temperature increases from the top to the bottom.

basic mechanisms work together giving rise to non-trivial properties is an important task to make progress in the study of the mechanical properties of amorphous systems, and there still remain many aspects to be understand and studied for the future.

References

Agoritsas, Elisabeth, Bertin, Eric, Martens, Kirsten, and Barrat, Jean-Louis. On the relevance of disorder in athermal amorphous materials under shear. *Eur. Phys. J. E*, 38(7):71, 2015. doi: 10.1140/epje/i2015-15071-x. URL `http://dx.doi.org/10.1140/epje/i2015-15071-x`.

T Albaret, A Tanguy, F Boioli, and D Rodney. Mapping between atomistic simulations and eshelby inclusions in the shear deformation of an amorphous silicon model. *Physical Review E*, 93(5):053002, 2016.

Axelle Amon, Ary Bruand, Jérôme Crassous, Eric Clément, et al. Hot spots in an athermal system. *Physical review letters*, 108(13):135502, 2012.

James Antonaglia, Wendelin J. Wright, Xiaojun Gu, Rachel R. Byer, Todd C. Hufnagel, Michael LeBlanc, Jonathan T. Uhl, and Karin A. Dahmen. Bulk metallic glasses deform via slip avalanches. *Physical Review Letters*, 112(15), 2014. ISSN 0031-9007. URL `<Go to ISI>://WOS:000337352600015`.

A. Arbe, D. Richter, J. Colmenero, and B. Farago. Merging of the α and β relaxations in polybutadiene: A neutron spin echo and dielectric study. *Phys. Rev. E*, 54:3853–3869, Oct 1996. doi: 10.1103/PhysRevE.54.3853. URL `http://link.aps.org/doi/10.1103/PhysRevE.54.3853`.

AS Argon. Plastic deformation in metallic glasses. *Acta metallurgica*, 27(1):47–58, 1979.

Nicholas P Bailey, Jakob Schiøtz, Anaël Lemaître, and Karsten W Jacobsen. Avalanche size scaling in sheared three-dimensional amorphous solid. *Physical review letters*, 98(9):095501, 2007.

Jean-Christophe Baret, Damien Vandembroucq, and Stéphane Roux. Extremal model for amorphous media plasticity. *Phys. Rev. Lett.*, 89:195506, Oct 2002. doi: 10.1103/PhysRevLett.89.195506. URL `http://link.aps.org/doi/10.1103/PhysRevLett.89.195506`.

H. Barkhausen. Zwei mit hilfe der neuen verstaerker entdeckte erscheinugen. *Physik Z.*, 20:401–403, 1917.

Lydiane Bécu, Sébastien Manneville, and Annie Colin. Yielding and flow in adhesive and nonadhesive concentrated emulsions. *Physical review letters*, 96(13):138302, 2006.

Ludovic Berthier and Giulio Biroli. Theoretical perspective on the glass transition and amorphous materials. *Rev. Mod. Phys.*, 83: 587–645, Jun 2011. doi: 10.1103/RevModPhys.83.587. URL `http://link.aps.org/doi/10.1103/RevModPhys.83.587`.

Kurt Binder and Walter Kob. *Glassy materials and disordered solids: An introduction to their statistical mechanics*. World Scientific, 2011.

Lydéric Bocquet, Annie Colin, and Armand Ajdari. Kinetic theory of plastic flow in soft glassy materials. *Physical review letters*, 103(3):036001, 2009.

D. Bonamy, S. Santucci, and L. Ponson. Crackling dynamics in material failure as the signature of a self-organized dynamic phase transition. *Phys. Rev. Lett.*, 101:045501, Jul 2008. doi: 10.1103/PhysRevLett.101.045501. URL `http://link.aps.org/doi/10.1103/PhysRevLett.101.045501`.

Daniel Bonn, Jose Paredes, Morton M Denn, Ludovic Berthier, Thibaut Divoux, and Sébastien Manneville. Yield stress materials in soft condensed matter. *arXiv preprint arXiv:1502.05281*, 2015.

Jean-Philippe Bouchaud. Weak ergodicity breaking and aging in disordered systems. *Journal de Physique I*, 2(9):1705–1713, 1992.

Zoe Budrikis and Stefano Zapperi. Avalanche localization and crossover scaling in amorphous plasticity. *Phys. Rev. E*, 88: 062403, Dec 2013. doi: 10.1103/PhysRevE.88.062403. URL `http://link.aps.org/doi/10.1103/PhysRevE.88.062403`.

VV Bulatov and AS Argon. Stochastic continuum simulations of structural relaxations in solids. *Journal of non-crystalline solids*, 172:876–883, 1994.

Isabelle Cantat and Olivier Pitois. Stokes experiment in a liquid foam. *Physics of Fluids (1994-present)*, 18(8):083302, 2006.

Pinaki Chaudhuri and Jürgen Horbach. Onset of flow in a confined colloidal glass under an imposed shear stress. *Physical Review E*, 88(4):040301, 2013.

V Chikkadi and P Schall. Nonaffine measures of particle displacements in sheared colloidal glasses. *Physical Review E*, 85(3):031402, 2012.

V Chikkadi, S Mandal, B Nienhuis, D Raabe, F Varnik, and P Schall. Shear-induced anisotropic decay of correlations in hard-sphere colloidal glasses. *EPL (Europhysics Letters)*, 100(5):56001, 2012.

Vijayakumar Chikkadi, Gerard Wegdam, Daniel Bonn, Bernard Nienhuis, and Peter Schall. Long-range strain correlations in sheared colloidal glasses. *Physical review letters*, 107(19):198303, 2011.

Philippe Coussot, Laurent Tocquer, C Lanos, and Guillaume Ovarlez. Macroscopic vs. local rheology of yield stress fluids. *Journal of Non-Newtonian Fluid Mechanics*, 158(1):85–90, 2009.

Karin A Dahmen, Yehuda Ben-Zion, and Jonathan T Uhl. Micromechanical model for deformation in solids with universal predictions for stress-strain curves and slip avalanches. *Physical review letters*, 102(17):175501, 2009.

Karin A Dahmen, Yehuda Ben-Zion, and Jonathan T Uhl. A simple analytic theory for the statistics of avalanches in sheared granular materials. *Nature Physics*, 7 (7):554–557, 2011. doi: 10.1038/nphys1957.

Y.N. Dastur and W.C. Lesley. Mechanism of work hardening hadfield manganese steel. *Metall. Trans. A.*, 12, 1981.

Pablo G Debenedetti and Frank H Stillinger. Supercooled liquids and the glass transition. *Nature*, 410(6825):259–267, 2001.

Michael Dennin. Statistics of bubble rearrangements in a slowly sheared two-dimensional foam. *Physical Review E*, 70(4):041406, 2004.

Thibaut Divoux, David Tamarii, Catherine Barentin, and Sébastien Manneville. Transient shear banding in a simple yield stress fluid. *Physical review letters*, 104 (20):208301, 2010.

Thibaut Divoux, Catherine Barentin, and Sébastien Manneville. From stress-induced fluidization processes to herschel-bulkley behaviour in simple yield stress fluids. *Soft Matter*, 7(18):8409–8418, 2011.

Thibaut Divoux, David Tamarii, Catherine Barentin, Stephen Teitel, and Sébastien Manneville. Yielding dynamics of a herschel–bulkley fluid: A critical-like fluidization behaviour. *Soft Matter*, 8(15):4151–4164, 2012.

DJ Durian. Foam mechanics at the bubble scale. *Physical review letters*, 75(26): 4780, 1995.

G. Durin and S. Zapperi. The barkhausen effect. In G. Bertotti and I. Mayergoyz, editors, *The Science of Hysteresis*, pages 181–267. Elsevier, Amsterdam, 2006.

Gianfranco Durin and Stefano Zapperi. Scaling exponents for barkhausen avalanches in polycrystalline and amorphous ferromagnets. *Phys. Rev. Lett.*, 84:4705–4708, May 2000. doi: 10.1103/PhysRevLett.84.4705. URL `http://link.aps.org/doi/10.1103/PhysRevLett.84.4705`.

John D Eshelby. The determination of the elastic field of an ellipsoidal inclusion, and related problems. In *Proceedings of the Royal Society of London A: Mathematical, Physical and Engineering Sciences*, volume 241, pages 376–396. The Royal Society, 1957.

ML Falk and JS Langer. Dynamics of viscoplastic deformation in amorphous solids. *Physical Review E*, 57(6):7192, 1998.

Abdoulaye Fall, Jose Paredes, and Daniel Bonn. Yielding and shear banding in soft glassy materials. *Phys. Rev. Lett.*, 105: 225502, Nov 2010. doi: 10.1103/PhysRevLett.105.225502. URL `http://link.aps.org/doi/10.1103/PhysRevLett.105.225502`.

Ezequiel Ferrero, Agoritsas Elisabeth, Liu Chen, Bertin Eric, and Martens Kirsten. Mechanical noise in amorphous systems: from the mean-field to non mean-field. *To be submitted*, 2016.

Ezequiel E Ferrero, Sebastian Bustingorry, Alejandro B Kolton, and Alberto Rosso. Numerical approaches on driven elastic interfaces in random media. *Comptes Rendus Physique*, 14(8):641–650, 2013.

Thomas Gibaud, Damien Frelat, and Sébastien Manneville. Heterogeneous yielding dynamics in a colloidal gel. *Soft Matter*, 6(15):3482–3488, 2010.

Julian H Gibbs and Edmund A DiMarzio. Nature of the glass transition and the glassy state. *The Journal of Chemical Physics*, 28(3):373–383, 1958.

I Goldhirsch and C Goldenberg. On the microscopic foundations of elasticity. *The European Physical Journal E*, 9(3):245–251, 2002.

V Gopalakrishnan and CF Zukoski. Delayed flow in thermo-reversible colloidal gels. *Journal of Rheology (1978-present)*, 51(4):623–644, 2007.

J Goyon, A Colin, G Ovarlez, A Ajdari, and L Bocquet. Spatial cooperativity in soft glassy flows. *Nature*, 454(7200):84–87, 2008.

Vincent Grenard, Thibaut Divoux, Nicolas Taberlet, and Sébastien Manneville. Timescales in creep and yielding of attractive gels. *Soft matter*, 10(10):1555–1571, 2014.

Jean-Pierre Hansen and Ian R McDonald. *Theory of simple liquids*. Elsevier, 1990.

P. Hébraud and F. Lequeux. Mode-coupling theory for the pasty rheology of soft glassy materials. *Phys. Rev. Lett.*, 81:2934–2937, Oct 1998. doi: 10.1103/PhysRevLett.81.2934. URL `http://link.aps.org/doi/10.1103/PhysRevLett.81.2934`.

Jürgen Horbach and Walter Kob. Static and dynamic properties of a viscous silica melt. *Phys. Rev. B*, 60:3169–3181, Aug 1999. doi: 10.1103/PhysRevB.60.3169. URL `http://link.aps.org/doi/10.1103/PhysRevB.60.3169`.

Jürgen Horbach and Walter Kob. Relaxation dynamics of a viscous silica melt: The intermediate scattering functions. *Phys. Rev. E*, 64:041503, Sep 2001. doi: 10.1103/PhysRevE.64.041503. URL `http://link.aps.org/doi/10.1103/PhysRevE.64.041503`.

JH Irving and John G Kirkwood. The statistical mechanical theory of transport processes. iv. the equations of hydrodynamics. *The Journal of chemical physics*, 18(6):817–829, 1950.

KE Jensen, David A Weitz, and F Spaepen. Local shear transformations in deformed and quiescent hard-sphere colloidal glasses. *Physical Review E*, 90(4):042305, 2014.

Gyan P Johari and Martin Goldstein. Viscous liquids and the glass transition. ii. secondary relaxations in glasses of rigid molecules. *The Journal of chemical physics*, 53(6):2372–2388, 1970.

Walter Kauzmann. The nature of the glassy state and the behavior of liquids at low temperatures. *Chemical Reviews*, 43(2):219–256, 1948.

W Klement, RH Willens, and POL Duwez. Non-crystalline structure in solidified gold–silicon alloys. 1960.

Lev D Landau and EM Lifshitz. Theory of elasticity, vol. 7. *Course of Theoretical Physics*, 3:109, 1986.

John Lauridsen, Michael Twardos, and Michael Dennin. Shear-induced stress relaxation in a two-dimensional wet foam. *Physical review letters*, 89(9):098303, 2002.

Lasse Laurson, Stephane Santucci, and Stefano Zapperi. Avalanches and clusters in planar crack front propagation. *Physical Review E*, 81(4):046116, 2010.

Lasse Laurson, Xavier Illa, Stephane Santucci, Ken Tore Tallakstad, Knut Jorgen Maloy, and Mikko J. Alava. Evolution of the average avalanche shape with the universality class. *Nature Communications*, 4, 2013. ISSN 2041-1723. URL `<Go to ISI>://WOS:000329396500013`.

J. F. Nye Lawrence Bragg. A dynamical model of a crystal structure. *Proceedings of the Royal Society of London. Series A, Mathematical and Physical Sciences*, 190(1023):474–481, 1947. ISSN 00804630. URL `http://www.jstor.org/stable/97997`.

Antoine Le Bouil, Axelle Amon, Sean McNamara, and Jérôme Crassous. Emergence of cooperativity in plasticity of soft glassy materials. *Physical review letters*, 112 (24):246001, 2014.

Pierre Le Doussal and Kay Joerg Wiese. Avalanche dynamics of elastic interfaces. *Physical Review E*, 88(2), 2013. ISSN 1539-3755. URL `<Go to ISI>://WOS:000322786100001`.

Anaël Lemaître and Christiane Caroli. Plastic response of a two-dimensional amorphous solid to quasistatic shear: Transverse particle diffusion and phenomenology of dissipative events. *Phys. Rev. E*, 76:036104, Sep 2007. doi: 10.1103/PhysRevE.76.036104. URL `http://link.aps.org/doi/10.1103/PhysRevE.76.036104`.

Anaël Lemaître and Christiane Caroli. Rate-dependent avalanche size in athermally sheared amorphous solids. *Phys. Rev. Lett.*, 103: 065501, Aug 2009. doi: 10.1103/PhysRevLett.103.065501. URL `http://link.aps.org/doi/10.1103/PhysRevLett.103.065501`.

Anaël Lemaître and Craig Maloney. Sum rules for the quasi-static and visco-elastic response of disordered solids at zero temperature. *Journal of statistical physics*, 123(2):415–453, 2006.

Jie Lin, Edan Lerner, Alberto Rosso, and Matthieu Wyart. Scaling description of the yielding transition in soft amorphous solids at zero temperature. *Proceedings of the National Academy of Sciences*, 111(40):14382–14387, 2014a. doi: 10.1073/pnas.1406391111. URL `http://www.pnas.org/content/111/40/14382.abstract`.

Jie Lin, Alaa Saade, Edan Lerner, Alberto Rosso, and Matthieu Wyart. On the density of shear transformations in amorphous solids. *EPL (Europhysics Letters)*, 105 (2):26003, 2014b. URL `http://stacks.iop.org/0295-5075/105/i=2/a=26003`.

Stefan B Lindström, Thomas E Kodger, Joris Sprakel, and David A Weitz. Structures, stresses, and fluctuations in the delayed failure of colloidal gels. *Soft Matter*, 8(13):3657–3664, 2012.

Peter J Lu, Emanuela Zaccarelli, Fabio Ciulla, Andrew B Schofield, Francesco Sciortino, and David A Weitz. Gelation of particles with short-range attraction. *Nature*, 453(7194):499–503, 2008.

JF Lutsko. Stress and elastic constants in anisotropic solids: molecular dynamics techniques. *Journal of Applied Physics*, 64(3):1152–1154, 1988.

K Maeda and S Takeuchi. Computer simulation of deformation in two-dimensional amorphous structures. *Physica status solidi (a)*, 49(2):685–696, 1978.

Craig Maloney and Anael Lemaitre. Subextensive scaling in the athermal, quasistatic limit of amorphous matter in plastic shear flow. *Physical review letters*, 93(1):016001, 2004.

Marie K Mapes, Stephen F Swallen, and MD Ediger. Self-diffusion of supercooled o-terphenyl near the glass transition temperature. *The Journal of Physical Chemistry B*, 110(1):507–511, 2006.

Hideyuki Mizuno, Stefano Mossa, and Jean-Louis Barrat. Measuring spatial distribution of the local elastic modulus in glasses. *Physical Review E*, 87(4):042306, 2013.

Hazime Mori. Transport, collective motion, and brownian motion. *Progress of theoretical physics*, 33(3):423–455, 1965.

Alexandre Nicolas and Jean-Louis Barrat. A mesoscopic model for the rheology of soft amorphous solids, with application to microchannel flows. *Faraday discussions*, 167:567–600, 2013.

Alexandre Nicolas, Kirsten Martens, and Jean-Louis Barrat. Rheology of athermal amorphous solids: Revisiting simplified scenarios and the concept of mechanical noise temperature. *EPL (Europhysics Letters)*, 107(4):44003, 2014a.

Alexandre Nicolas, Joerg Rottler, and Jean-Louis Barrat. Spatiotemporal correlations between plastic events in the shear flow of athermal amorphous solids. *The European Physical Journal E*, 37(6):1–11, 2014b.

Kerstin N Nordstrom, E Verneuil, PE Arratia, Anindita Basu, Zheng Zhang, Arjun G Yodh, Jerry P Gollub, and Douglas J Durian. Microfluidic rheology of soft colloids above and below jamming. *Physical review letters*, 105(17):175701, 2010.

G. Ovarlez, S. Rodts, A. Ragouilliaux, P. Coussot, J. Goyon, and A. Colin. Wide-gap couette flows of dense emulsions: Local concentration measurements, and comparison between macroscopic and local constitutive law measurements through magnetic resonance imaging. *Phys. Rev. E*, 78:036307, Sep 2008. doi: 10.1103/PhysRevE.78.036307. URL `http://link.aps.org/doi/10.1103/PhysRevE.78.036307`.

Guillaume Ovarlez, Kapil Krishan, and Sylvie Cohen-Addad. Investigation of shear banding in three-dimensional foams. *EPL (Europhysics Letters)*, 91(6):68005, 2010.

Stefanos Papanikolaou, Felipe Bohn, Rubem Luis Sommer, Gianfranco Durin, Stefano Zapperi, and James P. Sethna. Universality beyond power laws and the average avalanche shape. *Nature Physics*, 7(4):316–320, 2011. ISSN 1745-2473. URL `<Go to ISI>://WOS:000289076000017`.

M Parrinello and A Rahman. Strain fluctuations and elastic constants. *The Journal of Chemical Physics*, 76(5):2662–2666, 1982.

Sylvain Patinet, Damien Vandembroucq, and Michael L. Falk. Connecting local yield stresses with plastic activity in amorphous solids. *Phys. Rev. Lett.*, 117:045501, Jul 2016. doi: 10.1103/PhysRevLett.117.045501. URL `http://link.aps.org/doi/10.1103/PhysRevLett.117.045501`.

Guillemette Picard, Armand Ajdari, François Lequeux, and Lydéric Bocquet. Elastic consequences of a single plastic event: A step towards the microscopic modeling of the flow of yield stress fluids. *The European Physical Journal E*, 15(4):371–381, 2004.

WCK Poon, F Renth, RML Evans, DJ Fairhurst, ME Cates, and PN Pusey. Colloid-polymer mixtures at triple coexistence: kinetic maps from free-energy landscapes. *Physical review letters*, 83(6):1239, 1999.

DL Price and JM Carpenter. Scattering function of vitreous silica. *Journal of non-crystalline solids*, 92(1):153–174, 1987.

HM Princen. Rheology of foams and highly concentrated emulsions: I. elastic properties and yield stress of a cylindrical model system. *Journal of Colloid and interface science*, 91(1):160–175, 1983.

Francesco Puosi, Joerg Rottler, and Jean-Louis Barrat. Time-dependent elastic response to a local shear transformation in amorphous solids. *Physical Review E*, 89(4):042302, 2014.

Peter N Pusey and William van Megen. Observation of a glass transition in suspensions of spherical colloidal particles. *Physical review letters*, 59(18):2083, 1987.

PN Pusey and W Van Megen. Phase behaviour of concentrated suspensions of nearly hard colloidal spheres. *Nature*, 320(6060):340–342, 1986.

V Repain, M Bauer, J-P Jamet, J Ferré, A Mougin, C Chappert, and H Bernas. Creep motion of a magnetic wall: Avalanche size divergence. *EPL (Europhysics Letters)*, 68(3):460, 2004.

David Rodney, Anne Tanguy, and Damien Vandembroucq. Modeling the mechanics of amorphous solids at different length scale and time scale. *Modelling and Simulation in Materials Science and Engineering*, 19(8):083001, 2011.

A Ruina. Slip instability and state variable friction laws. *Journal of Geophysical Research*, 88:10359–10370, 1983.

K. Michael Salerno and Mark O. Robbins. Effect of inertia on sheared disordered solids: Critical scaling of avalanches in two and three dimensions. *Phys. Rev. E*, 88:062206, Dec 2013. doi: 10.1103/PhysRevE.88.062206. URL `http://link.aps.org/doi/10.1103/PhysRevE.88.062206`.

K. Michael Salerno, Craig E. Maloney, and Mark O. Robbins. Avalanches in strained amorphous solids: Does inertia destroy critical behavior? *Phys. Rev. Lett.*, 109:105703, Sep 2012. doi: 10.1103/PhysRevLett.109.105703. URL `http://link.aps.org/doi/10.1103/PhysRevLett.109.105703`.

Srikanth Sastry, Pablo G Debenedetti, and Frank H Stillinger. Signatures of distinct dynamical regimes in the energy landscape of a glass-forming liquid. *Nature*, 393 (6685):554–557, 1998.

Peter Schall, David A Weitz, and Frans Spaepen. Structural rearrangements that govern flow in colloidal glasses. *Science*, 318(5858):1895–1899, 2007.

T Sentjabrskaja, P Chaudhuri, M Hermes, WCK Poon, J Horbach, SU Egelhaaf, and M Laurati. Creep and flow of glasses: strain response linked to the spatial distribution of dynamical heterogeneities. *Scientific reports*, 5, 2015.

J. P. Sethna, K. A. Dahmen, and C. R. Myers. Crackling noise. *Nature*, 410(6825): 242–250, 2001. ISSN 0028-0836. URL `<Go to ISI>://WOS:000167320500058`.

ZW Shan, Ju Li, YQ Cheng, AM Minor, SA Syed Asif, OL Warren, and E Ma. Plastic flow and failure resistance of metallic glass: Insight from in situ compression of nanopillars. *Physical Review B*, 77(15):155419, 2008.

Yunfeng Shi and Michael L. Falk. Strain localization and percolation of stable structure in amorphous solids. *Phys. Rev. Lett.*, 95: 095502, Aug 2005. doi: 10.1103/PhysRevLett.95.095502. URL `http://link.aps.org/doi/10.1103/PhysRevLett.95.095502`.

Yunfeng Shi, Michael B. Katz, Hui Li, and Michael L. Falk. Evaluation of the disorder temperature and free-volume formalisms via simulations of shear banding in amorphous solids. *Phys. Rev. Lett.*, 98:185505, May 2007. doi: 10.1103/PhysRevLett.98.185505. URL `http://link.aps.org/doi/10.1103/PhysRevLett.98.185505`.

Miriam Siebenbürger, Matthias Ballauff, and Th Voigtmann. Creep in colloidal glasses. *Physical review letters*, 108(25):255701, 2012.

Peter Sollich, François Lequeux, Pascal Hébraud, and Michael E Cates. Rheology of soft glassy materials. *Physical review letters*, 78(10):2020, 1997.

Frans Spaepen. A microscopic mechanism for steady state inhomogeneous flow in metallic glasses. *Acta metallurgica*, 25(4):407–415, 1977.

Joris Sprakel, Stefan B Lindström, Thomas E Kodger, and David A Weitz. Stress enhancement in the delayed yielding of colloidal gels. *Physical review letters*, 106 (24):248303, 2011.

Frank H. Stillinger. Exponential multiplicity of inherent structures. *Phys. Rev. E*, 59:48–51, Jan 1999. doi: 10.1103/PhysRevE.59.48. URL `http://link.aps.org/doi/10.1103/PhysRevE.59.48`.

BA Sun and WH Wang. Fractal nature of multiple shear bands in severely deformed metallic glass. *Applied Physics Letters*, 98(20):201902, 2011.

BA Sun, HB Yu, W Jiao, HY Bai, DQ Zhao, and WH Wang. Plasticity of ductile metallic glasses: A self-organized critical state. *Physical review letters*, 105(3): 035501, 2010.

BA Sun, S Pauly, J Tan, M Stoica, WH Wang, U Kühn, and J Eckert. Serrated flow and stick–slip deformation dynamics in the presence of shear-band interactions for a zr-based metallic glass. *Acta Materialia*, 60(10):4160–4171, 2012.

Mehdi Talamali, Viljo Petäjä, Damien Vandembroucq, and Stéphane Roux. Avalanches, precursors, and finite-size fluctuations in a mesoscopic model of amorphous plasticity. *Phys. Rev. E*, 84: 016115, Jul 2011. doi: 10.1103/PhysRevE.84.016115. URL `http://link.aps.org/doi/10.1103/PhysRevE.84.016115`.

Anne Tanguy, Fabien Leonforte, and J-L Barrat. Plastic response of a 2d lennard-jones amorphous solid: Detailed analysis of the local rearrangements at very slow strain rate. *The European Physical Journal E*, 20(3):355–364, 2006.

Michel Tsamados, Anne Tanguy, Chay Goldenberg, and Jean-Louis Barrat. Local elasticity map and plasticity in a model lennard-jones glass. *Physical Review E*, 80(2):026112, 2009.

Botond Tyukodi, Sylvain Patinet, Stéphane Roux, and Damien Vandembroucq. From depinning transition to plastic yielding of amorphous media: A soft-modes perspective. *Phys. Rev. E*, 93:

063005, Jun 2016. doi: 10.1103/PhysRevE.93.063005. URL `http://link.aps.org/doi/10.1103/PhysRevE.93.063005`.

G Wang, KC Chan, L Xia, P Yu, J Shen, and WH Wang. Self-organized intermittent plastic flow in bulk metallic glasses. *Acta Materialia*, 57(20):6146–6155, 2009.

Jérôme Weiss, Lucas Girard, Florent Gimbert, David Amitrano, and Damien Vandembroucq. (finite) statistical size effects on compressive strength. *Proceedings of the National Academy of Sciences*, 111(17):6231–6236, 2014.

J Wuttke, W Petry, and S Pouget. Structural relaxation in viscous glycerol: Coherent neutron scattering. *The Journal of chemical physics*, 105(12):5177–5182, 1996.

Kenji Yoshimoto, Tushar S. Jain, Kevin Van Workum, Paul F. Nealey, and Juan J. de Pablo. Mechanical heterogeneities in model polymer glasses at small length scales. *Phys. Rev. Lett.*, 93:175501, Oct 2004. doi: 10.1103/PhysRevLett.93.175501. URL `http://link.aps.org/doi/10.1103/PhysRevLett.93.175501`.

S. Zapperi, C. Castellano, F. Colaiori, and G. Durin. Signature of effective mass in crackling-noise asymmetry. *Nature Physics*, 1(1):46–49, 2005. ISSN 1745-2473. URL `<Go to ISI>://WOS:000234888200021`.

Z Zhao, X Ding, J Sun, and E K H Salje. Thermal and athermal crackling noise inÂ ferroelastic nanostructures. *Journal of Physics: Condensed Matter*, 26(14): 142201, 2014. URL `http://stacks.iop.org/0953-8984/26/i=14/a=142201`.

Robert Zwanzig. Ensemble method in the theory of irreversibility. *The Journal of Chemical Physics*, 33(5):1338–1341, 1960.

Appendix A

Shear band formation with continuum mechanics

Instability of velocity profile

Imagine two infinite flat planes with a gap h perpendicular to the z direction. The bottom one of altitude $z = 0$, and the upper one $z = h$. A viscous non-newtonian incompressible fluid flows between the gap along direction x, so that the steady state velocity field under constant shear rate along x is simply the $v_x = u(z)$ and $v_y = v_z = 0$.

The local momentum conservation reads (using the notation of Einstein's summing convention):

$$\partial_t(\rho v_i) + v_j \partial_j(\rho v_i) = \partial_j \sigma_{ij} \tag{A.1}$$

For incompressible fluids:

$$\partial_t v_i + v_j \partial_j v_i = -\frac{1}{\rho}\partial_i P + \frac{1}{\rho}\partial_j \sigma^S_{ij} \tag{A.2}$$

where P the hydrostatic pressure separated from the pure shear stress σ^S_{ij}.

If we deal with a Newtonian fluid we have: $\partial_j \sigma^S_{ij} = \eta(\partial_j \partial_j) v_i$. For non-newtonian fluids, in general we write : $\sigma^S_{ij}(\vec{x}^*, t) = \Sigma_{ij}(\partial_k v_l|_{\vec{x}=\vec{x}^*,t})$. $\sigma^S_{xx} = \sigma^S_{zz} = 0$ for the pure shear along x, and $\sigma^S_{xz} = \sigma^S_{zx} = \Sigma(\partial_z u) = \Sigma(\dot{\gamma})$, $\dot{\gamma} = \partial_z u$ is the local shear rate. Here $\Sigma(\dot{\gamma})$ is then the constitutive law flow curve. A.2 is written explicitly:

$$\partial_t u = -\frac{1}{\rho}\partial_x P + \frac{1}{\rho}\partial_z \Sigma(\partial_z u(z, t)) \tag{A.3}$$

$$0 = -\frac{1}{\rho}\partial_z P + \frac{1}{\rho}\partial_x \Sigma(\partial_z u(z,t)) \tag{A.4}$$

In the steady state we can write $u(z,t) = \dot{\gamma} z$ and $P = P_o$ everywhere. This corresponds to the case where we do not impose any pressure gradient at the extremities of the system, and drive the fluid only by imposing a shear rate $\dot{\gamma}$ on the two plans with gap of h. Now we investigate if this steady velocity profile is stable.

We keep always the zero pressure gradient at the extremities of the system. And we add a small perturbation $\delta u(z,t)$ on the velocity profile, where $\delta u(z,t)$ depends only on z (and on t). And we denote δP as perturbation on the pressure field. The equation A.4 keep its form for δP and δu, when we replace P and u by $P + \delta P$ and $u + \delta u$ and reduce to the first order of δ. A.3 turns out to be:

$$\partial_t \delta u - \frac{1}{\rho}\frac{d\Sigma}{d\dot{\gamma}}(\dot{\gamma})\partial_z^2 \delta u = \frac{1}{\rho}\partial_x \delta P \tag{A.5}$$

The left hand side only depends on z, such that we have throughout the system $\delta P = L.H.S(z,t)x + cst(z,t)$. Since we keep always the zero pressure gradient at the ends of the system, we should have that the left hand side of the equation is zero ($L.H.S(z,t) = 0$). Therefore it follows that

$$\partial_t \delta u = \frac{1}{\rho}\frac{d\Sigma}{d\dot{\gamma}}(\dot{\gamma})\partial_z^2 \delta u \tag{A.6}$$

and in Fourier space:

$$\partial_t \delta u_k = -k^2 \frac{1}{\rho}\frac{d\Sigma}{d\dot{\gamma}} \delta u_k \tag{A.7}$$

It is clear that the perturbation will vanish if $\frac{d\Sigma}{d\dot{\gamma}} > 0$ and the perturbation will grow if $\frac{d\Sigma}{d\dot{\gamma}} < 0$ which means that the homogeneous profile of velocity is unstable.

Shear banding

Shear bands can be formed in systems with a constitutive law exhibiting a negative slope regime if it is driven to flow from a solid state with a fixed shear rate smaller than a critical value $\dot{\gamma}_c$. Typically $\Sigma(\dot{\gamma} \to 0) = \sigma_y$; $\Sigma(\dot{\gamma} > 0) > 0$; $\frac{d\Sigma}{d\dot{\gamma}}|_{0<\dot{\gamma}<\dot{\gamma}_{min}} < 0$; $\frac{d\Sigma}{d\dot{\gamma}}|_{\dot{\gamma}>\dot{\gamma}_{min}} > 0$; $\Sigma(\dot{\gamma}_{min}) = \sigma_{min}$. $\dot{\gamma}_c \neq 0$ is defined as $\Sigma(\dot{\gamma}_c) = \sigma_y$.

When sheared starting from a solid state with any fixed shear rate $\dot{\gamma}$, the system begin to flow only when $\dot{\gamma} t \sim \sigma(t)$ reaches σ_y. If $\dot{\gamma} < \dot{\gamma}_c$, since any velocity profile for $\dot{\gamma} < \dot{\gamma}_{min}$ is unstable, at the moment $\sigma(t)$ reaches σ_y, the reasonable way to keep macroscopic shear rate $\dot{\gamma} < \dot{\gamma}_c$ is to separate the flow into two parts: one with zero velocity, the other one with velocity profile $\dot{\gamma}_c$ and its width occupies a portion $q = \dot{\gamma}/\dot{\gamma}_c$ of the entire width of the bulk system. At the same time the bulk applied stress is always σ_y as far as $\dot{\gamma} < \dot{\gamma}_c$.

When decreasing the shear rate step by step from a high shear rate steady state and at each step waiting for the system to achieve the new steady state, the flow velocity profile would be linearly homogeneous (no shear banding) for $\dot{\gamma} > \dot{\gamma}_{min}$ and the flowing state is situated on the positive slope regime of the flow curve. Below $\dot{\gamma}_{min}$, the bulk stress stays at σ_{min} and the shear band appears again with one part of zero velocity profile and the other at $\dot{\gamma}_{min}$.

The apparent bulk flow curve for this kind of systems also presents a hysteresis but only below $\dot{\gamma}_c$. Above $\dot{\gamma}_c$ upward-downward loop of rheological test gives the same bulk flow curve in contrast with the so-called "thixotropic" yield stress materials

Appendix B

Fourier space calculation of the elastic propagator

Compressible mechanical equilibrium

The mechanical equilibrium for a compressible displacement field $\mathbf{u}(\mathbf{x}) \equiv u_i(x_j)$ under a arbitrary body force $\mathbf{f}(\mathbf{x}) \equiv f_i(x_j)$ leads to the equation(4.10), which is recalled here

$$(\lambda + \mu)\partial_i(\partial_l u_l) + \mu(\partial_l \partial_l)u_i = -f_i \tag{B.1}$$

The linearity of this equation is convenient for the resolution in the fourier space, since $TF(\partial_i \cdot) = -\mathbf{i}q_i \cdot$ where q_i is the wave vector component along the direction i. Hence in fourier space the equation(B.1), becomes

$$-(\lambda + \mu)q_i q_l \hat{u}_l - \mu q_l q_l \hat{u}_i = -\hat{f}_i \tag{B.2}$$

By defining

$$\Xi_{ij} = (\lambda + \mu)q_i q_j + \mu q_l q_l \delta_{ij} \tag{B.3}$$

the equation(B.2) becomes

$$\Xi_{ij}\hat{u}_j = \hat{f}_i \tag{B.4}$$

Hence

$$\hat{u}_i = \Xi_{ij}^{-1}\hat{f}_j \tag{B.5}$$

Non-compressible mechanical equilibrium

The mechanical equilibrium for a non-compressible diplacement field $\mathbf{u}(\mathbf{x}) \equiv u_i(x_j)$ under a arbitrary body force $\mathbf{f}^I(\mathbf{x}) \equiv f_i^I(x_j)$ leads to the equation(4.14), which is recalled here

$$-\partial_i P^\Delta + \mu(\partial_l\partial_l)u_i = -f_i^I \tag{B.6}$$

The non-compressible displacement field satisfies

$$\partial_i u_i = 0 \tag{B.7}$$

In fourier space

$$\mathbf{i}q_i\hat{P}^\Delta - \mu q_l q_l \hat{u}_i = -\hat{f}_i^I \tag{B.8}$$

and

$$-\mathbf{i}q_i\hat{u}_i = 0 \tag{B.9}$$

Taking the inner product of both sides of the equation(B.8) with the wave vector, thanks to the equation(B.9), one arrives, for $\left|\mathbf{q}\right| \neq 0$,

$$\hat{P}^\Delta = \mathbf{i}\frac{q_i\hat{f}_i^I}{q^2} \tag{B.10}$$

Then inserting the above equation into the equation(B.8), one gets

$$\hat{u}_i = \frac{1}{\mu}\left(\frac{1}{q^2}\hat{f}_i^I - \frac{q_i q_l}{q^4}\hat{f}_l^I\right) \tag{B.11}$$

Let us recall that the local stress $\sigma_{ij}^\Delta = 2\mu\epsilon_{ij}^{el} = 2\mu(\epsilon_{ij}^\Delta - \epsilon_{ij}^{pl,\Delta})$ with $\epsilon_{ij}^\Delta = \frac{1}{2}(\partial_i u_j + \partial_j u_i)$ (see the equation(4.3)) and the body force due to plastic strain is, the equation(4.15), $f_i^I = -2\mu\partial_j\epsilon_{ij}^{pl,\Delta}$. In fourier space

$$\hat{\sigma}_{ij}^\Delta = -\mathbf{i}\mu(q_j\hat{u}_i + q_i\hat{u}_j) - 2\mu\hat{\epsilon}_{ij}^{pl,\Delta} \tag{B.12}$$

$$\hat{f}_i^I = 2\mathbf{i}\mu q_j\hat{\epsilon}_{ij}^{pl,\Delta} \tag{B.13}$$

Inserting (B.11) and (B.13) into (B.12), one arrives

$$\hat{\sigma}_{ij}^\Delta = 2\mu\left(\frac{\delta_{jk}q_i q_l + \delta_{ik}q_j q_l}{q2} - 2\frac{q_i q_j q_k q_l}{q^4} - \delta_{ik}\delta_{jl}\right)\hat{\epsilon}_{kl}^{pl,\Delta} \tag{B.14}$$

Because of the symmetry $\epsilon_{kl}^{pl,\Delta} = \epsilon_{lk}^{pl,\Delta}$, one can exchange the index k and l in the first term of the numerator of the first fraction in the parenthesis to get

$$\hat{\sigma}_{ij}^{\Delta} = 2\mu\left(\frac{\delta_{jl}q_i q_k + \delta_{ik}q_j q_l}{q2} - 2\frac{q_i q_j q_k q_l}{q^4} - \delta_{ik}\delta_{jl}\right)\hat{\epsilon}_{kl}^{pl,\Delta} \tag{B.15}$$

One can defined a propagator $\hat{G}_{ij,kl}$ as

$$\hat{G}_{ij,kl} \hat{=} \frac{\delta_{jl}q_i q_k + \delta_{ik}q_j q_l}{q2} - 2\frac{q_i q_j q_k q_l}{q^4} - \delta_{ik}\delta_{jl} \tag{B.16}$$

The equation (B.15) reads then

$$\hat{\sigma}_{ij}^{\Delta} = 2\mu\hat{G}_{ij,kl}\hat{\epsilon}_{kl}^{pl,\Delta} \tag{B.17}$$

It is worth to notice that the propagator $\hat{G}_{ij,kl}$ is defined only for the non-zero modes, i.e. $\left|\mathbf{q}\right| \neq 0$.

Appendix C

The supplementary material

Here after is the supplementary material of our paper Driving Rate Dependence of Avalanche Statistics and Shapes at the Yielding Transition, including some details of the model parameter, the numerical implementation on GPU parallel computing and fitting procedures.

Supplemental Material for: "Driving Rate Dependence of Avalanche Statistics and Shapes at the Yielding Transition"

Chen Liu,[1, 2] Ezequiel E. Ferrero,[1, 2] Francesco Puosi,[3, 1, 2] Jean-Louis Barrat,[1, 2] and Kirsten Martens[1, 2]
[1] *Université Grenoble Alpes, LIPHY, F-38000 Grenoble, France*
[2] *CNRS, LIPHY, F-38000 Grenoble, France*
[3] *Université de Lyon, Laboratoire de Physique, ENS Lyon, CNRS, 46 Alleé d'Italie, F-69007 Lyon, FranceUniv. Grenoble Alpes, LIPHY, F-38000 Grenoble, France*
(Dated: January 22, 2016)

We describe in detail the model used in the manuscript and explain our numerical implementation set to run in parallel on GPUs. We provide also some details about the post-processing and analysis of the raw simulation results.

THE MESOPLASTIC MODEL

We study the scalar elasto-plastic model in two ($2d$) and three dimensions ($3d$) under the presence of an imposed shear-rate, following the modifications proposed by Nicolas et al. [1] to the model of Picard and coworkers [2, 3].

An amorphous system is represented by a coarse-grained scalar field $\sigma(\boldsymbol{r},t)$, denoting the instantaneous deviatoric shear stress of the system at spatial position $\boldsymbol{r}$ and time t upon the application of a simple shear. An over-damped dynamics is imposed for this scalar quantity following some basic rules: (i) The stress loads locally in an elastic manner while it is *below* a certain yield stress $\sigma_{\mathtt{Y}}(\boldsymbol{r})$. (ii) When the local stress overcomes the local yield stress, a *plastic event* occurs. Dissipation occurs locally, expressed as a progressive drop of the local stress, together with a redistribution of the stresses in the rest of the system, provided by a long-range elastic perturbation. This process stops when a criterion for the accumulated local strain is met, the region recovers its elastic properties and a new local yield threshold is chosen from a given distribution.

The shear stress perturbation caused on the system is computed within the framework of tensorial linear elasticity assuming an isotropic incompressible material [2]. A Green's function $G(\boldsymbol{r},\boldsymbol{r}')$ relates the stress variation $\delta\sigma$ at each point in space with the corresponding component of the plastic strain $\gamma^{pl}(\boldsymbol{r}';t)$ associated with a plastic event occurring at $\boldsymbol{r}'$. The perturbation given by the elastic propagator $G(\boldsymbol{r},\boldsymbol{r}')$ can be approximated by the far field expression [2, 3] of the continuum mechanics solution [4]

$$\delta\sigma(\boldsymbol{r},t) = \mu \int d\boldsymbol{r}' G(\boldsymbol{r},\boldsymbol{r}')\gamma^{pl}(\boldsymbol{r}';t) \qquad (1)$$

where μ is the shear modulus. This kernel decays with the distance as $1/r^d$ ($r \equiv |\boldsymbol{r}-\boldsymbol{r}'|$) and changes sign according to the angle sustained between the shear direction and the interaction vector $\theta \equiv \arccos((\boldsymbol{r}-\boldsymbol{r}')\cdot\boldsymbol{r}_{\dot{\gamma}^{(\mathtt{ext})}})$, with a particular quadrupolar symmetry. For example, in $2d$ we have $G(\boldsymbol{r},\boldsymbol{r}') \equiv G(r,\theta) \sim \frac{1}{\pi r^2} cos(4\theta)$ in polar coordinates. The self interaction $G_0 \equiv G(\boldsymbol{r},\boldsymbol{r})$ is chosen to be a negative constant that rules the local dissipation rate.

Dynamics at zero temperature

We can define the model as a d-dimensional scalar field $\sigma(\boldsymbol{r})$, $\boldsymbol{r} \equiv (x_1, x_2, \ldots, x_d)$ subjected to the following evolution in real space

$$\begin{aligned} \frac{d}{dt}\sigma(\boldsymbol{r},t) &= \mu\dot{\gamma}^{(\mathtt{ext})} + \frac{d}{dt}\delta\sigma(\boldsymbol{r},t) && (2) \\ &= \mu\dot{\gamma}^{(\mathtt{ext})} + \mu\int d\boldsymbol{r}' G(\boldsymbol{r},\boldsymbol{r}')\frac{d}{dt}\gamma^{pl}(\boldsymbol{r}';t) && (3) \end{aligned}$$

where we have imposed a global elastic loading $\dot{\gamma}^{(\mathtt{ext})}$ on top of the perturbation induced by plastic events.

The picture is completed by a dynamical law for the plastic strain γ^{pl}. Following [3], we use a law relating the plastic strain velocity of a region undergoing a plastic deformation to the instantaneous local stress.

$$\frac{d}{dt}\gamma^{pl}(\boldsymbol{r},t) = \frac{1}{\mu\tau} n(\boldsymbol{r},t)\sigma(\boldsymbol{r},t) \qquad (4)$$

Here τ is just a mechanical relaxation time that fixes the time units, $n(\boldsymbol{r})$ is a local "state variable" which takes values $n = \{0,1\}$ indicating whereas the system at position $\boldsymbol{r}$ is plastically active ($n = 1$) or not ($n = 0$).

The concept of "active" and "inactive" regions is intimately related to the discretization of space. Let us say for the moment that different "patches" of the system hold at each time a single value of $n(\boldsymbol{r})$, that is modified according to the following local rules:

$$n(\mathbf{r},t) : \begin{cases} 0 \to 1 & \text{if} \quad \sigma > \sigma_y \\ 0 \leftarrow 1 & \text{when} \ \int dt' |\partial_t \sigma(t')/\mu + \dot{\gamma}^{pl}(t')| \geq \gamma_c \end{cases} \qquad (5)$$

Model parameters

As in Ref [1] we choose randomly from a distribution the local yield thresholds σ_y. More precisely, we imagine a potential energy landscape (PEL) with energy barriers $E_y \equiv \sigma_y^2/4\mu$. This landscape is composed of metabasins of exponentially distributed depths E_y. Small jumps between PEL basins are neglected and only larger jumps corresponding to the irreversible rearrangements at low enough temperature are considered. In other words, a lower cutoff $E_y^{\mathtt{min}} = \mu\gamma_c^2/4$ is introduced in the energy barrier distribution

$$P(E_y) = \Theta(E_y - E_y^{\mathtt{min}})\lambda e^{-\lambda(E_y - E_y^{\mathtt{min}})}. \qquad (6)$$

The parameters λ and γ_c determine the average yield strain $\langle\gamma_y\rangle$. We have choose here $\gamma_c = 0.035$ and $\lambda = 700$ such that $\langle\gamma_y\rangle \simeq 7,7\%$, which is a realistic value. The distance (in terms of strain) among metabasins minima can be expressed in units of the strain γ_c used to define the cutoff $E_y^{\mathtt{min}}$. For simplicity, this distance is choosen to be equal to γ_c. Therefore, once it yields, a block will remain plastic until it has accumulated a total strain equal or greater than γ_c.

The time and stress units, τ and μ are chosen to be the unity without loose of generality.

NUMERICAL APPROACH

Our system is described by a $3d$ (or else $2d$) scalar field $\sigma(\boldsymbol{r})$, and a state variable $n(\boldsymbol{r})$ for each block of a spatially discretized space. This is, each spatial block of volume $v_0 = \delta x\delta y\delta z$, centered at position $\boldsymbol{r} = \{x, y, z\}$ is represented by a single value of the scalar fields in the nodes of a cubic lattice $\{x \pm \delta x/2, y \pm \delta y/2, z \pm \delta z/2\} \to (i, j, k)$.

In practice, we have a $L_x \times L_y \times L_z$ array of real variables σ_{ijz} representing the local stresses and a boolean array n_{ijz} with identical dimensions holding the binary state of the blocks. Further, we discretize also the time t in Eq.2, choosing a small discrete time step $dt \ll 1$ that we keep constant during all the simulation process.

In order to simulate the equation of motion (2) for the local stresses, beforehand we choose a *mechanically stable* initial configuration $\sigma_{ijz}(t = 0)$. Such a configuration has to ensure that the sum of all stresses in each column or row of the cubic box should be equal. Typically we choose $\sigma_{ijk} = 0$ for all $\{i, j, k\}$, and consistently, all state variables to be initially on the “inactive” state $n_{ijk} = 0$.

Once we have an initial configuration at hand, we evolve Eq.2 with a simple Euler integration method. We avoid any kind of numerical integration problems by choosing an integration time step dt small enough. We have used in this work $dt = 10^{-2}$ and 10^{-3}, which are sufficient to avoid integration problems. Notice nevertheless, that certain minor details of the resulting curves can depend on dt, as for example the lower cutoff of P_S and P_T. This effect of a finite integration step is more prominent at large driving rates as can be seen in Fig.2b-inset of the manuscript.

$$\sigma_{ijk}(t+dt) = \mu\dot{\gamma}^{(\mathtt{ext})}dt + \mu dt \sum_{i'j'k'} G_{(ijk),(i'j'k')} n_{i'j'k'}(t) \frac{\sigma_{i'j'k'}(t)}{\mu\tau} \qquad (7)$$

After each integration step for σ_{ijk} we update the state variables n_{ijk} according to the rules defined in Eq.5. In there, n changes from 0 to 1 as soon as the local stress overcomes the local threshold. If so, an auxiliary variable is set to accumulate (from zero) the local strain during its evolution. When the accumulated total strain reaches a given value γ_c the active phase stops, and n goes back to 0. The dynamics goes on, updating consistently σ_{ijk} and n_{ijk}, until a stop criterion is matched (total simulation time, total strain deformation, etc.).

Boundary conditions and spectral method for the dynamics

Numerical simulations are done in finite size systems. Contrary to fully-connected models, in this case space is defined and we are forced to define boundary conditions. Since we are interested in bulk quantities, we can choose periodic boundary conditions (p.b.c.) in all directions without loose of generality. In problems where the analysis of wall effects on the system rheology is particularly relevant, the numerical approach is different from the one we present here (see for example [2, 5]). The choice of p.b.c. will also simplify the numerical implementation. In particular, it allows for the use of a technique called pseudo-spectral method, that we describe in the following.

The second term on the RHS of Eq.2 is an integral over all space, since the kernel $G(\boldsymbol{r}, \boldsymbol{r'})$ is long-range. If we Fourier transform with respect to the variable $\boldsymbol{r'}$, the integral over space is simplified to independent products for each Fourier mode $\boldsymbol{q}$

$$\int d\boldsymbol{r'} G(|\boldsymbol{r} - \boldsymbol{r'}|) n(\boldsymbol{r'}) \sigma(\boldsymbol{r'}) \qquad \longrightarrow \qquad G_{\boldsymbol{q}} \tilde{n}(\boldsymbol{q}) \tilde{\sigma}(\boldsymbol{q}) \qquad (8)$$

This transforms a non-local, time-consuming, sum over spatial coordinates into a local operation in the Fourier modes that can be trivially performed in a parallel scheme. Therefore we can evolve the local stresses in Fourier space according to the transformed equation of motion

$$\frac{\partial\sigma_{\boldsymbol{q}}}{\partial t} = \mu\dot{\gamma}\delta(\boldsymbol{q}) + \frac{1}{\tau} G_{\boldsymbol{q}} \tilde{n}(\boldsymbol{q}) \tilde{\sigma}(\boldsymbol{q}) \qquad (9)$$

Of course, since after each update of $\sigma(\boldsymbol{r})$ we need to update also $n(\boldsymbol{r})$, it is necessary to transform stresses back to real space. So the process includes two Fourier transforms (one forward and one backward) at each time-step of the dynamics. Nevertheless, with this technique we reduce the computing time for the convolution (Eq.8) from $O(N^2)$ to $O(N\log(N))$. In addition, this operation is highly optimized in standard libraries (e.g., FFTW3, cuFFT) that make the method even more suitable for a parallel implementation.

PARALLEL IMPLEMENTATION ON GPU

In the last years the use of GPUs to accelerate simulations has burst out in many areas of physics and science in general.

Following previous GPU implementations from some of us [6**?** , 7], we have implemented a GPU-based parallel implementation of the elasto-plastic model described above. Our codes are written in C++ and C for CUDA [8]. For this project we had worked with NVIDIA GPUs. The CUDA programming framework makes it simpler the access to many low level directives, preserving a more compact and easy to read code[9]. Simulations were ran on Kepler architecture (GK208) GPUs, the Tesla K20.

Update routine, CUDA kernels and main stream

We use an algorithm developed from scratch to implement our model. Self-developed CUDA kernels and available optimized parallel libraries are used alternately. Among the libraries we can name: the GPU-suited Fast Fourier Transform library *cuFFT* [10] from the *NVIDIA CUDA Toolkit*, the *STL*-like *Thrust* library [11] of parallel standard algorithms (reductions, scannings, searches, etc.) and the counter-based Random Number Generator named PHILOX, from the *Random123* open-source library [12].

As anticipated in the previous section, the equation of motion for the local stresses is resolved in several steps:

1) Computation of $\dot\gamma^{pl}(\boldsymbol{r})$ in real space, basically the product $\sigma(\boldsymbol{r})n(\boldsymbol{r})$ times constants (Eq.4).

2) Discrete Fourier transform (DFT) of $\dot\gamma^{pl}(\boldsymbol{r})$.

3) $G_{\boldsymbol{q}}$ times $\dot\gamma^{pl}_{\boldsymbol{q}}$ pointwise multiplication (Eq. 8)

4) Euler step integration in Fourier space using the increment of Eq.7.

5) Inverse discrete Fourier transform of the resulting $\tilde\sigma(\boldsymbol{q})$ giving as a result the scalar stress field at the incremented time $\sigma(\boldsymbol{r}, t+dt)$.

6) Update of state variables $n(\boldsymbol{r})$ according to Eq.5.

From a computational viewpoint, steps 1, 3, 4 and 6 can be trivially computed in parallel, since we need only to read and write arrays locally with no interdependence. This is easily implemented in massively parallel routines with a SIMD (Single Instruction Multiple Data) approach. We use either self-developed CUDA kernels or Thrust well-settled functions for each of this steps. At steps 2 and 5, we make use of the cuFFT library, especially powerful in the transformations of real or complex arrays with an x dimension being strictly a power of two.

Besides the evolution of the system, we need also to calculate certain physical quantities with some frequency as time evolves. We are interested, for example, in instantaneous global values as the average stress and average activity. To account for this measurements, we make intensive use of *Thrust* routines, as the parallel *reduce*.

Our CUDA kernels are moderately optimized, trying to keep aligned and coalesced memory access, avoiding threads divergence and atomic functions. Further optimizations are still possible, but we choose to preserve code readability over elaborated tricks that obfuscate the code for a negligible speedup. As defensive programming techniques we use assertions and each routine is independently tested before implementation.

The structure of the main stream is simply as follows:

- Initialization
- Time loop:
  - System Update (as itemized above)
  - if (condition) Measures
  - if (condition) Print results
- Final averages, printing and cleaning.

We have created a C++ class to host our functions and keep a clean `main()` routine where we set up the physical protocol for the simulation. CUDA kernels, used by the class functions, are described in a separate file for further clearness.

Validation of the overall program is made by computing a full flow curve in a wide range of shear-rates and comparing with independent serial implementations of the same model. These tests also serve us to know that with the parallel implementation and the use of a GPU we obtain a speed up of 100x and beyond respect to a single-CPU serial version of the same algorithm.

Our source codes are freely available to download, modify and use under GNU GPL 3.0 at [13].

POST-PROCESSING AND DATA ANALYSIS

To obtain compound averages as the distributions of stress drop sizes or the avalanche shapes presented in the manuscript, we make use of *Python* scripts [14] doing a post-processing of the stress time series output by our algorithm. Since data files attain a considerable size (up to a couple of gigabytes), care is taken in using fast load functions and list operations rather than array operations, to reduce the processing time; which is, in any case, always much shorter than the simulation time to obtain the raw data.

Power-laws exponent fitting and error estimation procedure

In Fig. 1 and Fig. 2 of the manuscript scaling regimes at low shear rate span over wide ranges (about four decades for P_S and two decades for P_T or P_x). As the scaling regimes can be quite clearly identified by eye, we perform power-law fits in manually selected regions, avoiding the lower and upper cutoffs. Of course, this introduce a small variation of the fitted exponents and an uncertainty, that is considered in the error bar estimation of the measured exponents.

Having determined the values of τ and $\tau^{'}$ from P_S and P_T respectively, we fix them and proceed to scaling analyses of data at different L and $\dot{\gamma}$ to estimate the exponents d_f and α that provide the best collapse of the upper (exponential) cutoff of the distributions. We can qualify the collapse either by eye or by computing the relative deviations of the rescaled curves. This allows us to have an error of estimation for exponent values within the indicated error bars.

We have also tried a more sophisticated and systematic way of estimating the exponent of power law histogram as described in the work by Planet et al. [15]. However, it does not give us better estimations than the ones we extract from the ad hoc fittings.

In Table 1 of the manuscript we present all our fitted exponents with their corresponding error bars. The only non measured exponent is z, that is computed from the relation $z = d_f/\delta$.

Stress-drop shape averages and comparison with analytical predictions

Each stress-drop has a certain duration T. To analyze the stress-drop shapes, we consider only the stress-drops of durations T that belong to the scaling regime of P_T. This is, in the window of T in which P_T is a power law. We are interested in the average shape of stress drops at different T. In order to improve the statistics of the shape averages we do a logarithmic binning on T, with a rather small binning step, and consider the mid value in logarithmic scale of each bin as representative of the duration of all stress-drops found within the bin. In this way, we are able to collect a good amount of stress drops with the "same" duration. The average shape of the stress-drops within a bin centered at T, is computed as follows: Each stress-drop i can be represented as $V_i(t)$. First we rescale all stress-drops on their duration T_i defining $\tilde{V}_i(\tilde{t}) \equiv V_i(\tilde{t}T_i)$, where $\tilde{t} = t/T_i \in [0,1]$. Then, we define the average shape of the stress-drops as $V_T(\tilde{t}) \equiv \frac{1}{N_T}\sum_i \tilde{V}_i(\tilde{t})$, with N_T the number of stress-drops found in the interval.

Once we get $V_T(\tilde{t})$ for different T, we fit them with the equation proposed in [16], $V_T(\tilde{t}) \propto B(\tilde{t}(1-\tilde{t}))^c(1-a_s(\tilde{t}-0.5))$, leaving B, c and a_s as free parameters. From this fitting, we find the power law dependence of B on T, the exponent $c \approx \delta - 1$, and the behavior of $a_s(T)$, presented in Fig.3(b) of the manuscript.

Multi-parameter dependence of the shape asymmetric values a_s and a_g

We have characterized the "degree of asymmetry" of a stress drop shape with the parameters a_s and a_g defined in the manuscript.

We propose a common functional dependence for both of them with $\dot{\gamma}$, L, T as $a_x \approx CL^{-b}\dot{\gamma}^{-\epsilon}T^{-m}$, whit C being a prefactor. A first step is to rescale a_x getting $\tilde{a}_x \equiv a_x L^b \dot{\gamma}^{\epsilon}$. If our assumption is right and the value of b and ϵ are well chosen, $\tilde{a}_x(T)$ for different $\dot{\gamma}$ and L can be collapsed together on the same curve $\tilde{a}_x = CT^{-m}$. Indeed, this is what we observe. The rescaled and merged data sets are used to process a unique power law fitting. We fit $\log_{10}(\tilde{a}_x)$ versus $\log_{10}(T)$ with $y = kx + \kappa$ by a least-square method, where $k = -m$ and $C = 10^{\kappa}$. For a chosen pair (b, ϵ), the least-square fitting method gives us the error $E(b, \epsilon)$ qualifying the fit. We span our choices over a wide domain of (b, ϵ) and repeat the procedure for each pair, obtaining a surface $E(b, \epsilon)$. The minimum of $E(b, \epsilon)$ provides therefore the best possible choice of (b, ϵ). After fixing them, we extract the parameters m and C from the corresponding fit of the rescaled data.

This proposed functional dependence and the above explained procedure allow us to display a_s or a_g in a continuum plane L-$\dot{\gamma}$, as shown in the inset of Fig.3(a) in the manuscript.

REFERENCES

---

[1] A. Nicolas, K. Martens, and J. L. Barrat, Epl **107**, 6 (2014).

[2] G. Picard, A. Ajdari, F. Lequeux, and L. Bocquet, The European Physical Journal E **15**, 371 (2004).

[3] G. Picard, A. Ajdari, F. Lequeux, and L. Bocquet, Phys. Rev. E **71**, 010501 (2005).

[4] J. D. Eshelby, Proceedings of the Royal Society of London A: Mathematical, Physical and Engineering Sciences **241**, 376 (1957).

[5] A. Nicolas and J.-L. Barrat, Phys. Rev. Lett. **110**, 138304 (2013).

[6] K. Martens, L. Bocquet, and J.-L. Barrat, Phys. Rev. Lett. **106**, 156001 (2011).

[7] E. E. Ferrero, S. Bustingorry, and A. B. Kolton, Phys. Rev. E **87**, 032122 (2013).

[8] NVIDIA Corporation, "CUDA C Programming Guide Version 7.0," (2015).

[9] Nevertheless, all our routines could be straight-forward translated to a open standard platform, as OpenCL, and get in dependency on the hardware vendor.

[10] NVIDIA Corporation, "CUDA library for the Fast Fourier Transform, DU-06707-001_v7.0," (2015).

[11] J. Hoberock and N. Bell, "Thrust: A parallel template library," (2010), version 1.7.0.

[12] J. K. Salmon, M. A. Moraes, R. O. Dror, and D. E. Shaw, in *Proceedings of 2011 International Conference for High Performance Computing, Networking, Storage and Analysis*, SC '11 (ACM, New York, NY, USA, 2011) pp. 16:1–16:12.

[13] https://bitbucket.org/ezeferrero/epm.

[14] Python Software Foundation. Python Language Reference, version 2.7.6. Available at http://www.python.org.

[15] R. Planet, S. Santucci, and J. Ortín, Phys. Rev. Lett. **105**, 029402 (2010).

[16] L. Laurson, X. Illa, S. Santucci, K. T. Tallakstad, K. J. Maloy, and M. J. Alava, Nature Communications **4** (2013).

Appendix D

Self-similarity of time series and its power spectral density

Supposing $f(t)$ is a scale invariant zero mean stationary time series, defining $g(t)\hat{=}\lambda^{\alpha_s} f(t\lambda)$, the fact that $f(t)$ and $g(t)$ are statistically similar can be formulated as $C_f(\tau) \sim C_g(\tau)$, where the auto-correlation function

$$C_f(\tau) = \lim_{T\to\infty} \frac{1}{T} \int_{-\frac{T}{2}}^{+\frac{T}{2}} dt f(t) f(t+\tau) \tag{D.1}$$

By applying the definition of $g(t)$, the definition of the auto-correlation function and the property that the power spectral density is the fourier transform of auto-correlation function, one arrives at

$$\left|\hat{f}\right|^2(\omega) \sim \lambda^{2(\alpha_s-1)} \left|\hat{f}\right|^2(\frac{\omega}{\lambda}) \tag{D.2}$$

By taking the derivative on both sides with respect to λ of the above equation and imposing $\lambda = 1$, it is straight forward to get

$$\left|\hat{f}\right|^2(\omega) \sim \omega^{2(\alpha_s-1)} \sim \omega^{-\alpha_p} \tag{D.3}$$

so that

$$\alpha_p = 2(1-\alpha_s)$$

It is also worth to notice that $\langle f^2 \rangle_t = C_f(0) = \int d\omega \left|\hat{f}\right|^2(\omega)$, meaning, without losing generality, that the variance

$$Var(f) = \langle f^2 \rangle_t - \langle f \rangle_t^2 = \int d\omega \left|\hat{f}\right|^2(\omega) - \left|\hat{f}\right|^2(0) \tag{D.4}$$

which means that the average amplitude of the power spectral density is proportional to the variance of the time series $f(t)$.

Appendix E

Linear stability analysis of the effective dynamics of the Hebraud-Lequeux model

For any given $P_{\pm c}(t)$ and $P'_{\pm c}(t)$ at the moment t, there are two stationary states:

$$\Gamma_{s,1} = 0, \dot{\gamma}_{s,1} = 0 \tag{E.1}$$

and

$$\Gamma_{s,2}(t) = \frac{C(t)B(t)}{D(t)} - A(t), \dot{\gamma}_{s,2}(t) = \frac{A(t)D(t)}{C(t)} - B(t) \tag{E.2}$$

The first conclusion can be extracted here. For the system has a fix point of non zero $\dot{\gamma}$, we should have

$$\Gamma_{s,2} > 0, \dot{\gamma}_{s,2} > 0$$

which gives:

$$\frac{C}{D} < 0$$

$$\frac{AD}{C} > B$$

Linear stability analysis gives for point zeros

$$\frac{d}{dt}\delta\dot{\gamma} = A\delta\dot{\gamma} + B\delta\Gamma$$

$$\frac{d}{dt}\delta\Gamma = C\delta\dot{\gamma} + D\delta\Gamma$$

linear stability analysis gives for the non-zero point

$$\frac{d}{dt}\delta\dot{\gamma} = \frac{BC}{D}\delta\dot{\gamma} + \frac{AD}{C}\delta\Gamma$$

$$\frac{d}{dt}\delta\Gamma = C\delta\dot{\gamma} + D\delta\Gamma$$

let the following matrix the linearization of the fix points

$$(\begin{array}{cc} a & b \\ c & d \end{array})$$

The stability can be achieved by standard linear stability analysis. For that the system have eigen values in real space λ

$$\lambda = \frac{(a+d) \pm \sqrt{(a+d)^2 - 4(ad-bc)}}{2}$$

we should have

$$(a+d)^2 \geq 4(ad-bc)$$

for the fix point to be stable, one should impose

$$a+d<0$$

$$ad-bc>0$$

Trace of the zero fix point

$$\tau_0 = A + D$$

Determinant of zero fix point

$$\Delta_0 = AD - BC$$

Trace of the non-zero fix point

$$\tau^* = \frac{BC}{D} + D = A - \frac{\Delta_0}{D} + D = \tau_0 - \frac{\Delta_0}{D}$$

The determinant of non-zeros fix point

$$\Delta^* = BC - AD = -\Delta_0$$

The positivity of non-zero fix point gives:

$$\frac{C}{D} < 0$$

$$\frac{AD}{C} > B$$

The stability of the non-zero fix point implies:

$$\tau^* < 0$$

$$\Delta^* < 0$$

so that for the non-zeros fix point to be positive and stable:

$$C < 0$$

$$D > 0$$

$$A < -D$$

$$AD < BC < -D^2$$

Oscillatory stable spiral and Stable fix point corresponds respectively:

$$-4AD > (or <)\frac{B^2C^2}{D^2} + D^2 - 2BC$$